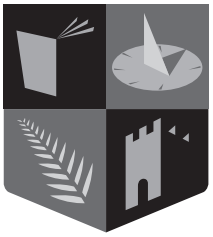
Development of a small scale wave powered data buoy



Ollscoil
Mhá Nuad
Ollscoil na hÉireann
Má Nuad

Iain McLeod

A thesis submitted for the degree of
Doctor of Philosophy

Maynooth University

Faculty of Science and Engineering, Electronic Engineering Department
Centre for Ocean Energy Research

April 2026

Head of the department: Prof. Gerard Lacey
Supervisor: **Prof. John V. Ringwood**

This thesis has been prepared in accordance with the PhD regulations of Maynooth University and is subject to copyright. For more information see PhD Regulations (December 2022).

Contents

Abstract **v**

Declaration of authorship **vii**

Acknowledgements **xi**

List of Figures **xiii**

Nomenclature **xxi**

List of abbreviations **xxvii**

1 Introduction **1**
1.1 Motivation 1
1.2 Objectives and contributions 3
1.3 Thesis structure 5
1.4 List of publications 6

2 Background **9**
2.1 Characteristics of data buoys 10
2.1.1 Data buoy applications 14
2.1.2 Data buoy power sources 15
2.1.3 Drawbacks of conventional power sources 17
2.1.4 Challenges and motivations for using wave energy to power data buoys 21
2.2 Literature review 24
2.2.1 Existing reviews 24
2.2.2 Wave-powered data buoy prototypes since 2011: by PTO mechanism 29
2.3 Chapter summary and conclusions 46

3 Hydrodynamic Modelling **49**
3.1 Linear wave theory 51
3.1.1 Wave number 51
3.1.2 Celerity 52

3.1.3 Velocity potential . . . 52
3.1.4 Assumptions . . . 52
3.1.5 Pressure . . . 56
3.1.6 Deep water vs. shallow water . . . 56
3.1.7 Energy . . . 58
3.1.8 Power . . . 58
3.2 Wave spectra . . . 59
3.2.1 JONSWAP . . . 60
3.2.2 Bretschneider . . . 62
3.2.3 Pseudo band-limited white noise . . . 62
3.3 Cummins' equation . . . 63
3.3.1 Hydrostatic force . . . 65
3.3.2 Radiation force . . . 65
3.3.3 Excitation force . . . 68
3.3.4 State space representation . . . 70
3.4 Chapter summary . . . 71

4 TENGs and OWCs as data buoy power sources 73
4.1 TENGs . . . 74
4.1.1 Operating principle of TENGs . . . 74
4.1.2 Modelling TENGs from first principles . . . 78
4.1.3 Challenges in modelling TENGs from first principles . . . 80
4.2 OWCs . . . 82
4.2.1 Operating principle of OWCs . . . 82
4.2.2 Modelling OWCs from first principles . . . 84
4.2.3 Turbines . . . 89
4.2.4 Known issues using OWCs at small scale . . . 93
4.3 Chapter summary . . . 94

5 Modelling TENGs using data based methods 95
5.1 Experimental data used . . . 96
5.2 A system identification approach to modelling a TENG powered data buoy 98
5.2.1 Signal preprocessing . . . 99
5.2.2 Input selection . . . 100
5.2.3 MISO linear ARX model identification . . . 101
5.2.4 MISO linear ARX model validation . . . 103
5.2.5 MISO nonlinear KGP model identification . . . 109
5.2.6 MISO nonlinear KGP model validation . . . 109
5.2.7 Simulated black box model on alternative floater geometries . 111
5.3 Discussion of results . . . 112
5.4 Limitations of applicability and conclusions . . . 113

6 Device description and experimental facilities 115
6.1 The JFC Marine Gannet G1250 as a floating OWC 117
6.1.1 Sealed chamber 119
6.1.2 Orifice plates 119
6.1.3 Venturi for turbine PTO 120
6.2 Sensors and data acquisition 121
6.2.1 Wave probes 123
6.2.2 Pressure sensor 125
6.2.3 Generator and encoder 127
6.3 Experimental set up at Dundalk Institute of Technology 130
6.4 Experimental set up at Lir National Ocean Test Facility 133
6.4.1 Wave tank limitations 137
6.4.2 Selection of test waves and spectra 138
6.5 Chapter summary 139

7 PTO turbine design 141
7.1 Design of a Wells turbine for use in a small-scale OWC 142
7.1.1 Testing the designed turbine 145
7.2 Design and control of the turbine load 153
7.3 Modelling turbines as equivalent orifice 157
7.3.1 Experimental determination of coefficient of discharge for orifice plate 158
7.3.2 Real turbine modelled as equivalent orifice 160
7.4 Chapter summary and conclusions 162

8 Design of a free surface elevation estimator as a sensor for data buoys 165
8.1 Choice of unknown input estimation technique 168
8.1.1 Kalman filter with random walk 170
8.1.2 Extended Kalman filter with random walk 171
8.2 Validation of estimator hydrodynamic models 171
8.2.1 Fully sealed moonpool 173
8.2.2 Fitted with orifice plates 175
8.2.3 Fitted with a controlled Wells turbine PTO 175
8.3 Chapter summary 182

9 Evaluation of a free surface elevation estimator as a sensor for data buoys 185
9.1 Simulation results 186
9.2 Test results based on first test campaign at Lir NOTF 189
9.2.1 Fully sealed device 190
9.2.2 Orifice plate representing turbine 193
9.3 Test results based on second test campaign at Lir NOTF 197
9.3.1 Controlled turbine PTO 197
9.4 Conclusions and limitations of case study 203

10 Conclusions and future work **207**
10.1 Conclusions 208
10.1.1 The state of the art of wave powered data buoys 208
10.1.2 Data based modelling of TENGs 208
10.1.3 Designing and testing a turbine specifically for small scale OWCs 209
10.1.4 Testing a full size wave powered data buoy prototype in a wave tank 210
10.1.5 Designing and testing a free surface elevation estimator for wave powered data buoys 211
10.2 Future work 212
10.3 Final Remarks 212

References **215**

Abstract

Wave-powered data buoys present an interesting opportunity for wave energy converters (WECs), with wave energy seeming a somewhat obvious power source for ocean monitoring buoys. Being small scale, and therefore relatively inexpensive when compared to large grid-scale industrial WECs, data buoys present a potential testbed for WECs; exposed to many similar challenges that large-scale projects face, at only a fraction the cost. However, wave energy at this small scale brings with it a number of challenges. With small scale devices experiencing exaggerated effects from friction and drag, the existing literature suggests that there is a split in the research community, with some advocating that for small scale devices, WEC solutions should be specifically designed for the small scale, such as triboelectric nanogenerators (TENGs); whereas others believe that scaling down a large-scale power take-off (PTO) is the more viable route to success for wave energy at the small scale.

This thesis studies both a specifically small scale PTO, in the form of a rolling-ball-type TENG, which has negligible impact on the device dynamics, and a more conventional oscillating water column (OWC) PTO, which does affect the device dynamics. To account for changes in device dynamics, a free surface elevation estimator is designed and tested, to counter the common assumption that a wave measuring data buoy must be a true wave follower in order to accurately return measurements of the characteristic wave parameters commonly required by data buoy end users.

Declaration of authorship

I, Iain McLeod, declare that this thesis titled 'Development of a small scale wave powered data buoy' and the work presented in it are my own. I confirm that:

- This work was done wholly or mainly while in candidature for a research degree at this University.
- Where any part of this thesis has previously been submitted for a degree or any other qualification at this University or any other institution, this has been clearly stated.
- Where I have consulted the published work of others, this is always clearly attributed.
- Where I have quoted from the work of others, the source is always given. With the exception of such quotations, this thesis is entirely my own work.
- I have acknowledged all main sources of help.
- Where the thesis is based on work done by myself jointly with others, I have made clear exactly what was done by others and what I have contributed myself.

Date: _____

Signature: _____

For Granny

Acknowledgements

This project (Grant-Aid Agreement No. ES/20/003) is carried out with the support of a Marine Institute Eoin Sweeney Scholarship and funded under the Marine Research Programme by the Irish Government. I would like to express my gratitude to the Marine Institute, especially to Veronica Cunningham and Martina Maloney, for their generosity and support throughout this PhD project.

I would like to thank my supervisor John V. Ringwood for his insights and guidance, and for all he has taught me about research and scientific writing.

Tom Kelly at Dundalk Institute of Technology is someone I could not have completed this project without, and I would like to sincerely thank him for all the time and energy he has committed to this project.

Throughout my time at the Centre for Ocean Energy Research (COER) there have been countless occasions where my peers and colleagues have helped me out. First of all I need to thank Carrie Anne Barry, who has gone above and beyond in all aspects to ensure I have felt supported at COER. In no particular order, I would also like to thank Yerai Peña-Sanchez and Pedro Fornaro for their help in my understanding of Kalman filters and unknown input estimators; Gastón Vergara-Hermosilla for his help in understanding system identification; Hafiz Ahsan Said and Marco Rosati for their help with oscillating water columns and WEC systems more generally; Matheus Mulherchen Golz Costa for all his help in understanding data sheets and for all his guidance in electronic circuits; as well as the countless other members who have made COER such a fantastic research group to do my PhD with.

The conversations I have had with those outside of COER have also played a vital role in shaping my understanding of data buoys and wave energy at the small scale. A special thank you goes to Daniel Clemente, who has been a great unofficial mentor throughout my PhD. I would also like to thank Josh Davidson, João C. C. Henriques, Zak Hawthorne, Matias Carandell Widmer, Barry Christy, Aoife Hegarty, Andrew Hamilton, Rayco Moran, and all those with whom I have had conversations at conferences and workshops throughout my PhD journey.

I am grateful to John Maloco and Denis Buckley for all their help sourcing components and preparing everything for testing. I would also like to thank Brendan Walsh, for sharing the results from his test campaign at Lir NOTF with me, and all the staff at Dundalk IT who helped me with the wave tank testing there, and preparing the device

for transport to Cork. I am also grateful to Cátia Rodrigues, Joao Ventura and the team at the University of Porto for sharing their TENG wave tank test data with me.
It was also lovely to see Mahdiyeh Farajvand again at Lir NOTF, thank you for all the photos! The other staff I worked with there, Milad Zabihi Kooykheily and Mahdi Ebrahimi Salari, made me feel very welcome and ensured a smooth wave tank test campaign in Cork.
I am indebted to my friend Tristan Nairn for giving up so much of his time to give me a crash course in LabVIEW, without which I would not have been able to get things running!
It would also be remiss of me not to mention the great staff at Trim library for providing such a fantastic study space for me to write my thesis in.
Thank you also to Mansoor Barati, Werner Schiffers, Kenny McFarlane, Patrick Norman and Alasdair Goodman for their letters of support, and enthusiasm for my pursuit of a PhD. I would like to show my appreciation also to Gerry Lacey for his words of encouragement, as well as to Fidelma Curley and the team at Student Counselling for helping me past the toughest point of my PhD.
A PhD journey is not an easy one, and it would not have been possible without the overwhelming support from my wife Yael, my sister Lydia, and the rest of my family in Scotland, Germany and Canada. I love you dearly.

List of Figures

2.1 Map of data buoys partnered with the National Data Buoy Center (NDBC), including Met Éireann's M-buoy network, and the UK Met Office's K-buoys. Created using the interactive map tool on the National Oceanic and Atmospheric Administration (NOAA) website [25]. . . . 11

2.2 Showing water damaged solar panel from one of Met Éireann's M-buoys. The red circle highlights how subtle such damage can look, while still causing operational failure. 19

3.1 Wave parameters describing a linear regular wave: where η is the free surface elevation, c_w is the wave celerity, A_w is the wave amplitude, H is the wave height, d is the water depth, L is the wavelength and T is the wave period. SWL marks the still water level. 51

3.2 Difference in wave particle motions (orbits shown in dashed blue, with the blue arrow indicating direction of orbit), depending on whether the wave is propagating in shallow or deep water. 57

3.3 Comparison of the shape of some example theoretical wave spectra sent to the wavemaker at Lir NOTF. 61

3.4 Showing the numbering convention for DoFs as set out by SNAME: where translational DoFs, 1, 2 and 3 (shown in blue), correspond with surge, sway and heave respectively; and rotational DoFs, 4, 5 and 6 (shown in red), correspond to roll, pitch and yaw respectively. 63

3.5 Pseudo free-body diagram of a heaving buoy, with the hydrostatic stiffness c shown as a spring, the radiation damping coefficient, $b_r(\omega)$, as a damper and the radiation added mass, $a_r(\omega)$, represented as an addition to the buoy mass M by the dashed red box. 64

3.6 Showing the variation in hydrostatic force against z-displacement for a floating object. Once the object has been fully submerged, f_{hs} becomes constant, and when the body leaves the water entirely, $f_{hs} = 0$. 66

3.7 An example comparing the impulse response functions of state space equivalents obtained using the FOAMM and the HSVD approaches. The best fit model is found to be of order 3, with a corresponding normalised MAE of 0.0212 and normalised RMSE of 0.0522. 68

3.8 A comparison of the noncausal impulse response function obtained from the WAMIT results, and the subsequent causalisation and the impulse response from the identified state space approximation. 69

4.1 The four main types of TENG mode classification: a) Translational contact separation mode b) Lateral sliding mode c) Single electrode mode d) Free standing triboelectric layer mode. 75
4.2 Operating principle of the rolling-ball type TENG used in this project. Periodic contact separation is driven by ball movement and a PTFE film designed to elastically return to a position where a gap is formed between it and the triboelectrically opposed Nylon 6,6 film. 77
4.3 Photograph of rolling-ball-type TENG prototype, manufactured at the University of Porto. The free movement of the spheres over the film makes obtaining a model from first principles impractical. 81
4.4 Operating principle of floating OWC with a vertical moonpool. Changes in free surface elevation η drive relative motion between the buoy heave mode z_3 and the piston mode of the water column z_7 forcing air through the orifice in which a turbine PTO can be installed. 83
4.5 Example of added mass for the piston mode of an OWC, reconstructed from the radiation damping to correct the trend towards $-\infty$, which is symptomatic of the massless disc approximation approach. Also achieved is the removal of 'irregular frequencies'. 89
4.6 The Wells turbine uses a number of evenly spaced symmetrical aerofoils, angled at 0 degrees, meaning the airflow across the blade behaves identically irrespective of direction. The rotational speed of the turbine produces an angle of attack in the airflow, generating lift. 91
4.7 An axial flow impulse turbine consists of two stators with guide vanes, which channel air to the central rotor, such that the tangential force on the rotor is always in the same direction, irrespective of airflow direction, maintaining unidirectional spin. 92

5.1 Section view of UL-TENG consisting of parallel channels orientated to the direction of wave propagation for wave tank testing. Each channel contains two steel balls driving contact separation as shown in Fig. 4.2. Additional contact separation occurs between the hinged Nylon 6,6 flaps and the PTFE wall when a ball reaches the end of the channel. 97
5.2 Initial black box model with all 6 DoFs considered. 98
5.3 Comparison of current signal with and without noise filtering applied. The filtered current has also been linearly interpolated to ensure the same timesteps for the current data and the movement data are used. . 100

5.4 10-step ahead prediction model output current ($\hat{y}$), compared with validation data (y) for a single linear ARX model trained using all 8 wave conditions. a) Wave condition 1 b) Wave condition 2 c) Wave condition 3 d) Wave condition 4 e) Wave condition 5 f) Wave condition 6 g) Wave condition 7 h) Wave condition 8. 106
5.5 Uncorrected simulation model output current ($\hat{y}$), compared with validation data (y) for a single linear ARX model trained using all 8 wave conditions. a) Wave condition 1 b) Wave condition 2 c) Wave condition 3 d) Wave condition 4 e) Wave condition 5 f) Wave condition 6 g) Wave condition 7 h) Wave condition 8. 107
5.6 Uncorrected simulation model output current ($\hat{y}$), compared with validation data (y) for the linear ARX model trained only on wave conditions 1-3. a) Wave condition 1 b) Wave condition 2 c) Wave condition 3. 108
5.7 10-step ahead prediction model output currents for the KGP and ARX model compared with validation data (y) for wave condition 4. 110
5.8 Uncorrected simulation output using the displacements of a 1:8 Froude-scaled Balizamar B1600S buoy. Since the magnitude of current readings is similar to that of tests on the Sealite buoy, there is some promise for the applicability of the model on the Balizamar test geometry. 112
5.9 Uncorrected simulation output using the displacements of a cylinder of similar size to the model of the Sealite Atlantic-2600. Though the magnitude of current readings is again similar to that of tests on the Sealite buoy, the shape of the generated response is quite different, likely due to a lack of geometric similarity. 113

6.1 Diagram of JFC Gannet G1250, where 1250 refers to its 1.25 m diameter. Note the modifications made for use as a floating OWC, specifically a custom top plate, and the open central chamber in the steel core frame. 118
6.2 Design of frame holding two 25 mm thick steel plates representing the mass of the batteries that would be mounted on a data buoy in an at sea deployment. 120
6.3 Exploded view of Venturi assembly, manufactured from an 8 mm thick stainless steel baseplate to which the lower funnel is welded. The central cylindrical section is clamped to the lower funnel via a rubber gasket and tri-clamp. The cross-shaped mounting for the generator slots into grooves in the central section again secured by a tri-clamp and rubber gasket. 122
6.4 Showing how the turbine was digitally split in two to ensure no post-processing of the turbine 3D-print, to remove supports, was required. . 123

6.5 Example of resistive wave probes used in testing. The plastic spacer is held in place with silicon to stop it from detaching during tests. 124
6.6 Example calibration of a resistive wave probe used in wave tank testing. Changes in vertical position are achieved by moving the probe with respect to its datum position. The equation of the resultant straight line ($y = 0.683x - 0.294$, with an R^2 fit of 0.9999) is used to convert the voltage readings into metres of wave elevation. 125
6.7 Set up for calibrating Honeywell 176PC14HD2 pressure sensor. A U-bend made of glass piping is filled with incremental amounts of water causing pressure build up in the silicon tubing connecting both the digital manometer and the chosen port of the pressure sensor. . . . 126
6.8 Calibration for Honeywell 176PC14HD2 pressure sensor. The equation of the resultant straight line ($y = 979576x - 10.7$ with an R^2 fit of 0.9999) is used to define the multiplication blocks in LabVIEW which convert the voltage into pressure readings in Pascals. 127
6.9 Design of initial circuit with variable load. The speed of the generator, G, is read by the counter function a NI9401 module. Note that the functions of ammeter, A, and voltmeter, V, are performed by the NI9219 and used to acquire real-time readings of the generator power. 128
6.10 KidWind generator efficiency curve. Scanned from printout found with the generator. No longer available online. The straight line marked I shows the linear relationship between generator torque and current, which is typical of permanent magnet DC generators. 129
6.11 Section view of wave tank testing layout at DkIT, showing the position of wave probes, wavemaker, and the fixed OWC to which the orifice plates and Venturi were alternatively attached. 132
6.12 Experimental set up for determining C_d, using a pressure sensor and a single wave probe in a wooden chamber with the 25 mm orifice plate attached to the opening at the top. The test area with glass observation pane is located approximately 10.6 m from the wave maker. 133
6.13 Experimental set up for characterising the behaviour of the Wells turbine. A variable aperture seals where the encoder and generator lines enter the Venturi. The upper and lower pressure sensors are connected to 1/4" BSP fittings to obtain an airtight connection to the air inside the Venturi. 134
6.14 Plan view and section view of wave tank testing layout at Lir NOTF, showing the position of wave probes, wavemaker, and the mooring location of the G1250 Gannet buoy. 135
6.15 a) Shows the experimental set up used for the first campaign with a mass to represent the batteries, and the orifice plate or seal with fitted pressure sensor. b) Shows the set up for the second test campaign with a pressure sensor on both the lower and upper Venturi, as well as cables to transfer power from the generator and encoder readings back to shore. 136

6.16 Tank envelope for the Deep OCean Basin at Lir NOTF. Note that waves to the left of the dashed red line are limited by the paddle stroke of the wave makers, while those to the right are limited by wave breaking. . 137

7.1 Final dimensions (in mm) of Wells turbine used in experimental testing. The aerofoil profile used for the blades is approximately NACA0026, with turbine diameter 81 mm, hub diameter 45.5 mm, chord length 19 mm and span length 17.7 mm. The 7.9 mm extrusion from the flat side of the turbine hub is bored to accommodate the shaft of the DC generator used. 145
7.2 Comparison of volumetric flow rates for a 0.85 Hz wave with a 30 mm wave height. As with the pressure, shown in Fig. 7.3 it can be seen that the turbine speed has almost no effect on the behaviour of the volumetric flow rate inside the OWC chamber. 150
7.3 Comparison of moonpool pressures for a 0.85 Hz wave with a 30 mm wave height. Again it can be seen that the turbine speed has almost no effect on the behaviour of the pressure inside the OWC chamber. . . . 151
7.4 The dimensionless characteristic curves resulting, when grouping experimental results by wave height. As the wave height is reduced, lower pneumatic to turbine power efficiency peaks are reached, with 25 mm waves reaching a peak efficiency almost 5 times lower than for 40 mm waves. 152
7.5 Showing the relationship between the dimensionless pressure and volumetric flow rate. As expected for a Wells turbine, the relationship appears to be mostly linear, though as dimensionless volumetric flow rate drops a change in the linear relationship can be noted. 153
7.6 Showing design of electronic load which can be varied by the PWM output from the NI9401. Note that the functions of ammeter and voltmeter are performed by the NI9219. The PWM conditioning was found not to be required, and dropped in later experiments. 154
7.7 Showing the effects of PWM duty cycle on the rotational speed of the generator under steady state waves with a wave height of 0.03 m and frequency of 0.85 Hz. Increasing the duty cycle increases the current drawn, in turn reducing the rotational speed of the turbine. 156
7.8 Showing the effects of PWM duty cycle on the power captured by the generator for the same waves used in Fig. 7.7. As the generator speed drops, voltage also drops, meaning at slow rotations little power is generated, despite drawing higher current. 157
7.9 Showing comparison of the step responses of the experimental system and the identified transfer function describing the system. The response shown is used to determine the time constant and the rotational speed reached when the system is excited with a 1V step input. 158

7.10 Showing the set point tracking controller in a regular wave with a frequency of 0.725 Hz wave and a wave height of 150 mm. A set point speed of 265 rad/s is set to correspond with the maximum power point for this wave condition. 159
7.11 Showing the set point tracking controller in irregular Bretschneider waves with a modal frequency of 0.775 Hz, and significant wave height of 100 mm. The set point is determined to be at 25 rad/s, to ensure some control action is generated, since this irregular wave condition produces a maximum free spin velocity of only around 70 rad/s. . . . 160
7.12 Determination of C_d for the 25 mm orifice from experimental results, plotting the measured volumetric flow rate, against the theoretical volumetric flow rate. 161
7.13 Determination of C_d for a turbine modelled as an equivalent orifice from experimental results, plotting measured volumetric flow rate, against the theoretical volumetric flow rate calculated by orifice equation (7.16). 162

8.1 Schematic showing how an existing motion sensor feeds buoy heave measurements, z_3, to the estimator which estimates the external free surface elevation, $\hat{\eta}$, accounting for the effects of the piston mode of the OWC, z_7, on the device dynamics. The orifice plate represents the turbine PTO, a functioning version of which is also designed and tested as part of this project. 166
8.2 Regular wave validation of the linear hydrodynamic model, showing the effects of the additional damping term introduced in (8.8). 173
8.3 Irregular wave validation of the linear hydrodynamic model, showing the effects of the additional damping term introduced in (8.8). Note the anomalous spike in magnitude at approximately 36 s, which is an indicator of a snatch load at this time step. 174
8.4 Validation results comparing the heave displacement calculated by the 25 mm orifice plate model and the measured heave displacement from Qualisys. Note the imperceptible difference when accounting for air compressibility and the model assuming air incompressibility. 175
8.5 Comparison of device heave motion with turbine speed controlled at a set point of 200 rad/s compared to when the turbine is in uncontrolled free spin (approximately 400 rad/s). As shown in Fig. 8.6, any differences in device displacement are due to slight differences in wave height caused by inaccuracies in the wavemaker, rather than turbine speed. 177
8.6 Comparison of wave probe measurements for the tests compared in Fig. 8.5. It can be seen that though the wavemaker attempts to recreate identical waves for both runs, the inaccuracies in the wave maker mean that there are variations between the two waves, reflecting the trends seen in Fig. 8.5. 178

8.7 A comparison in irregular waves considering the device heave motion with the PWM signal set to 0 (no load/fastest rotation) for one run, and then 100 (maximum load/slowest rotation) for the next. Again there is a very small difference between runs which can again be attributed to slight differences in the waves produced by the wavemaker. 179
8.8 Comparison of wave probe measurements of free surface elevation for the tests shown in Fig. 8.7. Like in the regular wave tests, shown in Figs. 8.5 and 8.6, there are slight variations in the free surface elevation between the two irregular wave tests, which again show that turbine speed has a negligible effect on the device dynamics. 180
8.9 Validation results comparing the sensitivity of the OWC model with a turbine to chosen values of C_d. The model output "Min. Cd" uses a C_d of 0.203 and an A_{ori} of 0.0054 m^2, with "Max. Cd" using a C_d of 1 with the minimum A_{ori} of 0.0011 m^2. In both cases the product of A_{ori} and C_d is 0.0011. 181
8.10 Validation results comparing the heave displacement of the model for the floating OWC fitted with a working PTO in irregular waves to the measured heave displacement from Qualisys. 182

9.1 Comparison of measured free surface elevation, estimator output and buoy displacement, for the Gannet G1250 with a fully sealed moonpool, in irregular waves, reflective of those at the PLOCAN test site. The device heave motion is close to the measured free surface, since the sealed buoy exhibits behaviour close to a true wave follower. 187
9.2 Estimator output, compared to measured free surface elevation, and buoy displacement, for the Gannet G1250 fitted with a 25 mm orifice plate, in the same irregular waves used in Fig. 9.1. 188
9.3 Estimator output, compared to measured free surface elevation, and buoy displacement, for the Gannet G1250 fitted with a Venturi and working turbine PTO, in the same irregular waves used in Figs. 9.1 and 9.2. 188
9.4 Estimated free surface elevation in regular waves for the fully sealed moonpool, compared against the measured free surface, and the heave displacement of the buoy itself. 191
9.5 Estimated free surface elevation in irregular waves for the fully sealed moonpool, compared against the measured free surface, and the heave displacement of the buoy itself. Again, note the presence of snatch loads at 15 s and 48 s. 192
9.6 Estimated free surface elevation in irregular waves for the fully sealed moonpool, as in Fig. 9.5; here showing performance after running for more than 12 minutes in irregular waves. 192

9.7 Scatter plot for the fully sealed moonpool tests, showing the errors in obtaining T_z and H_s, with positive errors showing overestimation, and negative errors showing underestimation. 193
9.8 Estimated free surface elevation in regular waves for the 25 mm orifice plate, compared against the measured free surface, and buoy heave displacement. Though buoy heave motion follows the free surface elevation closely during the initial transient period, once steady state oscillation is reached the estimator output is a significantly closer match. 195
9.9 Scatter plot for the 25 mm orifice plate tests, showing the errors in obtaining T_z and H_s, with positive errors showing overestimation, and negative errors showing underestimation. 196
9.10 Estimated free surface elevation in irregular waves for the 25 mm orifice plate, compared against the measured free surface, and the heave displacement of the buoy itself. 197
9.11 Estimated free surface elevation in regular waves, for the test case using a real turbine, compared against the measured free surface, and the heave displacement of the buoy itself. 198
9.12 Estimated free surface elevation in irregular waves, generated by a JONSWAP spectrum for the test case using a real turbine, compared against the measured free surface, and the heave displacement of the buoy itself. 199
9.13 Scatter plot for the real turbine tests, showing the errors in obtaining T_z and H_s, with positive errors showing overestimation, and negative errors showing underestimation. 200
9.14 Estimated free surface elevation in irregular waves, generated by a Bretschneider spectrum for the test case using a real turbine, compared against the measured free surface, and the heave displacement of the buoy itself. 201
9.15 Comparison of estimator performance in irregular waves, generated by a pseudo band-limited white-noise spectrum for the test case using a real turbine. Buoy surge motion is also included on the right y-axis, showing the effects that drifting in the surge direction has on the estimator phase (positive surge is in the direction of wave propagation). 202
9.16 Power output during testing at Lir NOTF, in irregular waves generated from a pseudo band-limited white-noise spectrum. 204

Nomenclature

A, B, C, D	State space matrices obtained from the physical description of the system
A_e, B_e, C_e, D_e	State space matrices referring to the excitation force approximation
$A_{nl}, B_{nl}, C_{nl}, D_{nl}$	State space matrices referring to the nonlinear model of the system fitted with an orifice plate or turbine
$A_{rc}, B_{rc}, C_{rc}, D_{rc}$	State space matrices referring to the radiation convolution force approximation
A_{ori}	Cross-sectional area of the orifice
A_{owc}	Cross-sectional area of the OWC chamber
A_w	Wave amplitde
a	Infinite frequency added mass
a_r	Radiation added mass
AR	Blade aspect ratio
b_{add}	Additional damping term
$\boldsymbol{B}$	Magnetic field
b_r	Radiation damping coefficient
c	Hydrostatic stiffness
C_d	Coefficient of discharge of the orifice
c_s	Speed of sound in air
c_w	Wave celerity
C_v	Heat capacity at constant volume
d	Water depth
$d(\omega)$	Bandwidth
$\boldsymbol{D}$	Displacement of the medium
$\boldsymbol{D'}$	Electric field displacement
D_{hub}	Hub diameter

D_h	Hydraulic diameter
D_{turb}	Turbine diameter
D_{vent}	Venturi diameter
E_k	Kinetic energy
$\boldsymbol{E}$	Applied electric field
E_p	Potential energy
E_w	Total energy in wave
f_{ex}	Excitation force
f_{hs}	Hydrostatic restoring force
f_{pto}	Force from the PTO
f_r	Radiation force
f_{rc}	Force due to the radiation convolution term
g	Acceleration due to gravity
H	Wave height
h_0	Height of the still water level within the chamber, measured from the bottom of the chamber
H_{ex}	Excitation force frequency response function
H_{mo}	Significant wave height approximated in the spectral domain
H_s	Significant wave height
HTR	Hub to tip ratio
I	Identity matrix
I_D	Drain current of the MOSFET
I_L	Load current
I_{stall}	Generator stall current
$\boldsymbol{J}_f$	Free electric current density
k_{ex}	Excitation force impulse response kernel
k_r	Radiation force kernel
k_w	Wave number
K_T	Generator torque constant
L_c	Characteristic length
L	Wavelength

l_{chord} . . . . . Chord length

l_{span} . . . . . Span length

m_0 . . . . . Variance, or zero-order moment

m_2 . . . . . Second spectral moment

M . . . . . Buoy mass

$\dot{m}$ . . . . . Mass flow rate of air

n_a, n_b . . . . . KGP and ARX model orders

n_k . . . . . KGP and ARX model delay

N_b . . . . . Number of turbine blades

$NRMSE$ . . . . Normalised root mean square error

p . . . . . Gauge pressure

p_{atmos} . . . . . Atmospheric pressure

$\boldsymbol{P}$ . . . . . Local polarisation caused by free charges

$\boldsymbol{P}_{\mathrm{s}}$ . . . . . Polarisation of surface charges already present on the medium

P_{turb} . . . . . Turbine power output

P_w . . . . . Power in the wave

$\%_{GoF}$ . . . . . Percentage goodness of fit

q . . . . . Volumetric flow rate

q_t . . . . . Theoretical volumetric flow rate

$\dot{Q}$ . . . . . Rate of change of heat energy

Q . . . . . Process white noise covariance matrix

R . . . . . Measurement white noise covariance matrix

R_{eq} . . . . . Equivalent resistance of the electronic load

R_g . . . . . Gas constant

R_s . . . . . Resistance of the resistor connecting the MOSFET source to ground

Re_{turb} . . . . . Reynolds number related to the blade performance

Re_{vent} . . . . . Reynolds number relating to the airflow through the venturi

$S(\omega)$ . . . . . Spectral density for each frequency band

T . . . . . Period

T_d . . . . . Dominant period of the sea state

t_c . . . . . Causalisation time

T_g	Temperature of the gas
T_{stall}	Generator stall torque
T_{turb}	Turbine torque
T_z	Zero-crossing period
u	Fluid velocity
u	System input vector
$\dot{U}$	Rate of change of internal energy
u_x, u_z	Water particle velocities in x and z
V_c	Controller output voltage
V_{gen}	Generator voltage
$\boldsymbol{v}$	Velocity of the medium
$\dot{V}$	Rate of change of air volume in the moonpool chamber
v_{rel}	Relative velocity between the v_{vent} and v_{tip}
v_{tip}	Tip velocity of the turbine
v_{vent}	Velocity of the air flow across the turbine
$\dot{W}$	Rate of change of work done
X	Vector of state variables
X_e	States required for the excitation force approximation
X_{rc}	States required for the radiation convolution term approximation
x, y, z	Directions in three-dimensions
$\hat{\boldsymbol{y}}$	Model output vector containing $[\hat{y}(1), \hat{y}(2), \hat{y}(3), ...\hat{y}(N)]^T$
$\hat{y}(k)$	Model predicted at time k
$y(k), u(k)$	k^{th} output and input samples respectively
Y	System output vector
z_3, z_7	Heave displacement for the buoy and piston mode of the OWC respectively
α	Philips constant relating fetch length and wind speed
η	Free surface elevation
η^{KFRW}	Estimate for the free surface elevation
$\dot{\eta}_{owc}$	Differentiated signal of the free surface elevation within the chamber
ϵ	Process white noise

ε_0 . . . . . Vacuum permittivity

γ, σ . . . . . Defining parameters of a JONSWAP spectrum

γ_{air} . . . . . Heat capacity ratio of air

$\mathbf{\Lambda}$ . . . . . Regression matrix

μ_{air} . . . . . Dynamic viscosity of air

μ . . . . . Measurement white noise

ν_{air} . . . . . Kinematic viscosity of air

ω_l, ω_u . . . . . Lower and upper spectral limits respectively

ω_m . . . . . Modal frequency

ω_p . . . . . Peak frequency

$\mathbf{\Omega}$ . . . . . Rotational or angular velocity of turbine

$\mathbf{\Omega}_{mep}$ . . . . . Maximum efficiency point angular velocity of turbine

$\mathbf{\Phi}$ . . . . . Dimensionless flow coefficient

ϕ . . . . . Velocity potential

Π . . . . . Dimensionless power

$\mathbf{\Psi}$ . . . . . Dimensionless pressure head

$\mathbf{\Psi}_{mep}$ . . . . . Maximum efficiency point dimensionless pressure head

ρ_{air} . . . . . Density of air

ρ_{atmos} . . . . . Atmospheric air density

ρ_f . . . . . Space charge density of free charges

σ_{turb} . . . . . Turbine solidity

ζ . . . . . Turbine efficiency

$\zeta_\eta(k)$ . . . . . Random number, independently and identically distributed in size

List of abbreviations

AMOC . . . . . Atlantic Meridional Overturning Circulation

ARX . . . . . Autoregressive with exogenous variable

AUVs . . . . . Autonomous underwater vehicles

AWSNs . . . . . Aerial wireless sensor networks

BEM . . . . . Boundary element method

BSP . . . . . British standard pipe

CFD . . . . . Computational fluid dynamics

CoG . . . . . Centre of gravity

CPGU . . . . . Core power generation unit

DkIT . . . . . Dundalk Institute of Technology

DoF . . . . . Degree of freedom

DTU . . . . . Technical University of Denmark

EAHs . . . . . Electroactive polymers harvesters

EKFRW . . . . Extended Kalman filter with random walk

EMHs . . . . . Electromagnetic harvesters

EMF . . . . . Electromotive force

ESA . . . . . European Space Agency

FDM . . . . . Fused deposition modelling

FEA . . . . . Finite element analysis

FOAMM . . . . Finite Order Approximation by Moment-Matching

FPGA . . . . . Field programmable gate array

GNSS . . . . . Global navigation satellite system

GoF . . . . . Goodness of fit

HHs . . . . . Hybrid harvesters

HiL . . . . . Hardware in the loop

HSVD . . . . . Hankel singular value decomposition

IEEE . . . . . Institute of Electrical and Electronics Engineers

IMDBON . . . Irish Marine Data Buoy Observation Network

IMU . . . . . Inertial measurement unit

IP . . . . . Intellectual property

IST . . . . . Instituto Superior Técnico

JONSWAP . . . Joint North Sea Wave Project

KFRW . . . . . Kalman filter with Random Walk

KFHO . . . . . Kalman filter with harmonic oscillator

KGP . . . . . Kolmogorov–Gabor polynomial

LiDAR . . . . . Light detection and ranging

Lir NOTF . . . Lir National Ocean Test Facility

MAE . . . . . Mean absolute error

MaREI . . . . . Science Foundation Ireland Research Centre for Energy, Climate and Marine

MBARI . . . . . Monterey Bay Aquarium Research Institute

MELOA . . . . Multi-purpose/Multi-sensor Extra Light Oceanography Apparatus

MISO . . . . . Multiple input single output

MOSFET . . . Metal-oxide-semiconductor field-effect transistor

MPC . . . . . Model predictive control

MPPT . . . . . Maximum power point tracking

NACA . . . . . National Advisory Committee for Aeronautics

NDBC . . . . . National Data Buoy Center

NOAA . . . . . National Oceanic and Atmospheric Administration

NRMSE . . . . Normalised root mean square error

op-amp . . . . . Operational amplifier

OPT . . . . . Ocean Power Technologies

OWC . . . . . Oscillating water column

PB . . . . . POWERBUOY

P . . . . . Proportional

PI . . . . . Proportional-integral

PID . . . . . Proportional-integral-derivative

PLOCAN . . . . Oceanic Platform of the Canary Islands

PTFE . . . . . Polytetrafluoroethylene

PTO . . . . . Power take-off

PV . . . . . Photovoltaic

PWM . . . . . Pulse-width modulation

RAO . . . . . Response amplitude operator

RC . . . . . Resistor-capacitor

RHE . . . . . Receding horizon estimation

RM3 . . . . . Reference Model 3

RMSE . . . . . Root mean square error

ROVs . . . . . Remotely operated vehicles

SI . . . . . System identification

SNAME . . . . Society of Naval Architects and Marine Engineers

SWL . . . . . Still water level

TENG . . . . . Triboelectric nanogenerator

TRL . . . . . Technology Readiness Level

UIO . . . . . Unknown input observer

UL-TENG . . . Unidirectional lateral-based TENG

UN . . . . . United Nations

UWSNs . . . . . Underwater wireless sensor networks

WASP . . . . . Wave Activated Sensor Power Buoy

WEC . . . . . Wave energy converter

WSNs . . . . . Wireless sensor networks

"An ocean of knowledge is apt to drown you long before it educates you."

— Mark Lawrence, *The Book That Wouldn't Burn*.

1 Introduction

Contents

1.1 Motivation **1**
1.2 Objectives and contributions **3**
1.3 Thesis structure **5**
1.4 List of publications **6**

1.1 Motivation

Data buoys are one of the most useful tools available for ocean monitoring. As small-scale independent units or as part of a larger sensor network, data buoys have become a mainstay of weather forecasting and coastal surveillance. Early iterations of data buoys relied on diesel generators as their power source [1], but with advancements in battery technology and the reliability of photovoltaic (PV) solar panels, these technologies have replaced the diesel generators of old and become the conventional power sources for the majority of data buoys in use today. PV panels and batteries provide data buoys with a reliable supply of power which requires only infrequent maintenance and can otherwise function independently; providing either real-time or periodic packaged transmissions of the information they have gathered. This thesis considers the use of wave energy as an alternative power source to the solar and battery power prevalent in data buoys today, and considers the challenges posed in using wave energy as a power source for data buoys.

Wave energy has been considered for powering small scale buoys since Yoshio Masuda's oscillating water column (OWC) based navigation buoy, which he began working on in 1945 [2] and still inspires research carried out on OWCs in the last decade [3].
Moreover this study proposes solutions to using wave energy at the small scale that may help wave energy converters (WECs) reach the same stage of advanced development as PV panels and batteries, which currently out-compete wave power in the data buoy field.
A secondary motivation for using wave energy on data buoys is the potential for data buoys to act as a low-cost testbed from which lessons learnt can be applied to larger scale WEC projects. Full-scale prototypes for large-scale WECs are often prohibitively expensive, which has led to the demise of a number of prominent wave energy companies (see [4], [5] and [6]). Even where upfront investment costs have been met, the monetary value of full-scale prototypes means that testing is fraught with high financial risk, where mistakes can lead to disaster, as happened to Oceanlinx [7], where the destruction of their 1:1 prototype during the deployment passage sent the company into administration [5]. Being small scale devices with an immediately useful output, data buoys are proposed as a lower risk testbed for these large scale WECs, facing similar in-service issues, but with a much lower capital cost. In [8] it is noted that wave energy projects rarely proceed beyond the development mid-point, mostly due to the rapidly increasing amount of capital required. Using wave energy for data buoys, where costs are far more modest, in comparison to grid-scale devices, has the potential to establish wave energy as a viable renewable source of energy.
However, initial research does throw up some caveats which must be noted. Firstly, a commercial example of where data buoys were used as a proof of concept for powering a wave farm, consisting of a network of buoys using the same power take-off (PTO), can be found in [9]. In [9], Ocean Power Technologies (OPT) (one of the few companies to have successfully deployed wave-powered data buoys) proposed to use their wave powered electromagnetic drive PB3 data buoys, most commonly used for surveillance [10], as an array on a wave farm to generate up to 62MW off the coast of Australia, in a project partnered with Lockheed Martin [9]. Unfortunately, even with the PB3's proven track record as a data buoy, the project soon collapsed with the developers deciding it was not commercially viable [11]. This highlights the power industry's current lack of confidence in scaling the performance of individual data buoys to large-scale applications.
Furthermore, the findings of a review on triboelectric nanogenerators (TENGs), [12], state that the reason small scale wave power projects have previously failed is precisely because they have tried to scale down a solution for a larger device. One key issue with scaling PTO mechanisms is that the magnified effects of friction at a small scale may significantly change the effectiveness of a particular PTO mechanism. Hence [12] insists that, for small-scale projects, the solutions must also be small-scale, in

their belief: TENGs. This sentiment is echoed by another recent review [13], which finds that the typical requirements of data buoys are generally at odds with the typical specifications of an electromagnetic generator. [13] advocates the use of TENGs as a promising solution to small-scale wave energy applications.
This thesis seeks to investigate the challenges around using wave energy at the small scale. Considering the rift in the research landscape between those advocating for PTOs designed specifically for small scale applications and those with the belief that established PTOs should be scaled down, two PTOs are considered.
Representing a PTO designed specifically for the small scale, TENGs are considered. An advantage of TENGs, for data buoys specifically, is that the rolling-ball-type TENGs investigated in [12] are found to have negligible impact on device dynamics, and therefore are unlikely to interfere with onboard sensor requirements.
Representing an established PTO, scaled down for data buoy applications, OWCs are considered, since these are one of the best established wave energy PTOs, which still pose significant challenges at the small scale, particularly with regard to the self-rectifying turbines required. Furthermore, OWCs have some impact on the dynamics of the device, meaning that they are not necessarily wave followers, which is a particular requirement for data buoys measuring characteristic wave parameters, such as dominant period and significant wave height. Therefore, an estimator is proposed which can take into account the dynamics of a wave energy PTO and return free surface elevation measurements from device motion recorded from an existing sensor, such as an inertial measurement unit (IMU).

1.2 Objectives and contributions

Objective 1: To identify the current state of the art of wave energy as it pertains to data buoys and to identify challenges obstructing the wider adoption of wave energy as a power source for data buoys.
Contribution 1: Extensive literature review considering not only wave powered data buoy projects to date, but also an investigation into the requirements of data buoys powered by conventional means. The work carried out as part of this literature review is published in part in [14], which has garnered more than 50 citations to date.
Objective 2: Investigate how some of the challenges around PTOs for small scale devices can be overcome.
Contribution 2: Two contrasting PTOs identified in the literature as potentially suitable for data buoys are investigated. TENGs, while potentially having a number of advantages for data buoy applications, have a paucity of research around their modelling, particularly mid-fidelity models that could better identify the relationship between TENG output

and floater dynamics. The lack of mid-fidelity models of TENGs is tackled via the use of system identification methods to develop a data-based model of a TENG that could potentially be used to gauge the suitability of other floater geometries as the basis for mounting such PTOs. The work is published in part in [15], and presented at IEEE OCEANS 2023 in Limerick.

The problem with OWCs at the small scale is identified to be primarily due to issues with turbines operating in low Reynolds numbers. A dearth of research considering turbines at low Reynolds numbers is identified as a gap in the research landscape, with few studies considering aerofoils in flows with a Reynolds number lower than 100,000. A self-starting Wells turbine is developed specifically for low Reynolds number flows, and experimentally characterised and tested to ensure that it does not act purely as a drag turbine. The work carried out on small scale turbines is part of the basis for a funding application granted to collaborators at DkIT and Maynooth as part of a seed fund between these two institutions, to further develop the research around Wells turbines in low Reynolds number flows.

Objective 3: The design, construction and testing of a wave powered data buoy, within the limitations of a research project budget. Since many large grid-scale wave power projects fail, showing wave energy to work on a small, but full scale, data buoy could help boost visibility of wave energy as an alternative renewable energy source for sensing applications.

Contribution 3: An off-the-shelf navigation buoy is modified to behave as a floating OWC. A Venturi housing a Wells turbine is attached, with a set point tracking controller to keep the turbine spinning close to its maximum power point. In wave tank testing, albeit against smaller waves than would be realistic for the full size device built, power output in the range of 10s-100s of mW is achieved depending on the wave condition; comparable to the power output of other wave powered data buoy projects found elsewhere in the literature.

Objective 4: To disprove the assumption that wave monitoring buoys must be true wave followers. Through engaging with data buoy end users at the Irish Marine Data Buoy Observation Network, P&O Maritime, the Commissioners of Irish Lights, and TechWorks Marine, the perception that any changes to the device dynamics of a wave monitoring buoy would impede the ability to return measurements of characteristic wave parameters is identified as a concern preventing the adoption of wave energy PTOs on data buoys.

Contribution 4: A free surface elevation estimator is designed as a soft wave sensor for data buoys which are not true wave followers. The estimator, designed to be used in conjunction with an existing motion sensor such as an IMU, is tested in simulation and against experimental data. The sensor is found to return time series free surface elevation

estimates from which measurements of zero-crossing period and significant wave height can be retrieved to a similar degree of accuracy currently used on conventionally powered data buoys. The work carried out is published in part in [16].

1.3 Thesis structure

Beyond this current introductory chapter the thesis comprises another 9 chapters. Chapters 2, 5, 6, 7, 8 and 9 relate directly to the contributions set out in Section 1.2, with Chapters 3 and 4 giving the technical background necessary for the work in the subsequent chapters. The content of each chapter is as follows:

Chapter 2 comprises an in-depth description of the requirements of conventional data buoys and the problems posed by the conventional methods of providing power that they currently rely on. Challenges to using wave energy as an alternative power source are also discussed. The latter part of the chapter is a review of wave powered data buoy projects in development, found within the literature.

Chapter 3 gives technical background to the hydrodynamic modelling approaches used in this thesis, including how the input to the model is changed from the commonly used excitation force, to free surface elevation. The change of model input is to allow the hydrodynamic models produced to be used within the estimator designed and tested in Chapters 8 and 9 respectively.

Chapter 4 is split between the two contrasting PTOs considered in the remainder of the thesis: namely TENGs and OWCs. The chapter discusses the issues around modelling TENGs from first principles and describes the motivation behind the data-based modelling approach used in Chapter 5.

The modelling of OWCs from first principles is also discussed, and a hydrodynamic model of a floating OWC produced, which models the effects of the turbine PTO as an equivalent orifice plate. The challenges around using OWCs at a small scale, especially with regards to the turbines used in the PTO, are also discussed as motivation for the design of a turbine specifically for small scale OWCs carried out in Chapter 7.

Chapter 5 uses a system identification approach to develop a data-based model of a TENG which could potentially be used across different floater geometries (given some geometric similarity). The data used for the modelling is provided by collaborators at the University of Porto.

Chapter 6 describes the design related part of Contribution 3. It describes the design of a floating OWC based on an off-the-shelf JFC Marine Gannet G1250 buoy. Details of modifications made to the buoy are given, as well as a description of the experimental equipment and facilities used at two test locations: a fixed OWC in the wave flume at Dundalk Institute of Technology (DkIT), used for developing the small scale turbine

PTO described in Chapter 7; and the deep ocean basin at Lir National Ocean Test Facility (Lir NOTF) used to test the full size OWC-based data buoy for validation of the estimator designed and tested in Chapters 8 and 9 respectively. Three test cases for the experiments at Lir NOTF are described: the first using a fully sealed moonpool, the second using an orifice plate to represent the effects of a turbine PTO, and the third using a turbine PTO, controlled to produce power.

Chapter 7 describes the design process behind a Wells turbine designed specifically for the low Reynolds number flows expected in the small OWC tested as part of this project. Characteristic performance curves for the turbine are obtained through experiments using the fixed OWC at DkIT. The set point tracking controller is also described and tested. A number of tests using the fixed OWC at DkIT to determine the coefficient of discharge for the orifice plate used at Lir NOTF are also carried out. Finally the validity of modelling a real turbine PTO as an equivalent orifice is also shown, further validated in Chapter 8.

Chapter 8 describes an unknown input estimator designed to recover time series estimates of free surface elevation from a data buoy which is affected by the change in dynamics that an OWC introduces. A Kalman filter with random walk is chosen as a basis for the estimator, since it can be extended to account for a nonlinear system such as an OWC fitted with an orifice plate or turbine PTO. Hydrodynamic models of three test cases (fully sealed moonpool, orifice plate, and real turbine PTO) are validated against experimental data obtained at Lir NOTF, since a model of the system is an integral part of a Kalman filter-based unknown input estimator. The effects of the turbine speed on the dynamics of the device are also investigated, and found to be negligible, further validating the modelling of the turbine behaviour as an equivalent orifice.

Chapter 9 describes the evaluation of the free surface elevation estimator for the three test cases considered. The estimator performance is evaluated in simulated waves reflective of real ocean waves, as well as against experimental data obtained during wave tank testing at Lir NOTF. The estimator is found to return time series free surface elevation estimates, from which measurements of zero-crossing period and significant wave height can be retrieved to a degree of accuracy close to the current industry standard.

Chapter 10 concludes the thesis, outlining the main conclusions that can be drawn from the work contained herein, and suggesting future work that could arise from this thesis.

1.4 List of publications

Journal publications:

I. McLeod and J. V. Ringwood, Powering data buoys using wave energy: a review of possibilities" in Journal of Ocean Engineering and Marine Energy, vol. 8, pp. 417–432, 2022.

I. McLeod, B. Walsh, T. Kelly and J. V. Ringwood, "Free Surface Elevation Estimator as a Sensor for Wave-Powered Data Buoys," in IEEE Journal of Oceanic Engineering, vol. 50, pp. 2232–2247, 2025.

Conference publication:

I. McLeod, D. Clemente, P. R. Santos, F. T. Pinto, M. Rosati and J. V. Ringwood, "Mathematical Modelling of a TENG-Powered Data Buoy," in Proc. OCEANS 2023, Limerick, Ireland, pp. 1–10, 2023.

2
Background

Contents

2.1 Characteristics of data buoys 10
2.1.1 Data buoy applications 14
2.1.2 Data buoy power sources 15
2.1.3 Drawbacks of conventional power sources 17
2.1.4 Challenges and motivations for using wave energy to power data buoys 21
2.2 Literature review 24
2.2.1 Existing reviews 24
2.2.2 Wave-powered data buoy prototypes since 2011: by PTO mechanism 29
2.3 Chapter summary and conclusions 46

As alluded to in Chapter 1, data buoys present a unique opportunity for wave energy, where the financial risks and lead times required for large scale WECs are replaced by new challenges - such as the scalability of PTO mechanisms and the application specific requirements of sensing and data acquisition - that are quite different to the energy maximisation goals of large scale devices. Indeed, in many cases data buoys have relatively modest power requirements, with some devices, such as the MBARI-WEC already producing more power than required by their onboard sensors [17]. In this chapter the current state of the art of data buoys is considered, and while data buoys are currently largely solar or battery powered, Section 2.2 discusses the not insignificant number of projects that involve the use of wave energy in powering buoys across a range

of application areas: from aquaculture, to arctic monitoring and even similarly scaled peripheral applications such as providing power to isolated communities.

2.1 Characteristics of data buoys

Data buoys in their broadest definition are floating offshore devices which are designed to measure parameters in their local environment, either storing this data for collection, or transmitting it via satellite, radio or mobile communications. With near boundless potential applications, it can be difficult to fully characterise data buoys, though some common archetypes do present themselves. Most commonly these fall under the broad umbrella of weather and climate monitoring, with the most common classes being weather buoys, Lagrangian drifters and tsunami buoys. The widespread deployment of such buoys can be seen in Fig. 2.1, and though only buoys partnered with the National Data Buoy Centre are included in Fig. 2.1, it is estimated that approximately 4000 profiling floats, 1500 drifters and 400 moored buoys are currently deployed worldwide for ocean observation [18]. Tsunami buoys are an unusual form of data buoy in that, rather than having wave measurement sensors onboard the floater itself, pressure sensors are mounted upon the seabed [19] to ensure wave height measurements are not limited by mooring length; as they would be in a more traditional wave monitoring buoy such as a Datawell Waverider [20], or their recent competitor the Spotter [21]. Allowing measurements of tsunami waves to be made purely through bottom mounted pressure sensors is down to tsunamis being gravity waves whose wavelength far exceeds ocean depth, meaning bottom pressure fluctuations are directly proportional to the time-varying sea surface elevation [19]. With tsunami buoys there still exists a floating surface buoy, but rather than carrying the instrumentation directly, it merely transmits, via Iridium satellite communications, the measurements taken by the submerged unit, which are communicated to the surface buoy using an acoustic link.

Drifters are a class of unmoored data buoy which are most often used to measure currents, important in many climate models, such as those monitoring the potential collapse of the Atlantic meridional overturning circulation (AMOC) [22]. Being unmoored, drifters follow the ocean current, transmitting global navigation satellite system (GNSS) location data via satellite, usually once every 15 minutes, with some also sending characteristic wave parameters once per hour [23]. Drifters can be either drogued or un-drogued, and require a very low emersed profile, to minimise the influence of wind on their movements. Curiously, current data is generally absent from commonly used reanalysis datasets such as ERA5 [24]. In [24], it was found that although ERA5 has relatively good agreement with a network of drifters measuring wave height, ERA5 it did generally

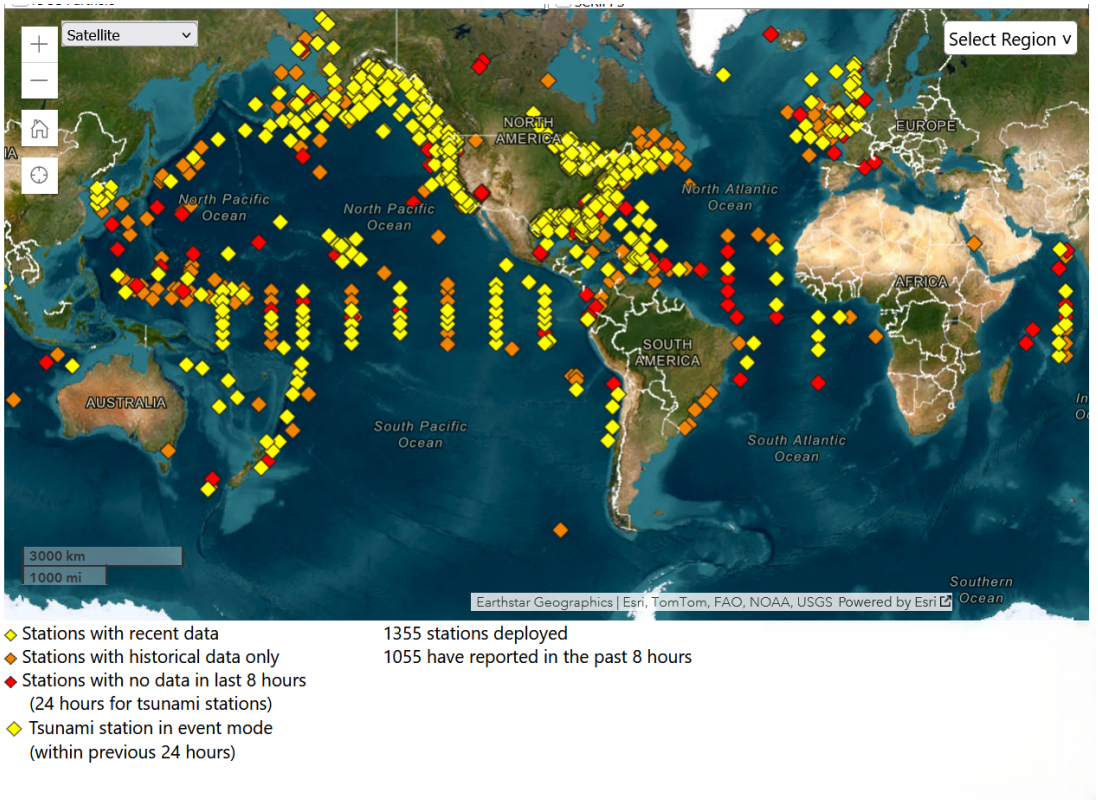


Figure 2.1: Map of data buoys partnered with the National Data Buoy Center (NDBC), including Met Éireann's M-buoy network, and the UK Met Office's K-buoys. Created using the interactive map tool on the National Oceanic and Atmospheric Administration (NOAA) website [25].

underestimate wave heights in the case of opposing currents and overestimates them in the case of a following current, with errors of up to 20% in some cases.

Though data buoy applications are myriad, as discussed in Section 2.1.1, the most common, and perhaps most typical, are weather buoys. Data buoys measuring atmospheric pressure, sea temperature, air temperature, wave height and wind speed are a cornerstone of weather forecasting. Weather buoys are dotted around coastlines to provide a stream of data to meteorological offices, such as the Mobilis K-buoys deployed by the UK Met Office [26] or the five JFC Marine M-buoys utilised by Met Éireann [27]. These buoys record a range of parameters: from significant wave height; to atmospheric pressure; air, sea and dew point temperature; and wind velocity at key locations around their country's coastlines. Weather centres gather hourly summaries of these parameters, which are usually measured over a 5-10 minute period. The requirement to only have sensors on for 5-10 minutes every hour significantly lessens the power requirement of these buoys, with the M-buoys used by Met Éireann requiring only around 100 W for each of the two sides of sensor banks (it should be noted that M-buoy sensors are duplicated on both sides of the buoy to ensure inbuilt redundancy).

In the remainder of this section, the Irish Marine Data Buoy Observation Network (IMDBON) is considered as an example data buoy network [28], with the M-series weather buoys presenting a typical data buoy application.
All data gathered by the M-buoys is transmitted over the satellite communications system Iridium. Iridium is a highly reliable network which charges operational costs based on the amount of data transferred. As the M-Buoys transfer only around 80 bytes of data every hour, the total subscription cost for the network is approximately €100 per month. Such limited data transfer highlights why only hourly averages of the measured parameters are sent, as time series free surface elevation data would significantly increase the operating costs of these devices.
However, IMDBON also runs more data intensive projects such as those carried out for universities and research institutes. An example of this would be the COMPASS project, which was a joint Irish, Northern Irish and Scottish government venture monitoring changes in the water chemistry in Ireland [29]. The COMPASS buoys, which measure nitrates, nitrites, pH and CO2 levels use Vodaphone's 4G network, which allows large amounts of data to be sent for a significantly lower cost than Iridium. This is only facilitated by the location of the COMPASS buoy, in Galway Bay, where 4G mobile signal has significant nearshore coverage.
The COMPASS Buoy carried out a four year deployment, with sensor calibration the main driver behind the maintenance schedule for this buoy. The water chemistry sensors required calibrating every 6 months over the four year period with the mooring being replaced every two years. Biofouling was a significant an issue for the COMPASS buoy as the sensors, which monitor changes in water chemistry, are all submerged below the waterline, contributing to the relatively short maintenance cycle for this buoy. As the buoy was measuring water chemistry, anti-biofouling coatings were not possible on the COMPASS buoy, as such coatings leech chemicals into the surrounding water, contaminating any water chemistry readings.
As with the COMPASS buoy, maintenance on the M-buoys is driven by the need to calibrate sensors. Such maintenance is carried out annually by P&O Maritime, with one buoy brought in and returned before the next is collected [28]. The World Meteorological Organisation has strict guidelines regarding accuracy of sensors, so annual maintenance is a non-negotiable factor in operating the M-buoy network. During maintenance sensors are either recalibrated or replaced. As each sensor has a duplicate on board, M-buoys can operate normally even if one sensor has been damaged, but the longer a buoy is left on a single sensor, the higher the risk of that measurand being left unrecorded. During maintenance the moorings of the M-buoys are also replaced every year.
Maintenance and the concomitant retrieval and redeployment of the buoys is one of the most significant expenses for a weather buoy network. Hiring fees of ships run into the

tens of thousands of Euros per day, which means that retrievals and deployments should operate as smoothly as possible. This is a significant influencing factor on the choice of using cheap solar panels, as mariners having to worry about preserving the exposed solar panels when raising or lowering the buoys would significantly increase the time taken for deployment and has historically led to disagreements regarding liability.
Beyond the annual (or twice-annual for the COMPASS Buoy) maintenance missions, IMDBON data buoys are left untouched for the majority of the year. Thanks to the inbuilt redundancy in both the power supply and the sensors even strong storms can pass by without impacting the ability of the buoys to monitor the environmental conditions. The exception to this is if a buoy breaks its moorings. This is an event which occurs from time to time, and requires a team to recover the adrift buoy to be dispatched as quickly as is practicable. However, given buoys often break free during stormy weather, sometimes it is not possible to recover them for as much as a couple of weeks, as happened to M6 in the winter of 2021.
Along with every transmission of weather data, each buoy sends a GPS location of where those measurements were taken. Each buoy has a certain radius from its set locations from which it is allowed to travel before an alert is raised that it has drifted free. The radius of this location varies from buoy to buoy, as the length of mooring has significant influence on how far a buoy can move. For example the M6 buoy has a 3 km mooring attached to a heavy chain on the seabed. The chain itself acts as end-stop protection for particularly large swells (M6 is known to encounter waves of around 30 metres [28]). As a result the drift radius for M6 is quite large.
GNSS data for the buoys is sent from multiple sources onboard the buoy, recently including the navigation lights which now come fitted with GPS tracking as standard. As it is possible for buoys to lose all power from the solar panels, there are two GPS systems each using a different power source which can be used to track the position of a buoy which has ceased operation. A potential application for wave energy PTOs as a backup power source for buoys which have ceased operation and require retrieval, is suggested for gyroscopic drifters developed in [30] [31] and [32].
Though the buoys on the IMDBON network are almost entirely solar powered, many of the same considerations need to be made no matter what power source is used on board. With the World Meteorological Organization dictating the maintenance and calibration schedule, wave-powered data buoys should also expect to be beholden to such a schedule.

2.1.1 Data buoy applications

As discussed in Section 2.1, the most widespread use of data buoys is in the field of weather forecasting and climate monitoring. Monitoring ocean parameters more generally allows effects such as desalination to be measured [33], and through their ability to function independently, data buoys could even replace expensive manned field studies on coral reefs and other key environments where the effects of climate change are felt most harshly [34]. Long term monitoring of a location of interest is often supported by benthic landers and even autonomous underwater vehicles and gliders [35] [36]. To enable landers mounted on the seabed to release stored data without a direct cable to the surface, pop up buoys have recently been developed in [37] and [38]. These pop up buoys are sunk with the lander, and once their onboard storage is exhausted, they self release, and become drifters, transmitting GNSS location until they are collected. Wave-powered ocean observatories are suggested in both [39] and [40] as a key application area for WECs, with [40] even suggesting a single full-scale WEC be used as a centralised power source for a network of data buoys. In fact, such wave-powered observatories are already feasible, with [41] using a single commercial OPT PB3 wave-powered data buoy to provide power for a coastal observatory off the coast of Chile.

Wave-powered sensing platforms are also identified in [42] as a vital component for persistent ocean observation. [42] aligns this need for ocean observation with conserving and sustainably using oceans, seas and marine resources, which was identified by the United Nations (UN) as one of their 17 goals towards sustainable development. [42] explores the constraints currently imposed on observation of deep sea areas because of a lack of available resources to supply power to these remote marine locations. [42] also specifically mentions the problem that the buoys that do pass through these deep water areas are mostly drifters, and are therefore designed for only very low power equipment, limiting the data that can be collected by these buoys. [42] highlights the need for wave energy harvesting to provide power for both long- and short-term ocean observation of remote marine areas.

Data buoy applications are almost countless, with research and development continually pushing the boundaries of where data buoys can be applied: from feeding or finding fish [43] [44] to monitoring the structural health of structures at sea [45]. Data buoys, in their strictest definition, perform a sensory role, but some small-scale buoy devices on the periphery of this definition that have similar power and environmental demands are also included in this review. For example, providing power to Autonomous Underwater Vehicles (AUVs), or Remotely Operated Vehicles (ROVs), is a commonly listed application of data buoys. To provide AUVs and ROVs with power, the buoy essentially forms a docking station for these vessels, allowing the energy stored or

harvested by the buoy to be transferred to the vehicle periodically; or the buoy provides the AUV with a continuous power supply by means of a tether. Resen Waves [46] visualise a means of transferring the energy harvested by their flywheel-based PTO via the mooring line to a battery pack or docking station on the seabed which AUVs can utilise as a charging point.

A peripheral application, often at a similar scale to data buoys in in powering island communities is included in [47] where a small-scale buoy fitted with a WEC can be used to supply power to remote coastal communities in Indonesia. The scale of the PTO mechanism used in [47] allows it to be included in this review, as the challenges a device of this size this will face in its development, are likely to reflect those faced in developing PTOs for measurement buoys with a similar power demand.

The current range of applications for data buoys is multitudinous and highly varied, with new applications regularly being proposed. However, pushing the boundaries of data buoy applications furthest are the self-propelled data buoys. First mooted in [48], self-positioning data buoy designs are driven by the belief that allowing data buoys to position themselves would be an advantageous development in the field. This proposal was not just a one-off, with [49] further building on this idea. However, for the purposes of this review, self-propelled data buoys remain curios beyond the scope of this research.

2.1.2 Data buoy power sources

To allow data buoys to operate independently, a reliable means of providing power to the system is a crucial element of data buoy design. With the earliest data buoys having onboard diesel generators (and some even experimenting with nuclear reactors! [1]), the advent of reliable batteries and efficient solar PV panels has led to widespread adoption of these two technologies as the staple for providing a power source for most commercial data buoys.

The pairing of a battery which can be sporadically recharged by an array of PV panels adorns TechWorks Marine's data buoys used by the European Space Agency (ESA) [33], [50], and the majority of meteorological buoys, including the JFC Marine data buoys used by Met Éireann [27] and the Mobilis buoys used by the UK Met Office [26]. Some designs include a second renewable energy harvesting mechanism, usually a wind turbine, to allow for some redundancy in the energy sources available for recharging the battery pack. Examples of these hybrid data buoys would include AXYS Technologies' WindSentinel used by the US Government's Office for Energy Efficiency and Renewable Energy for wind profiling on potential wind farm sites [51] [52], and the aquaculture buoy described in [44]. Research on purely wind powered data buoys has also been ongoing since before the millennium [1] with papers still being published today [53], though

wind power still remains a less popular choice than batteries or solar. A local example of where wave energy has been used in conjunction with solar panels is the Commissioners of Irish Lights, who are the lighthouse authority of Ireland, some of whose navigation buoys historically utilised an oscillating water column to supply yearlong power to the filament bulbs in plastic lenses [54]. Unfortunately, due to the ever increasing efficiency of solar panels, whose power output by area has almost doubled in 20 years, and the switch from filament bulbs to LEDs resulting in a significant drop in power demand, the Commissioners of Irish Lights ultimately saw no need for incorporating WECs in their navigation buoys, and have used only solar PV for many years.

Using batteries as a sole power source remains a popular option, favoured by the commonly used DataWell WaveRider buoys present at many test sites [20]. The sole use of battery power is particularly common at the smaller end of the data buoy scale, such as the *Basic* and *Littoral* WAVY drifters by MELOA [30].

Although the predominant trend in existing buoys is to use PV panels or batteries, a key proposal in developing data buoys further is to incorporate WECs as their PTOs. As discussed in Section 2.1.3, each method of powering data buoys has its own drawbacks. Offering data buoy developers the option of using wave energy could open up new renewable energy solutions for data buoy applications, where using wind or solar may not be suitable, such as at higher latitudes or in deep seas. This is especially notable in recent papers advocating for the use of wave-powered data buoys in Arctic environments. Both [55] and [56] propose PTOs suitable for operation in Arctic conditions, with [56] tying their research in with the broader arctic buoy monitoring network [57]. A recent review of renewable marine energy in the arctic [58], suggests tidal is best suited to power underwater hydrophones and wave energy is most appropriate for surface observation. Though being fully frozen in place would render most wave energy PTOs as ineffective as a solar panel in the long polar winter, [58] shows that the Bering sea is now potentially usable for 9 months of the year for harvesting wave energy. In fact [56] compounds this by showing that sea ice retreat is producing longer fetch and higher waves, increasing the available wave resource in arctic seas. The power demands of arctic data buoys are relatively modest at 1-10W, and though such wave-powered data buoys are not currently available for arctic climates, the buoy being developed in [56], seeks to fulfil this niche using a commercial off the shelf WITT Energy pendulum electricity generation device. Given the marine environment in which data buoys are deployed, wave energy presents itself as a PTO solution too fitting to ignore.

2.1.3 Drawbacks of conventional power sources

2.1.3.1 Batteries

Regardless of the energy harvesting method used, battery storage is required for most data buoys. This means the general drawbacks of batteries can be applied across the data buoy spectrum. However, where batteries are used as a rechargeable power source in conjunction with onboard energy harvesting, the decline in their capacity to hold charge was identified in [42] as being of low concern. [42] finds that even after ten years batteries fade by only 12.3-12.9% of their nominal storage capacity, with this number expected to decrease as battery technology develops in the future. Another risk with batteries, is if they are allowed to fully discharge. Draining batteries fully can lead to them becoming damaged, with lithium batteries particularly dangerous, as damaged lithium batteries can be prone to catching fire. In Ireland, it is for this reason that all M-buoys used by Met Éireann had their expensive military grade lithium ion batteries replaced with lead acid batteries which are cheaper and significantly more stable.
Moving to lead acid batteries did require the M-buoys solar panels to be connected in series rather than parallel, to boost voltage levels rather than current, for charging the onboard lead acid batteries. Lead acid batteries require a minimum voltage of 17-20 V to ensure reliable charging.
The key shortcoming specifically applicable to batteries, where they are exclusively used as the power source for a data buoy, is the limited lifespan of such a power source. In the absence of an onboard power source to recharge them, batteries can only be recharged via expensive maintenance operations. The frequency of replacement varies by model, but as an example, DataWell's WaveRider buoys have battery lives ranging from 1.6-3.5 years [20]. The alternative to manned maintenance operations, which is sometimes considered for single use applications, is for the buoys to be sunk. The environmental impacts of such an action make sinking buoys with batteries on board an undesirable solution, with the potential for leaching chemicals to pollute the surrounding ocean.
A final shortcoming of batteries is energy density. Though battery energy density is improving year on year they are still unable to match the energy density of liquid fuel generators [59]. Where more intensive monitoring is required, such as for research projects which may want real time monitoring of a large number of parameters, or where such parameters require energy intensive instrumentation. The solution to the onboard power for high energy projects is to use diesel generators onboard, which carry enough fuel for the deployment period (generally 14 days or less). Currently no batteries can match the energy density and reliability of diesel generator sand as such, no other options currently exist for such research projects. With many wave-powered data buoys finding they are generating more power than needed, they could represent a clean alternative to diesel.

2.1.3.2 Solar

By far the most popular method of energy harvesting for data buoys, being cheap to produce and relatively reliable, solar PV panels still have their disadvantages. Most obvious is the fact that solar power is dependent on favourable weather conditions, where sunlight is required in order for the PV cells to generate a current. The technology for manufacturing PV panels continues to evolve, generating ever higher amounts of electricity at lower and lower light levels. In terms of the Irish climate, solar panels are now so sensitive that even in the darkest months of the year, a small array of solar panels is more than sufficient for the energy demands aboard a weather buoy. Though graphs showing solar power captured under a full moon exhibit a small spike in energy capture, during a phase at which power capture would be expected to be zero, such small amounts generated by a full moon cannot compensate for the fact that PV panels will not produce sufficient power at night or under very thick cloud cover.
Pertinent to data buoy applications is the ability to survive in a harsh environment, and it is here that the true drawbacks of PV panels lie. According to P&O Maritime, who service Ireland's M-buoy network, the biggest cause of failure in solar panels is water ingress, with one panel expected to fail due to water damage after 7 months, and a second after 11 months. Water ingress on solar panels is the primary factor which causes them to stop working during deployment. Even a small amount of water ingress, as shown in Fig. 2.2, can cause a panel to cease operation.
It is also not uncommon to lose a solar panel immediately during deployment due to the crane itself, or for rogue waves to rip panels from the buoy hull. Solar panels used on the M-buoys cost approximately EUR100 each, with a homemade foam backing to protect against impacts from large waves. Some companies do offer more rugged solar panels with steel and glass protection and higher tolerance to water ingress, but the additional costs of such panels make them impractical for at sea deployments. Therefore keeping the costs of the panels down ensures they remain disposable components and reduces the financial implications of damaging them.
Another risk to solar panels in the current configuration of Ireland's 6 weather buoys is panels being ripped off by large waves. The recent addition of DIY foam backing has stopped this from being much of a problem, but panel loss is still considered a risk of being deployed at sea. Redundancy is built into the buoys to account for solar panel damage over time, and every 12 months the M-buoys are collected for maintenance and calibration according to the standards set out by the World Meteorological Organization. The redundancy built into the power system design ensures that 3 panels can be lost without affecting the operation of the buoy, and in extreme cases one side of the buoy could function on only two working panels, as the maximum power requirement for all of the sensors on one side is approximately 100 W.

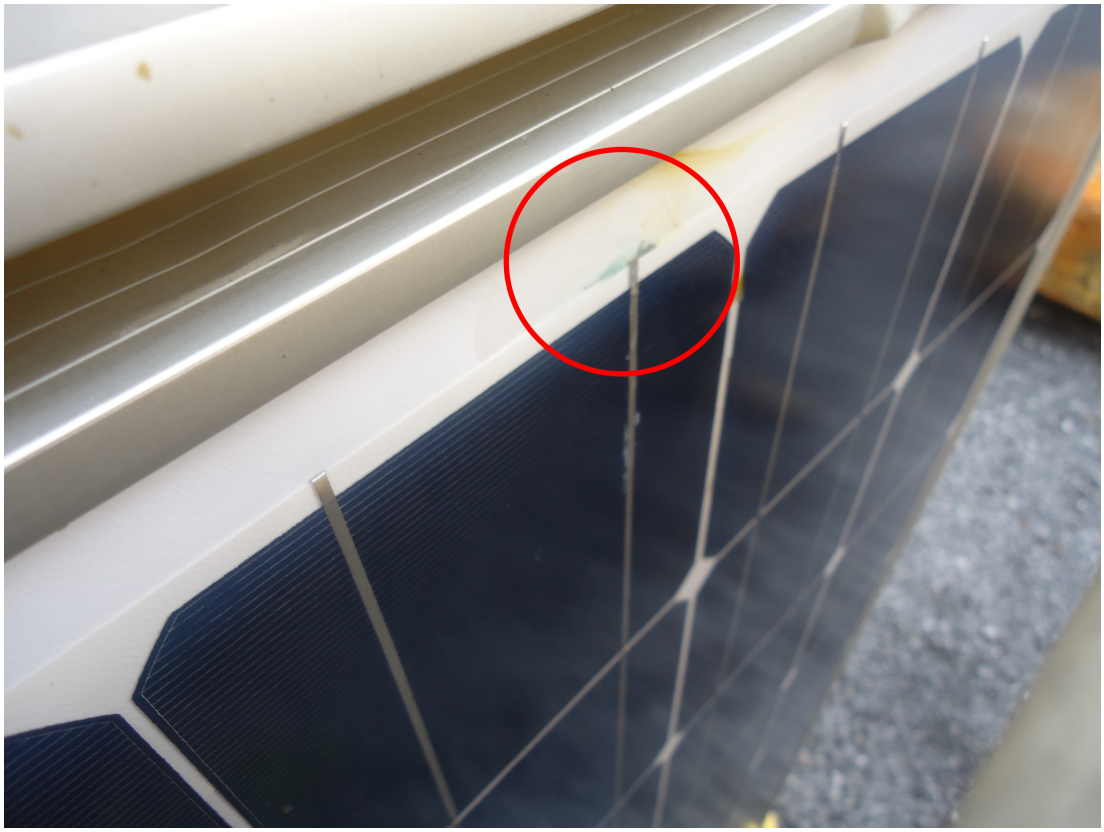


Figure 2.2: Showing water damaged solar panel from one of Met Éireann's M-buoys. The red circle highlights how subtle such damage can look, while still causing operational failure.

Beyond direct damage from the harsh environment and deployment, adding to the degradation in performance of PV panels at sea, is the fact that in an offshore environment a patina of salt, algae and other seaborne matter builds up on the flat surfaces of the panels. This layer obscures the light and over time reduces the efficiency and effectiveness of the PV panels, in essence mirroring the effect of dust build up in desert-based solar farms [60]. Additionally, data buoys form floating islands attractive to resting seabirds, whose guano contributes further to the fouling of the panels. Therefore periodic maintenance operations are required to clean the surfaces of the panels, bringing with them the same financial disadvantages as replacing batteries. A compromise is to change the panel angle to reduce the risk of bird fouling, but this comes at the cost of the panels no longer being normal to the sun's rays.

Previously the Irish weather network utilised Fugro buoys, which had four solar panels mounted at a near horizontal angle just above the water line. Such panels were often fully covered in algae and other biofouling at the time of recovery, and even had incidences of losing charge to the buoy altogether during winter months. However the new configuration on the JFC Marine buoys uses vertically mounted panels mounted significantly above the waterline where the accumulation of operation impeding biofouling is negligible.

Furthermore, PV panels must be placed above the water line, which can increase metacentric height and catch the wind, increasing the risk of instability in the water. The need to remain above the surface can also make PV panels an impractical choice where a low emersed profile must be kept, for example in the case of drifters.

2.1.3.3 Wind

Wind carries with it many of the same disadvantages as solar, namely the reliability on favourable weather conditions, and the requirement to sit significantly above the waterline. The effects on stability are even more pronounced with wind than solar, as the wind shear curve dictates that the turbines should be placed as high above the surface as possible. This instability is further increased by the turbine exerting a pitching torque on the buoy below during operation.

2.1.3.4 Hybrids

Hybrid systems combining two or more different power sources are one solution to overcoming the challenges associated with particular power sources and PTO mechanisms. Projects such as the Wavy *Ocean Atmo* and *Ocean Plus* Drifters by MELOA [30], and the OWC in [61] and [62], believe that solar panels (which have a proven performance track record) should be used in conjunction with experimental WECs to improve reliability in performance. This allows buoys fitted with WECs to be deployed at sea without the risk of being without power. In future, the plan for the Wave Activated Sensor Power Buoy (WASP) at Dundalk Institute of Technology [61], [62] is to prioritise the WEC as a power source to gauge the feasibility of using the WEC as a primary source of power, but will retain the existing solar panels as a reliable backup over the at sea test periods planned for this device.
Furthermore, the WindSentinel by AXYS technologies [51], [52], and the fish-feeding buoy described in [44], combine wind and solar to ensure redundancy exists across power sources; demonstrating the appeal of hybrid systems even when using more established energy harvesting methods. Combining wind, wave and solar energy harvesting on a single data buoy has also been considered with the 'Tribrid' in [63], further discussed in Section 2.2.2.6.
Beyond the data buoy field, projects such as [64] demonstrate the synergy between the effects that gyroscopic WECs have on dampening pitch whilst generating electricity, and the advantage this stabilising force can have when combined with a floating wind turbine platform. This stabilising effect of gyroscopic WECs could also aid in bypassing the problems surrounding the control paradox discussed in Section 2.1.4,

with small-scale data buoys potentially reaping the benefits of a technology developed for much larger scale applications.
Hybrid systems are, unfortunately, not a panacea to all the issues surrounding the utilisation of a single energy harvesting method. The additional complexity involved in balancing two or more power sources, as well as the additional costs of including a second power converter as a back-up, can often outweigh the benefits of the extra reliability and greater margin of redundancy that they bring. A summary of the drawbacks of hybrid wave energy converters, and further external examples of hybridising wave energy with other power sources, are discussed in [65].

2.1.4 Challenges and motivations for using wave energy to power data buoys

Although less susceptible to hourly variation in weather conditions, and with better forecastability than solar and wind [66], WECs still require a sufficiently excited surface to operate. However, this is not the main drawback of using wave-power. Wave energy is still very much a developing field without the established range of commercial off-the-shelf technologies available for wind and solar power sources. This low Technology Readiness Level (TRL) makes it a far more challenging PTO to implement on data buoys, although some companies such as OPT have successfully deployed wave-powered data buoys [10]. The main challenge to developing this technology is that the irregular, low frequency of ocean waves presents a challenge to conventional electricity generation methods, which have been designed for more regular, higher frequency energy sources. Of the power sources considered for data buoys, wave power is the most susceptible to marine fouling below the water line. This build up of marine organisms, attaching themselves to the underside of the buoy, may impair the ability of the device to generate power. A traditional solution to marine biofouling is the application of an anti-fouling coating to the hull. However, despite a total ban on ecologically harmful tributyltin from 2008, modern anti-fouling coatings have also been found to release toxic biocidal agents into the surrounding ocean [67]. The effects of biofouling on WECs, may be rather limited, as [68] shows. In [68] two Datawell Waveriders, one clean, one severely biofouled, were compared. In terms of their response to incident waves, [68] found biofouling to only affect the high frequency response of the devices. Losing responsiveness to high frequencies, is not generally considered a drawback for large scale WECs, though data buoys, with their higher resonant frequencies may be more affected, especially if the high frequency tail of a wave spectrum is being specifically targeted [69]. Besides the challenges posed by the marine environment, for data buoys in particular, wave power presents an interesting challenge, which will be referred to as the *control*

paradox in this review. It refers to the dichotomy that wave-powered sensing devices face: to harvest more energy the control system increases the motion of the buoy, violating the requirement of many sensors and transmission antennae for a stable platform to operate effectively. [70] addresses this paradox directly and investigates whether it presents a prohibitive barrier in developing a wave-powered data buoy fitted with a Light Detection and Ranging (LiDAR) array. The control paradox also has parallels to the *modelling paradox* discussed in [71], where the increase in device motion caused by the control system, violates the assumption of small motion used to develop the hydrodynamic model of the WEC being controlled.

2.1.4.1 Sensor requirements

Though data buoys can be fitted with a myriad of different sensors, each potentially with their own stability requirements, all weather buoys currently monitor the sea state, as this feeds directly into weather forecasting data.
To measure wave parameters, data buoys use onboard inclinometers, accelerometers or pressure sensors. Limited by bandwidth, particularly in locations far from shore, spectral data gathered over the chosen wave acquisition time (set by the end user), is used to give an indication of changes in sea state, typically defined by the significant wave height, and the zero-crossing or dominant period. These wave parameters are calculated in the spectral domain, using equations (2.1)-(2.4) given in [72] and [73], with the significant wave height, H_s, theoretically given as the average of the highest 1/3 of the waves, approximated in the spectral domain as H_{mo} :

$$H_{mo} = 4\sqrt{m_0}, \tag{2.1}$$

where m_0 is the variance, or zero-order moment, of the free surface elevation time series, as given by:

$$m_0 = \sum_{\omega_l}^{\omega_u} S(\omega)d(\omega), \tag{2.2}$$

where $S(\omega)$ is the spectral density for each frequency band and $d(\omega)$ the bandwidth. ω_l and ω_u represent the lower and upper spectral limits respectively. The dominant period of the sea state, T_d, is calculated simply as the inverse of the identified frequency band with the highest spectral density [72]. Alternatively the zero-crossing period, T_z, can be calculated using:

$$T_z = 2\pi\sqrt{\frac{m_0}{m_2}}, \tag{2.3}$$

with 2π accounting for frequencies in radians, and where m_2 is the second spectral moment:

$$m_2 = \sum_{\omega_l}^{\omega_u} S(\omega)d(\omega)\omega^2. \tag{2.4}$$

It is generally assumed that data buoys designed to monitor waves should be true wave followers, i.e. the frequency response of the buoy is uniform and unitary. The motion of a wave follower is thus assumed to directly correlate with the movement of the free surface. The notion of true wave followers is idealistic, as floating devices will always have some variation in dynamic response with frequency. Data buoys deemed to be wave followers, are therefore designed with high resonant frequencies, significantly higher than the highest expected wave frequency, to minimise colouring their dynamic response to incident waves.

Aside from the challenges surrounding the scalability of wave energy PTOs discussed elsewhere in this chapter, the perception that wave data can only be gathered by true wave followers further throws into question the possibility of using wave energy to power data buoys. Wave energy PTOs generally necessitate device dynamics with a resonant frequency close to the expected frequencies of incident waves. Such dynamic behaviour is further exaggerated by the introduction of energy maximising control [74], further moving wave energy converters (WECs) away from the behaviour of true wave followers. This means one of most common sensor requirements for data buoys presents a significant challenge to wave-powered data buoys, as any wave energy harvesting mechanism would need to ensure that the motion of the buoy itself remains unaffected. As such, PTOs and control systems which affect buoy motion are perceived as being unsuitable for weather buoys, unless an accurate method of back-calculating the sea state can be incorporated. Chapters 8 and 9 describe the design and testing of a free surface elevation estimator designed to counter the argument that wave parameters can only be gathered by true wave followers, by proposing a soft sensor, based on Kalman filter-based unknown input estimation techniques, designed to be used in conjunction with an existing motion sensor such as an IMU and takes into account the dynamics of an OWC based data buoy.

2.1.4.2 High resonant frequency of data buoys

Being small devices, data buoys in general have a naturally high resonant frequency when compared to their full-scale counterparts. While this has advantages in terms of mimicking the behaviour of true wave followers, it represents somewhat of a challenge to conventional WEC control strategies where the goal is often to actively manipulate the resonant frequency of the device to match the frequency of incoming waves [74]. Furthermore, WECs are often designed to target specific wave climates, with the

resonant frequency of the uncontrolled device designed to be close to the dominant frequencies of the targeted seas.
In [69] a solution to this problem with small-scale WECs is presented. In [69], it is proposed that instead of targeting the dominant wave frequency for harvesting energy with small devices, the high frequency tail of wave spectra (above 2.5 rad/s) in a location should be targeted instead. This not only solves the general incompatibility of the high natural frequencies of such devices with conventional energy maximising WEC control approaches, but [69] finds that this high frequency tail in the sea spectra, studied at various locations around the coast of Australia, offers a more persistent and stable energy resource than the large power peak. Of course there is a trade off to consider as the available energy in the high frequency tail is significantly lower than at the power peak of the spectrum, but as frequently discussed in papers relating to data buoy applications, their power demands are often around 20W or less [75], and certain projects, such as the MBARI-WEC [17], find that they are producing more power than required by onboard sensors.

2.2 Literature review

Though many challenges exist in using wave energy to power data buoys, there are a number of projects that seek to make wave energy a viable alternative to the ubiquitous solar and battery powered buoys that currently dominate in today's market. This section considers wave-powered data buoy projects at various stages of development, starting with those included in the published review paper [14], summarised in Table 2.1, and updating it with projects which have appeared since its publication in early 2022, summarised in Table 2.2.

2.2.1 Existing reviews

To set the parameters for this review, and to assess the surrounding research landscape, a search for other reviews covering relevant subjects was carried out. These are explored in the subsections 2.2.1.1 to 2.2.1.5.

2.2.1.1 Wave power measurements

Of existing reviews, one of the most comprehensive is [76], which is a review of wave power measurements. [76] covers a wide range of wave power measurement applications; a broad scope which also encompasses wave-powered data buoys. The focus of [76] is on devices which have an at sea deployment history, demonstrating which projects made it to this advanced stage of development. Published in 2011, [76]

includes data buoys all the way back to Yoshio Masuda's navigation buoy, and all data buoy devices deployed at sea up to the year of publication.
A clear trend that can be observed in [76] is the almost exclusive use of OWCs as the PTO for wave-powered data buoys: from the IPS Buoy and the N2 Buoy in 1980 and 1981 respectively, and even in the case of the Ocean Energy Buoy. The Ocean Energy Buoy was a 1:4 scale commercial device for electricity generation first tested at Galway Bay in 2006, but had a measurement system fitted in 2008 [76]. However, a key takeaway from [76] is that from this significant number of OWC powered data buoys, a recurring impediment to their further development was the low power that they generated in a real ocean environment.

2.2.1.2 Wireless sensor networks

Ocean-based Wireless Sensor Networks (WSNs) are a key application area for data buoys, and are therefore included in this review. Three reviews were found concerning ocean-based WSNs: two focussing on Aerial Wireless Sensor Networks (AWSNs) [77], [78] and one concerning Underwater Wireless Sensor Networks (UWSNs) [79].
[77] specifically excludes solitary data buoys, but does find 12 unique applications of WSNs at sea. However the focus of [77] is more on the architecture of building ad-hoc networks from existing sensor buoys, and the challenges that this presents, rather than highlighting the progress of wave-powered data buoys in the field of WSNs. Conversely, although [78] proposes itself as a continuation of [77], it does include a solitary wave-powered data buoy - specifically the one described in [34], which is a prototype for a reef monitoring buoy, further discussed in Section 2.2.2.4.
Whilst the UWSNs considered in [79] are mostly unrelated to data buoys, there are underwater sensor nodes which are of a similar size to data buoys and could provide rich ground for cross pollination of ideas and lessons learned in their development. One such example is CalWave's xNode [80], which utilises a WEC as its PTO system, to power onboard underwater sensors. The xNode is also small-scale and is designed to be incorporated into UWSNs. However, being a commercial product, available details about the xNode's design are scarce, but monitoring its success once deployed could highlight issues that similarly sized wave-powered data buoys will also have to overcome at sea.

2.2.1.3 Triboelectric nanogenerators

In the field of small-scale wave-powered devices, a technology impossible to overlook is the triboelectric nanogenerator, or TENG for short. Developed in 2012 by a group headed by material scientist, Zhong Lin Wang, this PTO mechanism is an adroit solution

to the problems posed in harvesting a low frequency, stochastic energy source such as a person's body motion - or in the case of data buoys: the ocean's waves.

TENGs are clearly currently topical with developers refining the mechanism and constantly exploring potential new applications. A glut of recent review papers concerning TENGs exists, making it currently the most researched PTO for small-scale wave energy applications. Indeed, the versatility of TENG applications means that many of the TENG review papers have ocean monitoring, or harvesting as a mere subsection of larger TENG reviews considering applications from dissolvable biomedical devices, to emergency Morse code generators and landslide detection [81] [82] [83] [84]. A number of reviews also exist which consider improvements to specific TENG energy harvesting techniques, independent of end application [85] in [86].

Four reviews were found concerning only ocean-based applications of this nascent technology: [87], [12], [88] and [13]. The reviews of [87] and [88] are general and apply to all notable ocean-based TENG developments since their invention in 2012, exploring the myriad ideas in this incipient field.

However, most apposite to this review is the approach taken in [12], which specifically considers TENGs in relation to their application aboard data buoys. [12] only includes TENGs which have been developed to at least the physical prototype stage, disregarding some of the exploratory 'blue sky' ideas included in [87] and [88]. Using this approach [12] observed that no TENGs had been tested in realistic sea conditions (only in idealised set ups). This observation formed the basis for the lead author's of [12] to publish a follow-up paper on testing TENGs in realistic sea conditions [89]. The group's focus on TENGs in relation to data buoys, is a product of developing their own TENG powered data buoy in Portugal. Their review [12] is presented as an argument for using TENGs in small-scale wave power applications and as a counter-argument against the scalability of TENGs and other PTOs.

[88] and [87] also promote the use of TENGs, presenting them as the most power dense of ocean energy harvesting mechanisms at a small-scale. Whilst [87] considers all TENG developments, the focus of [88] is on TENG applications as distributed ocean sensors, particularly where they can act as part of a WSN, such as those discussed in Section 2.2.1.2. However, also included in [88] are some examples of other more unusual PTOs that could be used in sensor buoys, categorised as electromagnetic harvesters (EMHs), electroactive polymers harvesters (EAHs), triboelectric nanogenerators (TENGs), and hybrid harvesters (HHs). Although the majority of these examples are very theoretical, and not specific towards developing a particular device, included amongst them is a wave-induction turbine which has undergone sea testing [90], and a double backwards bent duct OWC for fish farms [91], both of which are further discussed in Section

2.2.2.2. Also included in [88] is [92], which is a pendulum based WEC drifter - included in Section 2.2.2.8.
With TENGs being such a new technology the three reviews covering their uses at sea, [87] [12] [88], are quite comprehensive, with this review considering further TENG developments made after the publication of [88]. In addition, [13], a recently published review discussed in Section 2.2.1.4, has a considerable focus on TENGs, so effort has been made to avoid overlap between the devices considered in [13] and this review.

2.2.1.4 Applications of wave energy marine buoys

[13] presents a review of wave energy marine buoys with a focus on the applications of marine energy buoys at sea. The Introduction of [13] finds some commonality with this review, acknowledging the predominance of solar power within the field, and touching on some of the drawbacks that wind and solar encounter in an offshore environment, including the reduction in effectiveness of solar panels in a dynamic environment. [13] follows the Introduction with an overview of common PTOs related to wave power in general, and categorises the common PTOs in wave energy as overtopping devices, OWCs and oscillating bodies. However, finding no overtopping devices in the field of marine buoys, [13] instead looks at the other two classifications and discusses the applications of these PTO types in general, and with respect to large-scale wave energy production, as well as relating some examples of smaller scale buoys which utilise these PTOs. A particularly interesting finding from [13] in relation to this review, is that for oscillating body WECs the requirements for buoys are "fundamentally different from large floating platforms", with buoys requiring:

- Smaller size
- Structure simplicity
- Axisymmetry

According to [13], these requirements put data buoys at odds with electromagnetic generators typically used in wave energy, which require complex structures and often achieve inefficient performance in mild sea states. The review goes on to suggest that TENGs are a more suitable choice for small-scale applications. However, one aspect overlooked by [13] in this statement, is the role that having a control system can play in improving the performance of small-scale WECs in milder sea states, for example, as proposed in [75] or [18]. Indeed, the lack of control in TENG devices is later listed specifically by [13] as an advantage of TENG-based devices over conventional WECs, due to the added simplicity this brings to the system.

[13] comes from the Dalian Maritime University's Marine Micro/Nano Energy and Self-Powered Systems Lab, who specialise in small-scale marine energy, particularly focussed on TENGs. The laboratory at Dalian Maritime University are responsible for the 7 s-shaped TENG array in [93], further detailed in Section 2.2.2.5. It is therefore unsurprising that the section on TENGs in [13] is particularly detailed, and that the paper establishes an argument that promotes TENGs as the most promising solution for small-scale wave energy applications. Table 2 of [13] lists the power outputs of example TENGs as power densities, which although a good method by which to compare TENGs to one another, can make TENGs look particularly favourable as a PTO choice for WECs when compared with other PTOs, due to the small volume that a typical TENG occupies. However, [13] does address some of the engineering problems currently surrounding TENGs. Namely, these are listed as load matching, system integration and output stability.
[13] presents a contemporary complement to this review, focussing primarily on applications, and includes a number of useful figures that establish a basis for many of the concepts discussed in both [13] and in this review. [13] also contains a discussion of two examples of hybridising TENGs with a secondary PTO [94], [95], which present a particularly interesting development in the field. Interested readers are encouraged to consider [13] in conjunction with this paper, as the two differing approaches, considering similar subject matter, combine to give a comprehensive picture of the current wave-powered data buoy research landscape.

2.2.1.5 Powering remote communities

Powering off-grid communities is a peripheral WEC application that shares some common interests with developing wave-powered data buoys. Indeed [47] was included within the literature review for developing a small-scale buoy that could equally be used to power ocean monitoring buoys. A recent paper, [96], models a WEC being used to provide power to a small community, including how a stable 50 Hz AC voltage can be established from a linked energy storage system. Though many of the considerations in [96] are beyond the scope of wave-powered data buoys, a review of recent advancements in powering island communities using wave energy is included, showing how [96] combines lessons learned from previous work, to offer a holistic model of a wave to isolated grid system.

2.2.2 Wave-powered data buoy prototypes since 2011: by PTO mechanism

Unlike the well established renewable sectors of solar and wind, where the focus of research and development is refining the existing technologies of PV panels and turbines respectively, wave energy is still a nascent technology where there is no 'go-to' solution. This has led to a range of device concepts and PTO mechanisms for harvesting wave energy: from the OWC used in Yoshio Masuda's pioneering navigation buoy [3], [97]; to the TENG invented in 2012 by Zhong Lin Wang's research group [98]. Section 2.2.2 of this review categorises recent developments made in wave-powered data buoys by their PTO mechanism in order to observe the current state of the art of wave-powered data buoys and examine the advantages of each PTO mechanism in the context of small-scale data buoys, as well as the challenges and potential drawbacks of using these as a testbed for larger devices and as a PTO for data buoys in their own right. A key aim of reviewing existing wave-powered data buoys is to highlight the novel concepts behind each development and the impact of these on advancing the use of wave energy in the field of data buoys.

Section 2.1 looks at the characteristics of data buoys in terms of applications, current power sources, and a discussion of their potential as testbeds for larger WECs. Significant reviews relevant to the field of wave-powered data buoys are discussed in Section 2.2.1. Section 2.2.2 focusses on developments in wave-powered data buoys made after 2011, as [76] presents a comprehensive review of developments made in offshore wave power measurements throughout the 20th century, and those developed in the first decade of the 21st, including wave-powered data buoys with a history of deployment at sea. Section 2.2.2 aims to give an overview of advancements in wave-powered data buoys since 2011, including those which refer to themselves as Smart Buoys, Sensor Buoys or Nodes. Categorisation by PTO was considered most appropriate for Section 2.2.2 as many of the data buoys investigated are still in development, leading to a lack of detail in other categorisations considered such as deployment history, sensor type, or mooring method. Table 2.1 includes all the categorisations considered, with dashes where certain information was not available or not explicitly stated. Table 2.1 contains a summary of wave-powered data buoy prototypes that have had research published between 2011 (when [76] was published) and 2021 (when this project's review paper was published [14]). Table 2.2 is a companion to Table 2.1, updating it by including wave-powered data buoy projects from 2022 to 2025. As well as academic publications selected commercial ventures within the field, where companies have made active progress in this same time frame are included. Section 2.1.1 provides justification for the inclusion of some peripheral examples of small-scale buoys that are not data buoys, but are of a scale

where the challenges they face, and the lessons learnt in overcoming these challenges, can be applied to data buoys. The review of PTO methods in [65] is a summary of the various mechanisms by which wave energy is currently harvested, and given the comprehensive coverage of available PTOs included in [65], the same bin names were used for the PTO categorisations in Subsections 2.2.2.1 to 2.2.2.6.

2.2.2.1 Hydraulic motor system

Identified by [65] as the most suitable PTO device for generating usable electricity from wave energy, one of the identified wave-powered data buoys in development uses this form of energy harvesting to recharge its onboard batteries. This is the data buoy being developed by a team from the Monterey Bay Aquarium Research Institute (MBARI) and Sandia National Labs, named the MBARI-WEC in [17]. Although started in 2009, it is an active project with new papers surrounding its development still being published [17]. The goal of the MBARI-WEC is to avoid dependence on batteries, which are the industry standard for marine monitoring buoys.

The MBARI-WEC uses a point absorber design, adapted from an off-the-shelf hydraulic motor converted to be used as a generator. This data buoy is one of the few wave-powered data buoys identified which has withstood numerous full-scale trials within the ocean, including overwintering in 2015 for a total of 131 days at sea. Indeed, in [17], it is stated that this data buoy is the very first of its kind with an extended deployment history, and the project to develop the buoy further is still ongoing. The plans outlined in [17] are to include a control system (currently absent from the design) with which to optimise the power capture of the device and thereby improve its efficiency. Though such an energy maximising control system has not yet been implemented on the real device, a new software package has been released based on a validated model of the MBARI-WEC as a tool for developing control strategies for the device [109]. The software is based on the robotics packages ROS2 and Gazebo. An example using this new software, and comparing it to WEC-Sim is found in [107]. Validated against real data collected from at sea deployments of the MBARI-WEC the comparison between Gazebo and WEC-Sim implementations showed that both simulations overestimate the average electrical power produced by the device. The Gazebo model overestimated produced power by 13% with WEC-Sim overpredicting by 22% respectively. The study in [107] highlights the importance of real deployment data and shows how optimistic many of the simulation-only reports of WEC power output could be. The MBARI model is under ongoing refinement, with a recent paper [108] seeking to validate the numerical model of the MBARI-WEC by using experimental rig tests of the PTO to better understand the nonlinear dynamics of this component. With the MBARI-WEC

Table 2.1: Wave-powered data buoy prototypes since 2011: by PTO mechanism (included in [14])

PTO Mechanism	Leading Institution/-Company	Citation	Development Status	PTO Control Used?	Mooring	DoFs Harnessed	PTO Power Output	Novelty
Hydraulic Motor System	MBARI (USA)	[17]	Deployed at sea	No*	Heave cone or single-point	Heave	100's of W	Extensive deployment history (*Planned soon).
Turbine Transfer System/OWCs	Uni. de Lisboa (Portugal)	[3] [99]	Wave tank testing	Yes	4-point in tests but TBD	Heave	100's of W	Biradial turbine for latching control.
	Uni. do Porto (Portugal)	[70]	Rig testing	Yes	Single-point catenary	Heave	10's of W	LiDAR application, addresses control paradox.
	Uni. de Lisboa (Portugal)	[100]	Computer sim.	Yes	Yes - type not specified	Surge	kW-scale	Backwards bent duct shape.
	Sunchon National Uni. (Rep. of Korea)	[88] [91]	Computer sim.	No	-	Surge	100's of W	Double backwards bent duct shape.
	DkIT (Ireland)	[62] [61]	Deployed at sea (no PTO**)	None	Single-point	Heave	0 W**	Planned dual-use of OWC sensor and PTO (**PV panels used).
	Uni. of Indonesia (Indonesia)	[47]	Computer sim.	-	Yes - type not specified	Heave	mW-scale	Piezoelectric generator instead of turbine.
	Pohang Uni. of Science and Technology (Rep. of Korea)	[88] [90]	Deployed at sea	-	None	Heave	10's of W	Mooring free PTO for deep sea deployment.
	Beihang Uni. (PRC)	[101]	Rig testing	Yes	Yes - type not specified	Heave	mW-scale	Dual turbine PTO with belt power transmission.
Direct Mechanical Drive	Resen Waves (Denmark)	[46]	Wave tank testing	-	Single-point	Heave	100's of W	Commercial project hoping to offer off-the-shelf "Smart Buoy".
	Southwest Jiaotong Uni. (PRC)	[45]	Wave tank testing	None	None	Heave	1's of W	Double-x shaped mechanism for unidirectional rotation.
	Shanghai Maritime Uni. (PRC)	[102]	Rig testing	-	-	Pitch	Not specified***	Magnetic lead screw PTO (***40V peak output).
	Uni. of Hawai'i at Manoa (USA)	[103] [104]	Deployed at sea	-	Drogue or single-point	Heave	10's of W	Testing drogued vs. moored device, found drogue design unimportant in deep seas.
Direct Electrical Drive	OPT (USA)	[10]	Available commercially.	Yes	Single-point or 3-point	Heave	kW-scale	Commercially available data buoy.
	Politecnico di Milano (Italy)	[34]	Rig testing	Yes	-	Heave	100's of W	Genetic swarm algorithm used in control.
TENGS[1]	Uni. do Porto (Portugal)	[89]	Wave tank testing	-	Single-point	Surge, heave and pitch	mW-scale	First TENG test in realistic sea conditions.
	Dalian Maritime Uni. (PRC)	[105]	Wave tank testing	-	Double-point	Mostly pitch	10's of W	Array of 7-TENGs with rectifier to align AC frequencies.
Hybrid	Uni. of Limerick (Ireland)	[63]	Computer sim.	-	3-point	Heave	100's of W	Proposes 'Tribrid' wave, wind and solar buoy.
Piezoelectric	Ferdowsi Uni. of Mashhad (Iran)	[49]	Rig testing	Yes****	-	Heave	mW-scale	Harvests buoy vibrations (***in self-tuning mode).
Gyroscopic	MELOA (EU)	[30]	Available commercially	-	None	Pitch	mW-scale	Commercially available, low-cost, wave-solar hybrid drifters.
	Uni. Politècnica de Catalunya (Spain)	[106]	Wave Tank Testing	-	Yes - type not specified	Pitch	mW-scale	Testing MELOA gyroscope in anchored buoy.
	Soochow Uni. (PRC)	[88] [92]	Deployed at sea	None	None	Pitch	mW-scale	Gyroscope only drifter.

[1]: Also see existing reviews: [13], [88], [12], [87]

Table 2.2: Wave-powered data buoy prototypes since 2022: updated companion to Table 2.1

PTO Mechanism	Leading Institution/-Company	Citation	Development Status	PTO Control Used?	Mooring	DoFs Harnessed	PTO Power Output	Novelty
Hydraulic Motor System	MBARI (USA)	[107] [108] [109]	Deployed at sea	No*	Heave cone or single-point	Heave	100's of W	*New tool openly available to test controllers on MBARI-WEC model.
Turbine Transfer System/OWCs	DkIT (Ireland)	[110] [111]	Wave tank testing and deployed at sea (no PTO)	No	Single-point	Heave	0 W	Estimation of external sea state from pressure sensors within sealed moonpool.
	Shandong Uni. of Science and Tech. (PRC)	[112]	-	No	Heave	not specified**		Dielectric elastomer used instead of turbine (**1.67 J stated as energy converted).
Direct Mechanical Drive	Università degli Studi di Genova (Italy)	[113]	Rig testing	Yes - MPPT	Not specified	Pitch	mW-scale	PTO harnessing high frequency pitch oscillation using MPPT control.
	Various Uni. (PRC) and Aalborg Uni. (Denmark)	[114]	Rig testing	Yes - PI	-	Pitch	1's of W	Use of motion control to allow heavier sliding weight on PTO.
	Uni. of Washington (USA)	[42] [115] (preprint)	Computer sim.	Yes - Proportional	Single-point	Heave	100's of W	Cost focussed study on converting SCOOP buoys to wave energy.
	Southwest Jiaotong Uni. (PRC)	[116] [117]	Wave tank testing	No	Attached from above***	Heave	1's of W	Optimisation of floater shape for energy harvesting in the low energy seas used for aquaculture (***mounted on aquaculture cage).
	Southwest Jiaotong Uni. (PRC) Lahore Uni. (Pakistan)	[118]	Rig testing	No	-	Heave	10's of W	Rotary mechanical motion rectifier used (min. excitation freq. of 0.3 Hz required).
	Northwestern Poly. Uni. (PRC) and Maynooth Uni. (Ireland)	[18] [119] [120] [121]	Computer sim.	Yes - PI for data buoys	Slack mooring	Heave	kW-scale	Unusual vibro-impact design, suggests data buoy application in [18].
	Sun Yat-Sen Uni. (PRC)	[122]	Computer sim.	No	Single-point	Heave	100's of W	Similar to vibro-impact design, comparing performance of three diameters of hull: 3 m, 6 m & 10 m.
	Ningbo Uni. (PRC) and Manchester Uni. (UK)	[43] (preprint)	Wave tank testing	No	Single-point	Pitch	mW	Fish finding buoy, with WEC powering GNSS comms.
	Hunan Uni. (PRC)	[123]	Wave tank testing	No	Not specified	Heave	mW-scale	Suspended pendulum coupled with magnetic flywheel, intended for marine IoT applications.
	Sun Yat-Sen Uni. (PRC)	[124]	Wave tank testing	No****	Two-point tensioned	Pitch	mW-scale	Study on effects of moorings on wave to wire efficiency (****to be considered in future).
	Sun Yat-Sen Uni. (PRC)	[125] [126]	Deployed at sea	No	Drifter	Pitch and roll	mW-scale	Three pendulum drifter to harvest energy in 2 perpendicular DoFs.
	Manhattan College (USA)	[127]	Wave tank testing	No	Catenary	Heave	mW-scale to 1's of W	Modular bolt on PTO that can scale to power requirement.
TENGS[2]	Pacific Northwest Nat. Lab. (USA))	[55]	Rig testing	-	Heave plate	Pitch and roll	mW-scale	Rig tested against 1:1 real sea measurements, power sufficient for transmitting 500 bytes/day.
	Beijing Jiaotong Uni. (PRC))	[128]	Rig testing	-	Single-point	Surge, heave and pitch	mW-scale	TENG PTO specifically targeting low freq. waves (down to 0.2 Hz).
	Chinese Academy of Sciences (PRC)	[129]	Rig testing	-	-	Surge	mW-scale	Couples TENG with swinging electromagnet generator, powering LoRa radio comms.
	Dalian Maritime Uni. (PRC)	[130]	Rig testing	-	-	Pitch	mW-scale	Demonstrates stackability: 5-TENGs on top of one another.
	Dalian Maritime Uni. (PRC)	[131]	Deployed at sea	-	-	Surge, heave and pitch	mW-scale	Able to return mm accurate free surface readings in real seas.
Hybrid	Sandia Labs. (USA)	[75]	Computer sim.	Yes - pseudo spectral	Single point, fitted with subsurface sensors	Pitch	mW-scale	Co-design paper, of bolt on WEC for hybrid wind, wave and solar buoy.
Piezoelectric	Changchun Uni. of Technology (PRC)	[132] [133]	Wave tank testing	No	Attached from above like [116]	Heave	mW-scale	Exploring different mechanisms to harvest piezoelectricity from rods excited by magnets.
	Zhejiang Ocean Uni. (PRC) and Heriot-Watt Uni. (UK)	[134]	Rig testing	No	Drifter	Heave, surge and pitch	mW-scale	Again uses magnets to excite ceramic rods to harvest piezoelectricity.
	Shandong Uni. of Science and Tech. (PRC)	[135]	Rig testing	No	Heave plate	Heave	mW-scale	10 layer stack of piezoelectric harvesters used.
Gyroscopic	Uni. Politècnica de Catalunya (Spain)	[136] [137]	Deployed at sea	Yes - MPPT	Drifter	Pitch	mW-scale	Faster sampling MPPT strategy used to triple energy harvested.
	Uni. Politècnica de Catalunya (Spain)	[23]	Deployed at sea	-	Drifter	Pitch	mW-scale	Comparing 3 different MELOA designs in real seas.
	Pacific Northwest Nat. Lab. (USA)	[56]	Deployed at sea	No	Single-point	Heave, pitch and roll	1's of W	Designed for arctic conditions, constructed from commercially available components.

[2]: Selected examples

already reliably producing 250 W of energy in at sea deployments, the developers are looking beyond merely powering instrumentation and providing power to Autonomous Underwater Vehicles, which MBARI has a strong interest in.
In [116] buoy for providing auxiliary power to aquaculture installations is proposed. Attached directly to aquaculture cages, a hydraulic PTO is used to to provide remote power to such installations. The main novelty in [116] is in the design of the floater, which is optimised for low energy seas, as aquaculture installations are usually in located in sheltered areas. Experimental results in a wave flume using a 0.4 m buoy found it could produce around 1W of power, though the floater optimisation was done for a much larger device of 8m diameter. This is another example of data buoys being used as an end application for a scaled down version of a larger WEC. This scalability is further explored in [117], and also in another data buoy application from the same group at Southwest Jiaotong University [118], which is further discussed in Section 2.2.2.3.

2.2.2.2 Turbine transfer system and OWCs

From the plethora of OWC powered data buoys in [76] discussed in Section 2.2.1.1, OWCs seem to be the closest that wave-powered data buoys have as a somewhat standard PTO. However, as pointed out in [76], the low amount of power captured by OWCs in real sea conditions presents a challenge to the widespread adoption of this PTO system. In spite of this, OWCs are still one of the most widespread PTO methods documented by wave-powered data buoy projects since 2011, with Portuguese universities leading the way.
In [3], from a group at the Instituto Superior Técnico (IST), at the Universidade de Lisboa, Portugal, the performance of two oceanographic buoys is compared: one a spar buoy based on the shape of Yoshio Masuda's navigation buoy, and the other a coaxial-duct OWC based on a design by Takahashi Takashi from the 1980s. [3] updates both buoy designs by optimising their hydrodynamic shape and adding a biradial turbine. The use of a biradial turbine in [3] is the key novelty behind these buoys, as a biradial turbine enables latching control on an OWC, something not previously possible with the more common Wells turbine. Further justification for using a biradial turbine is explained in [138], and in the group's review of OWCs and turbines [97]. A wealth of other papers support the spar buoy project at IST, with the most recent, [99], describing 1:10th Froude-scale testing of the spar buoy in a wave tank, simulating the effects of the biradial turbine with an orifice plate. These experiments found an average power generation of 1kW can be expected for Portuguese open Atlantic climate and 0.4 kW for Mediterranean conditions, concluding that the design would be appropriate for powering the planned onboard sensory equipment in the open Atlantic but not the Mediterranean.

Building on the spar buoy design in [3] and [99], [70] presents a spar buoy project from the Universidade do Porto that adapts the designs in [3] and [99] for the novel application of LiDAR monitoring of offshore wind farms. Through its application of wind characterisation using LiDAR, which requires a stable platform, [70] tackles the control paradox, discussed in Section 2.1.4, head on, investigating the compromise between limiting the OWC's resonance motion and generating enough energy to power the LiDAR on a 1:16th scale device. Despite concluding that it is currently not possible to achieve the required power for a LiDAR within the restrictions posed by ensuring a stable enough platform for its operation, [70] remains hopeful that, as LiDARs become more energy efficient, OWCs could be used to power them in future. Additionally, [70] concludes that for buoys fitted with sensors that demand less power than LiDARs, yet still require a stable platform, OWCs could be used successfully as the PTO mechanism. Also from the Universidade de Lisboa, [100] describes optimising the shape of a backward bent duct OWC for deep water marine sensing. This purely theoretical design has not undergone any experimental testing, but simulations find that a 1 metre extension to the duct allows power capture to be increased by more than 1 kW. Similarly, [91] is a backward bent duct OWC being developed at Suncheon National University of Korea, included as an example of an OWC in [88]. [91] is further pushing the design of backward bent duct OWCs, by proposing a design which couples two ducts facing opposite directions to a single turbine, allowing surge motion in both directions to be captured. Outside of Portugal, the WASP OWC project described in [62] and [61], at Dundalk Institute of Technology, currently uses the OWC chamber purely as a pressure sensor for wave profiling, with PV panels providing onboard power. [110] takes this further by proposing a method by which the pressure measurements from inside the chamber can be used to estimate spectral parameters of the external seastate. However, plans are outlined in [62] and [61] to include a turbine in the OWC chamber from which to harvest energy, while maintaining the pressure sensor function. Initial plans are to couple harnessed wave energy with the existing solar panels for deployment reliability, but with the power output of the OWC prioritised to assess its feasibility as a main power source. The Dundalk OWC has undergone deployments at the SmartBay 1:4 test site in Galway Bay, though plans to test it further were plagued by offshore licensing issues from the test site. A smaller version of the WASP, dubbed the BabyWASP, has been tested at the deep ocean basin Lir National Ocean Test Facility in Cork, with [111] extending the strategy described in [110] to include results from a fully sealed version of this smaller buoy. The same device is described in Chapter 6, as it forms the basis of the data buoy used in this thesis.

[47] is an Indonesian study that aims to tackle the problem of low access to electricity faced by much of the country's population. In Indonesia 20% of the population have no

access to electricity and this buoy is proposed as a solution for providing a small-scale power source for remote coastal communities facing this problem. The novelty in [47], is that it proposes a piezoelectric generator in place of the more usual air turbine, in order to convert the changes in pressure within the OWC chamber to useful electricity. Although not a data buoy as such, [47] is still a small-scale wave-powered buoy and the unusual approach of using a piezoelectric generator in place of a turbine is an interesting consideration for similarly sized OWC-based data buoys.
A similar idea to [47] is also found in [112], where a dielectric elastomer is used to replace the turbine PTO over an oscillating water column. As dielectric materials require an external bias voltage, the design described in [112] is in fact proposed as a hybrid device, using a small wind turbine to provide the bias voltage to the dielectric elastomer, with a solution to stepping up the 12 V turbine output voltage above the 600 V threshold required by the dielectric elastomer. Though only tested on a rig simulating the pressure variations in a fixed frame air chamber, future work will focus on testing on a prototype buoy to assess the suitability of the system for recharging batteries on data buoys. The output energy achieved in test conditions was 1.67 J for a deformation displacement of 120 mm. Though the results presented in [112] do not make use of energy maximising control, the paper concludes by suggesting the bias voltage could be optimised based on air pressure to improve the performance of the device.
Beyond the OWC, other PTOs which use turbines as their fundamental component also exist in the field of data buoys. The review of TENGs and other small-scale PTOs, [88], includes [90], which is a design where a dual water turbine suspended below the buoy is used to generate power. Initially developed in [90], to allow wave-powered data buoys to be deployed in deep sea environments by removing the need for a mooring, the successful testing of this buoy at sea (generating a peak power of 38 W) puts it among the few that have successfully carried out deployment at sea. [101] proposes a very similar design, but where a belt drive transmission system is used to absorb load fluctuations and vibrations due to the waves. Rig testing of a scale prototype achieved power capture of 26 mW. Future plans for [101] are to hybridize the turbine WEC with a second PTO (a two-body point absorber). However, with no mention of a specific application, sensory or otherwise, [101] remains a small-scale buoy on the periphery of this review.

2.2.2.3 Direct mechanical drive

Resen Waves' Smart Power Buoy, [46], is mentioned in [65] as an example of devices using a direct mechanical drive PTO. It uses a flywheel based direct mechanical drive PTO, where a tether to the seabed turns the flywheel which is in turn connected to a generator. The mooring line for the buoy forms a power cable to a fixed point on the

seabed where it can be used to power a range of underwater sensors or AUVs. The Resen Waves device has been in development since 2015 and claims to be the first wave-powered "Smart Buoy". 1:20 scale 2D wave-tank testing was concluded in 2021, with 300 runs used to validate the company's numerical model [139]. Resen Waves was formed as a spin-out from the Technical University of Denmark (DTU), and being a commercial venture has its focus on protecting its intellectual property (IP) via the use of patents (patent number: 3513058, in all EU countries and Norway; pending approval elsewhere).
Other direct mechanical drive data buoys include [45], which proposes a novel double-X-shaped mechanism for directly turning heave motion into unidirectional rotation. Not only is the mechanism in [45] novel in itself, but the proposed application of monitoring the structural health of sea bridges is also unusual. Monitoring ageing of material, overload operations, etc. is usually done by battery powered sensors, the replacement of which is labour intensive and time consuming. Other energy harvesting solutions have been proposed elsewhere, which harness the vibration of the bridge itself, but the device in [45] is claimed to have higher energy conversion efficiency at a lower cost than the bridge vibration harvesting devices it seeks to out-compete. The device has undergone testing in experimental rigs, but is yet to be deployed in realistic sea conditions.
[102] is a feasibility study to prove the magnetic lead screw WEC as a suitable PTO for data buoys. The magnetic lead screw mechanism uses the pitching motion of a data buoy to cause the onboard power generation unit (in this case a modified DC motor) to slide along the magnetic lead screw beneath, resulting in a rotational speed of up to 4700 rpm within the generator. [102] describes both the Computational Fluid Dynamics (CFD), and the experimental testing of the WEC using a rocking rig to simulate the pitching motion generated by waves striking a data buoy, allowing a range of tilt angles and their resultant voltage to be investigated. A peak voltage of 40 V is recorded for a wave with a height of 1.4 m and a period of 4.5 s, but no explicit power outputs are given.
Another magnetic screw-based wave-powered data buoy is given in [114], which is a collaborative effort between a number of Chinese universities and Aalborg University in Denmark. The key novelty in [114] is in the design of a motion control strategy, which is specifically designed for small-scale WECs rather than the more commonly studied high power PTOs. The aim of the control strategy used is to reduce magnetic slip in the core power generation unit (CPGU), to allow a heavier CPGU to be used. The controller is developed in simulation and tested on a 6 degree of freedom (DoF) hardware in the loop (HiL) rig, where the weight of the sliding power generation unit on the magnetic lead screw is increased from 70 kg to 90 kg, with a concomitant increase in generator power of 24.3%, for an average power output of 7.28 W.
Using a rolling magnetic cylinder instead of a magnetic screw pitch motion [113] describes a PTO designed to harness the higher frequency pitch oscillations of a small

environmental monitoring buoy. The research in [113] is notable as it uses maximum power point tracking control on a DC/DC converter, to optimise DC voltage as a function of the maximum pitch angle. The device in [113] was rig tested, producing 4-6 mW at a pitch oscillation frequency of 0.9 Hz.

From the same group at Southwest Jiaotong as developed the scalable PTO in [116] and [117], a data buoy end application prototype is given in [118]. This prototype is generated 13.5 W in low frequency 0.3 Hz waves, tested using a dry rig, to which the ball screw mechanical motion rectifier PTO was mounted. Mooted as suitable for oceanographic applications, [118] proposes that their data buoy be used for powering satellite communications, with applications in aquaculture, weather forecasting and detection of submarines described. It is interesting to note that [118] mirrors OPT in its proposed military application. As well as rig testing of the PTO, smaller scale wave tank testing was also carried out to compare hull shapes, finding best performance with an hourglass profile buoy compared to a hemispheric one, with these small-scale hull geometry tests carried out in a wave flume.

[127] describes a modular PTO consisting of four internal magnets suspended by springs moving between coils. This PTO is specifically designed for data and navigation buoy applications, with its modular nature allowing the available power to be scaled through the addition of more PTO units. A scale prototype is tested in [127] against sea states based on locations in California and Hawai'i. The scale model produced 81 mW in wave tank tests, with [127] suggesting that a full scale model using one PTO unit, would be capable of providing 3-4 W to an offshore monitoring buoy.

From Hawai'i [103] presents a summary of in-ocean experiments carried out on both a moored- and a drogued heaving point source WEC, equipped with sensors to measure the external sea-state. The device in [103] builds on previous work detailed in [140] and [141], but brings the device to the important development milestone of at sea testing. This project shares many similarities with the MBARI-WEC in [17], with both having been deployed at sea, although the device in [103] is of a smaller scale than that in [17]. However, both the MBARI-WEC and the device in [103] have the option of using either a single point mooring or a drogue/heave cone, allowing them to be deployed without the need to secure them to the seabed. The ability to produce power without a mooring line to the ocean floor, is a key stepping stone towards the deep-ocean sensing capabilities, proffered by [42], as an advantage of wave-powered data buoys over the more common PV panels and batteries currently used, as discussed in Section 2.1.1. In contrast to the MBARI-WEC, which achieved around 300 W of power from the heave cone configuration, [103] found the drogued configuration of their WEC to have significantly lower power capture, when compared with the single-point mooring configuration. However, despite the single-point mooring outperforming the drogued

WEC in [103], the authors conclude the paper by saying that a redesign of the drogue (specifically the drogue depth and sizing) could allow the drogued version to obtain similar power output to the moored WEC configuration. This hypothesis is tested by [104], which numerically predicts and compares the power generated by two different drogue designs attached to the device. [104] finds that although a redesigned drogue can capture more energy in shallow waters (10.6 m long drogue in 18 m ocean depth), the size of the drogue becomes unimportant if the drogue is deeply submerged (100 m long drogue in 2000 m ocean depth). This is an important conclusion, which has direct ramifications for designing deep water drogued data buoys for the applications suggested in [42]. A final conclusion of [104] is that although control theory could be implemented on the moored device, to apply control theory to the drogued version a second generator would be required to allow the device to produce power throughout the entire wave cycle.
Although not explicitly stated as a direct mechanical drive device, [42] uses a scaled down Reference Model 3 (RM3) floating point absorber WEC, to assess the costs of replacing the NDBC's Self-Contained Ocean Observations Payload (SCOOP) data buoys [142], with wave-powered data buoys across five locations. As [42] presents a like-for-like replacement for the SCOOP buoys, the costs presented in the study assume that mooring and installation for wave-powered buoys would be the same as for the existing solar powered buoys. The study in [42] is of particular relevance as it is one of the few wave-powered data buoy projects to assess the economic viability alongside the technical challenges, including estimates for operation, maintenance and potential failure scenarios. A preprint of the extension to this study, submitted to *Renewable Energy* is also available [115], though it is yet to be peer reviewed and published.
Another project which is thus far also only available as a preprint, is a collaboration between Ningbo University and the University of Manchester [43]. Though not yet peer reviewed, the application of choice for the device described in [43] is testament to the diversity of data buoy applications. Specifically [43] proposes that their pendulum based WEC (inspired by the PeWEC design from Politecnico di Torino [143]) can provide sufficient power for the modest energy demands of the onboard GNSS system of a fish finding buoy. Indeed the inertial WEC designs of Politecnico di Torino appear to have inspired a wealth of pendulum-based PTOs for data buoys.
One such pendulum WEC is wave tank tested in [124], with the end application intended as a marine observation buoy. A power output 160mW was achieved in 6cm waves, with the main focus of [124] being the mooring design. By considering a wave to wire model of the system, a two point mooring was developed, achieving a wave to wire efficiency of 7.1%. Moorings are another oft overlooked aspect of wave-powered data buoy design, which makes the approach in [124] all the more notable. Though

the wave to wire approach described in [124] did not consider a control system for the PTO this is stated as a focus of future work on the project.
A three pendulum based WEC drifter is described in [125], again following a wave to wire approach, this time to optimise the floater geometry, following the approach in [126]. The drifter in [125] is tested at sea with a power output of around 9 mW. This is found to be considerably lower than that achieved in dry rig tests, with the device having a limited response to real waves. This highlights the importance of real sea deployments, as rig testing and wave tank testing do not always reflect entirely realistic sea conditions. The three pendulum design was also somewhat problematic, as the three pendulums were found to collide with the floater hull in which they were mounted, requiring cushioning to minimise damage. Such PTO issues, could also perhaps be resolved using control to keep movements within the physical constraints of the system, but no such control is considered in [125].
Similar to inertial WECs, where a second body is suspended within a floater, the vibro-impact WEC has produced a great many papers, [119] [120] [18] [121] and [18]. This is a collaborative project between Maynooth University in Ireland, and Northwestern Polytechnic University in China. Though the vibro-impact WEC is intended as a full scale grid integrated WEC, [18], which incorporates a PI controller to maximise the energy harvested, contextualises this unusual PTO in the field of data buoys.
A rather similar design to the vibro-impact WEC is shown in [122] from Sun Yat-sen University. As well as its design, the vibration energy harvesting WEC in [122] also shares a number of other commonalities with the vibro-impact project, being a numerical study on three different diameters of device: 3m, 6m and 10 m, the smallest of which is suggested as use for a data buoy. Unlike [119] [120] [18] [121] it does not consider a control system, instead focussing purely on the sensitivity of the power output to device diameter. Both the vibro-impact WEC in [18], and the vibration energy harvesting WEC in [122], see data buoys as a stepping stone en route to a full scale WEC.
The PTO proposed in [123] is also similar to the vibro impact WEC, though a magnetic flywheel based generator is incorporated into the design. The application in [123] is to target IoT applications at sea. Using a mass block on springs, as a bistable mechanism, a connector from this moving mass maintains the inertia of the internal flywheel. A nonlinear model of the system in two DoFs is described, and validated against experimental tests in a wave flume, producing 0.07 W of power.

2.2.2.4 Direct electrical drive

Ocean Power Technologies (OPT) are one of the few companies to have successfully deployed wave-powered data buoys through their POWERBUOY (PB) range, of which the PB3 is the flagship. The PB3 buoy utilises direct electrical drive as its onboard power supply [10]. With its proven success as a surveillance device, extensively deployed by the US Navy in American coastal waters, it was proposed that an array of PB3 buoys would be combined to act as a wave farm ([11] being a real world example of using data buoys as a proof of concept for a large-scale project) but unfortunately, as discussed in Chapter 1, this project did not come into fruition. The OPT has been used in Chile to form the backbone of a wave-powered coastal ocean observatory [41], not only providing power along seabed cables to two underwater monitoring stations, but also transmitting the recorded data back to shore via WiFi.
Experimental testing of a reef monitoring buoy which uses a tubular permanent magnet linear generator is described in [34]. The unique concept behind this buoy is the optimisation used in its control system, which is based on a hybrid of Particle Swarm Optimisation and the Genetic Algorithm, concatenated by the authors to 'Genetic Swarm Optimisation'. The buoy is proposed as alternative to expensive manned field studies, by providing key water parameter data in a reef area (normally gathered by divers), through building up a UWSN powered by these buoys.
A comparison of a small-scale direct drive linear generator based PTO to what the authors call a resonant drive PTO is described in [144]. The direct drive PTO uses a heave plate as the lower reference point for the linear generator. The resonant drive PTO uses an inertial mass suspended within a central spar buoy, with four equally spaced external spar buoys providing stability against roll. Both PTOs are tested in 1:4 scale prototypes at sea and found to be suitable for sensing applications requiring 1-10W. [144] specify that the buoys are designed for small-scale low energy applications, and suggest the designs would not be suitable for scaling up for applications beyond low power data buoys.

2.2.2.5 Triboelectric nanogenerators

As discussed in Section 2.2.1.3, TENGs are one of the most researched PTO types for wave energy on the small scale. Due to the vast scope of potential applications, the reviews suggested concerning the use of TENGs in small-scale wave energy applications are [12], [87], [88]. These reviews are comprehensive lending themselves well to discerning the main advantages and challenges in using TENGs on data buoys. It should be noted that power density rather than absolute power is used to describe many TENGs, which can be a somewhat misleading metric, due to the very small size of these devices.

However, more recent papers seem to be moving away from this with many of them now stating the absolute power produced, even if power density is still used in the abstract. Interested readers are recommended to read [12] in particular, as all aspects of TENG applications in the data buoy field are covered. However, it is worth reiterating that the key conclusion of [12] is the distinct lack of any tests of TENGs in realistic sea conditions. TENGs are repeatedly described by their proponents as having appealing characteristics such as their light-weight and low cost, high power density, high efficiency and the ability to operate at low frequencies. However, with this hypothesis only proven in simplified experimental set-ups under ideal sea conditions, the authors of [12] went on to publish the first paper detailing TENG testing under realistic sea conditions in [89]. In [89] the focus is on testing three different TENG prototypes at 1:8 scale in a 28 $\times$ 12 $\times$ 1.2 metre wave basin, under conditions designed to represent conditions off the Portuguese west coast. The three 3D-printed prototypes each used a different design of TENG in order to determine the most effective type for harnessing wave energy, in a set-up designed to simulate realistic conditions. The three types tested are:

- Anisotropic circular TENG
- Unidirectional flat-based TENG
- Unidirectional lateral-based TENG

These prototypes were separately fitted to a model of a commercial navigation buoy, with Bluetooth used for wirelessly transmitting results. The tests found that, although TENGs theoretically capture all 6 DoFs, in realistic sea conditions surge, heave and pitch were found to be most relevant to harvesting energy from the wave motion. Other findings were that the TENGs electrical power outputs tend to rise with increasing pitch amplitudes and decreasing period due to the increase in the sphere velocity. Overall the unidirectional lateral-based TENG was found to be most efficient under the imposed experimental conditions.
The other recent paper regarding TENGs for use as PTOs in data buoys, also published in 2021, and therefore also not included in [12], is the array described in [105]. In [105], 7 s-shaped TENGs are stacked to form a single array designed as a PTO for a data buoy.[105] proposes the use of a rectifier bridge to align the AC frequencies of the 7 TENGs on board with one another. Published in the same issue of *Nano Energy* as [89], the prototype in [105] was also tested in a wave basin, measuring 50x3x1 metres, to study the TENG's performance over a variety of wave directions. The buoy was shown to have a maximum power density of 34.65 W/m^2 in tests, enough to directly light a 12W LED. The ability to stack TENGs on top of one another is a

major advantage of this type of PTO, with [130] and [105] stacking 5 TENGs and 7 TENGs on top of one another respectively. The novelty in [105] is that proposes a solution for combining their outputs into a usable AC signal.

Though many TENG papers exist, with the search "TENG Wave Energy" returning more than 10,000 results on Science Direct, a trend that can be observed in recent years is a focus to move from theoretical designs to more tangible real world issues facing these devices in small-scale wave energy applications. As studies on TENGs to provide power for data buoys are so numerous, a selection of the most promising breakthroughs in recent years is included in the rest of this subsection.

The TENG device described in [129] focusses on harnessing lateral motion in the surge DoF, and while this is relatively unusual in TENGs which are often more focusses on pitch, it is the fact that the device in [129] is able to provide enough power for LoRa radio transmission that is particularly notable. This means that the device in [129] would be sufficient for transmission of data over 1.5 km. Though integral to almost all data buoys, the particular transmission system is often not described in wave-powered data buoy literature, so seeing this sort of detail in a TENG paper shows how seriously developers are pushing for these devices to be used in real world applications. Another project considering transmission systems used with TENGs is [55], from the Pacific Northwest National Laboratory, with another arctic ocean targeted application. Though the device in [55] was not directly tested at sea, it was tested against real sea conditions. To relate the IMU readings from the arctic buoy to the wave elevation a Spotter wave measuring buoy was deployed next to it. By feeding IMU measurements from the deployed arctic buoy to move a dry test rig with the TENG fitted, low frequency performance in waves down to 0.2 Hz could be assessed. The power output was found to be on average 10-20 mW, which the authors of [55] suggest is actually sufficient to support satellite communication transferring 500 bytes/day. Future work will consider low temperature testing of the PTO to assess how true arctic conditions will affect performance.

The wave tank testing of the TENG in [128] similarly focusses on covering more realistic sea conditions, also considering waves as low as 0.2 Hz. Small devices often perform better in high frequency waves, so the fact that TENGs are more regularly being tested in low frequency waves signals a shift in moving ever closer to real world deployments. Indeed, [131] is perhaps the TENG closest to becoming a complete functional data buoy. Using an unusual TENG design based on coral tendrils, [131] has not only been tested in a real sea deployments, but during deployment demonstrated a strong linear relationship between the power generated and incident wave height, allowing for millimetre accurate readings of free surface elevation to be returned. This is a significant milestone in TENGs, as they look to become viable PTOs for low power data buoys just over a decade after their invention.

2.2.2.6 Hybrid

This heading is used in [65] primarily for hybrid systems where an additional method of energy harvesting, such as PV panels or wind turbines, is used in conjunction with a WEC to add some redundancy to the power supply, as touched on in Section 2.1.3.4. In this review, the only true hybrids by this definition, are the PTOs used by the MELOA Wavy *Ocean Atmo* and *Ocean Plus* Drifters [30] which combine gyroscopic energy harvesting with solar power, and the 'Tribrid' buoy in [63] which proposes adding wind, wave and solar energy harvesting to a Mobilis DB 8000 buoy.

The 'Tribrid' buoy detailed in [63], is a feasibility study on a surface buoy designed to provide power to an ROV at an offshore testing facility. The modelling of the 'Tribrid' was carried out by Exceedence Ltd., collaborating with researchers at the Science Foundation Ireland Research Centre for Energy, Climate and Marine (MaREI), to compare the performance of two different PTOs. Firstly, an OWC based WEC was modelled, followed by a model using the *Gator* spring pump and hydroelectric turbine [145]. The study concluded that the *Gator* had the greater energy output, and that combining it with an onboard wind turbine and PV panels would allow the buoy to provide sufficient year-round power to operate an ROV for 1 hour every day. However, [63] acknowledges that this modelling is hypothetical and that full-scale testing would be needed to verify that sufficient power output could be achieved.

Another device seeking to combine wave with wind and solar power on data buoys is [75] from Sandia Labs. [75] seeks to simplify the design of existing pendulum and suspended mass WECs through its pitch resonator concept. Modelled as a linear motion system, the moving mass concept in [75] is again similar to the PeWEC [143], but is designed to be bolted onto existing solar and wind powered data buoys as an alternative power source. [75] is in fact quite detailed on which existing buoys it should be fitted to, using the Pioneer Coastal Surface Monitoring array planned at Norfolk Virginia Beach as a case study. Not yet in service, these buoys will not only carry instrumentation on the buoy itself, but measure subsurface parameters too, with monitoring stations at 10 m depth on the mooring and at the seabed anchor. Furthermore, [75] utilises pseudospectral control in its PTO model, making it one of the few wave-powered data buoy projects to include some form of energy maximising control.

Other devices that could be considered hybrids in a broader definition would be the WASP OWC from Dundalk Institute of Technology [61] [62], where PV panels are planned as a back-up power supply once the OWC is converted to a WEC, and the Indonesian buoy which proposes the use of a piezoelectric generator in place of the usual air turbine. However, with the PV panels proposed as a stepping stone to a fully wave-powered device in the WASP, and the piezoelectric generator being a redesign

of an OWC rather than a second PTO system, it was deemed appropriate to include these buoys in Section 2.2.2.2 instead.
With the MELOA drifters being closely linked to the other gyroscope projects (in particular [106]) it was chosen to categorise them in Section 2.2.2.8, with the remainder of this section being an exploration of the more unusual 'other' PTOs used by data buoys.

2.2.2.7 Piezoelectric

Unlike [47] or [112], where a piezoelectric or dielectric generator replaces the turbine in an OWC design, [49] uses a piezoelectric beam as a direct method of harnessing the vibrations of a buoy at sea. Two different designs (one self-tuning and one not) are proposed and an experimental test rig is set up. The experimental testing uses real world wave excitation data from buoys in two locations, one in San Francisco Bay and one off the coast of Boston, to drive the motions of the rig in a realistic manner. Using this method, power is captured on the mW-scale, making it appropriate only for very low power applications. The work in [49] directly builds on that of [146], in which a number of different piezoelectric-based WEC ideas are proposed.
Also from the same authors as [112] is [135], which seeks to exploit a commonality piezoelectric energy harvester share with TENGs, namely their stackablity. This is implemented in [135] by stacking the piezoelectric layers 10 deep at the end of flexible links excited by a heave plate to which the buoy is attached. Despite the stacking of 10 layers, only 3.5 mW of power was achieved in rig testing, even with forces of 500-1000N which result in an equivalent buoy displacement of 0.37 m.
[132] proposes a piezoelectric wave energy harvester, which harnesses the vibrations through rods fitted with piezoelectric patches and magnets at their ends to repel them from touching other patches. Similar to [116], this is a WEC designed to be mounted to existing structures such as bridges and offshore rigs. With an end application proposed in powering temperature and structural monitoring of cables, a power output 41.5 mW was obtained. Tests were carried out in very small demonstrator tank similar to the one described in [147]. The idea proposed in [132] has been expanded on by researchers from the same group from Changchun University of Technology, in [133]. Here a similar piezoelectric wave energy harvester based on a gear mechanism and magnetic rotor cause piezoelectric rods fitted with repelling magnets to bend. Again, the amount of energy harvested is rather low at 28.33 mW in wave tank testing. Interestingly the WEC described in [132] and [133] is designed as a top referenced device to be mounted directly on an offshore structure, similar to the method suggested in [116]. However, where [116] is designed to support aquaculture cages, [133] suggests monitoring environmental parameters around an oil rig as its application.

Finally, a joint project from Zhejiang Ocean University in China and and Heriot-Watt University in Scotland, is given in [134]. Cognisant of the low power requirements of drifters, it is proposed that a piezoelectric wave energy harvester could be used to fulfil the onboard power requirements. As with [132] and [133], [134] induces vibrations in the piezoelectric ceramic rods using magnets; this time using a pendulum driven by the movement of the drifter hull. The device was rig tested producing 1.25 mW.
Piezoelectric PTOs, like TENGs are likely only suitable for very low power power applications, such as those of drifters. However, as discussed in Section 2.2.2.8 gyroscopic WECs appear to be the most developed in the field of drifters, with the MELOA gyroscopic drifters already commercially available.

2.2.2.8 Gyroscopic

The gyroscopic energy harvesters, developed by MELOA and used in their Wavy Drifter line, combine gyroscopic energy harvesting with solar power. The PTOs within these drifters utilise the pitching motion of the buoy to drive a gyroscope inside. However, being such small-scale devices (even by data buoy standards) the exaggerated frictional effects allow energy capture only in the the largest models of the series: namely the *Ocean Atmo* and *Ocean Plus* [30] [31] [32]. A detailed design of the gyroscope PTO system created in the development of these drifters, and the concomitant testing in an anchored buoy, is described in [106], where a power output 0.22 mW was achieved. Testing of the MELOA drifters has continued with [23], in which three different designs of the WAVY Ocean drifters are compared in real sea deployment. During testing the drifters in [23] were exposed mostly to wind waves and short gravity waves, experiencing winds of up to 12 m/s and significant wave heights of up to 2.5 m.
Focussing on the power management of the gyroscopic drifters developed at the Universitat Politècnica de Catalunya, [136], builds on [148] and [137] to improve the maximum power point tracking (MPPT) strategy used. [136] shows that through increasing the sampling rate of the MPPT, three times more energy can be harvested by the PTO. [136] is a rare example of at sea testing of a controlled wave-powered data buoy, as the majority of other projects developing control strategies for use on data buoys are carried out in a purely simulation based environment [18] [75] [42], with only [114] and [113] coming close, testing their control system using a hardware in the loop rig.
Described in the review of TENGs and other small-scale PTOs [88], the drifter in [92] also uses a pendulum mechanism, to drive the WEC on board. Published in 2019, the same year as [106], the drifter in [92] achieved a power output of 0.13 W during at sea testing.
Gyroscopic PTOs seem to be mostly focussed around providing power to small drifters. However, [56] proposes a dual pendulum design attached to a gyroscopic flywheel

designed for arctic monitoring buoys, which seem to be a focus of the Pacific Northwest National Laboratory [43]. The gyroscopic PTO used in [56] is unusual, in that it is a commercial off the shelf component purchased from WITT Energy. The buoy too, in which the WITT pendulum electricity generation device is installed is also commercially available, from Pacific Gyre and was previously used in arctic deployments. The Pacific Gyre buoy was selected as the PTO in [56] is designed to target pitch and roll, which the buoy is designed to facilitate. A heave plate for station keeping was used during at sea deployment in Sequim Bay off the North coast of Washington State's Olympic Peninsula. During deployment a peak power of 5W was achieved, though the sheltered nature of the bay (the highest wave being 0.4 m) meant the average power across the full deployment period was nearer 40 mW. As arctic operations are the end application for this device, all testing was done using including low temperature lubricant for all moving parts. The most striking thing about [56] is that a buoy, built with readily available components, successfully completed a deployment in real seas. The bespoke nature of many PTOs is oft discussed in wave energy, with little convergence on a final design, so a buoy built from off the shelf parts points towards wave energy becoming much more accessible to those wanting to power small-scale data buoys.

2.3 Chapter summary and conclusions

From the array of small-scale wave-powered data buoys investigated since 2011, some observations about the state of the art can be made. It is clear that OWCs remain a popular solution as a PTO mechanism for small-scale data buoy prototypes, though their prominence has been eclipsed by a host of suspended pendulum and gyroscopic WECs in recent years.

OWCs are oft cited as one of the most promising WECs [149], and looking at PTO choices for wave-powered data buoys since the 20th century [76], this appears also to be the case with small-scale devices. However, given the paucity of successfully deployed OWC data buoys, this lack of success over such a long period could be viewed as concerning. On the other hand, this experience gained does mean that more recently developed OWC-based buoys can be more targeted in their research: for example the projects at IST integrating latching control via the use of a biradial turbine to improve energy capture [3] [138] [97], [99], or exploring options to avoid the use of turbines altogether [47] [112].

Interestingly, by far most popular PTO mechanism documented over the past decade is the TENG, which has the opposite problem to the OWC. Though there is not the long history of unsuccessful deployments associated with TENGs as with OWCs, TENGs are only just beginning to be tested at sea [131], so little is known about the additional challenges they may face when exposed to harsh conditions at sea.

A lack of real deployment history is not a drawback unique to TENGs. At the time of publishing the review paper [14] in 2022, the MBARI-WEC in [17], with its 131 day overwintering in 2015, and the commercially available OPT PB3 [10], were notable for being the only data buoys to have at sea deployments where wave energy has been successfully harnessed as a primary power source (with the noteworthy exception of the gyroscopic drifters described in Section 2.2.2.8). While gyroscopic drifters remain at a relatively mature level of development, in the past couple of years other data buoys have developed at a remarkable pace, with Table 2.2 showing that the majority of recent small-scale WECs have been tested using either dry rigs or wave tanks; with [56] and [131] joining the ranks of those wave-powered data buoys that have been deployed at sea. Additionally, many of the more recent projects around TENGs have had an increased focus on more realistic low frequency waves, and been more forthcoming with the actual power produced by these devices, rather than the somewhat specious power density metric previously used.

Another noteworthy trend that can be observed in tables 2.1 and 2.2 is the under-representation of hybrid systems. Although [61] and [47] deserve an honourable mention, the 'Tribrid' buoy in [63], the coastal monitoring buoy in [75] and the larger MELOA drifters [30] are the only true hybrid wave-powered data buoys found during this research. With data buoys outside of wave power utilising a combination of power sources [44] [52], it could be expected for more data buoys to follow along the lines of [61] and [30], using reliable solar panels as a back-up energy supply. However, perhaps the issue is the perception of wave energy by end users as solar PV has become ever more effective, leading those who previously combined WECs with solar panels to abandon them, such as the Commissioners of Irish Lights [54], who saw no need to continue using wave energy alongside solar, once more efficient LEDs replaced the old filament bulbs previously in service.

A final noteworthy trend can be drawn when considering data buoys in development since 2011, and that is the relative dearth of projects using any form of control on the PTO. Of the projects that do include control, the majority are only tested in computer simulation [75] [18] [42], with [113] and [114] being rig tested, and only [136] [137] tested at sea. Many projects acknowledge that control could be an important tool in developing their designs further, with the MBARI-WEC being a particularly noticeable example [17]. It remains to be seen how effective MBARI's tool for testing controllers against a real world validated data buoy will be [107] [108] [109], but there is a possibility it will broaden the number of WEC controllers using data buoys as an example, since such controllers currently use full scale devices as test cases.

3
Hydrodynamic Modelling

Contents

3.1 Linear wave theory 51
3.1.1 Wave number 51
3.1.2 Celerity 52
3.1.3 Velocity potential 52
3.1.4 Assumptions 52
3.1.5 Pressure 56
3.1.6 Deep water vs. shallow water 56
3.1.7 Energy 58
3.1.8 Power 58
3.2 Wave spectra 59
3.2.1 JONSWAP 60
3.2.2 Bretschneider 62
3.2.3 Pseudo band-limited white noise 62
3.3 Cummins' equation 63
3.3.1 Hydrostatic force 65
3.3.2 Radiation force 65
3.3.3 Excitation force 68
3.3.4 State space representation 70
3.4 Chapter summary 71

A fundamental pillar of hydrodynamics is the Navier-Stokes equations, named after respectively French and Irish physicists Claude-Louis Navier and George Gabriel Stokes. The Navier-Stokes equations describe the behaviour of a fluid and its fluid-structure interactions with bodies within the fluid. To this day the Navier-Stokes

equations have no analytical solution, requiring numerical methods to solve them. Indeed, the Navier-Stokes equations are still not fully theoretically understood with the *Navier–Stokes existence and smoothness problem* a yet unsolved Millennium Prize Problem [150]. To obtain numerical solutions to the Navier-Stokes equations, high fidelity methods using CFD [151] or smoothed particle hydrodynamics (SPH) [152] are required. CFD approaches, using numerical wave tanks which simulate fluid dynamics and fluid-structure interactions, are generally used in WEC prototyping as a cost effective alternative to wave tank testing. However, the high computational requirements, and nonparametric nature of such solvers, prevents their direct use in applications requiring computationally efficient models, further requiring methods such as system identification or machine learning to obtain surrogate models of the dynamic behaviour of the system [153].

Models obtained through data-based methods, such as system identification [154] and [155], do have their drawbacks, being limited in applicability to the range of the inputs used in the training data. With numerical wave tank testing, or indeed real wave tank testing, being a time consuming endeavour, it is often preferable to use hydrodynamic models based on first principles. However, hydrodynamics is a complex science that rarely produces a closed solution. Therefore, the majority of solutions are purely numerical and specific to a particular scenario. Even linear hydrodynamic modelling, discussed in this chapter, requires the use of boundary element method (BEM) solvers such as WAMIT, NEMOH or AQWA to obtain values for the frequency dependent terms of added mass, radiation damping and the excitation force frequency response function. BEM solvers are based on frequency domain linear wave theory and assume the same set of assumptions and boundary conditions discussed in Section 3.1.4. BEM solvers use the panel method to break the surface of the floater geometry into a mesh of panels, and assume forces act in the the centre of each panel. BEM solvers differ from finite element analysis, by only considering the surface of the object being analysed. Most BEM solvers, for marine applications, use square panels and are classified as lower order solvers. Of the BEM solvers currently available, WAMIT has the only higher order solver capability, using curved panels. As discussed in Section 4.2, WAMIT can also be used with the massless disc approximation when modelling OWCs. This chapter discusses linear wave theory, wave spectra, and the forces acting on a floating object, as described by Cummins' equation.

3.1 Linear wave theory

Small amplitude linear (or Airy) regular waves are two-dimensional waves which are assumed to be periodic and invariant in time and space. Waves are described by a number of parameters, most easily defined in regular (monochromatic) waves, but which have applicability also to irregular waves (discussed in Section 3.2). These parameters and their meanings are most succinctly expressed diagrammatically, and are shown in Fig. 3.1. In Fig. 3.1, η is the free surface elevation (dependent on time), c_w is the wave celerity, A_w is the wave amplitude, H is the wave height (equal to twice the amplitude) and d is the water depth. The wavelength L is measured as the shortest horizontal distance of two successive points whose oscillations are in phase, and the period T is the time taken to complete a single oscillation.

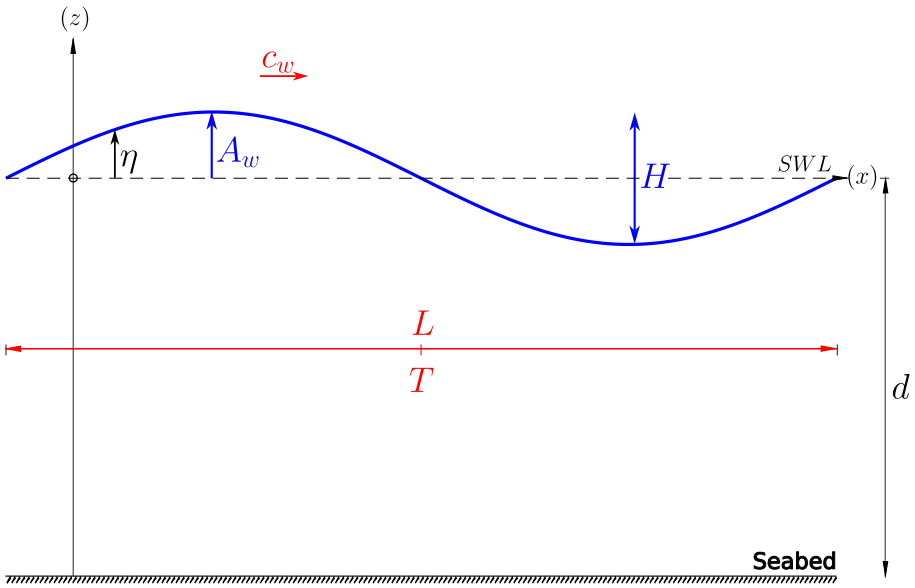


Figure 3.1: Wave parameters describing a linear regular wave: where η is the free surface elevation, c_w is the wave celerity, A_w is the wave amplitude, H is the wave height, d is the water depth, L is the wavelength and T is the wave period. SWL marks the still water level.

3.1.1 Wave number

The wave number k_w is also called the spatial frequency and is a measure of the number of complete wavelengths per unit length. It is defined by [156]:

$$k_w = \frac{2\pi}{L}. \tag{3.1}$$

3.1.2 Celerity

The wave celerity, c_w, describes the speed of wave propagation and is given by [156]:

$$c_w = \frac{L}{T} = \frac{\omega}{k_w}. \tag{3.2}$$

Waves are dispersive, which means that celerity is dependent on frequency. This means that, in water, low frequency waves have a higher celerity than high frequency waves. This is in contrast to light, which is non-dispersive and always travels at the same speed in the same medium.
It should be noted that celerity refers to the speed of wave propagation, not the velocity of the water particles, as waves carry only energy, rather than material. The displacement of water that is observed as waves is the result of the waves energy moving those particles. When wave particles move, they always follow an orbital motion, where the orbit radius decreases with depth, as shown in Fig. 3.2. Velocity potential gives a method to describe the velocity of water particles in a wave.

3.1.3 Velocity potential

Velocity potential ϕ is a scalar which comes from Bernoulli's format of the Navier-Stokes equations, which relates velocity potential to pressure. The velocity potential, when partially differentiated with respect to a direction gives the water particle velocity in that direction.
The Laplace wave equation for a two dimensional wave is given by [157]:

$$\frac{\delta^2\phi}{\delta x^2} + \frac{\delta^2\phi}{\delta z^2} = 0. \tag{3.3}$$

Solving for ϕ is ultimately what is done by BEM solvers [158]. However, in order to do this, a number of assumptions and boundary conditions are required.

3.1.4 Assumptions

To solve for ϕ, the minimum number of assumptions that must be made are:

- **Irrotationality** - whilst water particles move with circular motion, they themselves do not spin. This means there is no vortex shedding in the water and therefore no drag. Furthermore, irrotationality implies the water is also **inviscid**, meaning there is no viscous friction to cause wave decay when propagating through the fluid.

- **Incompressibility** - the density of the water is constant.

- **Surface tension is ignored** - the waves are pure gravity waves.
- **Uniform surface pressure** - there is no variation in surface pressure, and it is usually assumed to be atmospheric.
- **Impermeable seabed** - no water can go below seabed level.
- **Small motion** - this assumes that there is negligible variation in wetted surface. It also allows the assumption that, though $z = \eta$ at the surface, it can be assumed $z = 0$.
- **No wave breaking** - a water particle on the surface stays on the surface.
- **Periodic and invariant** - the wave is periodic and invariant in time and space.

BEM solvers assume that the wetted area of a device remains constant, and this is generally acceptable as long as the small motion assumption is not violated. Where WECs are affected by reactive power in energy maximising control strategies however, this assumption is sometimes violated [71]. In cases where the small motion assumption is violated approaches such as the 'nonlinear Froude-Krylov' method described in [159] can be used, which account for the changing wetted area of a device. In [159] the 'nonlinear Froude-Krylov' effects are most noticeable as the device experiences larger motions, with small device motions effectively causing an overlap with the approach considering a constant wetted area. This finding of [159] highlights that, when all assumptions are adhered to, linear wave theory remains an effective method of describing device dynamics in a computationally efficient manner.
For this thesis, two different PTOs were considered: namely TENGs and OWCs. One commonality shared by these PTOs is that neither can be used to effectively inject reactive power back into the system [160]. In terms of hydrodynamic modelling, the lack of reactive power exaggerating the motion of the device means that the devices considered in this thesis are unlikely to violate the small motion assumption used in linear wave theory.
From the assumptions listed previously in this section, a number of boundary conditions can be applied to (3.3). In [161] these boundary conditions are expressed mathematically, defining Equations (3.4), (3.5), (3.7), (3.10) and (3.13).

3.1.4.1 Bottom boundary condition

$$\frac{\delta \phi}{\delta z} = 0 \text{ at } z = -d \tag{3.4}$$

3.1.4.2 Surface boundary condition (kinematic)

$$\frac{\delta\eta}{\delta t} + \frac{\delta\phi}{\delta x}\frac{\delta\eta}{\delta x} - \frac{\delta\phi}{\delta z} = 0 \text{ at } z = \eta, \tag{3.5}$$

where the term representing the surface rotation (shown in red) is assumed to be very small, allowing (3.5) to be simplified to:

$$\frac{\delta\eta}{\delta t} - \frac{\delta\phi}{\delta z} = 0 \text{ at } z = 0. \tag{3.6}$$

Note that $z = \eta$ has also been simplified to $z = 0$ thanks to the small wave assumption.

3.1.4.3 Surface boundary condition (dynamic)

$$\frac{\delta\phi}{\delta t} + \frac{1}{2}\left[\left(\frac{\delta\phi}{\delta x}\right)^2 + \left(\frac{\delta\phi}{\delta z}\right)^2\right] + g\eta = 0 \text{ at } z = \eta, \tag{3.7}$$

where the kinetic terms (shown in red) are also assumed to be very small and can be neglected:

$$\frac{\delta\phi}{\delta t} + g\eta = 0 \text{ at } z = 0. \tag{3.8}$$

The removal of those components known to be very small, in (3.5) and (3.7), also removes any nonlinear terms. This allows the two surface boundary conditions to be combined into a single free surface condition equation:

$$\frac{\delta\phi}{\delta z} + \frac{1}{g}\frac{\delta^2\phi}{\delta t^2} = 0 \text{ at } z = 0. \tag{3.9}$$

3.1.4.4 Constant waves

The constant wave assumption implies that waves separated by an integer amount of wave periods (or wavelengths) must be the same:

$$\eta(x,t) = \eta(x + nL, t) = \eta(x, t + nT), \text{ for } n = 1, 2, 3, \ldots \tag{3.10}$$

where (x,t) can be combined in the variable $(L\frac{t}{T} - x)$ as:

$$\eta\left(L\frac{t}{T} - x\right) = \eta\left(L\frac{t + nT}{T} - (x + nL)\right). \tag{3.11}$$

Equation (3.11) can then be expressed in nondimensional form by dividing by L:

$$\frac{2\pi}{L}\left(L\frac{t}{T} - x\right) = 2\pi\left(\frac{t}{T} - \frac{x}{L}\right) = \omega t - k_w x = \theta. \tag{3.12}$$

For brevity, θ will be used henceforth to represent $\omega t - k_w x$.

3.1.4.5 Periodicity

Periodicity can now be introduced into (3.3) in terms of θ. Considering horizontal water particle velocity u_x:

$$u_x = \frac{\delta\phi}{\delta x} = -k_w \frac{\delta\phi}{\delta\theta}, \tag{3.13}$$

allowing (3.3) to be rewritten in terms of the wave number k_w:

$$k_w{}^2 \frac{\delta^2\phi}{\delta\theta^2} + \frac{\delta^2\phi}{\delta z^2} = 0. \tag{3.14}$$

At $x = 0$:

$$\frac{\delta\phi}{\delta x}(0, t, z) = \frac{\delta\phi}{\delta x}(L, t, z), \tag{3.15}$$

because of the periodicity of the wave. Therefore at $x = 0$ and $t = t$, $\theta = 2\pi\frac{t}{T}$; and at $x = L$ and $t = t$, $\theta = 2\pi\frac{t}{T} - 2\pi$.
Considering (3.13), and $\phi(\theta, z)$:

$$-k_w \frac{\delta\phi}{\delta x}\left(2\pi\frac{t}{T}, z\right) = -k_w \frac{\delta\phi}{\delta x}\left(2\pi\frac{t}{T}, z - 2\pi\right), \tag{3.16}$$

which holds true for all t, including $t = 0$.
Equation (3.3) can be solved for ϕ by applying the boundary conditions in (3.4) and (3.9), and considering the periodicity and constant wave assumptions using the separation of variables technique, to give:

$$\phi = \frac{gH}{2\omega}\frac{\cosh(z + d)}{\cosh(k_w d)}\sin(\theta). \tag{3.17}$$

As previously mentioned, the velocity potential, when differentiated with respect to a particular direction gives the water particle velocity in that direction. Therefore, differentiating (3.17) with respect to the x and z directions respectively, the velocity in the x and z directions can be found:

$$u_x = \frac{\delta\phi}{\delta x} = \frac{H\pi}{T}\frac{\cosh(k_w(z + d))}{\sinh(k_w d)}\cos(\theta), \tag{3.18}$$

$$u_z = \frac{\delta\phi}{\delta z} = \frac{k_w H\pi}{k_w T}\frac{\sinh(k_w(z + d))}{\sinh(k_w d)}\sin(\theta), \tag{3.19}$$

where the subscripts x and z refer to the water particle velocity u in their respective directions. Water particle displacement and acceleration can be obtained from (3.18) and (3.19) by integrating to obtain obtain water particle displacements, and differentiating to obtain water particle accelerations.

3.1.5 Pressure

An expression for the pressure term, upon which the Froude-Krylov method is reliant, can also be obtained from (3.17). From the Unsteady Bernoulli Equation [162], gauge pressure p can be expressed as the sum of static and dynamic pressure:

$$p = -\rho g z - \rho \frac{\delta \phi}{\delta t}, \tag{3.20}$$

where $\rho g z$ represents the static pressure, and the remaining terms represent the dynamic pressure. Note the negative symbol in both terms indicating the direction of the pressure. Solving the partial derivative for dynamic pressure, (3.20) becomes:

$$p = -\rho g z + \frac{\rho g H \pi}{2} \frac{\cosh\left(k_w \left(z + d\right)\right)}{\cosh\left(k_w d\right)} \cos\left(\theta\right). \tag{3.21}$$

As well as the pressure in the wave, the potential and kinetic energy of the wave and the dispersion relation ω^2 can be found:

$$\omega^2 = g k \tanh\left(k_w d\right). \tag{3.22}$$

To simplify the expressions obtained from (3.17) certain assumptions made about water depth in relationship to wavelength can be made.

3.1.6 Deep water vs. shallow water

As shown in Fig. 3.2, wave particle orbits differ depending on water depth. Knowledge of whether a wave is in deep or shallow water allows different assumptions to be made about bottom effects based on the ratio of wavelength to water depth. Though defined by the ratio of wavelength to water depth, the physical meaning of shallow water waves is that the wave still has horizontal velocity at the seabed, whereas deep water waves have no interaction with the seabed.

WECs which harness heave motion are best suited to deep water, whereas surge WECs are best suited for shallow water [163] [164] [165] [166]. Transitional waves which occur in the range between shallow and deep water make no assumptions about the waves, meaning transitional wave equations can be used for any wave.

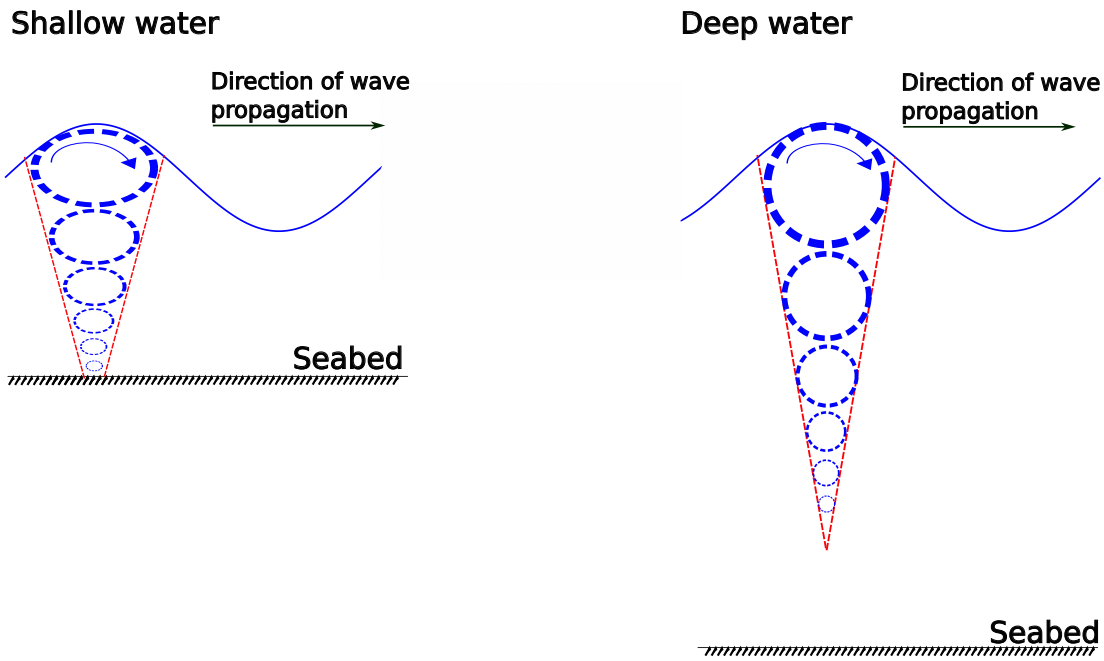


Figure 3.2: Difference in wave particle motions (orbits shown in dashed blue, with the blue arrow indicating direction of orbit), depending on whether the wave is propagating in shallow or deep water.

3.1.6.1 Shallow water

There are three common definitions of shallow water waves, which all express the ratio between water depth and wavelength in different ways:

$$\frac{d}{L} < \frac{1}{20}, \text{ or } k_w d < \frac{\pi}{10}, \text{ or } \frac{d}{gT^2} < 0.0025, \tag{3.23}$$

as given in [167]. For shallow water waves, it can be assumed that:

$$\begin{aligned} \sin(k_w d) \approx \tanh(k_w d) \approx k_w d, \\ \cosh(k_w d) \approx 1. \end{aligned} \tag{3.24}$$

3.1.6.2 Deep water

Similarly, for deep water waves, there are three common definitions [167]:

$$\frac{d}{L} > \frac{1}{2}, \text{ or } k_w d > \pi, \text{ or } \frac{d}{gT^2} > 0.08, \tag{3.25}$$

again given in [167]. For deep water waves it can be assumed that:

$$\begin{aligned} \sinh(k_w d) \approx \cosh(k_w d) \approx \frac{1}{2} e^{k_w d}, \\ \tanh(k_w d) \approx 1. \end{aligned} \tag{3.26}$$

The assumption of deep water is a common assumption when designing point absorbers [168], as it can be used to simplify the expressions for energy, as shown in Section 3.1.7.

3.1.7 Energy

Waves carry potential and kinetic energy. The potential energy E_p at a given time point is [169]:

$$E_p = \frac{1}{2}\rho g \left(d + \eta\right). \tag{3.27}$$

Since η is constantly changing with time usually the potential energy in the wave is calculated as a time averaged energy over a single wave period giving:

$$E_p = \frac{1}{16}\rho g H^2. \tag{3.28}$$

The kinetic energy E_k in a two-dimensional wave can be expressed as [169]:

$$E_k = \frac{1}{2}\rho \left(U_x^2 + U_z^2\right). \tag{3.29}$$

Using deep water assumptions (3.18) and (3.19), (3.29) simplifies to:

$$\begin{aligned} u_x &= \frac{H\omega}{2} e^{k_w z} \cos\left(\theta\right), \\ u_x &= \frac{H\omega}{2} e^{k_w z} \sin\left(\theta\right), \end{aligned} \tag{3.30}$$

which gives an expression for kinetic energy in deep water as:

$$E_k = \frac{1}{16}\rho g H^2. \tag{3.31}$$

The similarity between (3.28) and (3.31) allows the total energy in a deep water wave, E_w to be simply expressed as:

$$E_w = \frac{1}{8}\rho g H^2. \tag{3.32}$$

3.1.8 Power

A similar approach can also be applied to the power in a wave. Per unit area, the time averaged power in a wave, P_w, is given by [162]:

$$P_w = \int_{-d}^{0} p u_x dz \tag{3.33}$$

Again using deep water assumptions the expression for pressure in (3.21) simplifies to:

$$p = \frac{1}{2}\rho g H e^{k_w z}\cos(\theta) \tag{3.34}$$

Using the expression for u_x obtained in (3.30), (3.33) becomes:

$$P_w = \frac{1}{32\pi}\rho g^2 H^2 T. \tag{3.35}$$

Since power is the time derivative of the total energy, the expression in (3.35) can also be obtained from (3.32), again assuming deep water.

3.2 Wave spectra

Regular waves, or monochromatic waves, are essentially defined by a simple sine wave with a constant amplitude and frequency. Regular waves are often used in the early stages of testing WECs. Regular waves are particularly helpful in control, as the otherwise theoretical impedance matching control conditions can be fully realised for monochromatic waves [170]. Furthermore, polychromatic waves, which are an approximation to true panchromatic (irregular) waves, can be described through the superposition of a set of monochromatic waves [171]. Therefore testing in regular waves can provide some indications as to how a device will perform in real seas, with the advantage that a steady state oscillation can be reached. Such a steady state behaviour is important for the type of turbine characterisation carried out in Chapter 7. Not all regular waves are linear and they have to be sufficiently small and flat to satisfy the limitations of linear wave theory, especially in that they have a small ratio of wave height to wavelength. To test devices in more realistic sea states, there are a number of methods for defining irregular wave spectra. Where a single wave is easy to define in regular sea states as a single period of a sine wave, as shown in Fig. 3.1 irregular waves are far more difficult to describe and, as mentioned in [172], there is no absolute method of definition. Therefore, an approximation is commonly made when defining irregular waves, by either the *zero-up crossing* or *zero-down crossing* period where the time between one zero-crossing in the chosen direction (up or down) and the next is taken to be the period of that individual wave, with the horizontal distance between neighbouring zero-crossings in the chosen direction taken to be the wavelength.

Defining frequency spectral characteristics of waves has been widely studied [173], with a number of models commonly used in testing devices both in wave tanks and in a simulation environment. Most models for wave spectra focus on wind waves, with many accounting for fetch length and wind speed in their definition. The Pierson-Moskowitz spectrum, used to describe spectra for fully developed seas, is of particular note in this category, since it was originally described with wind velocity as its principal parameter,

though versions using statistical measures of wave height and period have since been derived [174]. Statistical measures of wave height and period are commonly used to describe wave spectra, since they reflect the characteristic parameters most commonly gathered by wave measuring data buoys, as discussed in Section 2.1.4.1.
As already alluded to, a number of wave spectral models exist, and though there are variations between them, those described by Bretschneider and Mitsuyasu have come closest to becoming a general wave spectrum definition for real ocean waves [172]. While the majority of wave spectral models have a single frequency peak, the Ochi Hubble spectrum is useful for its ability to produce double peaked spectra [175], which occur in seas where wind waves combine with swell waves creating two peaks at the dominant frequency of each wave type respectively.
In this project, three different approaches for generating irregular waves were used. The first of these is the JONSWAP spectrum, designed to produce the fetch limited waves observed in the North Sea. Due to the peak enhancement factor used to define JONSWAP spectra, the waves generated by the JONSWAP are more narrow-banded than the likes of those produced by Bretschneider. Bretschneider spectra, which produce more broad-banded irregular waves, have also been tested in this project.
Though not at all representative of real seas, for this project random waves are also generated using by sending a pseudo band-limited white noise spectrum to the wavemaker. In reality the wavemaker is itself also band-limited with a non-uniform frequency response, and the waves generated cannot support a white noise shape. However, pseudo band-limited white noise is an approach commonly used in system identification [176], in this case limited to the frequencies appropriate for testing at Lir NOTF, further discussed in Section 6.4.2.
The difference in theoretical spectral shapes defined by the three approaches used in experimental testing at Lir NOTF is shown in Fig. 3.3.
The remainder of this section comprises a brief discussion of the three wave spectrum definitions used to generate the irregular waves used in this project.

3.2.1 JONSWAP

JONSWAP (Joint North Sea Wave Project) spectra are a popular method of generating irregular waves. In the field of WEC control, examples can be found using JONSWAP spectra to produce irregular waves for wave tank testing [177], HiL assessments [178], or in simulation for developing WEC arrays [179]. Though its full name implies it should relate to North Sea locations, JONSWAP Spectra have been broadly used, and according to Edinburgh Designs, have even been used for testing inland river flood defences in the UK, due to their ability to produce fetch limited waves.

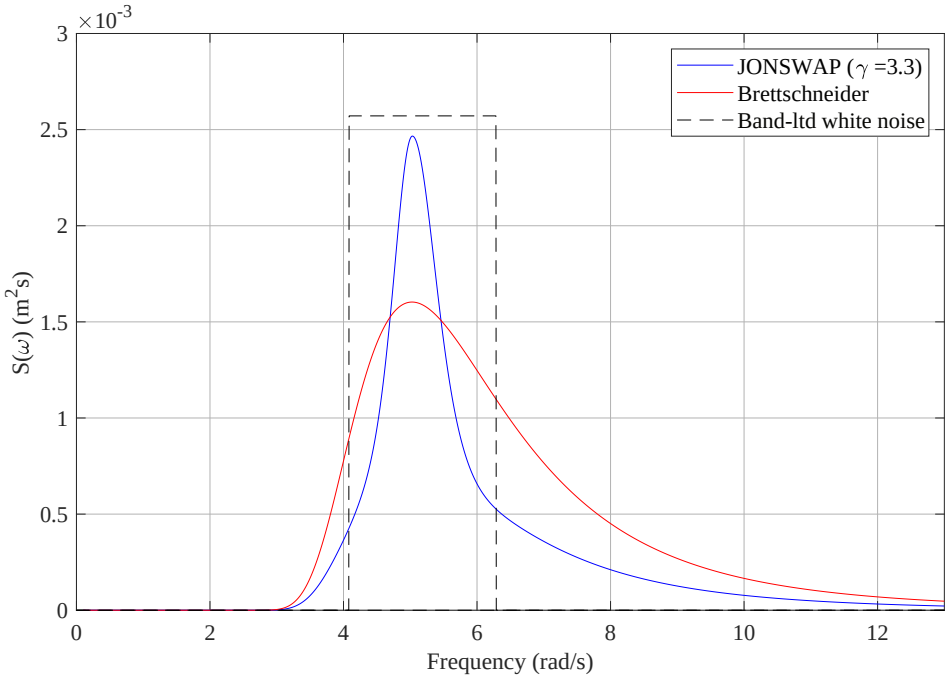


Figure 3.3: Comparison of the shape of some example theoretical wave spectra sent to the wavemaker at Lir NOTF.

The JONSWAP spectrum is essentially the Pierson Moskowitz spectrum multiplied by a peak enhancement factor, γ^a. Indeed, by setting the peak enhancement factor to 1 the Pierson Moskowitz spectrum can be recovered from (3.36). Conversely, increasing the peak enhancement factor brings the waves generated by the JONSWAP spectrum ever closer to monochromatic regular waves. The JONSWAP spectrum can be described by [172]:

$$S(\omega) = \frac{\alpha g^2}{\omega^5} \exp\left[-\beta \frac{\omega_p^4}{\omega^4}\right] \gamma^a, \tag{3.36}$$

where:

$$\begin{aligned} a &= \exp\left[-\frac{(\omega - \omega_p)^2}{2w_p^2\sigma^2}\right], \\ \sigma &= \begin{cases} 0.07, & \text{if } \omega \leq \omega_p \\ 0.09, & \text{if } \omega > \omega_p \end{cases}, \\ \beta &= \frac{5}{4}, \end{aligned} \tag{3.37}$$

where ω_p the peak frequency, and where g is the acceleration due to gravity, with α the Philips constant relating fetch length and wind speed for the location the spectrum is describing [180].

Setting $\gamma = 3.3$ has become general practice for defining JONSWAP spectra. Though for some locations waves are as narrow-banded as a $\gamma = 3.3$ JONSWAP spectrum, such as certain North Sea and Tropical coasts, [181], through comparing hindcast data from data buoys, demonstrates that this value is generally too high for most locations, with $\gamma = 2.4$ or lower generally more appropriate for most coastal areas around the world.

3.2.2 Bretschneider

In [182], the Bretschneider spectrum is described as the most realistic for producing irregular waves reflective of those in real seas. The Bretschneider spectrum can be defined using the wave characteristic parameters of the modal frequency, ω_m, and significant wave height, H_s, as [182]:

$$S(\omega) = \frac{5}{16}\frac{\omega_m^4}{\omega^5}H_s^2 e^{-5\omega_m^4/4\omega^4}. \tag{3.38}$$

The lack of a peak enhancement factor means that waves produced by a Bretschneider spectrum are more broad-banded than those produced by JONSWAP spectra. This means that for evaluating the estimator in Chapter 9 both narrow-banded and broad-banded irregular waves could be tested.

3.2.3 Pseudo band-limited white noise

A pseudo band-limited white noise spectrum can also be used to generate irregular waves, though such waves are not reflective of real sea conditions, and indeed the resultant waves cannot be described as white noise as such. As shown in Fig. 3.3, band limited white noise in theory maintains the same spectral density across all frequency bands for which it is defined. In practical applications, sending a wave maker a band-limited white noise spectrum results in the wavemaker attempting to maintain a near uniform spectral density across the specified frequency band, using a finite number of sinusoids to produce polychromatic waves.

Such pseudo band-limited white noise spectra are often used in system identification to determine the dynamic response of a device to a range of frequencies. This is particularly useful in marine applications to determine the response amplitude operator (RAO) [176]. Usually such waves are designed to cover a wide frequency range, but their purpose for this project is somewhat different. Instead of seeking to excite the device for the purposes of system identification, the aim of this project is to assess the estimator ability to return free surface estimates in random waves, while simultaneously generating power from the waves it is trying to estimate. As discussed further in Chapter 6, waves generated as using a band-limited white noise spectrum were highly effective at exciting the turbine PTO in wave tank testing, whilst providing irregular waves against which the estimator performance could be assessed.

3.3 Cummins' equation

To describe fluid-structure interactions, Cummins' equation remains the predominant method for modelling WECs [183]. For point absorbers, and other WECs which harness power in only a single DoF, models of WECs are often constrained to just a single DoF. For WECs which have more complex dynamics or coupling between different DoFs, a greater number of degrees of freedom must be considered. Floating bodies can have movement in 6 DoFs, shown in Fig. 3.4, and models of OWCs can sometimes even include more (as discussed in Section 4.2). Each additional degree of freedom included in the model of a WEC adds to the complexity of the model, and therefore the computation time, meaning that where possible, only those DoFs directly affecting the performance of the WEC should be included. Note that, despite moving in many hydrodynamic DoFs, conventional WECs usually have only one PTO DoF. Where appropriate data is available, input selection methods, discussed in Section 5.2.2, can be used to determine which DoFs should be included in the WEC model.

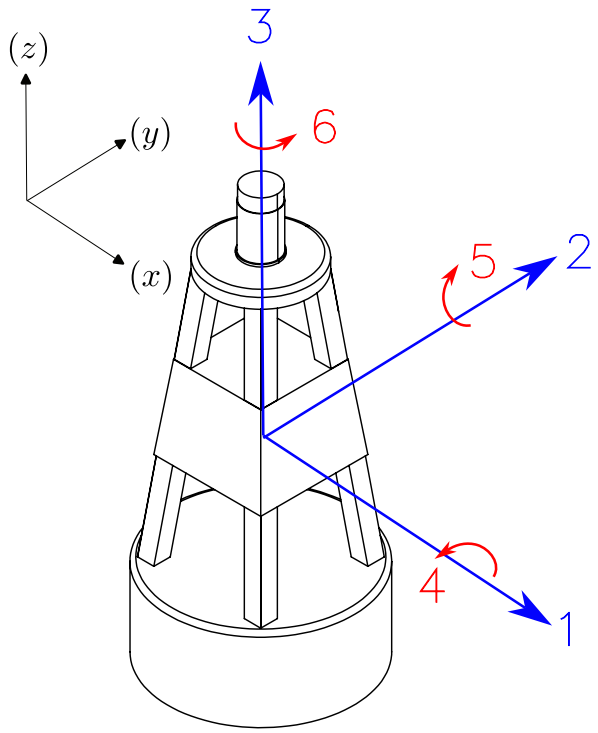


Figure 3.4: Showing the numbering convention for DoFs as set out by SNAME: where translational DoFs, 1, 2 and 3 (shown in blue), correspond with surge, sway and heave respectively; and rotational DoFs, 4, 5 and 6 (shown in red), correspond to roll, pitch and yaw respectively.

From the pseudo free-body diagram shown in Fig. 3.5 the equation of motion for a heaving buoy can be derived. The forces considered are gravity and buoyancy forces,

which in a linear system are dependent only on spring stiffness and displacement, damping forces which are dependent on velocity and the damping coefficient, and inertia forces which relate to mass and acceleration.

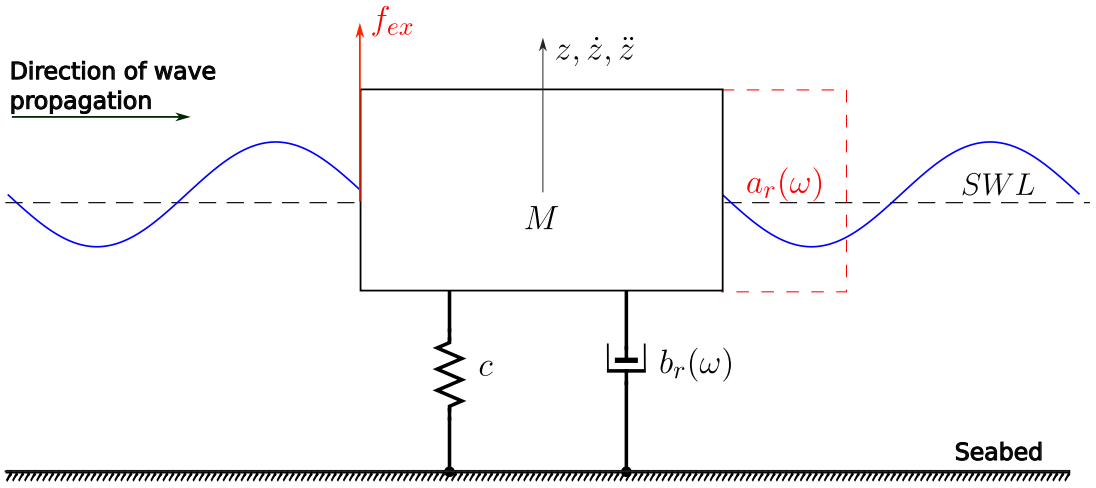


Figure 3.5: Pseudo free-body diagram of a heaving buoy, with the hydrostatic stiffness c shown as a spring, the radiation damping coefficient, $b_r(\omega)$, as a damper and the radiation added mass, $a_r(\omega)$, represented as an addition to the buoy mass M by the dashed red box.

For a buoy moving only in the heave direction, z, the time domain dynamics of the system can be represented by [184]:

$$M\ddot{z}(t) = f_{ex} + f_r + f_{hs} + f_{pto}, \tag{3.39}$$

where M is the mass of the buoy, f_{ex} the excitation force, f_r the radiation force, f_{hs} the hydrostatic restoring force, and additionally for WECs, f_{pto} is the force from the PTO. Forces that are not captured in (3.39) are the viscous drag force, due to the linear flow theory assumptions discussed in Section 3.1.4, and the forces from the mooring lines, which are nonlinear and come with a significant computational cost [185].
The force from the PTO will be discussed in Chapter 4, since different PTOs are represented in different ways. The remaining forces in (3.39) are described in the remainder of this section.
There are three basic ways by which the total force acting on a floating buoy can be calculated. These are:

- **Morison's equation** - based on empirical results, which accounts for flow separation and includes terms for drag forces.
- **Froude-Krylov method** - an attempt at an a priori analytical representation, and assumes the pressure in the wave is unaffected by the object.

- **Diffraction theory** - uses linear superposition. It splits the forces into scattering and radiation forces and solves them separately.

Diffraction theory assumes that the wetted surface remains constant and is the basis for boundary element method solvers such as WAMIT [158].

3.3.1 Hydrostatic force

The hydrostatic force, f_{hs}, is represented in Cummins' equation as a linear spring force [186]. It is simply calculated as:

$$f_{hs} = -cz(t), \tag{3.40}$$

where c is the hydrostatic stiffness, sometimes also called the coefficient of buoyancy. It effectively represents the spring that would be required to hold the floating body if the body was suspended in air. It is dependent on the cross sectional area of the device at the still water level. Hydrostatic force is a restoring force which generally increases upwards the further an object is pushed down. However, once an object is fully out of the water or fully submerged the hydrostatic force becomes a constant, as illustrated by Fig. 3.6. This means to avoid violating the constant wetted area assumption devices modelled using linear wave theory should not be allowed to become fully submerged or leave the water during operation.

3.3.2 Radiation force

Radiation force, is the name given to the force generated by a floating object. When a floating object moves in water it creates its own wave which radiates away from it. This is the radiation force. Velocity and acceleration are always 90° out of phase with one another. The vector sum of velocity and acceleration gives the force that comprises the radiated wave. According to Cummins' equation [186], the radiation force is given by:

$$f_r = -a\ddot{z} - k_r * \dot{z}, \tag{3.41}$$

where $*$ denotes the convolution operator, k_r is the radiation force kernel and a is the infinite frequency added mass. The radiation kernel can be expressed in terms of radiation added mass, a_r, and radiation damping coefficient, b_r, (which are both frequency dependent) as given by the Ogilvie relations [187]:

$$a_r(\omega) = a - \frac{1}{\omega}\int_0^\infty k_r(t)\sin(\omega t)dt, \tag{3.42}$$

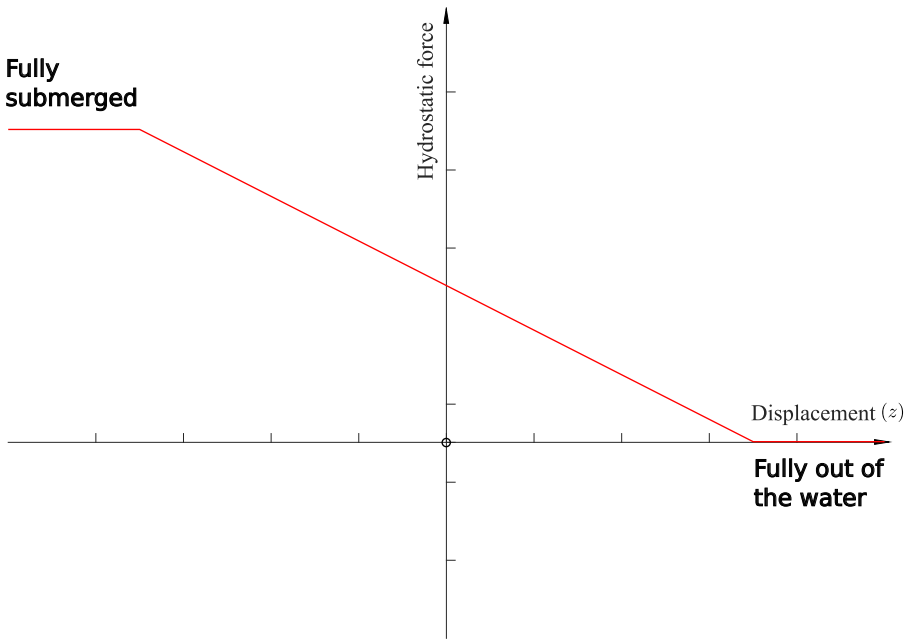


Figure 3.6: Showing the variation in hydrostatic force against z-displacement for a floating object. Once the object has been fully submerged, f_{hs} becomes constant, and when the body leaves the water entirely, $f_{hs} = 0$.

$$b_r(\omega) = \int_0^\infty k_r(t)\cos(\omega t)dt. \tag{3.43}$$

Equation (3.43) can then be used to express $k_r(t)$ only in terms of the radiation damping terms:

$$k_r(t) = \frac{2}{\pi}\int_0^\infty b_r(\omega)\cos(\omega t)d\omega. \tag{3.44}$$

The radiation force kernels used in this thesis were obtained through BEM solvers which use Green's function to relate the device geometry to the radiation damping coefficient and added mass.
Defining f_{rc} as:

$$f_{rc} = k_r * \dot{z}, \tag{3.45}$$

allows for (3.39) to be rewritten as:

$$(M + a)\ddot{z}(t) = f_{ex} + f_{rc} + f_{hs} + f_{pto}. \tag{3.46}$$

The radiation convolution integral given in (3.45) is a drawback of using Cummins' equation, as significant computational effort is required to solve it. To overcome the issues associated with the radiation convolution integral, f_{rc} can also be approximated as a finite order state space system approximation, with velocity $\dot{z}$ as the input:

$$\begin{aligned} \dot{X}_{rc}(t) &= A_{rc}X_{rc}(t) + B_{rc}\dot{z}(t), \\ f_{rc} &\approx C_{rc}X_{rc}(t), \end{aligned} \tag{3.47}$$

where X_{rc} represents the states required for the radiation convolution term approximation. Approximating the radiation convolution term is carried out by obtaining the impulse response function, or kernel, of the radiation frequency response function from WAMIT and reducing the order using Hankel singular value decomposition (HSVD) [188]. Hankel singular value decomposition, is used as the basis of balanced model order reduction [189]. Balanced realisations of a system are ones where the controllability and observability gramians are diagonal and equal. Essentially HSVD is an eigenvalue decomposition for symmetric matrices, where the ordering of eigenvalues can be chosen, with strongly observable (and therefore strongly controllable, since the observability and controllability gramians are diagonal and equal) states ordered first, and weakly controllable and weakly observable states later. Then by removing the weakly controllable states, the model reduction error is minimal, and a model order can be chosen until a low model order system with suitably low model reduction error is obtained.

A model order appropriate for inclusion in the model is determined by considering various model orders and comparing their mean absolute error (MAE) and root mean square error (RMSE), both of which are normalised to the standard deviation. A common alternative approach to obtaining a state space equivalent of the radiation kernel is the moment matching approach facilitated by the FOAMM toolbox [190]. The moment matching approach is useful in that it returns an approximated system where key frequencies (chosen by the user) are matched exactly, which makes it well suited for frequency domain applications.

As shown in Fig. 3.7, comparing the time domain impulse response of the approximated radiation force kernel, the best fit for the example shown is an order 3 model obtained using the HSVD approach. The fact that a HSVD approximation is better able to produce an approximated model of the radiation force kernel than FOAMM in the time domain (which is the focus of the work in this thesis), is perhaps unsurprising since FOAMM is best suited to applications where a close fit in the frequency domain is required. Furthermore, reducing an impulse response function using HSVD is a flexible approach which can also be applied to approximating the excitation force kernel, as discussed in Section 3.3.3.

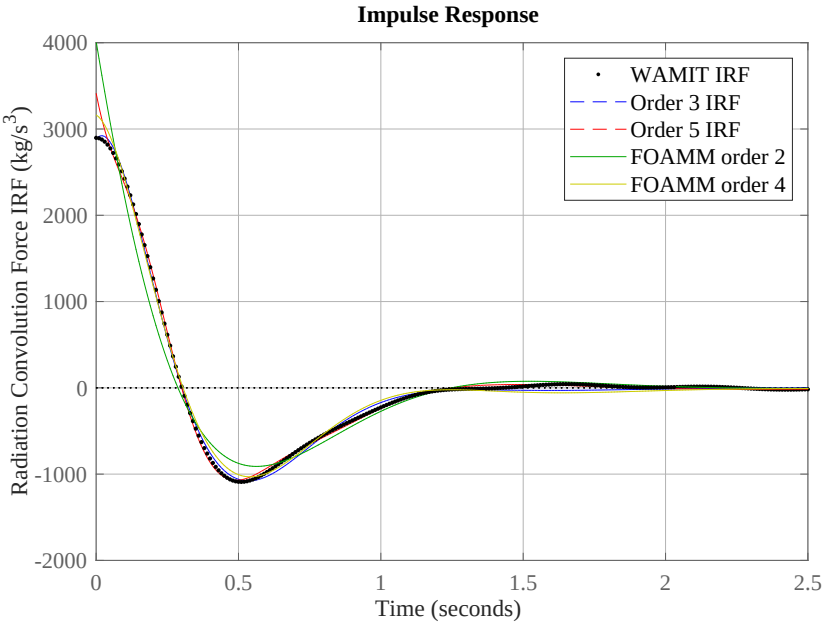


Figure 3.7: An example comparing the impulse response functions of state space equivalents obtained using the FOAMM and the HSVD approaches. The best fit model is found to be of order 3, with a corresponding normalised MAE of 0.0212 and normalised RMSE of 0.0522.

3.3.3 Excitation force

Normally in wave energy the input to the dynamic system is considered to be the excitation force. However, the ultimate goal for obtaining a hydrodynamic model for this thesis is for use in an unknown input estimator, where the unknown input is the free surface elevation. To convert the excitation force input from Cummins' equation to be free surface elevation, the excitation force impulse response kernel, k_{ex}, is approximated as a separate state space system, following a similar approach to that used for approximating the radiation convolution term. In the time domain, free surface elevation, η, is related to excitation force by [188]:

$$f_{ex}(t) = k_{ex}(t) * \eta(t) = \int_{-\infty}^{\infty} k_{ex}(t-\tau)\eta(\tau)d\tau, \tag{3.48}$$

where $*$ denotes the convolution operator.
The excitation force kernel, or impulse response function, k_{ex}, is defined by:

$$k_{ex}(t) = \frac{1}{2\pi}\int_{-\infty}^{\infty} H_{ex}(j\omega)e^{j\omega t}d\omega, \tag{3.49}$$

where H_{ex} is the excitation force frequency response function obtained from WAMIT. Due to the manner in which the reference frame for modelling the hydrodynamics of floating bodies is chosen, most commonly set at the centre of the device, the excitation

force acting on the device is assumed to be due to the wave elevation at the centre of the device, resulting in a noncausal process [177]. The resulting noncausality can be observed in Fig. 3.8, where k_{ex} has both a component before t = 0 s and after. To approximate a state space equivalent, without losing dynamic information, k_{ex} is causalised following the method outlined in [188], where k_{ex} is shifted by a causalisation time, t_c, until there is no significant component below 0 seconds; affecting the relationship between k_{ex} and η, as described by (3.50).

$$f_{ex} = k_{ex}(t)^{*}\eta(t) = k_{ex}\left(t - t_c\right)^{*}\eta\left(t + t_c\right), \tag{3.50}$$

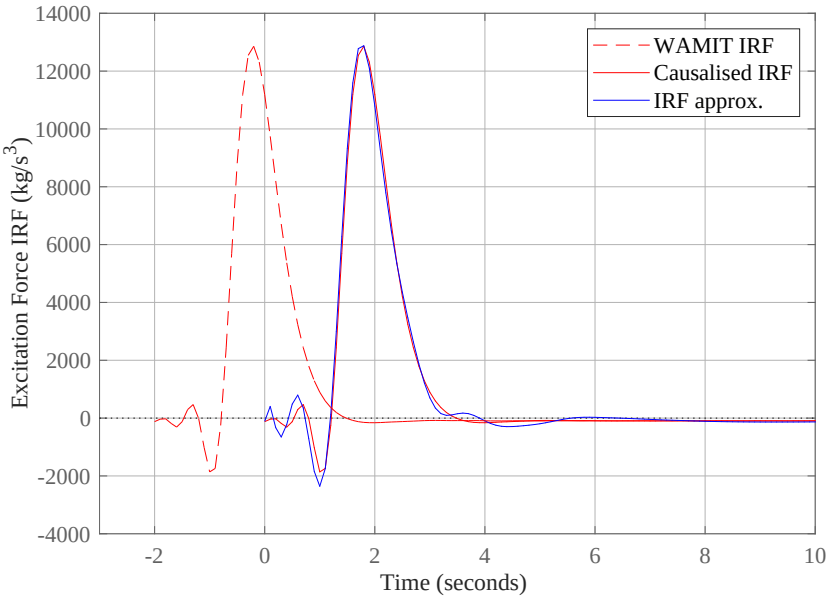


Figure 3.8: A comparison of the noncausal impulse response function obtained from the WAMIT results, and the subsequent causalisation and the impulse response from the identified state space approximation.

As demonstrated by (3.50), causalising k_{ex} introduces a timeshift in the related free surface elevation equal to the causalisation time. To generate a state space approximation of the causalised excitation kernel, a Hankel singular value decomposition is used to reduce the impulse response function to an order suitable for inclusion in the model, again using the metrics of MAE and RMSE used in determining a reduced order model for the radiation force kernel. Equation (3.50) can then be approximated in state space form as:

$$\begin{aligned} \dot{X}_e(t) &= A_e X_e(t) + B_e \eta(t + t_c), \\ f_{ex} &\approx C_e X_e(t), \end{aligned} \tag{3.51}$$

where X_e refers to the states required for the excitation force approximation.

3.3.4 State space representation

Linear dynamic systems can be described in either the time domain or in the s or ω frequency domains. Frequency domain models are usually represented as parametric transfer functions which represent the ratio of the input to the output in the frequency domain (assuming initial conditions are zero) [191]. Transfer functions represent a useful method by which the dynamics of the system can be represented; though by their nature, such transfer functions are limited to the frequency domain, which is not well suited to handling nonlinearities or systems which are not time invariant. In linear time-invariant systems, linear superposition applies. However for nonlinear or time-variant systems, a time domain representation is required. Though the model discussed in this chapter is purely linear, as shown in Section 4.2.2, modelling OWCs introduces nonlinearity into the dynamic model of the system, meaning a time domain modelling approach is required. In the time domain, a dynamic system is represented by the form of a differential equation, which can become unwieldy especially as systems become more complex, which is usually the case for hydrodynamic models of WECs. While not necessarily less complex, state space equations give a systematic framework which allows a dynamic system to be described in terms of a vector of state variables, which follows the same form regardless of system order, and can be initialised at non-zero values. The general form of a state space system in continuous time, representing a WEC, is:

$$\begin{aligned} \dot{X} &= AX + Bu, \\ Y &= CX + Du, \end{aligned} \tag{3.52}$$

where X is the vector of state variables, Y is the system output vector and u is the system input vector. The matrices A, B, C and D are obtained from the physical description of the system depending upon which variables are chosen as the state variables. For a floating body constrained to move only in the heave direction, with η as the input, the state space representation of the system becomes:

$$\begin{aligned} A &= \begin{bmatrix} A_e & 0 & 0 & 0 \\ 0 & A_{rc} & 0 & B_{rc} \\ 0 & 0 & 0 & 1 \\ \frac{C_e}{M+a} & \frac{C_{rc}}{M+a} & -\frac{c}{M+a} & 0 \end{bmatrix}, \\ B &= \begin{bmatrix} B_e \\ 0 \\ 0 \\ 0 \end{bmatrix}, X = \begin{bmatrix} X_e \\ X_{rc} \\ z \\ \dot{z} \end{bmatrix}, u = \eta, \end{aligned} \tag{3.53}$$

with the subscript rc referring to the state space representation of the radiation convolution integral given in (3.47), and the subscript e referring to the excitation force approximation in (3.51).

Every additional hydrodynamic degree of freedom increases the size of the state space matrices, adding a new row and column to A for the radiation convolution term and excitation force approximations, with corresponding increases in the lengths of B and X. This again highlights the importance of including only relevant DoFs when obtaining a computationally efficient dynamic model of the system.

3.4 Chapter summary

In this chapter the background to the hydrodynamic theory used in the remainder of this thesis is presented. Though limited to linear wave theory, the PTOs that will be considered in subsequent chapters are unlikely to violate the assumptions stated in Section 3.1.4. Obtaining relatively simple hydrodynamic models is essential to minimise the computational time required for the free surface estimator, described in Chapter 8, and evaluated in Chapter 9, to operate. Moreover, the nonlinearity that is introduced to the dynamic model through the addition of an OWC-based PTO, the modelling of which is described in Section 4.2, significantly adds to the complexity of the dynamic model of the system to be used by the estimator. Also described in this chapter, specifically Section 3.3.3, is the method by which the input to the hydrodynamic model is set to be the free surface elevation. Approximating the excitation force kernel in the manner described in Section 3.3.3 introduces a delay in the resulting hydrodynamic model, due to the causalisation of the excitation force kernel. Such a delay is in the magnitude of 1-2 s for the devices considered in this thesis, which is unlikely to be an issue for users requiring measures of free surface elevation, as such measurements are rarely required in real time. Furthermore, when compared to real ocean waves, a delay of 1-2 s generally represents only a fraction of a wave period.

4

TENGs and OWCs as data buoy power sources

Contents

4.1 TENGs 74
4.1.1 Operating principle of TENGs 74
4.1.2 Modelling TENGs from first principles 78
4.1.3 Challenges in modelling TENGs from first principles 80
4.2 OWCs 82
4.2.1 Operating principle of OWCs 82
4.2.2 Modelling OWCs from first principles 84
4.2.3 Turbines 89
4.2.4 Known issues using OWCs at small scale 93
4.3 Chapter summary 94

A trend observed in Chapter 2 was a split in the research landscape between those advocating for the scaling down of larger WEC designs, such as point absorbers and OWCs, and those arguing that small scale applications require PTO systems designed specifically for the small scale. Among the most prominent of the PTO systems identified in Chapter 2, specifically for small scale applications, is the triboelectric nanogenerator, commonly abbreviated to TENG. TENGs are designed to harvest energy from sources of irregular motion, with potential applications in wearable technology, environmental monitoring, and medical science [98]. The ability of TENGs to generate energy from irregular, chaotic motions has led to a large number of research papers, as demonstrated in Chapter 2, focussing on their potential as a PTO for WECs, where the stochastic nature

of waves creates a challenge for many conventional generators. However, one of the main challenges in using TENGs is that they are almost entirely tested using real prototypes, because modelling their behaviour from first principles represents a significant challenge. In contrast, modelling OWCs is a well established field which has been studied since the last century [192] [193] [194]. However, as discussed in Section 4.2.4, OWCs come with a number of challenges and unknowns when operating at the small scale.

4.1 TENGs

TENGs are arguably the most rapidly growing area of research in small scale wave energy applications. This section is split between a description of their operating principle and a discussion surrounding the challenges involved with modelling TENGs from first principles. A proposed solution to these challenges is described in Chapter 5.

4.1.1 Operating principle of TENGs

Triboelectricity is a form of electricity which, through the chemical bond formed when two triboelectrically opposed materials are brought into contact, causes a surface charge transfer [195], which can either be transferred by sliding or by the process of contact separation. An everyday example of triboelectricity is static electricity which can build up charge on fibres such as nylon or wool through rubbing with a triboelectrically opposed material, for example rubbing wool against a balloon. Triboelectric nanogenerators seek to harness this form of charge transfer in order to generate low level power, for a variety of applications where harnessing irregular stochastic motions is required. As a relatively adaptable technology, TENGs find applications beyond wave energy: in the medical field [196], wearable technology [84], or in powering sensors for smart cities [197].
Though TENGs can be highly varied in their designs, from rolling balls on triboelectric foils [89], to tendrils [131], and even TENGs mimicking rotational or linear generators [198] [199], the operating principle of all TENGs can be classified into four broad categories [200], depending on how the dielectric materials comprising the TENG are arranged, as shown in Fig. 4.1.
The four types of TENG arrangement can be summarised as:

a) **Translational contact separation mode** where two triboelectrically opposed surfaces are cyclically brought into contact across a gap, and subsequently separate. The periodic contact generates opposing surface charges on the triboelectric layers, and the separation creates a potential difference across the electrodes driving an alternating current (AC).

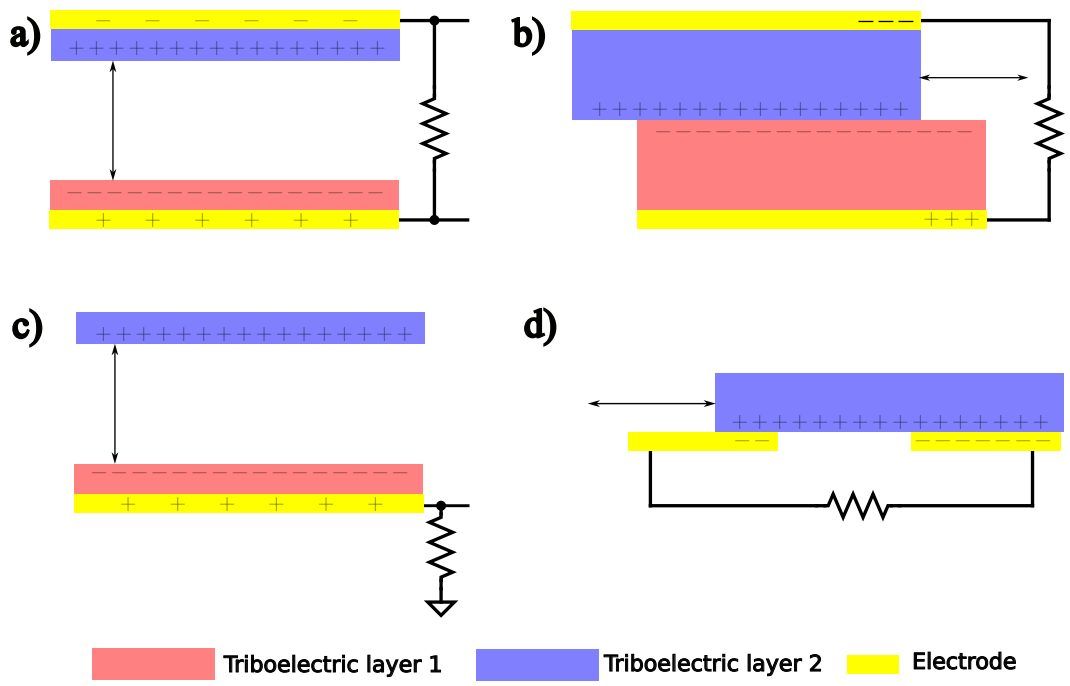


Figure 4.1: The four main types of TENG mode classification: a) Translational contact separation mode b) Lateral sliding mode c) Single electrode mode d) Free standing triboelectric layer mode.

b) **Lateral sliding mode** where the sliding of two triboelectrically opposed surfaces in contact with one another builds up opposing charges. The change in contact area creates a potential difference across the electrodes.

c) **Single electrode mode** is similar to the contact separation mode, but where only a single electrode is attached to the load, and the contact and separation between the triboelectric layers and the electrode induces changes in the electric field, causing electrons to flow through the load to the ground. Notably, one of the triboelectric layers does not need to be attached to an electrode, making this mode of TENG less limited by motion constraints than the contact separation mode TENG.

d) **Free standing triboelectric layer mode** is characterised by a single charged triboelectric layer that slides across two stationary electrodes which are not directly attached to it. The sliding motion asymmetrically builds up charge, and this imbalance of charges drives a current when a sufficient potential difference is induced between the electrodes.

Contact separation mode TENGs are particularly well suited to low frequency applications, and of the main TENG modes, are the most commonly proposed for wave energy applications; while lateral sliding mode TENGs require high frequency motion

and are less commonly suggested for applications in wave energy [195]. Free standing triboelectric layer mode TENGs are not affected by electrostatic shielding effects which can lower the efficiency of other TENGs [201]. Free standing triboelectric layer mode TENGs have the further advantage of being relatively flexible in their design as the electrodes do not need to be directly attached to the moving media; a flexibility somewhat shared by the single electrode mode TENGs which only require the electrode to be attached to a single triboelectric layer.

All four arrangements of TENGs rely on movement between surfaces, be it sliding or contact separation. In order to provide this movement an external force is required. The choice of external force to move the dielectric layers is a function of the application area, and is the driving factor behind the variability in TENG designs seen in the reviews [13], [88], [12], and [87]. As discussed in Section 4.1.2, the source of the external force is also the main driver behind the complexity of modelling TENGs designed to harvest wave energy.

TENGs which are designed to behave like linear or rotary generators can be modelled from first principles relatively easily, as the translation of the hydrodynamic DoF to the movement of the PTO is usually simple; with output power dependent on the rotational or translational velocity [198] [199]. However, such TENGs demonstrate little advantage over using either a conventional linear or rotary generator, since TENGs usually have a far lower power output than conventional electromechanical generators.

One of the key strengths of TENGs oft touted, regardless of application [83] [84], is in their ability to harness chaotic motion, such as that experienced by wearable technology, or indeed, WECs. TENG designs, which embrace the stochasticity of device movement, often use unusual approaches, such as the biomimicking coral tendrils in [131], or the rolling-ball-type TENGs in [89], and even, in the biomedical field, implantable vein-like TENGs which move with the body [202].

Rather than being merely a triboelectric twist on a conventional generator design, TENGs such as rolling-ball-types and tendril types produce electricity without requiring constraints on the number of degrees of freedom of device motion. Indeed, control of TENG powered data buoys is extremely rare, with [196] being one of the few TENG projects to attempt any form of energy maximising control, using maximum power point tracking and a spring mechanism to change the friction between triboelectric layers. However, [196] is another example of using TENGs in a manner similar to a more conventional PTO, and though the addition of control increases the output of the TENG in [196] dramatically, there is no clear argument presented as to why a TENG is beneficial in this case over a conventional linear generator.

In this thesis, the TENG that will be used as a case study is a rolling-ball-type TENG, which is an example of a TENG which harnesses chaotic motion, and is quite different

to any conventional WEC PTO mechanisms. Through collaborative work with the University of Porto, data from the wave tank tests carried out in [89] was made available for analysis in this thesis. Having access to experimental data from a rolling-ball-type TENG, which plays into the strengths that this PTO type has to offer, presents a test case for a PTO specifically designed for small scale applications.
The working principle of a rolling-ball-type TENG is shown in Fig. 4.2. Essentially this form of contact separation TENG consists of two triboelectrically opposed films, made of PTFE and Nylon 6,6 respectively, designed such that they are separated by a small gap and attached to a silver electrode. The movement of stainless steel ball-bearings across the PTFE film causes it to deform and contact with the stationary nylon 6,6 below, building up opposing charges on the two film surfaces. Once the ball has moved over the film, the dimensions of the PTFE cause it to rise again, separating contact between the layers creating a potential difference between the electrodes. This potential difference drives the electrons to flow through the resistive load, which over repeated cycles generates an AC output.

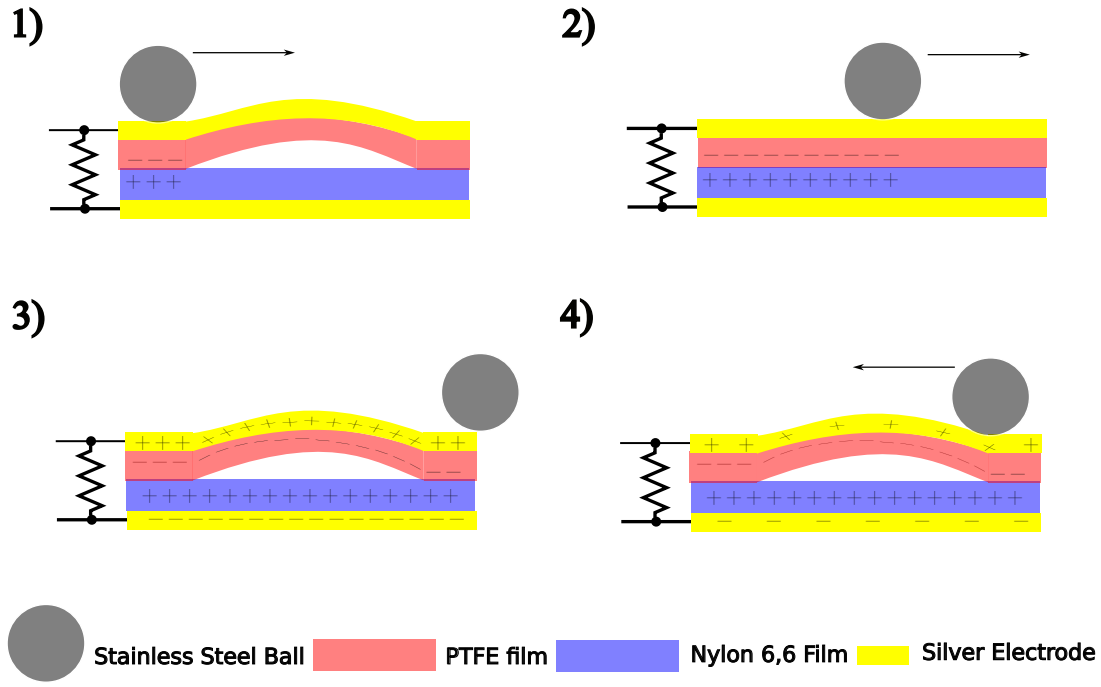


Figure 4.2: Operating principle of the rolling-ball type TENG used in this project. Periodic contact separation is driven by ball movement and a PTFE film designed to elastically return to a position where a gap is formed between it and the triboelectrically opposed Nylon 6,6 film.

The movement of the ball is driven by the motion of the buoy to which the TENG is mounted, harnessing the motion in multiple DoFs. It was found, in [89], that the effects of the moving spheres had negligible impact on device dynamics, highlighting

another feature of this type of TENG, which though it cannot enforce displacement constraints on the device itself, has some advantages when it comes to wave powered data buoys. Because TENGs generally have a negligible effect on device dynamics, recovering free surface elevation from TENG powered devices is relatively trivial, since they can be designed to move as wave followers. The ability of TENG powered devices to recover free surface elevation has even been proven at sea, with [131] able to recover millimetre accurate wave measurements.

4.1.2 Modelling TENGs from first principles

The fundamental theory describing the behaviour of a TENG is based on Maxwell's equations, named after physicist and mathematician (and fellow Kirkcudbrightshire local!) James Clerk Maxwell. Maxwell's equations were developed as a method of studying electromagnetic waves. They are derived from experimentally observed laws of physics such as Ampere's Law, and Faraday's Law, providing a governing set of equations that unify electricity and magnetism. Though there are limited cases where Maxwell's equations can be solved analytically, for the complex geometries and materials used in real world applications, this is not usually the case [203] and, similarly to the Navier-Stokes equations, numerical solutions must be found using high fidelity finite element analysis (FEA) solvers, such as COMSOL Multiphysics.
Maxwell's Equations are applicable across the full range of TENG designs, though with an important adjustment. Maxwell's equations are usually applied to media where the volumes and boundaries are fixed. Because the output of a TENG is dependent on movement, and therefore dependent on time, an expansion to Maxwell's equations is required, as described in [204].
In [204], written by the inventor of the TENG, material scientist Zhong Lin Wang, the integral form of Maxwell's equations is used as the starting point from which an expanded form is derived, which considers the medium moving as a rigid translated object. In addition to the moving medium, a new term is introduced to represent the polarisation in the displacement vector $\boldsymbol{P}_\mathrm{s}$; physically representing the electrostatic charges on the surface of the moving medium. This results in the form:

$$\begin{aligned}
&\nabla \bullet \boldsymbol{D}' = \rho_f - \nabla \bullet \boldsymbol{P}_\mathrm{s}, \\
&\nabla \bullet \boldsymbol{B} = 0, \\
&\nabla \times (\boldsymbol{E} - \boldsymbol{v} \times \boldsymbol{B}) = -\frac{\partial}{\partial t}\boldsymbol{B}, \\
&\nabla \times [\boldsymbol{H} + \boldsymbol{v} \times (\boldsymbol{D}' + \boldsymbol{P}_\mathrm{s})] = \boldsymbol{J}_f + \rho_f \boldsymbol{v} + \frac{\partial}{\partial t}\boldsymbol{D}' + \frac{\partial}{\partial t}\boldsymbol{P}_\mathrm{s}.
\end{aligned} \tag{4.1}$$

where $\boldsymbol{D}'$ is the electric field displacement, ρ_f is the space charge density of free charges, $\boldsymbol{B}$ is the magnetic field, $\boldsymbol{E}$ is the applied electric field, $\boldsymbol{v}$ is the velocity of the medium,

and $\boldsymbol{J}_f$ is the free electric current density, which is the conduction current received acoss the resistive load shown in Fig. 4.2. The bold font indicates that these symbols are vectors. From 4.1, the displacement of the medium $\boldsymbol{D}$ can be defined as:

$$\boldsymbol{D} = \varepsilon_0 \boldsymbol{E} + \boldsymbol{P} + \boldsymbol{P}_\mathrm{s}, \tag{4.2}$$

where ε_0 is the vacuum permittivity, and $\boldsymbol{P}$ is the local polarisation caused by the free charges represented by $\varepsilon_0 \boldsymbol{E}$. (4.2) captures the polarisation effects of the moving media, with the aforementioned $\varepsilon_0 \boldsymbol{E}$ representing the free charges exciting the medium, and P representing the local polarisation. The final term, describing the polarisation of the surface charges already present on the medium $\boldsymbol{P}_\mathrm{s}$, is a necessary addition to represent the contact separation principle.

Zhong Lin Wang's expansion of the Maxwell Equations is, in fact, based on a previous expansion by German physicist Rudolph Heinrich Hertz, who expanded Maxwell's equations to account for moving media, though this work is limited to modelling conductors [205]. The expansion described in [204] expands on Hertz's work to also include cases with dielectrics and empty space.

Interestingly, the advent of TENGs has led to a resurgence of interest in the electrodynamics of moving media. Minkowski's derivations for electrodynamics [206], named after Jewish mathematician Hermann Minkowski, who built on Einstein's theory of relativity, recasting it into four dimensions, until recently, remained relatively obscure. However, as interest has grown in modelling TENGs, Minkowski's equations on special relativity, which use Maxwell's equations as their foundation, are again being used to account for moving media in modelling TENGs [207]. In fact, Zhong Lin Wang acknowledges Minkowski's work on moving media in Maxwell's equations, [206], as a building block for his own derivation.

The requirement to solve Maxwell's equations, using high fidelity solvers for describing TENG behaviour from first principles, means that the majority of TENG projects in the literature begin at the prototyping stage, using physical models of the TENG and assessing performance based on rig tests and wave tank tests, and this is reflected in Tables 2.1 and 2.1. This need to manufacture TENGs for testing, makes study of this PTO type difficult for research institutes without appropriate manufacturing facilities. Though the materials required to build TENGs are generally low cost, the expertise required to successfully manufacture them remains a barrier to entry to data buoy researchers considering using TENGs in their devices.

4.1.3 Challenges in modelling TENGs from first principles

Although TENGs have many features which make them favourable for use as PTOs in small-scale wave energy applications, modelling their behaviour presents a significant practical challenge. Indeed, even where first principles modelling of TENGs is considered, such as in [208], it is usually at the atomic level, where the interaction between atoms is studied in order to select appropriate materials, rather than assess performance at a system level. While it is possible to model TENG behaviour at a high fidelity level, similar to CFD, an equivalent simplified modelling method to linear potential flow theory, does not exist for TENGs. For rolling-ball-type TENGs the modelling challenge is compounded, since the complex movement of the spheres within the device is highly chaotic, redolent of physicist Michael Berry's famous billiard ball experiment [209]. This becomes particularly clear in the image of a real prototype rolling-ball-type TENG at the University of Porto, shown in Fig. 4.3. As shown in Fig. 4.2, rolling-ball-type TENGs are a form of contact separation mode TENG, as shown in Fig. 4.1a), where the contact and separation of the triboelectrically opposed layers is driven by the movement of balls rolling across the upper layer.

Usually, modelling the movements of these spheres requires visual recordings or measurements from experimental testing, or the use of a high fidelity solver such as COMSOL. Furthermore, the relationship between the movement of the buoy and the performance of the TENG is not always clear, as rolling-ball-type TENGs are multi-modal devices, utilising motion in multiple DoFs.

This obfuscated relationship makes it difficult to assess the feasibility of using the same TENG across a range of different WEC devices and device shapes, and though a lack of control is often cited in the literature a s a strength of TENGs, the lack of mid-fidelity models to develop TENG control systems, means the effect of adding energy maximising control to TENG powered devices is largely unknown. Data based approaches to model TENGs present an interesting possibility for obtaining mid-fidelity models, though there are few examples in the literature. A previous approach to parameterizing rolling-ball-type TENGs in relation to buoy motion is detailed in [210], where an optimisation approach is used to find parameter coefficients that correlate some of the buoy motion with the TENG voltage outputs, for a number of wave tank tests. The model in [210] is based on the results of wave tank tests carried out in [89] on a 1:8 Froude-scaled model in regular waves. However, the parameterized model in [210] relies on the ability of particle swarm algorithms to handle a large number of inputs. As is often the case, where machine learning is used without considering input selection methods, the model described in [210] is highly complex, requiring 18 inputs covering the displacement, velocity and acceleration in each of the 6 DoFs.



Figure 4.3: Photograph of rolling-ball-type TENG prototype, manufactured at the University of Porto. The free movement of the spheres over the film makes obtaining a model from first principles impractical.

As part of this project, a system identification approach to creating a data-based model of a TENG is described in Chapter 5. The system identification approach reduces the number of model inputs required, by using an input selection process to identify only the key DoFs that affect the power capture of the TENG. However, data-based approaches also have limitations, as the models identified by such methods are limited in their applicability to the range of the training data used.
A recent development in modelling TENGs from first principles is in [198] and [199]. These papers, by the same authors at Hong Kong Polytechnic University, use a rotary triboelectric nanogenerator, where the rotational speed of the generator can be related to the output current. However, while the rotary TENG in [198] and [199] has the unique advantage of a relatively simple model from first principles, it is rather removed from those TENG designs which lean into the stochastic nature of ocean waves and the unique advantages this lends TENGs over more conventional PTOs.

4.2 OWCs

In stark contrast to TENGs, OWCs are one of the oldest and most established PTOs used in wave energy, and are one of the most common PTOs historically used for wave powered data buoy projects [76], with their invention attributed to Yoshio Masuda, who used the concept to provide onboard power to navigation buoys [2] [149]. Though OWCS can be floating, for use with data buoys, their design also allows them to be fixed to structures, such as breakwaters, as evidenced at the Mutriku power plant in the Basque Country, which is a rare example of a grid connected wave energy converter [211]. Since data buoys are floating devices, the focus of this section will be on floating OWCs, though their basic operating principle remains the same. OWCs can harness either heave or surge motion, based on the design of the moonpool chamber [97], with backward bent ducts, which harness surge motion, becoming increasingly popular [100] [65]. Though OWCs are well studied, they have some limitations when it comes to their use at the small scale, as further discussed in Section 4.2.4.

4.2.1 Operating principle of OWCs

The basic operating principle of an OWC requires a chamber, known as a moonpool, in which a volume of air is contained, and which is submerged and allowed to fill with water through the open base of the moonpool. Waves propagating in the water cause the surface of the moonpool to rise and fall, which in turn moves the air in the chamber. When the surface rises and falls, maintaining a horizontal water surface in the moonpool, this is called the piston or pumping mode of the OWC and is the main energy generating mode of the OWC. These incident waves also cause the buoy to move, and the relative velocity between the moving buoy and the moonpool surface forces air in and out of an orifice at the top of the chamber, in which a turbine can be mounted to harness the energy from the air moving across the turbine, as shown in Fig. 4.4.
Since the airflow through the orifice is bidirectional, OWCs require specialised turbine designs which are usually self-rectifying to produce unidirectional rotation. Conventional turbines can be used with bidirectional flows, where the oscillatory flow is dealt with either by using a twin turbine configuration [212], or in conjunction with valves to rectify the airflow prior to reaching the turbine, though both these approaches are less common than self-rectifying turbines [213]. The most common types of axial flow self-rectifying turbine used in OWCs are impulse and Wells turbines, which are further discussed in 4.2.3.
It can be seen in Fig. 4.4 that an OWC essentially consists of two coupled subsystems, one hydrodynamic, governing the motion of the floating device and the water inside the chamber, and a thermodynamic subsystem which describes the behaviour of the air in the chamber. The thermodynamic subsystem can be described from first principles

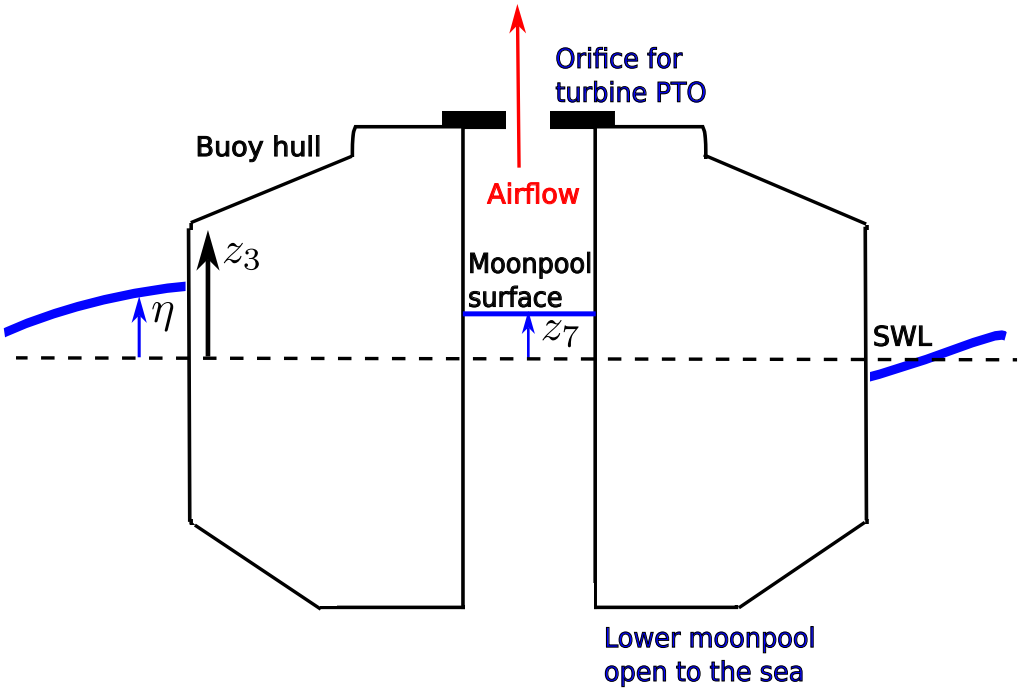


Figure 4.4: Operating principle of floating OWC with a vertical moonpool. Changes in free surface elevation η drive relative motion between the buoy heave mode z_3 and the piston mode of the water column z_7 forcing air through the orifice in which a turbine PTO can be installed.

using the first law of Thermodynamics, assuming that the processes inside the chamber are adiabatic [214] [215], meaning there is no heat transfer between the chamber and its surroundings, and that the air inside the chamber is an ideal gas. The motion of the water surface couples the two subsystems. The hydrodynamics of an OWC can be described by adapting Cummins' equation to include additional DoFs representing the different modes of motion within the moonpool chamber, and incorporating the effects of the thermodynamic subsystem. The additional DoFs represent the different modes of the water column inside the moonpool. In this project only the heave mode of the buoy and first piston (or pumping) mode of the water column inside the moonpool are considered, since these are the main power generating DoFs for a floating OWC with a vertical moonpool.

The numbering convention used in this thesis follows that of the Society of Naval Architects and Marine Engineers (SNAME), which, as shown in Fig. 3.4, number the translational DoFs surge, sway and heave as 1, 2 and 3, and the rotational DoFs roll, pitch and yaw, as 4, 5 and 6, respectively. Hence, the heave mode of the buoy itself is referred to as DoF 3 in this study. Since the piston mode of the water column inside the moonpool represents an additional degree of freedom, when describing OWCs, it is common to label this additional DoF as 7 [214], a convention which is followed in this study.

4.2.2 Modelling OWCs from first principles

The thermodynamic subsystem of an OWC can be described using the first law of thermodynamics for an open system, where matter and energy can be transferred to the surroundings, by the following representation [216]:

$$\dot{U} = \dot{Q}_{in} - \dot{Q}_{out} + \gamma_{air} C_v \dot{m}_{in} T_{in} - \gamma_{air} C_v \dot{m}_{out} T_{out} - \dot{W}, \tag{4.3}$$

where the subscripts *in* and *out* denote the direction of transfer into and out of the open system respectively, $\dot{U}$ is the rate of change of internal energy, $\dot{Q}$ is the rate of change of heat energy, γ_{air} is the heat capacity ratio of air (assumed to be 1.4), C_v is the heat capacity at constant volume, $\dot{m}$ is the mass flow rate of air, T is the temperature and $\dot{W}$ is the rate of change of pressure work done by the system:

$$\dot{W} = p\dot{V}, \tag{4.4}$$

where p is the moonpool pressure and $\dot{V}$ is the rate of change of air volume in the moonpool chamber. Assuming the processes inside the chamber are adiabatic, which is a common assumption for OWCs [214] [215], the terms describing the rate of change of heat energy transfer may be neglected (i.e. $\dot{Q}_{in} - \dot{Q}_{out} = 0$).
If the temperature outside the chamber is assumed to be equal to that inside the chamber, it follows that $T_{in} = T_{out} = T_g$. Where T_g is the temperature of the gas. This allows a simplified version of (4.3) to be written as:

$$\dot{U} = \gamma_{air} C_v T_g \left(\dot{m}_{in} - \dot{m}_{out}\right) - p\dot{V}. \tag{4.5}$$

For brevity, the change of mass flow rate into and out of the system will be simply written as $\dot{m} = \dot{m}_{in} - \dot{m}_{out}$.
The rate of change of internal energy in a system is given by:

$$\dot{U} = \frac{d}{dt}\left(C_v m T_g\right). \tag{4.6}$$

The ideal gas law states:

$$p = \rho_{air} R_g T_g, \tag{4.7}$$

where R_g is the gas constant, to which the specific heat capacity of air for a constant volume is related by:

$$C_v = \frac{R_g}{\gamma_{air} - 1}. \tag{4.8}$$

Volume can be expressed in terms of density and mass by:

$$V = \frac{m}{\rho_{air}}. \tag{4.9}$$

Substituting the expressions obtained from (4.7), (4.8) and (4.9), allows (4.6) to be rewritten in terms of pressure and volume:

$$\dot{U} = \frac{d}{dt}\left(\frac{R}{\gamma_{air}-1} m \frac{p}{\rho_{air} R}\right) = \left(\frac{1}{\gamma_{air}-1}\right)\frac{d}{dt}(pV) = \left(\frac{1}{\gamma_{air}-1}\right)\left(\dot{p}V + p\dot{V}\right). \tag{4.10}$$

Setting (4.10) as the left hand side of (4.5) yields:

$$\left(\frac{1}{\gamma_{air}-1}\right)\left(\dot{p}V + p\dot{V}\right) = \gamma_{air} C_v T \dot{m} - p\dot{V}. \tag{4.11}$$

Gathering like terms and rearranging, (4.11) becomes:

$$\left(\frac{\gamma_{air}}{\gamma_{air}-1}\right) p\dot{V} + \left(\frac{1}{\gamma_{air}-1}\right)\dot{p}V = \gamma_{air} C_v T_g \dot{m}. \tag{4.12}$$

Using (4.8) and (4.7) an expression for $\gamma_{air} C_v$ can be obtained:

$$\gamma_{air} C_v = \left(\frac{\gamma_{air}}{\gamma_{air}-1}\right)\frac{p}{\rho_{air} T_g} \tag{4.13}$$

Substituting (4.13) into (4.12) gives:

$$\left(\frac{1}{\gamma_{air}-1}\right)\dot{p}V = \left(\frac{\gamma_{air}}{\gamma_{air}-1}\right)\frac{p}{\rho_{air}}\dot{m} - \left(\frac{\gamma_{air}}{\gamma_{air}-1}\right)p\dot{V} = \left(\frac{\gamma_{air}}{\gamma_{air}-1}\right)\left(\frac{p}{\rho_{air}}\dot{m} - p\dot{V}\right). \tag{4.14}$$

Multiplying both sides of (4.14) by $(\gamma_{air} - 1)/V$ allows (4.14) to be rewritten as:

$$\dot{p} = \frac{\gamma_{air} p}{V \rho_{air}}\dot{m} - \frac{\gamma_{air}}{V} p\dot{V}. \tag{4.15}$$

From the ideal gas law [217], it can be found that:

$$\frac{\gamma_{air} p}{\rho_{air}} = c_s^2, \tag{4.16}$$

where c_s is the speed of sound in air.

Thus an expression describing the rate of change of pressure within an OWC chamber can be written as:

$$\dot{p} = \frac{c_s^2}{V}\dot{m} - \frac{\gamma_{air} p}{V}\dot{V}. \tag{4.17}$$

The term in (4.17), coupling the thermodynamic system to the hydrodynamic system, is the volume of air, which for a heaving OWC is a function of the water surface within the moonpool chamber:

$$\dot{m} = \begin{cases} -\frac{C_d}{\sqrt{1-\beta^4}} A_{\text{ori}} \sqrt{2\rho_{air} p \left(\frac{\gamma_{air}}{\gamma_{air}-1}\right) \left[(p_{atmos}/p)^{(2/\gamma_{air})} - (p_{atmos}/p)^{(\gamma_{air}+1/\gamma_{air})}\right]} & \text{if} \quad p > p_{atmos} \\ \frac{C_d}{\sqrt{1-\beta^4}} A_{\text{ori}} \sqrt{2\rho_{air} p_{atmos} \left(\frac{\gamma_{air}}{\gamma_{air}-1}\right) \left[(p/p_{atmos})^{(2/\gamma_{air})} - (p/p_{atmos})^{(\gamma_{air}+1/\gamma_{air})}\right]} & \text{if} \quad p < p_{atmos} \\ 0 & \text{if} \quad p = p_{atmos} \end{cases} \tag{4.21}$$

$$A_{owc}(h_0 - z_7), \tag{4.18}$$

with h_0 the height of the still water level within the chamber, measured from the bottom of the chamber, and z_7 representing the displacement of the water column inside the chamber.

The orifice which allows flow into and out of the moonpool chamber introduces nonlinearity into the system. This can be seen in the orifice equation describing the mass flow rate of air into and out of the orifice, given by piecewise equation (4.19):

$$\dot{m} = \begin{cases} -C_d A_{ori} \sqrt{2\rho_{air}|p - p_{atmos}|} & \text{if} \quad p > p_{atmos} \\ C_d A_{ori} \sqrt{2\rho_{air}|p_{atmos} - p|} & \text{if} \quad p < p_{atmos} \\ 0 & \text{if} \quad p = p_{atmos}, \end{cases} \tag{4.19}$$

where A_{ori} is the cross-sectional area of the orifice, C_d is the coefficient of discharge of the orifice, p_{atmos} is the atmospheric pressure.

Both compressible and incompressible cases can be considered. Introducing air compressibility requires the addition of a step calculating the changing air density, which for an adiabatic process, is given by:

$$\rho_{air} = \rho_{atmos} \left(1 + \frac{p}{\gamma_{air} p_{atmos}}\right), \tag{4.20}$$

where ρ_{atmos} is the atmospheric air density.

Following the derivation described in [214], accounting for air compressibility affects the mass flow rate equations in (4.19), giving the piecewise equation (4.21) (at the top of this page), where $\beta = \frac{A_{\text{ori}}}{A_{\text{owc}}}$.

Modelling a floating OWC, with an orifice and a vertical moonpool, requires the consideration of two vertical DoFs in the nonlinear system, the heave of the buoy (DoF 3) and the first heave mode of the massless disc representing the surface of the water column inside the chamber (DoF 7), as called the pumping or piston mode. Cummins' equation for the two DoFs required to describe a heaving OWC is given by (4.22) and (4.23).

$$\begin{aligned} f_{ex33} = M^*_{33}\ddot{z}_3(t) + f_{rc33} + c_{33}z_3(t) + \ldots \\ + f_{rc37} + a_{37}\ddot{z}_7(t) + \Delta p\,(A_{\text{owc}} - A_{\text{ori}}) + c_{73}z_3(t) \end{aligned} \tag{4.22}$$

$$\begin{aligned} f_{ex77} = a_{73}\ddot{z}_3(t) + f_{rc77} + c_{77}z_7(t) + f_{rc73} + \dots \\ +a_{77}\ddot{z}_7(t) + \Delta p A_{\text{owc}} + c_{37}z_7(t) \end{aligned} \tag{4.23}$$

In (4.22) and (4.23), subscripts 3 and 7 refer to their respective DoFs, and any coupling between them, z refers to the displacement in each DoF, a is the infinite frequency added mass, and c the hydrostatic stiffness, as described in Chapter 3. The mass of the buoy, and the infinite frequency added mass for the heave mode of the buoy are combined as $M^*_{33} = M + a_{33}$.

Because only the heave direction is considered, in the 2 DoF model described in (4.22) and (4.23), the rotational modes are ignored, allowing it to be assumed that $c_{37} = c_{73} = 0$. Following the same methodology described in Sections 3.3.2 and 3.3.3, separate state space approximations for the excitation force transfer functions relating to both DoFs are found. Similarly radiation convolution terms for DoFs 3 and 7, as well as the coupled radiation convolution terms are found. The coupled radiation terms f_{rc37} and f_{rc73}, are found to have almost identical state space approximations. Therefore, to simplify the state space matrices in (4.24), f_{rc73} has been used to represent both f_{rc73} and f_{rc37}. The infinite frequency added mass, for the coupled terms is similarly found to be equal, with a_{73} used to represent the coupling between DoFs 7 and 3, and 3 and 7.

The nonlinearity becomes most obvious when the full system is written out in state space format (4.24), since describing the behaviour of the OWC with an orifice plate requires multiplication between different states within the system. The resultant nonlinear system is a square polynomial in Δp. For brevity, where null matrices occur, they have been written as 0_m, representing appropriately dimensioned null matrices, where m is the matrix dimension.

The final shorthand used in (4.24) is k_M, given by:

$$k_M = \frac{M^*_{33}a_{77}}{M^*_{33}a_{77} - {a_{73}}^2}. \tag{4.25}$$

The large state space representation in (4.24) (at the top of the following page) shows the complexity added through the introduction of an orifice plate, even for a relatively simple hydrodynamic modelling approach, such as Cummins' equation, constrained to the heave direction only. The complexity of models of OWCs obtained using a first principles approach, also means that data-based approaches such as system identification are sometimes considered as an alternative, as shown in [218]. While system identification can result in simpler models than a first principles approach (as [218] demonstrates), the fact that such models are resetricted in their vaidity only to the range covered by the training data, means that models obtained using system identification are less flexible in their application, as demonstrated in Chapter 5.

$$A_{nl} = \begin{bmatrix} A_{e7} & 0_m & & & & \dots & & & & 0_m \\ 0_m & A_{e3} & 0_m & & & \dots & & & & 0_m \\ & 0_m & A_{rc73} & 0_m & 0_m & 0_m & B_{rc73} & 0_m & B_{rc73} & 0_m \\ \vdots & \vdots & 0_m & A_{rc77} & 0_m & 0_m & 0_m & 0_m & B_{rc77} & 0_m \\ & & 0_m & 0_m & A_{rc33} & 0_m & B_{rc33} & 0_m & 0_m & 0_m \\ 0_m & 0_m & 0_m & 0_m & 0_m & 0 & 1 & 0 & 0 & 0 \\ -\frac{a_{73}}{a_{77}}\frac{k_M C_{e7}}{M^*_{33}} & \frac{k_M C_{e3}}{M^*_{33}} & \frac{k_M C_{rc73}}{M^*_{33}}\left(\frac{a_{73}}{a_{77}}-1\right) & -\frac{a_{73}}{a_{77}}\frac{k_M C_{rc77}}{M^*_{33}} & -\frac{k_M C_{rc33}}{M^*_{33}} & -\frac{k_M c_{33}}{M^*_{33}} & 0 & \frac{k_M a_{37} c_{77}}{M^*_{33} a_{77}} & 0 & k_M\left(\frac{A_{ori}}{M^*_{33}} + \frac{A_{owc}\left(\frac{a_{37}}{a_{77}}-1\right)}{M^*_{33}}\right) \\ 0_m & & \dots & & 0_m & 0 & 0 & 0 & 1 & 0 \\ \frac{k_M C_{e7}}{a_{77}} & -\frac{a_{73}}{a_{77}}\frac{k_M C_{e3}}{M^*_{33}} & \frac{k_M C_{rc73}}{a_{77}}\left(\frac{a_{73}}{M^*_{33}}-1\right) & -\frac{k_M C_{rc77}}{a_{77}} & \frac{a_{73}}{a_{77}}\frac{k_M C_{rc33}}{M^*_{33}} & \frac{k_M a_{73}}{M^*_{33} a_{77}} & 0 & -\frac{k_M c_{77}}{a_{77}} & 0 & k_M\left(\frac{(A_{owc}-A_{ori})a_{73}-A_{owc}M^*_{33}}{M^*_{33} a_{77}}\right) \\ 0_m & & \dots & & 0_m & 0 & 0 & 0 & \frac{\gamma_{air}(\Delta p + P_{atmos})}{h_0 - z_7} & 0 \end{bmatrix},$$

$$B_{nl} = \begin{bmatrix} B_{e7} & 0_m \\ B_{e3} & \\ 0_m & \vdots \\ \vdots & \\ 0_m & 0_m \\ 0 & 0 \\ 0 & 0 \\ 0 & 0 \\ 0 & 0 \\ 0 & \frac{(c)^2}{A_{owc}(h_0 - z_7)} \end{bmatrix} \quad x_{nl} = \begin{bmatrix} X_{e7} \\ X_{e3} \\ X_{rc73} \\ X_{rc77} \\ X_{rc33} \\ z_3 \\ \dot{z}_3 \\ z_7 \\ \dot{z}_7 \\ \Delta p \end{bmatrix} \quad u_{nl} = \begin{bmatrix} \eta \\ \dot{m} \end{bmatrix} \tag{4.24}$$

4.2.2.1 Obtaining frequency dependent terms for OWCs using the massless disc approach

To obtain the frequency dependent terms of radiation added mass, a_r, radiation damping, b_r, and the excitation force frequency response function, H_{ex}, a BEM solver is used, following linear wave theory, as discussed in Chapter 3. However, to obtain these frequency dependent terms for an OWC, the water surface of the moonpool must be modelled in such a way that it can be handled by the BEM solver. A common approach for doing this is to approximate the water surface within the moonpool as an infinitely thin massless disc [192]. To account for the hydrodynamics of this infinitely thin massless disc, the additional degrees of freedom for the water column must be defined in the solver. This is not something that can be carried out by all BEM solvers and, indeed, WAMIT is one of the few BEM solvers that can handle OWCs. The water surface within the chamber can be set as the top patch in the BEM solver, which for other devices is normally used to close off the geometry to prevent so-called 'irregular frequencies' [158]. The term 'irregular frequencies' in BEM solvers refers to anomalous spikes in magnitude in the frequency dependent data for added mass and radiation damping. Removal of 'irregular frequencies' therefore must be carried out manually following the methods outlined in [219].

Another symptom of the massless disc modelling approach for OWCs, is that values obtained for added mass at higher frequencies tend towards negative infinity, rather than converging towards a finite value for infinite frequency added mass. Thus, the added

mass needs to be reconstructed from the radiation damping using the Ogilvie relations, given by (3.42), (3.43) and (3.44), which can be used to express the radiation kernel purely in terms of radiation damping, as shown in Section 3.3.2.
Following the method outlined in [219], 'irregular frequencies' are removed from the radiation damping results, which are then used to reconstruct the added mass curves. A limitation of reconstructing added mass in this way, is that any offset of added mass on the vertical axis is removed, meaning an initial estimate for infinite frequency added mass must be adjusted manually until the reconstructed added mass overlaps with the lower frequency added mass values from WAMIT, as demonstrated in Fig. 4.5.

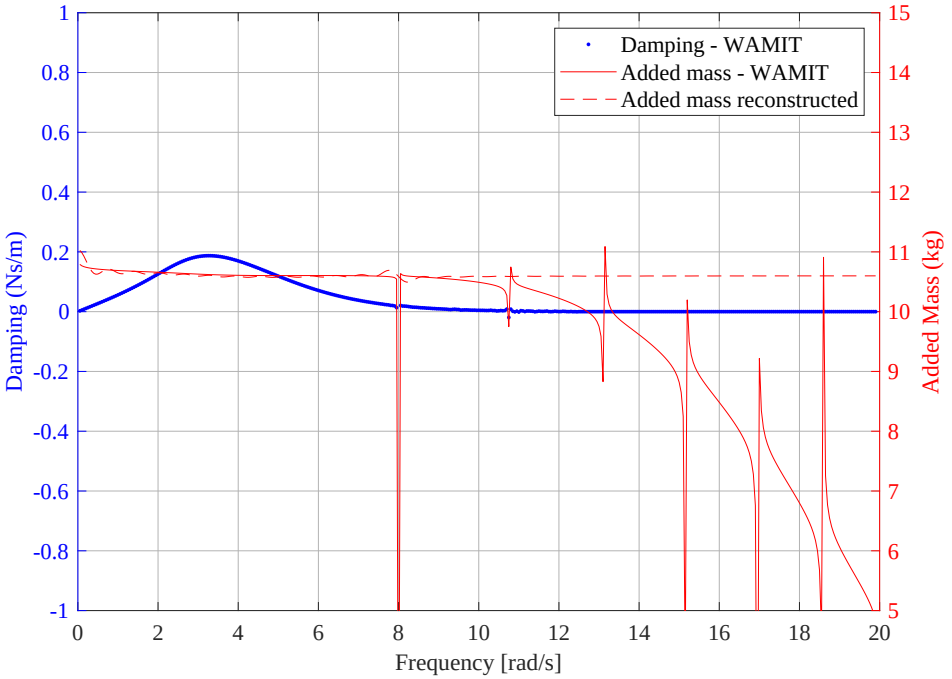


Figure 4.5: Example of added mass for the piston mode of an OWC, reconstructed from the radiation damping to correct the trend towards $-\infty$, which is symptomatic of the massless disc approximation approach. Also achieved is the removal of 'irregular frequencies'.

4.2.3 Turbines

The modelling shown thus far, for OWCs, assumes that the effect of the OWC PTO can be approximated as an appropriately dimensioned orifice with an associated coefficient of discharge, which must be experimentally determined. The validity of the assumption that the turbine behaves like an orifice needs to be verified, which is carried out in Chapter 7. The use of orifices to represent turbines is widespread in the literature [220] [221] [222], particularly for small scale models of OWCs, where using real turbines is problematic. Different orifice diameters can be used to vary the PTO damping and, in theory, this represents the turbine spinning at different speeds. Orifice plates can

be used to represent both impulse and Wells turbines, though through their nonlinear behaviour they are particularly well suited to the former. Impulse turbines are more strongly nonlinear than Wells turbines [223], with Wells turbines known to have a significant linear region, relating dimensionless pressure to dimensionless volumetric flow rate [138]. As shown in Fig. 7.5, even at the small scale and for low Reynolds numbers, the relationship between dimensionless pressure and volumetric flow rate remains relatively linear for Wells turbines.
The most common self-rectifying turbines are axial flow turbines, and these will be the main focus of this section. Self-rectifying radial flow turbines also exist, with perhaps the best known being the biradial turbine, developed at IST Lisbon by Antonio Falcão, Luís Gato and Elsa Nunes [224]. [213] argues that biradial turbine is the first high-efficiency radial flow impulse turbine, and [225] draws attention to [226] as an example of a radial flow Wells turbine.

4.2.3.1 Wells turbines

The Wells turbine was invented in 1976 at Queen's University Belfast, and is named after its inventor, Allan Wells [227]. The Wells turbine is comprised of a single solid piece, consisting of a central hub to which a number of aerofoil blades are attached. The self-rectifying behaviour of the Wells turbine is achieved by the design of the aerofoils, which are symmetrical and set at 0 degrees, most commonly a National Advisory Committee for Aeronautics (NACA) symmetrical profile in the 0012-0021 range [228], with thicker blade profiles better suited to lower pressures [193]. The digits after the 00 on the NACA profiles indicate the percentage of aerofoil thickness compared with the chord length. Due to the symmetrical design, the airflow over the aerofoil blade is identical whether the airflow is coming from above or below, with the angle of attack required to generate the lift force produced by the rotational speed of the Wells turbine itself. The fact that the angle of attack is generated by the turbine speed, means that Wells turbines are notorious for not self starting, and generally require an external input force to begin rotating [193].

4.2.3.2 Impulse turbines

The self-rectifying impulse turbine for wave energy was first patented by Russian inventor Ivan Andreevich Babintsev in 1978 [229]. It consists of a three part design consisting of two vaned stators and a central rotor. The rotor design is based on the Pelton wheel, which was designed as a water wheel for low flow streams, and patented in the 19th century [230]. However, while the Pelton wheel forms the basis of the central section of the impulse turbine, the vaned stators are what make it function as a

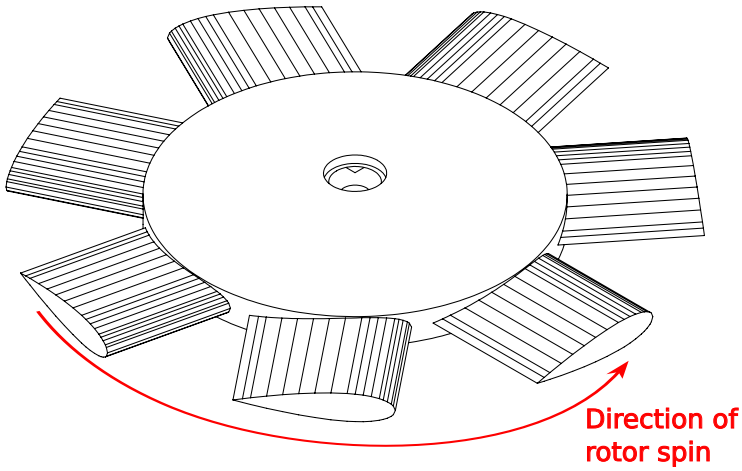


Figure 4.6: The Wells turbine uses a number of evenly spaced symmetrical aerofoils, angled at 0 degrees, meaning the airflow across the blade behaves identically irrespective of direction. The rotational speed of the turbine produces an angle of attack in the airflow, generating lift.

self-rectifying turbine. As shown in Fig. 4.7, the vanes on the stators guide the airflow, whether it comes from above or below the turbine, in such a way that it provides an impulse force on the rotor at a tangent which maintains the same direction of spin.

4.2.3.3 Comparison of Wells and Impulse turbines

The choice of whether to use Wells turbines or impulse turbines is generally dependent on the device and its location, since each design has its own inherent strengths and weaknesses.

Aside from any measures of performance, the first, and perhaps most obvious, advantage of the Wells turbine is its simplicity. Since it consists of only a single piece, the ease with which models can be made through rapid prototyping techniques, such stereolithography and even fused deposition modelling (FDM), is a key strength of the Wells turbine. Indeed, the use of a Wells turbine in this project is driven primarily by the ease with which it can be manufactured, and because of this, how quickly different designs can be iterated on and compared.

Beyond qualitative measures of simplicity, the performance of turbines is normally assessed using dimensionless characteristic curves [228]. These dimensionless variables are dimensionless pressure head Ψ, dimensionless volumetric flow rate (or flow coefficient) Φ, and dimensionless power Π:

$$\Psi = \frac{p}{\rho \Omega^2 D_{turb}^2}, \tag{4.26}$$

$$\Phi = \frac{q}{\Omega D_{turb}^3}, \tag{4.27}$$

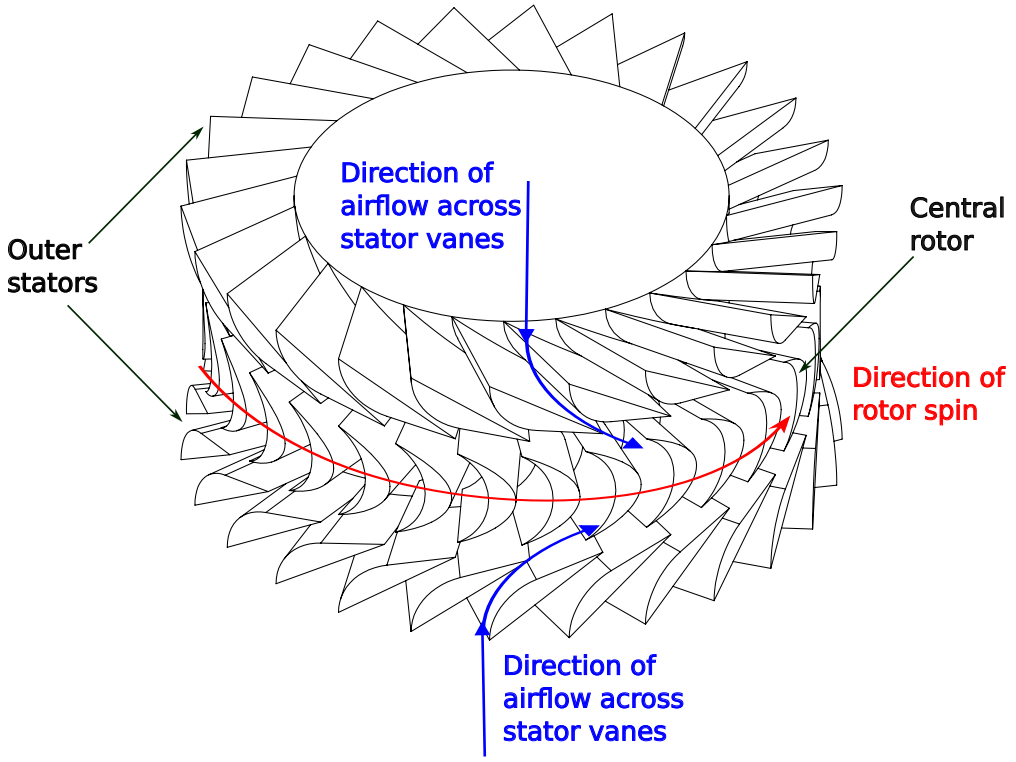


Figure 4.7: An axial flow impulse turbine consists of two stators with guide vanes, which channel air to the central rotor, such that the tangential force on the rotor is always in the same direction, irrespective of airflow direction, maintaining unidirectional spin.

$$\Pi = \frac{P_{turb}}{\rho \Omega^3 D_{turb}^5}, \tag{4.28}$$

where q is the volumetric flow rate, Ω is the rotational or angular velocity of the turbine, D_{turb} is the turbine diameter, and P_{turb} is the turbine power output. From (4.26), (4.27), and (4.28), an expression for the turbine efficiency ζ can be obtained:

$$\zeta = \frac{\Pi}{\Phi \Psi}. \tag{4.29}$$

Comparing the dimensionless characteristic curves of turbines, allows their main strengths and weaknesses to be summarised. Wells turbines have a sharp efficiency drop when the angle of attack exceeds the stall limit [231]. This means that Wells turbines have a relatively limited operating range, which becomes particularly problematic in high energy seas [232]. The impulse turbine, on the other hand, has a broader operating range, but at the cost of the peak efficiency it is able to achieve, due to the high aerodynamic losses from the guide vanes [233].

The use of dimensionless characteristic curves allows direct comparisons to be made between different turbine types. Provided that the governing geometry remains identical, dimensionless models based on experimental data can be found in the literature for Wells turbines, impulse and even biradial turbines, which through their dimensionless nature, can be scaled (within constraints, see Section 4.2.4) to suit a wide range of devices.

4.2.4 Known issues using OWCs at small scale

OWCs present an example of a conventional, well studied, PTO (which has even been used commercially), but where scaling down to the size required for small scale data buoy applications presents a number of challenges. The source of most of the issues surrounding using OWCs at the small scale comes from the turbines themselves, which are generally designed for high Reynolds number flows (>1,000,000 [213]) and, for general comparisons of performance characteristics, a minimum turbine diameter is suggested of at least 0.6 m in [228], though experimental test results for Wells turbines as small as 0.2 m diameter are available [234]. Since high flow rates are unlikely to be achieved for small scale data buoys, the Wells turbine becomes the most appropriate choice, given its higher peak efficiency and aforementioned simplicity to manufacture. Using Wells turbines in low Reynolds number flows, (<100,000) and at small diameters, is not a well studied topic. However, there are a number of pertinent studies which give an indication of the problems that are likely to be encountered when using turbines at small scale. Firstly, at low Reynolds number flows, Wells turbines are highly unlikely to achieve high efficiency, which requires the lift force to be much larger than the drag force in the direction of motion [225]. Considering the trend in the graphs of lift and drag coefficients for various aerofoil profiles, in flows down to a Reynolds number of 40,000, given in [235], it is clear that drag forces will become dominant in low Reynolds number flows, and that the angle of attack has a narrow window of operation before it reaches stall [236]. This points to Wells turbines operating principally as drag turbines at the small scale.

Furthermore, the dimensionless characteristic curves, used as standard models of turbines for OWCs, will not be applicable. In flows with an insufficiently high Reynolds number, the drag coefficient will become dependent on the Reynolds number of the flow [235], meaning the dimensionless curves will also vary with Reynolds number. This suggests three-dimensional surface plots, rather than two-dimensional curves, would be required to fully characterise the turbine at low Reynolds flows.

To obtain dimensionless characteristic curves of turbines, data from experiments or high fidelity solvers are required. However, the assumption of high Reynolds number flows is also used in CFD, meaning that simulation results using CFD at low Reynolds

number flows can not necessarily be trusted [237], in turn requiring experimental work to validate the CFD results.
The relative lack of knowledge as to how small scale turbines perform in low Reynolds number flows, highlights a gap in the literature, and poses another challenge in the use of wave energy to power data buoys.

4.3 Chapter summary

TENGs and OWCs represent almost polar opposite ends of the wave power PTO spectrum. TENGs represent an unconventional approach to harnessing wave energy, where the natural motion of the device is utilised to harness its motion in all 6 DoFs. TENG designs generally allow the device to move freely, and have negligible impact upon the device dynamics. This means that system models of devices with TENGs on board, can use simple hydrodynamic models which neglect any terms representing the PTO force. However, modelling TENGs as part of a full system presents a significant challenge, since modelling them from first principles requires high fidelity solvers to model the complex interactions of these chaotic PTOs. For the few cases where mid-fidelity models of TENGs exist in the literature, ([196], [198] and [199]) they have been constrained in such a way that they mimic conventional linear or rotational generators, and thereby present a less compelling case for the use of TENGs, since many of their advantages in capturing chaotic multimodal motion are lost.
In contrast, OWCs are arguably the most established PTO in the field of wave energy, and their modelling has been well studied [228] [193]. OWCs represent the other side of the split identified in Chapter 2, of a conventional PTO which has some issues operating at the small scale. Knowledge of OWC performance at the small scale, particularly when it comes to the turbines used, is limited. The use of Wells turbines at a scale and Reynolds number smaller than what is covered in the literature, is the basis of Chapter 7, and is one of the contributions of this thesis.

All models are wrong, but some are useful

— George Box.

5 Modelling TENGs using data based methods

Contents

5.1 Experimental data used 96
5.2 A system identification approach to modelling a TENG powered data buoy 98
5.2.1 Signal preprocessing 99
5.2.2 Input selection 100
5.2.3 MISO linear ARX model identification 101
5.2.4 MISO linear ARX model validation 103
5.2.5 MISO nonlinear KGP model identification 109
5.2.6 MISO nonlinear KGP model validation 109
5.2.7 Simulated black box model on alternative floater geometries 111
5.3 Discussion of results 112
5.4 Limitations of applicability and conclusions 113

In this chapter, a data based model of a rolling-ball-type TENG is created as a possible solution to obtaining a description of the relationship between buoy motion and the performance of a TENG. This is in response to the difficulty in modelling a TENG from first principles, as discussed in Section 4.1.3. Particularly for the more unusual TENG designs, which show some of the greatest strengths of TENGs, the obfuscated relationship between buoy motion and TENG output makes it difficult to assess the feasibility of using the same TENG across a range of different WEC devices and device shapes, and presents challenges for developing models of TENG powered data buoys.

For complex systems whose behaviour is difficult to model from first principles, such as rolling-ball-type TENGs, system identification (SI) can be used [238]. SI is a data-based modelling approach, which develops mathematical models for dynamic systems based on data observed from those systems. SI models which rely only on input-output data are called "black box" models, while "grey box" SI models incorporate, up to a variable extent [239], known physics influencing the behaviour of the system. In either case, the identified SI model must be validated against a separate set of validation input-output data, which are different from those used in the model identification phase. It should also be noted that the choice of suitable identification data is of critical importance, as the SI model validity is limited only to the range of equivalent frequencies, and amplitudes, of the input signals used in the identification phase.
As mentioned in Section 4.1.3, one example of data based modelling of TENGs can be found in [210], where the displacement velocity and acceleration data from wave tank tests were compared with the voltage output of a rolling-ball-type TENG. The model in [210] is based on the results of wave tank tests carried out on a 1:8 Froude-scaled model of a Sealite Atlantic-2600 navigation buoy in regular waves.The parameterised model in [210] is a complex multiple input single output (MISO) model which relies on particle swarm optimisation to relate the 18 inputs (based on 6 DoF motions: displacement, velocity, acceleration) to the voltage output of the TENG.
As with [210], the data for the parameterised TENG described in this chapter comes from the wave tank tests reported in [89], which were generously shared by collaborators at the University of Porto and the inanoEnergy spin-out company there. In [89], a number of different rolling-ball-type TENGs were tested, using regular waves. The TENG selected for parameterisation in this chapter is a rolling-ball-type, as shown in Fig. 4.2, though with some minor modifications, described in Section 5.1, and shown in Fig. 5.1. The SI approach described in this chapter reduces the number of model inputs required, by using an input selection process to identify only the key DoFs that affect the power capture of the TENG. Since SI models are dynamic, the model can also be simplified by considering only the displacements in each DoF as potential inputs, rather than the 18 inputs for displacement, velocity and acceleration in the 6 DoFs considered in [210].

5.1 Experimental data used

A full description of the experimental setup, which generated data used in this paper, can be found in [89]. In summary, a number of TENG configurations were tested on a 1:8 Froude-scaled model of a Sealite Atlantic-2600 navigation buoy, in a wave basin measuring 28.0 m long, 12.0 m wide and 1.2 m deep. The specifications for the buoy can be found at [240]. The wave conditions determined for use in the wave

tank tests were based on scaled down regular waves with amplitudes and periods reflective of sea states observed at Póvoa de Varzim, Portugal. The 8 regular wave conditions tested in [89] are summarised in Table 5.1, using the same numbering system for the wave conditions as applied in [210].
The three rolling-ball-type TENGs, described in [89], all used a similar basic working principle, where the movement of spheres promotes the periodic contact separation of the two triboelectrically opposed layers which form the surface upon which the spheres move, as described in Section 4.1.1. In the case of the experiments in [89], the two triboelectrically opposed layers are constructed from Nylon 6,6 and PTFE. The electrodes are made of conductive silver thin films (Ag), with the supporting structure FDM 3D-printed using polylactic acid (PLA).
Of the TENG designs tested in [89], the unidirectional lateral-based TENG (UL-TENG) was found to be the best performing, with a maximum power of 230 μW. The UL-TENG is a rolling-ball-type TENG, where the rolling spheres are guided along a series of parallel channels, as demonstrated in Fig. 5.1. In addition the UL-TENG features additional hinged TENGs at the ends of each channel, shown in Fig. 5.1 which create an additional source of power by utilising the impact force as the balls within the TENG collide with the end stops. This collision causes the hinged Nylon 6,6 flap to contact with, then separate from, the triboelectrically opposed PTFE wall.

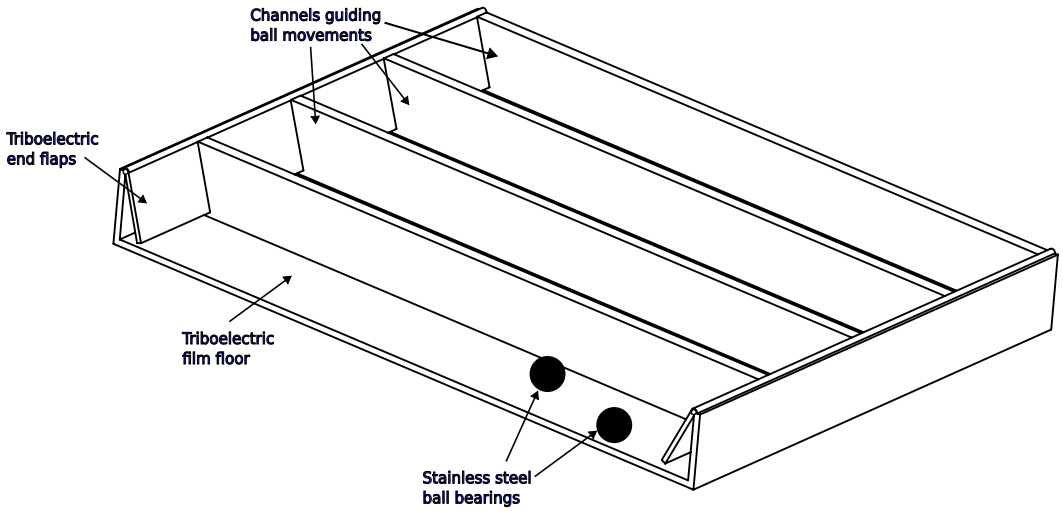


Figure 5.1: Section view of UL-TENG consisting of parallel channels orientated to the direction of wave propagation for wave tank testing. Each channel contains two steel balls driving contact separation as shown in Fig. 4.2. Additional contact separation occurs between the hinged Nylon 6,6 flaps and the PTFE wall when a ball reaches the end of the channel.

The TENGs tested in [89] were each tested at two locations: the first mounted at the location of the centre of gravity (CoG) of the buoy, and a second above the CoG. As

the TENG model in this chapter aims to create a model of just the behaviour of the TENG, the CoG position is chosen, as this is the reference point for monitoring the motion of the buoy, and therefore a direct correlation between the motion of the buoy and the motion experienced by the TENG can be assumed.

5.2 A system identification approach to modelling a TENG powered data buoy

In the wave energy field, a common approach for data-based WEC modelling is to use the free surface elevation, or the wave excitation force, as the SI model input. For instance, OWC WEC data-based hydrodynamic models which use the free surface elevation as the model inputs have been identified in [241] and [242]. However, the model developed in this chapter is designed to relate the motion of the TENG itself to the TENG output which, in theory, would allow it to be used across different floater geometries, provided that their movements fall within the range of movements that the model is trained on. Thus, a black box model for the isolated TENG is considered, using the displacement of the buoy (measured at its CoG) in 6 DoFs as the model inputs, which are assumed to be equal to the 6 DoF displacement of the TENG mounted at the buoy CoG.
In the initial model, shown in Fig. 5.2, the displacement in 6 DoFs is selected as the input, and the current produced by the TENG is selected as the output, due to the limitations in available data discussed later in this section. The time series values for the displacements in 6 DoFs, used to validate the SI models in this chapter, are from experimental data measured using a Qualisys motion capture system.

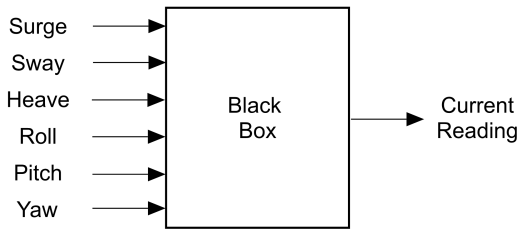


Figure 5.2: Initial black box model with all 6 DoFs considered.

The previous approach to parameterising a TENG, described in [210], focusses on voltage output, relating it to the frequencies of the displacements, velocities and accelerations in 6 DoFs. Unfortunately, accurate voltage data was unavailable for the construction of the model designed in this paper, so the alternating time series current response is used instead. The current readings provided, are, however, in almost raw form from the sensor used in the experiments. An exact conversion formula to relate these current readings to the actual current values in μA, was not provided alongside the data. Therefore any

graphs will refer to the current, purely as "current reading" and will not assign explicit units to the recorded values. Unfortunately, the research group which recorded the current data has disbanded, and it is has not been possible to dimension the current readings.

5.2.1 Signal preprocessing

A number of steps need to be taken to prepare the experimental signals for use in a SI model. Using data from the experiments in [89] presents some challenges, as the monitoring system used to sense the movement of the floater in the wave tank was switched on at a different time to the TENG sensor measuring current and voltage, creating a misalignment in the motion and current data. To temporally align the input and output traces, the beginning of the transient behaviour is compared, since this marks the time at which the waves from the tank reach the floater and trigger both movement and power production. A cross correlation of the heave and current signals is then used to check that the displacement and current signals are aligned for all 8 wave conditions.
A crucial step in preparing the data for an SI model is to remove noise, coming from sensors and/or external disturbances, from the signal. Indeed, a relatively poor signal-to-noise ratio in the input-output data can negatively affect the identification/validation performance of a model [241]. An order 6 Butterworth filter is used as a low pass filter in both the forward and reverse directions, to remove most of the high frequency noise from the data with zero phase distortion. A half-power frequency is selected for each of the wave conditions individually, as there is a significant variation in the wave frequencies between the different wave conditions (from 0.28 Hz to 1.34 Hz). The cut-off frequencies are tuned to remove the majority of noise spikes from the signal, while preserving the frequency content of interest. A comparison of the raw signal and filtered signal for the current reading for wave condition 1 is shown in Fig. 5.3.
Fig. 5.3 shows some noise variation in the signal is still present, particularly around the peaks and troughs, where the largest spikes in noise can be observed in the unfiltered signal. However, lowering the half-power frequency any further causes the signal to lose information around the peaks. The presence of noise in the current data increases with increases in wave height and period (i.e. for the more energetic wave conditions).
SI models are designed to capture the dynamic behaviour of a system. To aid identification, both input and output signals should, ideally, be zero mean. Therefore any offset in the current readings and displacements is also removed at this stage.
The final step of preparing the current data is to resample it at the same timestep of 0.01 s that the motion data is recorded at. The original current data timesteps are seemingly random and vary from 0s (where data points are repeated) up to 0.05s. The data is resampled onto a regular time base using linear interpolation, and a quick check is

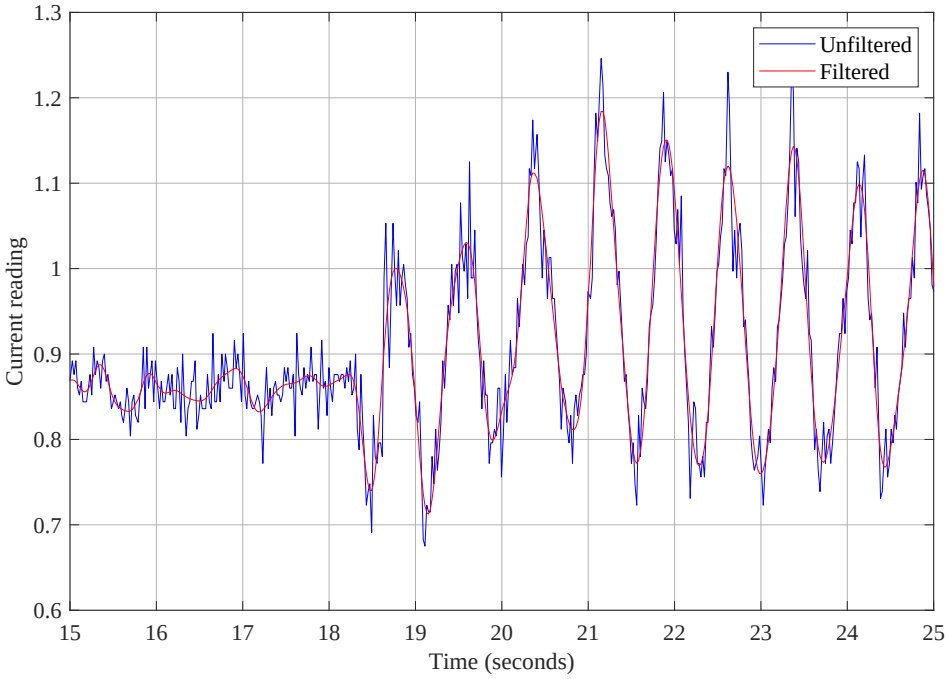


Figure 5.3: Comparison of current signal with and without noise filtering applied. The filtered current has also been linearly interpolated to ensure the same timesteps for the current data and the movement data are used.

carried out by plotting the resampled signal and the original signal, to ensure that no significant changes are imparted through the resampling process.
With the data prepared, the final step is to select how the available data should be divided into training and validation data sets. Both the training and the test data are taken from the steady-state response of the system. Therefore the data is selected only where any transient behaviour has ended. The steady state behaviour for each wave condition is identified and split at the midpoint of the steady state response, into two equal sets of training and validation data. As the experiments in [89] are run for different lengths of time for each wave condition, the training and validation data sets are both limited to 10s, to ensure the identified model is not biased towards the tests run for longer time periods.

5.2.2 Input selection

To keep a multiple input SI model as accurate and simple as possible, only those inputs which significantly affect the output should be included. In order to identify those inputs which most affect the output, forward selection is used. Forward selection is a common input selection method, and has applications in both linear and nonlinear modelling [243]. Forward selection considers a set of inputs, X, that are related to an output, Y. To ascertain which inputs in X, Y is dependent on, a test criterion must be established.

The process of forward selection is to start from a null model and sequentially select features from X that improve the fit to the selection criteria [244].
For the forward selection procedure, a generalized linear model (GLM) is used to relate the output current to a matrix of the 6 input DoFs for each wave condition. A chi-squared test is then determined as the fitting criterion. This criterion is used to cross-validate the deviance of the GLM with the 95th percentile of the chi-squared test for each degree of freedom. A 10-fold cross validation is sequentially carried out, comparing the deviance of the GLM with the 95th percentile of the chi-squared fit, iteratively selecting DoFs from the input matrix until adding more features does not further improve the fit.
A summary of the most important DoFs for each wave condition is given in Table 5.1.

Table 5.1: Inputs affecting output current depending on wave condition.

Wave Condition	Wave Period (s)	Wave Height (m)	DoFs Affecting Current
1	0.743	0.0625	Surge, heave, roll and pitch
2	0.920	0.1250	Heave and pitch
3	1.097	0.1250	Surge and heave
4	2.121	0.1250	Surge
5	2.828	0.1250	Heave
6	3.536	0.1250	Heave and pitch
7	2.828	0.2500	Surge, roll and pitch
8	3.536	0.2500	Surge, heave, roll and pitch

From Table 5.1 it can be observed that some combination of surge, heave, roll and pitch is required to predict the current output of the UL-TENG across the wave conditions considered. Therefore, sway and yaw may be disregarded as inputs from the model shown in Fig. 5.2, resulting in a black box model with four inputs and a single output. The elimination of sway and yaw is unsurprising for the wave tank tests in [89], as only two-dimensional waves are used, which have little effect on sway and yaw.

5.2.3 MISO linear ARX model identification

A linear ARX model is a well known black box model structure with a linear input-output relationship [238]. It is described by (5.1), where a_i and b_i are the unknown parameters:

$$\hat{y}(k) = -\sum_{i=1}^{n_a} a_i y(k-i) + \sum_{i=0}^{n_b} b_i u(k-n_k-i), \tag{5.1}$$

where $\hat{y}(k)$ is the model predicted at time k, and $y(k)$ and $u(k)$ are the k^{th} output and input samples respectively. n_a and n_b are the orders of the ARX model, again relating to the output and the input respectively. n_k represents the input delay and is

used to adjust for any delay that may exist between the input and output signal. The number of unknowns in (5.1) is equal to $n_a + n_b + 1$.
For a multiple input linear ARX model, (5.1) can be expanded to:

$$\hat{y}(k) = -\sum_{i=1}^{n_a} a_i y(k-i) + \sum_{j=1}^{q} \sum_{i=0}^{n_{bj}} b_{ij} u_j(k - n_{kj} - i), \tag{5.2}$$

where q is the number of model inputs.
To determine the orders of n_a and n_{bj} for each of the model inputs, a sequence of model identification trials is carried out with incremental changes in n_a, and the n_{bj} and n_{kj} values for each input. To compare the model performance during both the training and validation phases of the model identification trials the normalised root mean square error (NRMSE) is used:

$$NRMSE = \sqrt{\frac{\sum_k |y(k) - \hat{y}(k)|^2}{\sum_k |y(k)|^2}}. \tag{5.3}$$

Through an iterative process minimising the validation NRMSE [238], an n_a value can be found, and corresponding n_b values for the four inputs: n_{b1} (surge), n_{b2} (heave), n_{b3} (roll), and n_{b4} (pitch). The values of n_{k1}, n_{k2}, n_{k3} and n_{k4} are also determined at this step. In selecting the model orders, the principle of parsimony, defined in [245], is applied, which considers the trade-off between model accuracy and model complexity, since, in general, the loss function will continue decreasing with the number of parameters. The MATLAB function *arxstruc* allows for efficient calculation of a parsimonious ARX model, by iterating models across the user defined order ranges. In this model the order ranges considered are $n_a = 1:10$ for the output, and $n_b = 0:9$ and $n_k = 0:5$ for each input. An initial ARX model using all 8 wave conditions determined a parsimonious model to have orders: $n_a = 5$, $n_{b1} = 1$, $n_{b2} = 5$, $n_{b3} = 4$, and $n_{b4} = 7$ with delays of $n_{k1} = 2$, $n_{k2} = 0$, $n_{k3} = 1$, $n_{k3} = 0$.
The unknown parameters a_i, and the b_{ij} values for the four inputs are found by solving a least squares (LS) optimisation problem. In order to simplify (5.2), it can be split into vector form, with the regression vector, $\boldsymbol{\phi}$, given by:

$$\begin{aligned} \boldsymbol{\phi}(k) = [-y(k-1) \ldots -y(k-n_a) \quad & u_1(k-1+n_{k1}) \ldots \\ u_1(k-n_{b1}+n_{k1}) \quad \ldots \quad & u_q(k-1+n_{kq}) \ldots \\ & u_q(k-n_{bq}+n_{kq})]^T, \end{aligned} \tag{5.4}$$

and the parameter vector, $\boldsymbol{\theta}$:

$$\boldsymbol{\theta}(k) = [a_1\ a_2\ \ldots\ a_{na}\ b_{10}\ b_{11}\ \ldots\ b_{nb1}\ \ldots\ b_{q0}\ b_{q1}\ \ldots\ b_{nbq}]^T, \tag{5.5}$$

Having generated parameter and regression vectors to handle multiple inputs, (5.2), (5.4) and (5.5), can be combined to give:

$$\hat{\boldsymbol{y}}(k) = \boldsymbol{\theta}^T \boldsymbol{\phi}(k) = \boldsymbol{\phi}(k)^T \boldsymbol{\theta}. \tag{5.6}$$

Equation (5.6) is a simple linear regression, the solution of which is well documented [238]. Expanding for all time instants (k = 1,2,3, ... N) allows (5.6) to be rewritten as:

$$\hat{\boldsymbol{y}}(k) = \boldsymbol{\Lambda}\boldsymbol{\theta}, \tag{5.7}$$

where $\hat{\boldsymbol{y}}$ is the model output vector containing $[\hat{y}(1), \hat{y}(2), \hat{y}(3), ...\hat{y}(N)]^T$, and $\boldsymbol{\Lambda}$ is the regression matrix. The prediction error vector,$\boldsymbol{\epsilon}$, can then be defined as:

$$\boldsymbol{\epsilon} = \boldsymbol{y} - \hat{\boldsymbol{y}} = \boldsymbol{y} - \boldsymbol{\Lambda}\boldsymbol{\theta}. \tag{5.8}$$

This allows the least squares optimisation where $\boldsymbol{\theta}_{opt}$ can be found such that the LS error is minimised, to be written as:

$$\boldsymbol{\theta}_{\text{opt}} = \underset{\boldsymbol{\theta}}{argmin}(\boldsymbol{\epsilon}^T \boldsymbol{\epsilon}). \tag{5.9}$$

The least squares optimisation can then be solved using the solution:

$$\hat{\boldsymbol{\theta}}_{opt} = (\boldsymbol{\Lambda}^T \boldsymbol{\Lambda})^{-1} \boldsymbol{\Lambda}^T \boldsymbol{y}. \tag{5.10}$$

5.2.4 MISO linear ARX model validation

To validate the MISO linear ARX model, three different criteria are assessed which link directly to potential applications of the model. WEC models are typically required in model-based energy maximising control which, though rarely used with TENGs, could be an area of future research, particularly if mid-fidelity models of TENGs become available. To assess the model validity for use in control systems, the 1-step and 10-step ahead predicted outputs are computed, using the validation data. In a generic k-step ahead prediction, the i-th output value is predicted using n_a measured output, up to time instant $i - k$, and n_b inputs, up to the i-th time instant.

The final test of applicability is an output simulation, where the model response is calculated only from the relevant input data and a set of initial conditions, and no correction is made using measured values. This uncorrected output simulation is considered to assess the black box model's ability to be used across a range of potential new devices, where the current output is not known.

As shown by Table 5.1, each wave condition varies between being most dependent on surge, heave, roll, pitch or a combination of some or all four DoFs. The ARX model is

constructed to relate the test data from across all 8 tested wave conditions, reading in surge, heave, roll and pitch as the four inputs. For validation of the model, the NRMSE in (5.3) is once again used. In Table 5.2, model validation performance is reported in terms of goodness of fit (GoF), calculated as a percentage $\%_{GoF}$ as:

$$\%_{GoF} = 100(1 - NRMSE). \tag{5.11}$$

Note that negative values of $\%_{GoF}$ can result when the NRMSE exceeds 1. Using (5.11), a comparison of the ARX models performance for each wave condition can be assessed. Table 5.2 summarises the GoF values obtained for the single-step and 10-step ahead predictive models, and the GoF of the uncorrected simulation model, for the linear ARX model trained on all 8 wave conditions. All NRMSE values for the models are calculated after 2s to ensure only the steady state behaviour of the model is included in the GoF calculation.

Table 5.2: Goodness of fit for linear ARX model trained on all 8 wave conditions (negative values indicate an NRMSE > 1)

Wave Condition	GoF (%) 1-Step Ahead Prediction	GoF (%) 10-Step Ahead Prediction	GoF (%) Uncorrected Simulation
1	97.94	77.41	46.32
2	97.63	69.11	57.62
3	97.61	70.31	61.84
4	97.49	33.45	-126.02
5	98.31	74.34	14.16
6	97.81	72.27	16.41
7	98.10	67.30	-5.26
8	98.57	79.77	57.62

Table 5.2 shows that the overall GoF for the model trained to fit all 8 wave conditions, is above 97% for all of the single-step predictions. The 10-step ahead prediction performs best at wave condition 8 and the higher frequency wave conditions (1-3), with a GoF close to, or above, 70%. The uncorrected simulation output follows a similar pattern. In Fig. 5.4, the 10 step ahead prediction is shown to capture the general behaviour of the current output well for most wave conditions.

As shown in Fig. 5.5, for wave conditions 4-7, the low GoF simulated outputs correspond with the spikier validation waveforms, where the uncorrected simulated linear ARX model is unable to capture the more complex behaviour of current signals at these wave conditions.

Wave condition 4 is a particularly poor fit, both for 10-step ahead prediction and the uncorrected simulation. The simulated model output for wave condition 4, shown in Fig.

5.5d), is a clear example of the linear ARX model struggling to fit the current output to all 8 wave conditions using a single model. Since the model identified for all 8 wave conditions only has an associated surge input order of $n_{b1} = 1$, it is perhaps unsurprising that wave condition 8, which is found to be heavily dependent on surge in Table 5.1, has the lowest GoF for both 10-step ahead prediction and uncorrected simulation.

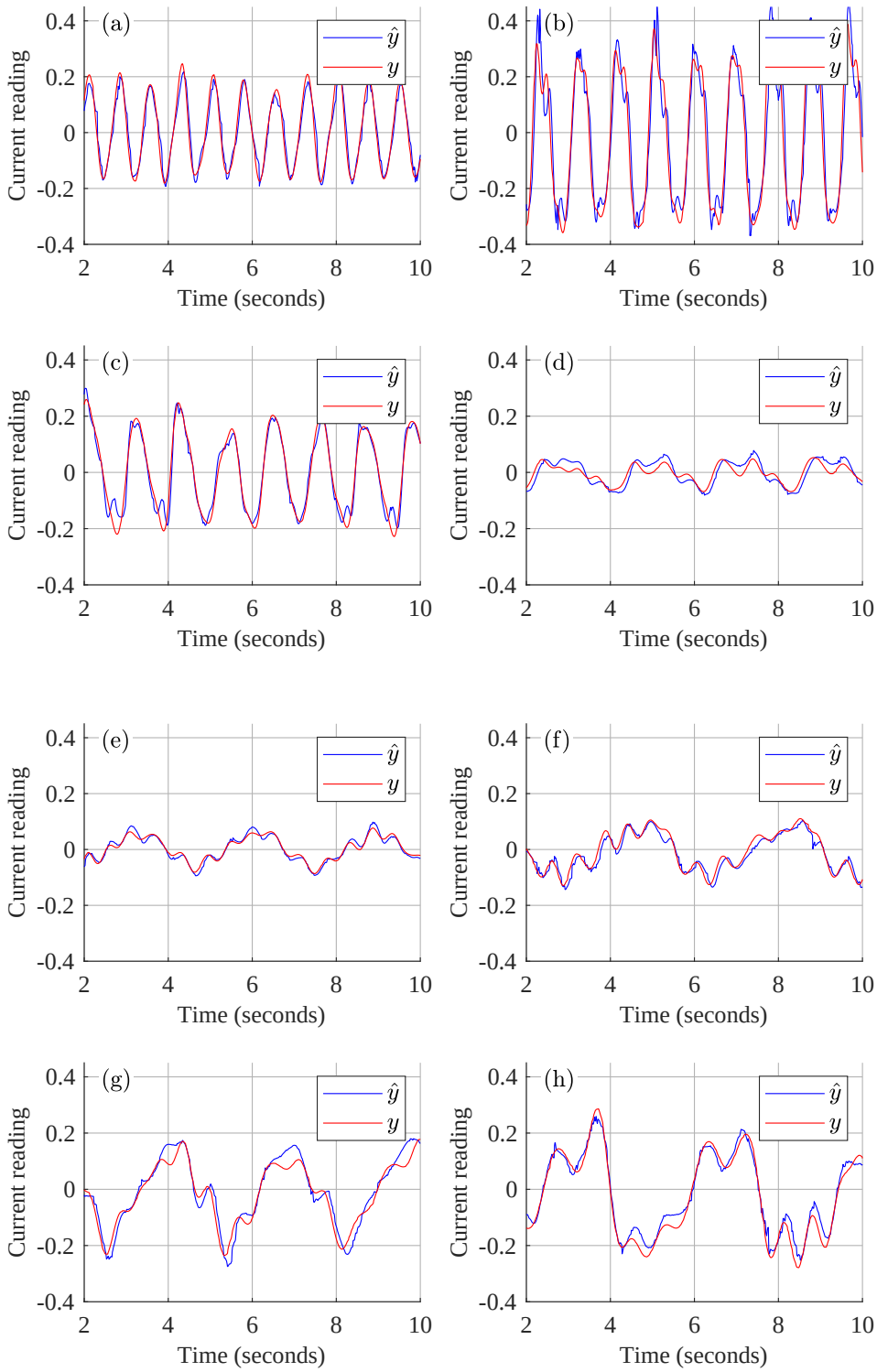


Figure 5.4: 10-step ahead prediction model output current ($\hat{y}$), compared with validation data (y) for a single linear ARX model trained using all 8 wave conditions. a) Wave condition 1 b) Wave condition 2 c) Wave condition 3 d) Wave condition 4 e) Wave condition 5 f) Wave condition 6 g) Wave condition 7 h) Wave condition 8.

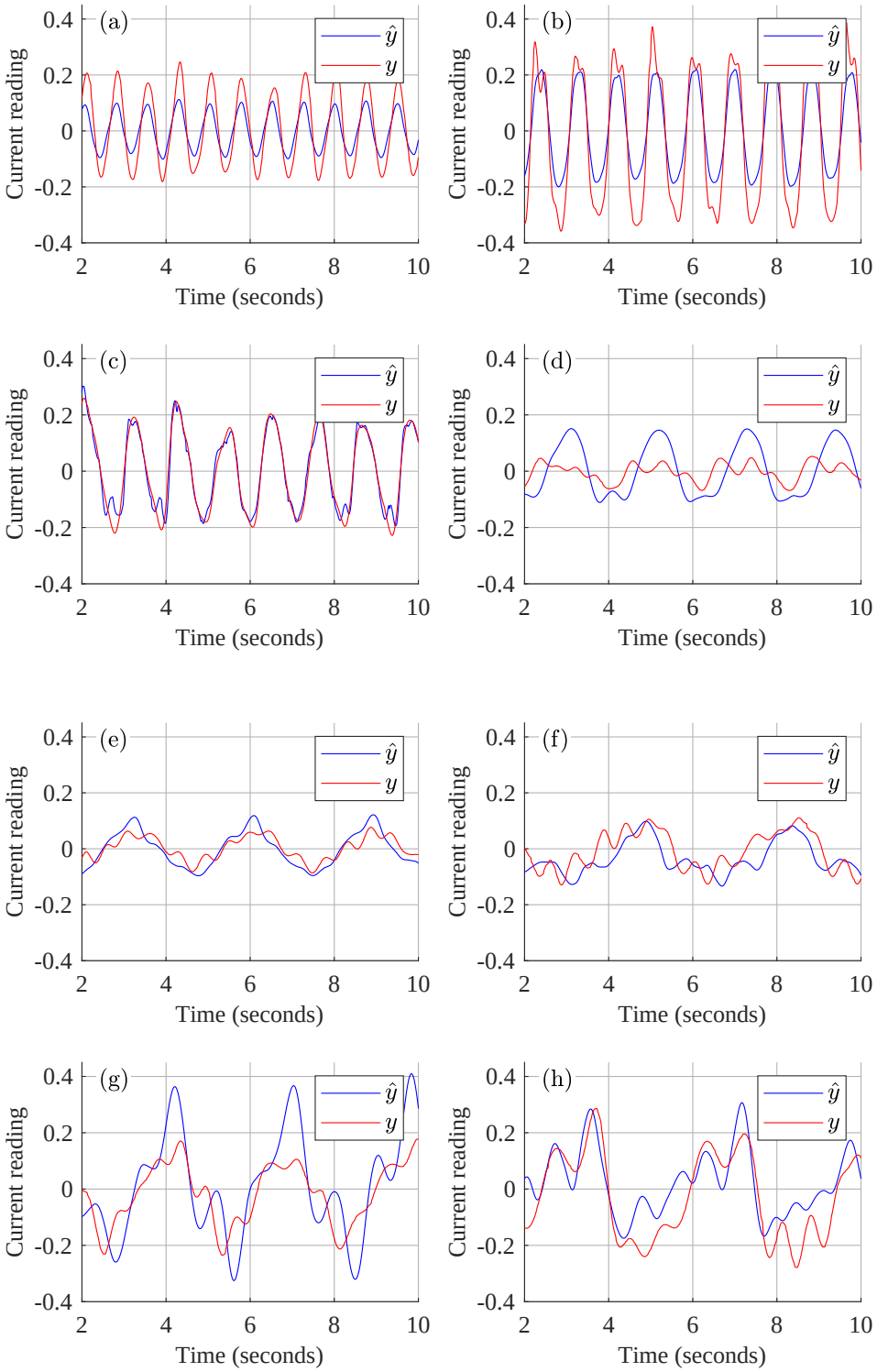


Figure 5.5: Uncorrected simulation model output current ($\hat{y}$), compared with validation data (y) for a single linear ARX model trained using all 8 wave conditions. a) Wave condition 1 b) Wave condition 2 c) Wave condition 3 d) Wave condition 4 e) Wave condition 5 f) Wave condition 6 g) Wave condition 7 h) Wave condition 8.

Given the strong prediction GoF, but poor uncorrected simulation GoF, for wave conditions 1-3, a linear ARX model is also created using only these three wave conditions for training and validation. Identifying this model results in orders of $n_a = 5$, $n_{b1} = 4$, $n_{b2} = 8$, $n_{b3} = 4$, and $n_{b4} = 7$ with delays of $n_{k1} = 2$, $n_{k2} = 2$, $n_{k3} = 2$, $n_{k3} = 0$. Using just the three high frequency wave conditions, results in an uncorrected simulation GoF of more than 70% for all three wave conditions, summarised in Table 5.3.

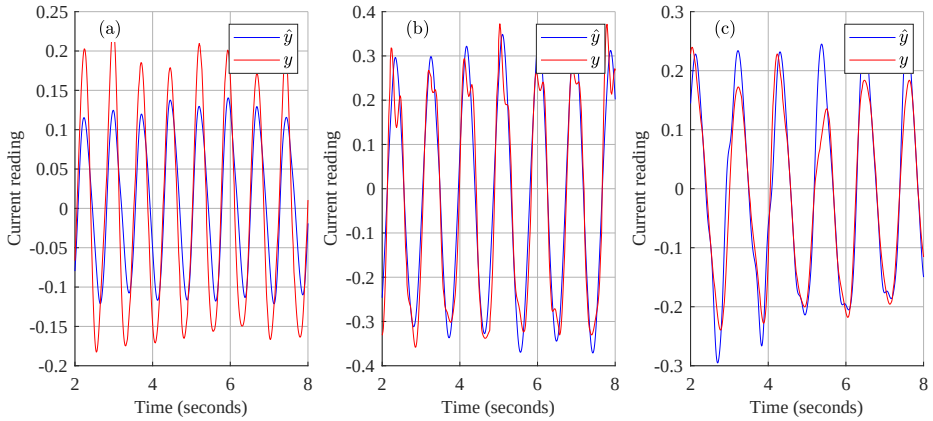


Figure 5.6: Uncorrected simulation model output current ($\hat{y}$), compared with validation data (y) for the linear ARX model trained only on wave conditions 1-3. a) Wave condition 1 b) Wave condition 2 c) Wave condition 3.

Plotting the uncorrected simulation current output of the linear ARX model trained on only wave conditions 1-3, shown in Fig. 5.6, a relatively close fit across the three high frequency wave conditions can be observed.

Table 5.3: Goodness of fit for linear ARX model trained only on wave conditions 1-3

Wave Condition	**GoF (%) Uncorrected Simulation**
1	73.73
2	77.71
3	64.00

The fact that the linear ARX model, trained using all 8 wave conditions, performs considerably differently for each wave condition in multi-step prediction, suggests that there may be a dynamic nonlinearity within the data sets. This is also suggested by the results of Table 5.1, where different DoFs become more or less dominant, depending on the wave conditions. Therefore, a nonlinear MISO model is also identified, described in Section 5.2.5.

5.2.5 MISO nonlinear KGP model identification

The model structure chosen to identify the dynamic nonlinearities in the system is a Kolmogorov–Gabor polynomial (KGP), which adds a polynomial nonlinearity to an ARX model. In [154], it is identified that the cross product terms of the conventional KGP equation can lead to instabilities in the model. Therefore, in this paper, the cross product terms of the KGP model are removed. The MISO KGP model used can then be described by:

$$\begin{aligned}\hat{y}(k) = \sum_{m=1}^{p} \Bigg[- \sum_{i=1}^{n_a} a_{im} y^m(k-i) + \dots \\ \sum_{j=1}^{q} \sum_{i=0}^{n_{bj}} b_{ijm} u_j^m(k - n_{kj} - i) \Bigg],\end{aligned} \tag{5.12}$$

where p is the maximum polynomial order. The number of unknowns in (5.12) is $p(n_a + n_b + 1)$, where n_b is the sum of the n_b values for each input. Although the KGP model has a nonlinear input-output relationship, the model is still linear in the parameters a_{im} and b_{ijm}, meaning that the KGP unknown parameters are also identified by solving a linear regression problem. Given the close relationship between KGP and linear ARX models, and the complexities in identifying the orders for a non-linear model, it is common practice to determine the n_a, n_b, and n_k values for a KGP model from a linear ARX model trained on the same data set [155]. Therefore, the orders used are as identified in Section 5.2.3. A comparison of model outputs with polynomial orders 2 and 3, identified a best fit at a polynomial order, $n_p = 2$.

5.2.6 MISO nonlinear KGP model validation

The nonlinear KGP model, trained on all 8 wave conditions, is again validated considering the GoF obtained in the 1-step ahead prediction, 10-step ahead prediction, and output simulation, using the validation data. The 10-step ahead prediction shows a general improvement for all wave conditions, with the fit for each wave condition achieving a GoF value of at least 60%, and most above 70% as shown in Table 5.4.
Interestingly, though there is mostly improvement shown in Table 5.4 when compared to the linear ARX results in Table 5.2, there is a small drop in the GoF for wave conditions 6, 7 and 8. The uncorrected simulation outputs from the KGP model do not show improvement across all sea conditions either, with some fits improving, and others becoming significantly worse. This suggests a KGP model is generally a good multi-step predictor of the behaviour of the UL-TENG, but that for applications

Table 5.4: Goodness of fit for KGP model trained on all 8 wave conditions (negative values indicate an NRMSE > 1)

Wave Condition	GoF (%) 1-Step Ahead Prediction	GoF (%) 10-Step Ahead Prediction	GoF (%) Uncorrected Simulation
1	97.86	77.92	36.67
2	97.56	77.66	62.30
3	98.23	70.21	43.98
4	97.09	66.77	-64.95
5	98.34	79.32	30.69
6	97.89	70.14	25.92
7	98.12	62.68	-0.48
8	98.54	79.77	48.82

simulating the UL-TENG with no knowledge of the output data, and using only the relevant inputs, a different approach is required.

The most significant improvement in the KGP model is with the 10-step ahead prediction for wave condition 4. The GoF value for the 10-step ahead prediction essentially doubles to 66%, bringing wave condition 4 in line with the GoF values for other sea states, for the 10-step ahead prediction. A comparison for wave condition 4 for the nonlinear KGP current output and the linear ARX model output is shown in Fig. 5.7.

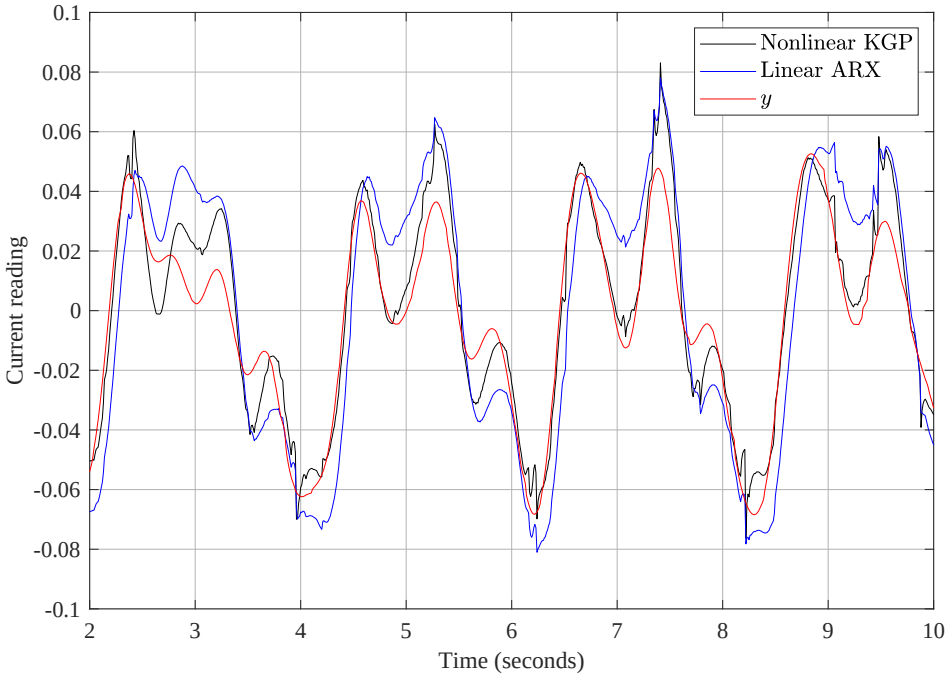


Figure 5.7: 10-step ahead prediction model output currents for the KGP and ARX model compared with validation data (y) for wave condition 4.

5.2.7 Simulated black box model on alternative floater geometries

Since the aim of this chapter is to develop a black box model of an 'isolated' UL-TENG, two alternative buoy geometries are considered to determine whether the performance of the TENG can be assessed over a variety of floater types. The buoys chosen for testing a alternative geometries are the Balizamar B1600S, a navigation buoy designed by Almarin (technical data for the full sized buoy available from [246]) as well as a simple cylindrical buoy of similar dimension to the scaled Sealite Atlantic-2600 buoy used in wave tank testing.

Since the black box model uses the displacements of each DoF as inputs, the motion of the alternative floater geometries needs to be determined. To do this Cummins' equation (see Section 3.3) is used to generate 4 DoF models for both a scaled version of the Balizamar, and for a cylinder equal in radius and draft to the scale model of the Sealite Atlantic-2600 (radius = 0.188 m and draft 0.096 m). The mooring force is included in both models as an additional stiffness term, adjusted to tune the behaviour of the alternative geometries, mostly to ensure surge displacement remains reasonable, by changing the line stiffness selected for the simulated mooring.

Since the uncorrected simulation GoF for both the ARX model and the KGP model trained on all 8 sea states is rather variable, to simulate the behaviour of the UL-TENG, the linear ARX model trained on only the three high frequency wave conditions (1, 2, and 3) is used, with the displacement data for the alternative floaters generated using a regular wave with a period of 0.9 s and a wave height of 0.125 m; staying within the range covered by wave conditions 1-3. The black box model estimates of the UL-TENG, mounted on the two alternate geometries, is shown in Fig. 5.8 and Fig. 5.9 for the Balizamar and cylindrical geometries respectively.

Fig. 5.8 and Fig. 5.9 show that the black box model predicts a current reading in the range of -0.1 to 0.1, which is not dissimilar to the magnitude of current readings in Fig. 5.6, which also use the same black box model. Considering the waveform shapes of the produced current readings, the trace for the Balizamar buoy is relatively similar to the shape of the current readings from the wave tank test results, which suggests that there may be some promise for the model to be used on other navigation buoys. However, such a statement cannot be verified without further experimental testing.

The shape of the waveform response for current reading on the cylindrical buoy, however, is quite different to any of those in the test data, which suggests that there is not enough geometric similarity in the dynamic behaviour of a cylindrical buoy for the identified black box model to be applicable.

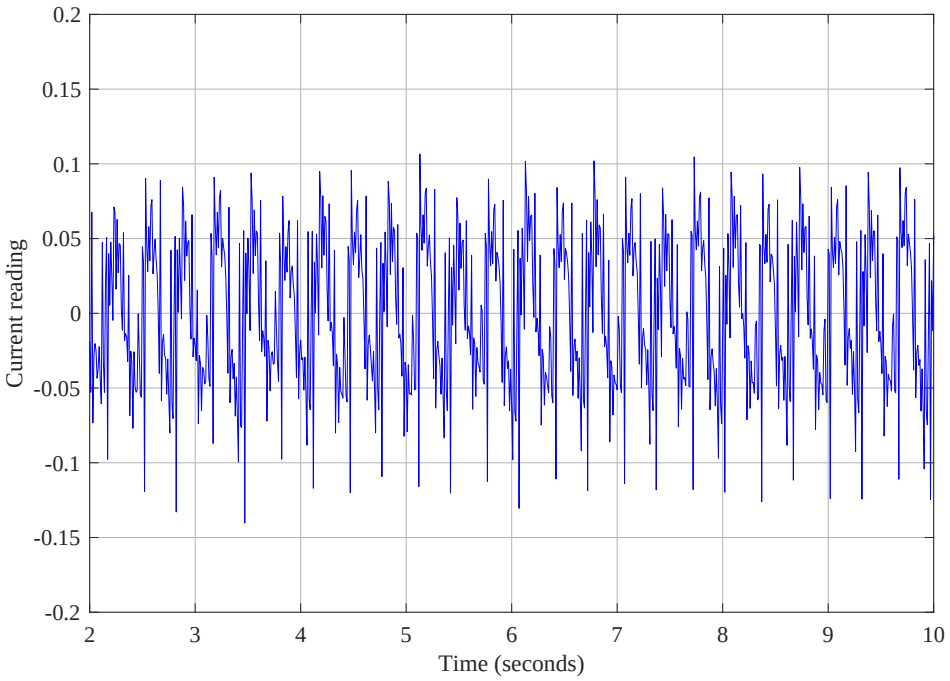


Figure 5.8: Uncorrected simulation output using the displacements of a 1:8 Froude-scaled Balizamar B1600S buoy. Since the magnitude of current readings is similar to that of tests on the Sealite buoy, there is some promise for the applicability of the model on the Balizamar test geometry.

5.3 Discussion of results

Tables 5.2 and 5.4 show that, for applications where a single-step prediction model is sufficient, both the linear ARX and the nonlinear KGP model give a high GoF output (above 97% for all 8 wave conditions). Since both KGP and ARX model GoFs are comparable for single step prediction, the linear ARX model should be used due to its simpler structure. However, applications for single-step models are limited, since a single step ahead in this case is equivalent to 0.01 s.

The linear ARX model structure is also the most appropriate for cases where the model output is initialised at 0 and remains uncorrected, but only when trained on a limited range of wave conditions (1, 2 and 3), and this model shows some promise for use on other navigation buoy hulls in similar wave conditions. The low uncorrected simulation GoF for the two models trained on all 8 wave conditions, suggests that a highly applicable, uncorrected black box model, for a TENG for simulation purposes across a range of buoys, would be difficult to achieve, particularly considering the large changes in wave period and wave height between most of the wave conditions considered.

For a 10-step ahead prediction, the nonlinear KGP model showed relatively consistent accuracy across all 8 wave conditions. The fact that the KGP model improves the average predictive ability of the model, across the 8 wave conditions, suggests it as the most appropriate choice for use with a predictive controller.

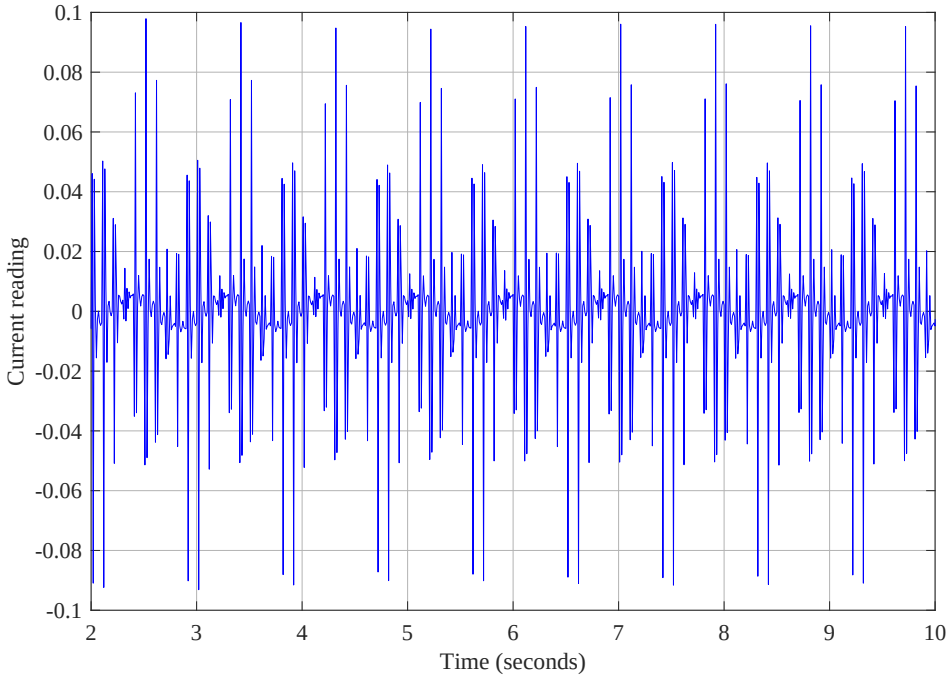


Figure 5.9: Uncorrected simulation output using the displacements of a cylinder of similar size to the model of the Sealite Atlantic-2600. Though the magnitude of current readings is again similar to that of tests on the Sealite buoy, the shape of the generated response is quite different, likely due to a lack of geometric similarity.

5.4 Limitations of applicability and conclusions

In this chapter, three black box models have been identified that predict the dynamic behaviour of a UL-TENG: a linear ARX, and a nonlinear KGP model, each combining the data from 8 different wave conditions; and a linear ARX model focussing only on the data from the 3 high frequency wave conditions. All three models identified are moderately successful in predicting the current output of the UL-TENG, but only the model trained on just three high frequency wave conditions is able to provide a satisfactory estimated model GoF for the uncorrected simulation case, where the output is solely dependent on the displacement inputs.

An interesting observation made in this chapter is the variability in which DoFs affect the current output most, given different wave conditions. This is a testament to the complexity of a rolling-ball-type TENG as a system. The variability between what DoFs most affect the output current presents a challenge in developing a generalised model, particularly in the uncorrected simulation case, where even the nonlinear KGP model performed inconsistently. The fact that the oscillations of a buoy directly depend upon its resonance frequency also presents a significant challenge for identifying black box models which are applicable for a range of devices. This is coupled with the fact that, as different frequencies of motion are experienced, different DoFs became dominant for

the Sealite Atlantic-2600, which suggests that the motion from other buoys will likely have similarly complex relationships with the TENG output current.

This chapter highlights the difficulty in modelling TENGs from experimental data, particularly the issues from filtering the noise. The lower frequency current waveforms have significantly more spikes around each peak, where noise cannot be further removed without losing signal information. Furthermore, the design of the UL-TENG includes end-stop TENGs which cause additional current spikes when the spheres collide with these end-stops. It is possible, that for high frequency motion, these end-stop spikes are not as clear, as a single peak current tends to dominate these signals, or it could be that the effects of the end-stop TENGs are removed from the higher frequency signals by noise filtering. High levels of noise are almost inevitable in experimental data from TENGs, as dataloggers need to be highly sensitive, due to the low power output. Potential future work could be to develop a simulated test programme in COMSOL or on a hardware in the loop rig, covering a greater range of displacements and frequencies, to increase the applicability of the uncorrected model across different WECs. Such testing could also be used to help identify whether the spiking behaviour observed in the lower frequency current data is purely from noise, or whether the additional spikes in current are also influenced by the end-stops in the UL-TENG.

The test data used in this chapter has significant variation between most of the 8 wave conditions, and the fact that a model trained on the three most similar performed well in simulation, suggests building up data across smaller ranges of sea conditions could help in developing more generalised models of TENGs. Future testing should aim for small increments when increasing period and wave height between test cases, as this would be more likely to result in a model that performs well in uncorrected simulation.

6

Device description and experimental facilities

Contents

6.1 The JFC Marine Gannet G1250 as a floating OWC 117
6.1.1 Sealed chamber 119
6.1.2 Orifice plates 119
6.1.3 Venturi for turbine PTO 120
6.2 Sensors and data acquisition 121
6.2.1 Wave probes 123
6.2.2 Pressure sensor 125
6.2.3 Generator and encoder 127
6.3 Experimental set up at Dundalk Institute of Technology 130
6.4 Experimental set up at Lir National Ocean Test Facility 133
6.4.1 Wave tank limitations 137
6.4.2 Selection of test waves and spectra 138
6.5 Chapter summary 139

As well as having the data from the wave tank testing of rolling-ball-type TENGs shared with this project, further wave tank test data was also obtained through collaborators at Dundalk Institute of Technology. This data relates to a test campaign of wave tank testing, at the Lir National Ocean Test Facility (Lir NOTF), of a small OWC-equipped buoy, based on a JFC Marine Gannet G1250 navigation buoy. DkIT have a long-running OWC-based data buoy project, titled the Wave Activated Sensor Power (WASP) project, which has already been tested at sea, albeit with a fully sealed moonpool [61] [62]

[110]. The full scale prototype of the WASP, which is based on a 3 m diameter JFC Seagull 5G3000 navigation buoy, was tested over a 5 month deployment in Galway Bay, with future tests planned for a working turbine PTO to be installed in the moonpool, which was fully sealed for initial tests. However, due to a number of issues with foreshore licensing at the test facility in Galway Bay, the WASP has not yet been able to return to the sea. Therefore, testing a device smaller than the 3 m diameter WASP was proposed by DkIT for use in a wave tank, where time series free surface elevation measurements are available and there is greater control of environmental variables. Thus, a first test campaign was carried out using the Gannet G1250 buoy in the wave tank at Lir NOTF, with a fully sealed moonpool, and mooring configuration to mimic that of the full size WASP deployed at sea.

Further to sharing data from the first experimental campaign with this project, the G1250 buoy itself was made available for alterations, so that a second test campaign, designed around the unique requirements of this author's project, could be carried out. A major objective of this project is to counter the common assumption that wave powered data buoys measuring waves must be true wave followers, discussed in detail in Section 2.1.4.1 and, in order to provide a solution to this problem, a test case is required.

With Chapter 5 exploring the modelling of a TENG powered data buoy, which has a negligible effect on the device dynamics, a PTO which affects the dynamics of a data buoy was considered. In this case an OWC was used, since the Gannet G1250 already had some modifications made to it to allow this device to utilise an OWC PTO. The aim of the wave tank testing was to produce test data from a buoy which has an active wave energy PTO and, from measurements of its motion, recover time series free surface elevation estimates, as demonstrated in Chapters 8 and 9. A key aspect of Chapters 8 and 9 is in providing a sensing solution that allows measurements of the free surface elevation to be recovered from motion measurements of a wave powered data buoy.

Another goal of this project is to use wave powered data buoys as a low cost test bed for WECs. Creating a functioning wave powered buoy, from which estimates of free surface elevation can be recovered, simultaneously shows the ability of wave energy to be used on data buoys measuring wave parameters, and demonstrates that wave powered data buoys can be built on a relatively modest budget. The process of adapting the PTO, to account for additional challenges that building at the small data buoy scale brings, is discussed in Chapter 7. With budgetary constraints set by the project funding, OWCs were the first consideration, since they offer one of the most affordable PTOs for a wave powered device. The limitations for turbines operating in low Reynolds number flows (<100,000) means that the smaller device tested at Lir NOTF essentially needs to be considered full scale, due to the scaling issues further discussed in Chapter 7.

Constructing a full size device, even at the data buoy scale, does present some challenges, especially with a limited budget. Designing a bespoke floater with optimised geometry for interacting with waves would be ideal, especially if such a geometry were designed with stability for sensors in mind. However, constructing such a device would exceed the budgetary and temporal constraints of this project, and thus a simpler solution using an existing buoy, and modifying it to function with a wave energy PTO, was chosen instead. This reflects the procedure used for the WASP, which also used a commercially available buoy, modified to behave as an OWC. Modifying off-the-shelf buoys to behave as wave powered data buoys has been successfully carried out elsewhere (as discussed in Section 2.2.2), the most notable being the arctic buoy described in [56], which even incorporated a commercially available gyroscopic PTO.
Since DkIT were already planning on building a smaller device as a pseudo-scaled model of the WASP, based on a smaller JFC marine navigation buoy hull, some test data was already available for this device. Indeed, [111] makes use of the results from the same experimental testing, described in Section 6.4 as the first test campaign there, developing a successful technique for estimating wave spectra, based on transfer functions obtained relating the pressure spectra in the moonpool chamber to the external sea state. However, where the focus of [111] is on obtaining the statistical characteristic parameters of waves from the pressure spectra across half hour windows, the primary objective, and novelty, of the tests planned for this project is in the use of an unknown input estimator. The designed estimator can return time domain free surface readings at 0.1 s intervals, taking into account the effects of an orifice plate simulating the effects of a turbine PTO, as well as considering tests using a real turbine attached to a generator with a variable load.
The remainder of this chapter is laid out as follows: Section 6.1 describes the Gannet G1250 buoy and the modifications made to equip it with an OWC. Section 6.2 describes the sensors used to acquire experimental data. Section 6.3 describes the experimental set up at Dundalk Institute of Technology (DkIT) for determining the coefficient of discharge for the 25 mm orifice plate and characterising the performance of the Wells turbine. In Section 6.4 the experimental set up for wave tank testing of the buoy at the Lir National Ocean Test Facility (Lir NOTF) in Cork is discussed. The chapter is summarised in Section 6.5.

6.1 The JFC Marine Gannet G1250 as a floating OWC

The buoy used as the basis for the OWC in this study is a JFC marine Gannet G1250 buoy, with a diameter of 1.25 m and a nominal draft of 0.58 m (schematics and full technical details are available from JFC Marine [247]). However, since this buoy is primarily intended as a navigation buoy, it is normally fitted with a range of daymarks

which all significantly add to the mass of the device, and the stated nominal draft reflects this. Since the experiments described in this thesis do not require the use of daymarks (and instead use a custom made attachment for mounting a sealing plate, orifice plates and a Venturi respectively) the actual draft of the buoy is in the range of 0.32 m to 0.37 m, depending on the attachment used. Fig. 6.1 shows the JFC G1250 buoy with the modifications made for the experiments described herein.

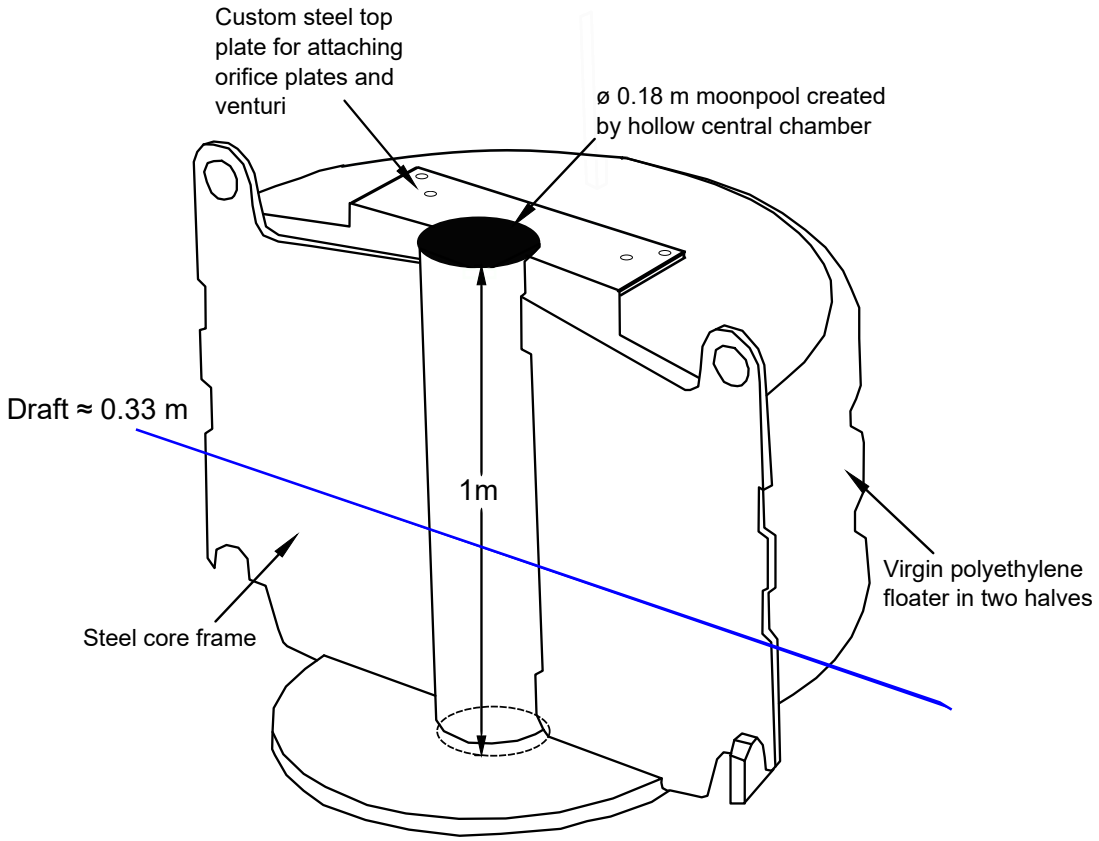


Figure 6.1: Diagram of JFC Gannet G1250, where 1250 refers to its 1.25 m diameter. Note the modifications made for use as a floating OWC, specifically a custom top plate, and the open central chamber in the steel core frame.

The most crucial change to the G1250 buoy, illustrated in Fig. 6.1, is that the centre core of the buoy has been left open at the base, creating a moonpool that acts as an OWC. The dimensions of the moonpool in the centre are of a diameter 0.18 m and a height of 1 m. The opening at the top of the moonpool is connected to the custom top plate which is the second notable change to the commercially available buoy. This mild steel plate around the top of the moonpool allows for a variety of fittings to be attached. Alongside a fully sealed plate, a number of orifice plates representing turbine PTO damping, or a Venturi with an actual DC generator and turbine, can be alternatively attached to the top of the moonpool chamber. The attachments are described in the following subsections.

6.1.1 Sealed chamber

Initial modifications to this off-the-shelf JFC buoy are originally for experiments reported in [111], forming the first test campaign at Lir NOTF carried out by collaborators from DkIT: Thomas Kelly and Brendan Walsh. Because the G1250 was initially designed to somewhat reflect the WASP tested in Galway bay, the majority of experiments from the first test campaign are carried out using a sealing plate across the top of the moonpool. The sealing plate is designed with a small hole into which a Honeywell 176PC14HD2 pressure sensor can be inserted; since the focus of DkIT's project is on retrieving spectral information related to the external sea state, based on pressure measurements from within the moonpool chamber. This configuration was tested extensively across a range of monochromatic waves, as well as a number of irregular waves.
Sealing the moonpool fully, essentially creates a wave follower, with minimal effects on device dynamics, since air compressibility at this scale is negligible (as further described in Chapter 8). However, if compressibility effects are ignored, the device dynamics are linear. Such a configuration allows for a simpler model of the estimator to be tested, since nonlinear effects from the orifice or turbine PTO need not be considered, with the motion of the moonpool surface likewise neglected.
The sealing plate is manufactured from 4 mm mild steel at 0.25×0.25 m, which align it with the inner holes in the top plate of the Gannet. The four outer mounting holes on this plate, shown in Fig 6.1, are there to mount a frame consisting of four legs supporting two 25 mm thick steel plates, which represent the mass of the batteries that would normally be required for energy provision on a data buoy.

6.1.2 Orifice plates

To simulate the effects of a turbine PTO on the dynamics of the device, a selection of three orifice plates have also been produced, with orifice diameters of 5, 15 and 25 mm. Simulating a turbine PTO via orifice plates is discussed in more depth in Chapter 7 but, in short, the restriction of the airflow caused by the orifice mimics the effects that a turbine would have on the airflow, with different diameters of orifice theoretically representing different turbine speeds [220] [221] [222].
Testing using orifice plates was included in the first test campaign at Lir NOTF, though the focus of the first campaign was primarily on fully sealed tests. Despite this, a number of regular wave tests were still carried out with each of the three orifice plates, allowing for initial testing of the nonlinear estimator on a more complex nonlinear dynamic system. Although no irregular wave tests were carried out with the orifice plates at Lir NOTF, synthetic data has been generated to assess the ability of the nonlinear estimator to handle irregular waves, described in Chapter 9.

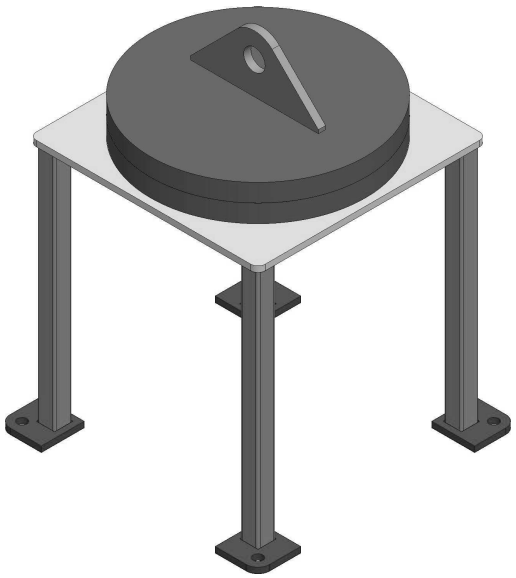


Figure 6.2: Design of frame holding two 25 mm thick steel plates representing the mass of the batteries that would be mounted on a data buoy in an at sea deployment.

Of the three orifice plates tested, only those test results using the 25 mm orifice are considered when testing the estimator, since this orifice diameter produces dynamics which are furthest from being a wave follower, representing a stronger test case for the free surface elevation estimator. All three orifice plates are manufactured to the same external dimensions as the sealing plate, from the same 4 mm mild steel, and likewise contained a hole to fit a Honeywell 176PC14HD2 pressure sensor. The orifice plate tests also use the frame representing the battery mass shown in Fig. 6.2.

6.1.3 Venturi for turbine PTO

In order to install a working turbine PTO at the top of a moonpool, some method of mounting the turbine and guiding the airflow towards it is required. As part of the WASP project, a Venturi to hold a Wells turbine had been manufactured, with the intention of being mounted on the full scale device at sea. Using a similar design, albeit scaled down to fit the dimensions of the Gannet G1250, a set of drawings was produced to obtain quotes from potential manufacturers. Working with steel to produce rounded forms at such a small scale is challenging, with some of the manufacturers contacted suggesting it is not possible to make such a design out of steel at the small size required. However, Total Welding Precision Ltd., who previously made the Venturi for the WASP, confirmed that it was possible to make a similar design for this smaller device.

Since the Gannet G1250 already has mounting holes in the custom steel top plate for attaching the various plates (shown in Fig. 6.1), the base of the Venturi is built to match, using not only the inner mounting holes, but also the outer ones, originally designed for the mass representing the batteries, for additional purchase and security. The thick base plate is also designed to hold an Aanderaa MOTUS Wave Sensor 5729 IMU, which was available from DkIT. As discussed in Section 6.4, the Lir NOTF uses a Qualisys motion capture system to record motion in six degrees of freedom. However, one drawback of Qualisys is that you cannot access the readings in real time for use in control or, in this case, an estimator. However, after some investigation, the Aanderaa IMU was also found not to return real time measurements of the device, being designed for at sea deployments where data transfer is limited to longer acquisition windows, though the base plate had at this point already been made. The base plate is constructed from 8 mm thick 304L stainless steel, which is a grade which lends itself to be easily welded to. Because this base is a relatively thick section, corrosion is less of a consideration and good joins are prioritised. The remaining sections of the Venturi, shown in Fig. 6.3, are considerably thinner at only 3 mm thick, necessitating a higher grade steel (316L) which is more expensive than 304L, but with higher corrosion resistance.
As can be seen in Fig. 6.3, the lower funnel is welded to the thick base plate, with the remaining sections detachable by means of tri-clamps with rubber gaskets to provide an airtight seal. The generator mount fits within groves machined into the central section to allow alternative generators to be used in future with minimal extra alteration required. The top and bottom funnels are also tapped to allow pressure sensors to be mounted, facilitating pressure readings on both sides of the central section housing the turbine. An additional tap is also included on the top cone to allow passage for the wires carrying the generator power and encoder signals, with a variable aperture valve to provide an airtight seal around the cables.
The turbine used is a Wells turbine with a diameter of 81 mm to fit within the central section of the Venturi. The turbine is 3D-printed using FDM rapid prototyping. To ensure a symmetric aerofoil the 3D model is split in two along the centre of the aerofoil, allowing the two halves to be laid flat on the bed of the printer, as shown in Fig. 6.4. A 0.1 mm nozzle was used to produce as smooth a blade profile as possible. The design of this turbine is discussed in detail in Chapter 7.

6.2 Sensors and data acquisition

The data acquisition system used in this project is based on the National Instruments (NI) CompactRIO 9067, which is a data acquisition chassis also capable of implementing real time control. Because the ultimate aim of the project is to test the estimator on a

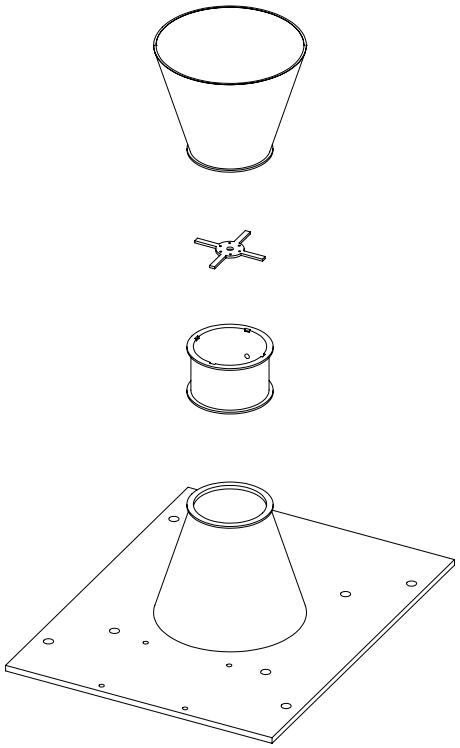


Figure 6.3: Exploded view of Venturi assembly, manufactured from an 8 mm thick stainless steel baseplate to which the lower funnel is welded. The central cylindrical section is clamped to the lower funnel via a rubber gasket and tri-clamp. The cross-shaped mounting for the generator slots into grooves in the central section again secured by a tri-clamp and rubber gasket.

device with a real PTO, some form of control is necessary to improve power capture from the turbine. The CompactRIO controller runs the NI Linux Real-Time operating system, which is coded in LabVIEW. While the CompactRIO has some features that allow for data acquisition, it lacks the features of NI-DAQmx, which is the popular, and user friendly, instrument driver most commonly used when simply acquiring sensor data. Instead the CompactRIO requires the use of its scan engine or FPGA interface. Since a Xilinx license is required for the FPGA interface, and only relatively simple control is needed for this project, the scan engine is chosen over the FPGA interface. The scan engine is limited to a maximum operating frequency of 1 kHz, meaning that, for applications where control loops at higher frequencies are required, the FPGA option must be used since it can reach rates in the MHz range.

To acquire readings from the sensors that are required for this project, a number of additional NI modules are used which plug into the CompactRIO chassis. These are summarised in Table 6.1.

A CompactRIO system is also used by Lir NOTF for their own data acquisition, meaning that it is trivial to install an electronic trigger in the CompactRIO used in this project to

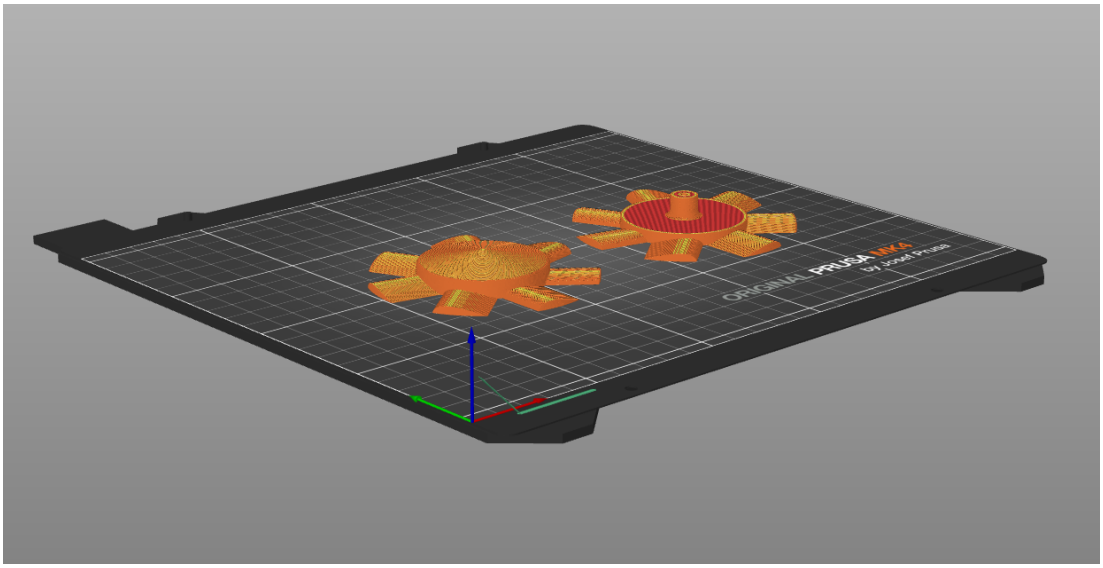


Figure 6.4: Showing how the turbine was digitally split in two to ensure no post-processing of the turbine 3D-print, to remove supports, was required.

Table 6.1: Summary of NI modules used for sensor data acquisition.

Module Name	Description	Channels	Function
2x NI9949	Screw terminal to RJ50 (ethernet) connector block	1	Interface with pressure sensors and NI9237 module
1x NI9237	Signal conditioning module for bridge-based sensors	4	Obtain voltage measurements from pressure sensors
1x NI9215	Differential analogue input module	4	Obtain voltage readings from wave probes
2x NI9401	Digital input/output module	4 or 8	One configured as counter for encoder, one for PWM output
1x NI9219	Analogue input module	4	Measure generator current and voltage output

synchronise all data acquisition systems, including the wave probe measurements and Qualisys Motion Capture recorded on Lir NOTF's own data acquisition system.

6.2.1 Wave probes

To obtain readings of the free surface elevation in the wave tank at Lir NOTF, and to measure the changes in the moonpool surface within the fixed OWC at DkIT, resistive wave probes are used. The wave probes used in both locations are almost identical, with a mix of custom made probes, described in [248], and commercially available Edinburgh Designs and Churchill Controls probes used at the two locations. With 3D printed fittings, the custom made probes at DkIT are otherwise identical to the Churchill Controls probes and, with the components being interchangeable, some probes used are likely a mix of both types.

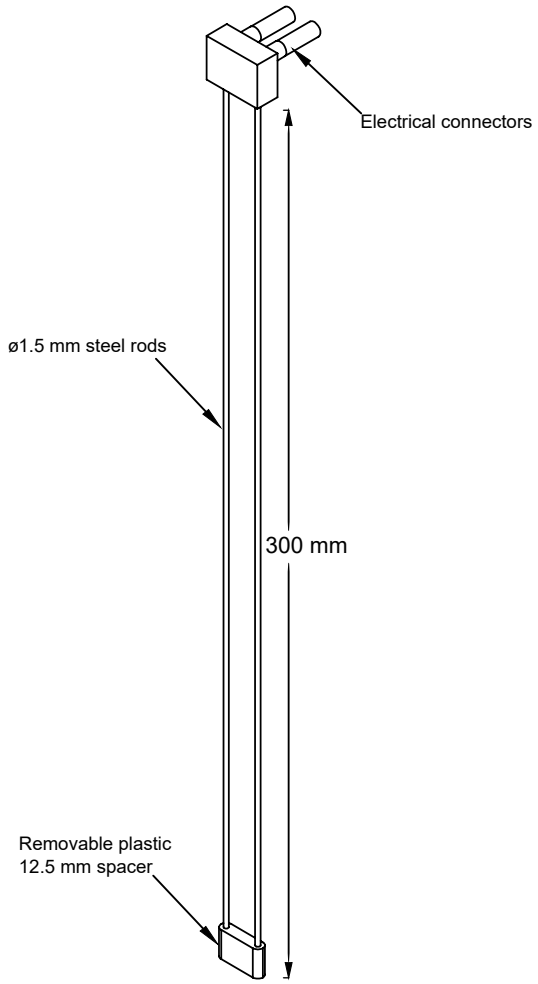


Figure 6.5: Example of resistive wave probes used in testing. The plastic spacer is held in place with silicon to stop it from detaching during tests.

The resistive wave probes are a simple design, consisting of two parallel steel rods with a diameter of 1.5 mm, held 12.5 mm apart by a plastic spacer, as shown in Fig. 6.5. The conductivity between the steel rods is proportional to the immersion depth of the probe. The plastic spacer is removable to allow for the probes to be inserted into housings such as the holes drilled in the fixed OWC described in Section 6.3 and shown in Fig. 6.12. The rods are connected to a wave monitoring module which provides a high frequency AC supply voltage of ±10 V and measures the current through the probes using a differential amplifier. The wave monitoring module at DkIT is a Churchill Controls one, whereas Lir NOTF use an Edinburgh Designs WG8USB wave gauge controller, but both essentially function the same way. The wave monitor module is wired to the NI9215 module, which has the ability to sample voltage signals of ±10 V. The NI9215 module measures changes in voltage across the probes, which are linearly proportional to the immersion depth of the probe.

As previously mentioned, the CompactRIO used for this project is not capable of running NI DAQmx software, meaning that calibration has to be implemented manually within the LabVIEW code. For calibration the probe is initialised at its datum position, with the associated voltage reading recorded. The probe is then moved vertically from this position changing the water depth in which it is submerged. This process is repeated to cover a number of points across the expected range of free surface elevation displacement. Voltage and displacement readings can now be plotted against one another, as shown in Fig. 6.6, to obtain the relationship between the measured voltage and the probe position (i.e. the inverse of the water level above: a -10 cm vertical offset represents a 10 cm rise in surface elevation).

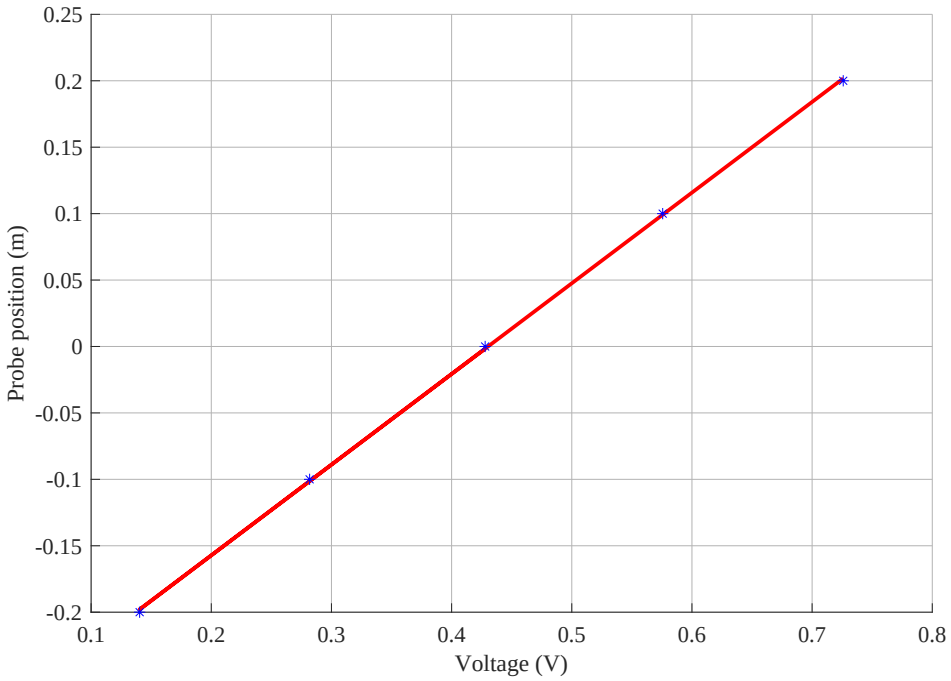


Figure 6.6: Example calibration of a resistive wave probe used in wave tank testing. Changes in vertical position are achieved by moving the probe with respect to its datum position. The equation of the resultant straight line ($y = 0.683x - 0.294$, with an R^2 fit of 0.9999) is used to convert the voltage readings into metres of wave elevation.

As can be observed from Fig. 6.6, the relationship between measured voltage and the vertical position of the probe is strongly linear with an R^2 value very close to 1. From the straight line equation a multiplier block and addition/subtraction block are added in LabVIEW to convert the changes in voltage signal acquired by the NI9215 into measurements of free surface elevation in metres.

6.2.2 Pressure sensor

To obtain pressure readings within the moonpool, on both the fixed OWC tested at DkIT and the buoy tested at Lir NOTF, Honeywell 176PC14HD2 pressure sensors are used.

These pressure sensors use four-active-element piezoresistive bridges, which produce a differential voltage proportional to the pressure difference between the two ports on the sensor, shown in Fig. 6.7. The ports are named P1 and P2, and P1 is only suitable for dry gases, whereas P2 is capable of handling moisture.

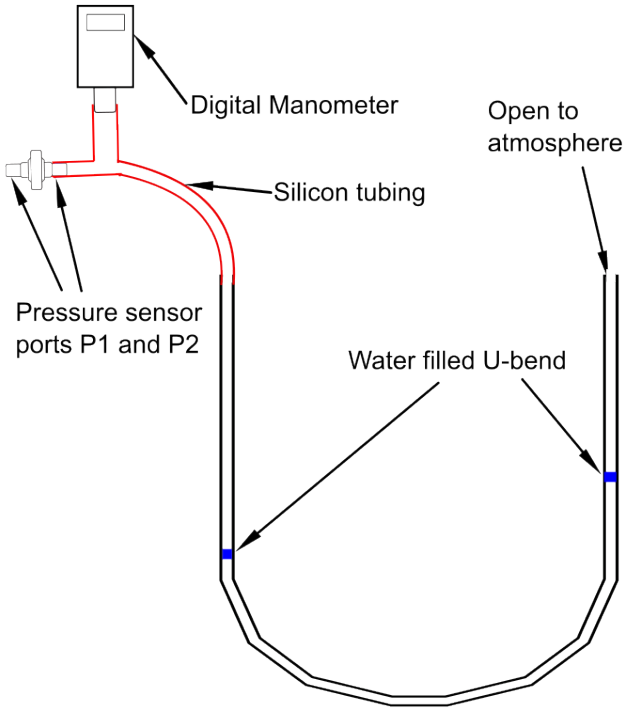


Figure 6.7: Set up for calibrating Honeywell 176PC14HD2 pressure sensor. A U-bend made of glass piping is filled with incremental amounts of water causing pressure build up in the silicon tubing connecting both the digital manometer and the chosen port of the pressure sensor.

The port P2 should therefore be facing towards the direction where there is the highest risk of water contact (facing into the moonpool for fixed OWC tests; and away from the moonpool when mounted on the floating buoy, where the moonpool surface is significantly further from the sensor position.)
To attach the pressure sensors to the orifice plates, an opening is included to fit the sensor and a silicone seal, as shown in Fig. 6.12.
For mounting the pressure sensors to the Venturi, 1/4" BSP fittings (commonly used in plumbing), are attached to a short length of 1/4" plastic pipe to obtain an airtight connection from the sensor to the air inside the chamber, as shown in Fig. 6.13.
To calibrate the sensors, the full length of wiring to be used in wave tank testing is first attached to the sensor, to ensure that the resistance of the cables is accounted for in calibration. The sensors are then connected to the NI9237 module on the CompactRIO. This module is capable of providing the voltage required by the pressure sensors

(typically 10 V) as well as reading small changes in the differential voltage output by the sensor. The sensors have a full operating range of 35 mV, so the inbuilt signal conditioning of the NI9237 module is vital for obtaining accurate readings.
For calibration, a range of pressures is produced using a tube with a U-bend, one end of which is incrementally filled with water, as shown in Fig. 6.7. Readings of pressure (using a manometer) and voltage are then recorded, in a similar manner to calibrating the wave probes, resulting in the calibration graph shown in Fig. 6.8.
Again, the relationship between recorded voltages and associated pressure values shows strong linearity, as demonstrated in Fig. 6.8. The straight line equation obtained from calibration can then be used to insert multiplication and addition/subtraction blocks in Labview to convert voltage readings from the NI9237 module to pressure values in Pascals.

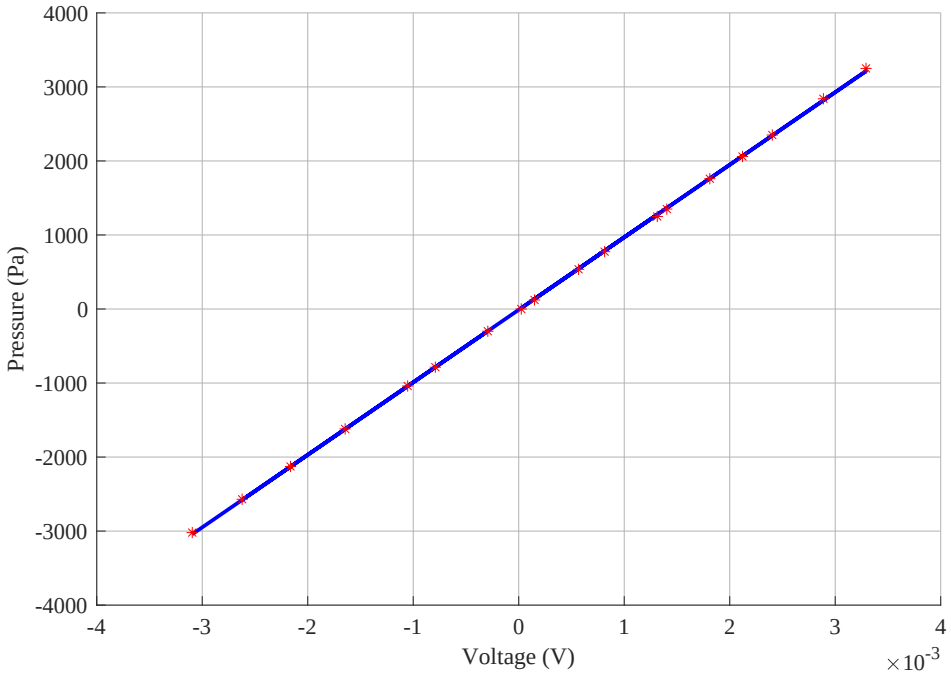


Figure 6.8: Calibration for Honeywell 176PC14HD2 pressure sensor. The equation of the resultant straight line ($y = 979576x - 10.7$ with an R^2 fit of 0.9999) is used to define the multiplication blocks in LabVIEW which convert the voltage into pressure readings in Pascals.

6.2.3 Generator and encoder

Since this project also seeks to investigate the effects of turbine control on the device dynamics, some method of controlling the turbine speed is also required. To vary generator torque, and thereby turbine rotational speed, a number of potentiometers is used in the initial experiments, as shown in Fig. 6.9. An electronic load is later added to adjust the turbine speed using the control output from the CompactRIO, described in Section 7.2.

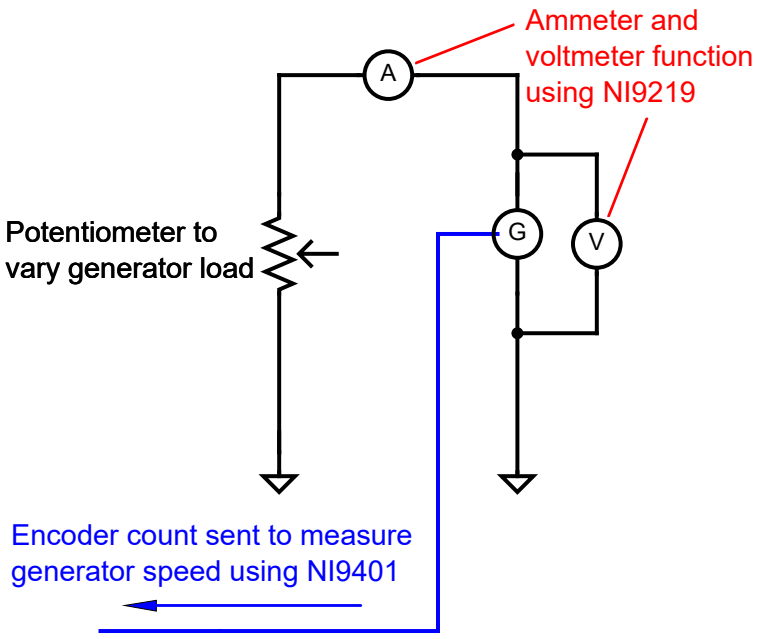


Figure 6.9: Design of initial circuit with variable load. The speed of the generator, G, is read by the counter function a NI9401 module. Note that the functions of ammeter, A, and voltmeter, V, are performed by the NI9219 and used to acquire real-time readings of the generator power.

Using the circuit in Fig. 6.9, an open circuit across the generator results in the fastest rotation because no back EMF is induced in the windings, allowing the turbine to spin freely. Conversely a short circuit slows the turbine down the furthest since the back EMF through the generator windings is maximised. Thus a potentiometer can be varied with high electrical resistance moving behaviour closer to open circuit and faster rotation, and a low resistance moving towards short circuit and lower speeds. The variation of the electrical load to alter the speed of the generator is the basis for the controller described in Chapter 7, where an electronic load can be varied through the PWM output by the CompactRio in maximum power point tracking control.

6.2.3.1 Measuring mechanical power

To characterise the behaviour of a Wells turbine, a measure of mechanical power is required. Mechanical power is normally calculated from the turbine toque, T_{turb}, as:

$$P_{turb} = T_{turb} * \Omega. \tag{6.1}$$

However, obtaining direct measurements of torque requires the use of a torquemeter, which are generally too large for the limited space inside the Venturi. Furthermore,

for the very low levels of torque generated by the turbine in the experiments used to characterise the turbine, a highly sensitive torquemeter would be required. To overcome issues around measuring torque, the characteristics of the permanent magnet DC generator are instead used.

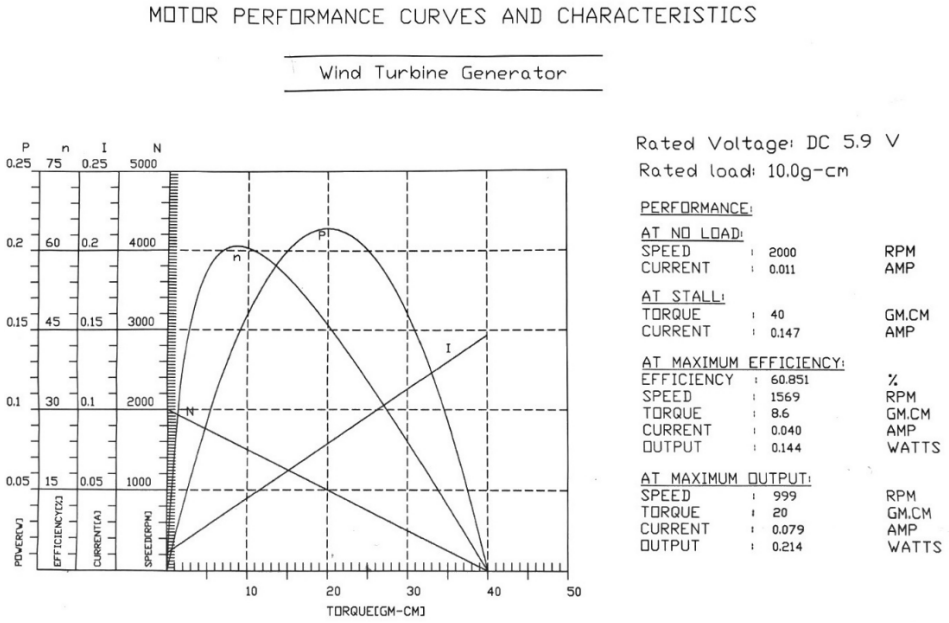


Figure 6.10: KidWind generator efficiency curve. Scanned from printout found with the generator. No longer available online. The straight line marked I shows the linear relationship between generator torque and current, which is typical of permanent magnet DC generators.

As shown in Fig. 6.10, the Vernier KidWind generator used as the generator for this project has a linear relationship between the current and the mechanical torque applied to the generator. The gradient of the straight line relating current to mechanical torque is determined by the stall current, I_{stall}, and stall torque, T_{stall}, also listed on the data sheet in Fig. 6.10. This relationship is called the torque constant K_T and is calculated as:

$$K_T = \frac{T_{stall}}{I_{stall}}. \tag{6.2}$$

Using the torque constant, measurements of the current through the electrical load, I_L, can be converted to mechanical torque:

$$T_{turb} = K_T I_L. \tag{6.3}$$

The drawback of the Vernier KidWind generator is that it does not come with an inbuilt encoder; essential for measuring turbine speed for the turbine characterisation described in Section 4.2.3. To remedy this shortcoming an external magnetic encoder kit from Polulu was purchased and adapted to fit the Kidwind generator. Magnetic encoders

are relatively robust when compared to optical ones, but despite this the poles were still counted after assembly to ensure that a correct value for counts per rotation (CPR) is found. Though the encoder is rated at 12 CPR, experiments determined that only 3 CPR are measured, so this number is used going forward with the characterisation of the turbine behaviour, described in Chapter 7. Though the Polulu encoder is built with two lines for quadrature encoding, which can be handled by the NI9401 module used to acquire encoder data, Wells turbines are designed to produce unidirectional rotation, thus rendering a single line sufficient for determining generator speed, with the second line used as a backup.

6.3 Experimental set up at Dundalk Institute of Technology

This project, through its collaboration with Dundalk Institute of Technology, was granted access to their wave tank, which is a narrow flume of width 0.35 m, with a length of 18 m and a water depth of 1 m. The tank was built by by Edinburgh Designs, who also designed the Deep Ocean Basin at Lir NOTF and was originally purchased in the 1990s by Queen's University Belfast. The wave tank was installed at DkIT as part of project collaborator Thomas Kelly's thesis [248]. A full description of the installation of the tank at DkIT can be found in [248]. The tank features two glass panels which create two testing areas where users can install devices and observe surface, air and subsurface activity, which is crucial for the work described in Chapter 7, since the water level within the moonpool must remain close to flat to allow for accurate measurements of volumetric flow rate.

Due to its narrow dimensions, and wavemaker design, the tank at DkIT can only be used for two-dimensional waves, with an absorbing beach at one end and force feedback in the paddle at the other to absorb, reduce and counteract waves reflecting lengthways along the tank. Since wave reflections can only be absorbed in the direction of wave propagation, it is best practice to fully block the width of the tank for any devices installed in it. This minimises the effect of radiated waves from the device reflecting from the side walls and creating crosswaves.

As demonstrated in Chapter 4, the effects of the orifice are the main driver behind nonlinearity in the system, and an accurate measurement of the coefficient of discharge for the orifice plates is required. Obtaining a measurement of the coefficient of discharge is the focus of the first set of experimental tests at DkIT. The second set of experimental tests is used to characterise the behaviour of the Wells turbine by obtaining dimensionless characteristic curves.The governing experimental set up, both

for determining coefficient of discharge and characterising the behaviour of the Wells turbine, is essentially identical, as described in this section.
Most experiments characterising the behaviour of Wells turbines, use an air chamber and unidirectional flow across the turbine, with only rare examples of studies considering bidirectional flow, when characterising the behaviour of Wells turbines [249] [250]. Since controllable air chambers are specialist pieces of equipment, which were not available to this project, a bidirectional flow approach using a fixed OWC in the DkIT wave flume is used, similar to that in [248] for determining the coefficient of discharge of the orifice plate. All experiments carried out on the fixed OWC use regular waves with results only considering steady state oscillating airflow, which is reached after a short transient period. The measurements required for the turbine characterisation and determination of C_d, and how these could be implemented is considered next. For both approaches these are largely identical, with both the determination of C_d and the obtention of dimensionless characteristic curves for the turbine necessitating:

- A measurement of the airflow through the turbine/orifice
- A measurement of the pressure within the moonpool chamber

For characterising the behaviour of the turbine, two additional parameters are also required:

- A measurement of the turbine rotational speed
- A measurement of the power transferred from the air to the turbine

To measure airflow through the orifice or turbine, the volumetric flow rate of air is measured at the moonpool surface, by measuring changes in moonpool surface elevation using a resistive wave probe, described in Section 6.2.1. Assuming the air is incompressible for such a small volume, conservation of volumetric flow rate allows the volumetric flow rate of the air across the turbine, or through the orifice, to be considered equal to that within the moonpool at the water surface.
The pressure within the fixed OWC is directly measured by a pressure sensor installed in the designated slot in the orifice plate, or the BSP fittings screwed into the Venturi, as described in Section 6.2.2. In addition, for characterising the turbine behaviour, a magnetic encoder is used on the generator shaft to measure rotational speed. The current and voltage output across the generator load is also measured to acquire electrical power readings that could be converted to equivalent mechanical power using prior knowledge of the generator torque constant, as discussed in Section 6.2.3. The full experimental set up is shown in Fig. 6.11.

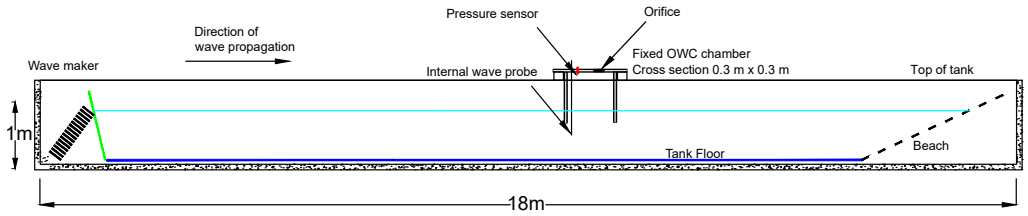


Figure 6.11: Section view of wave tank testing layout at DkIT, showing the position of wave probes, wavemaker, and the fixed OWC to which the orifice plates and Venturi were alternatively attached.

The fixed OWC itself is of a rather simple cubic design, open at the base, and with a hole in the top aligning with the orifice in the plate, which is lowered into the water of the wave tank, allowing the chamber to partially fill. With an internal cross sectional area of 0.30 m $\times$ 0.30 m, it blocks most of the width of the wave flume at DkIT, as shown in Fig. 6.13, while still allowing for easy insertion and removal from the tank. The construction of the fixed OWC consists mostly of 18 mm thick waterproof MDF, which is an affordable alternative to marine plywood, with many of the same water resistant properties. One side wall of the chamber is made from 3 mm thick clear acrylic to allow observation through the glass walls of the test section into the OWC chamber itself, as shown in Fig. 6.12. Having a view of the water surface within the chamber is of importance, since a measure of the volumetric flow rate of air within the chamber needs to be obtained. As previously mentioned, the method for doing this is to place a wave probe within the OWC chamber and relate the vertical motion of the water surface with the movement of the air into and out of the chamber. However, for such a relationship to be valid, the water surface must remain as horizontal as possible, since the sloshing modes of the water in the chamber disrupt the correlation between the airflow and the movement of the free surface of the water in the chamber. Therefore a clear view of the inside of the chamber is required to ensure such conditions are met and maintained. The fixed OWC was designed with a resonant frequency of 0.8 Hz, which means that when waves of this frequency are produced in the wave flume, the water surface within the chamber shows obvious signs of sloshing, making recordings of volumetric flow rate at this wave frequency unreliable. However, even at 0.85 Hz and 0.75 Hz, the water surface remains close to horizontal, resulting in only a narrow set of results that cannot be used for the work described in Chapter 7.

To attach the Venturi to the fixed OWC additional modification is required. The width of the Venturi baseplate is in excess of the tank width at DkIT, meaning the chamber has to be extended. To do this, a length of 220 mm diameter industrial piping (donated by Chadwicks Dundalk) is attached to the baseplate of the Venturi, raising it above the lip of the wave flume when placed on the fixed OWC. The hole in the top of the OWC also

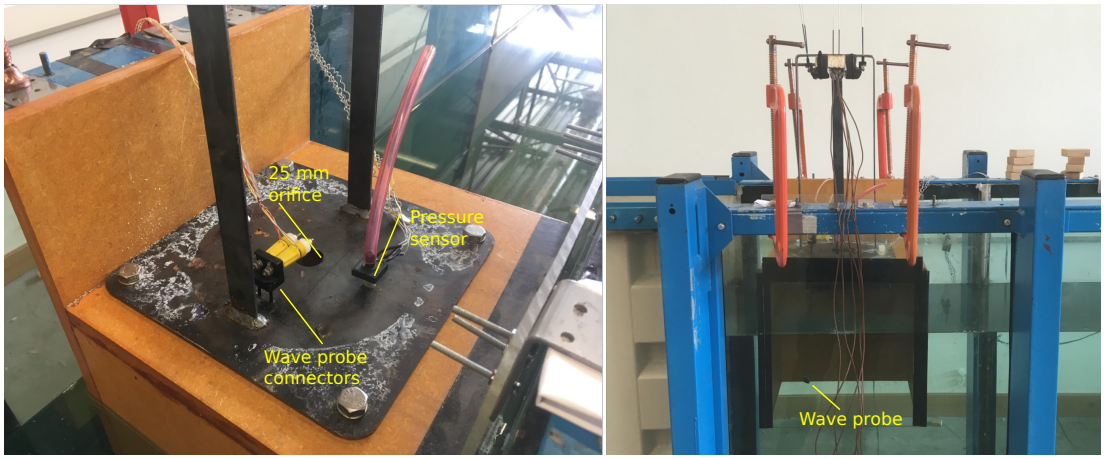


Figure 6.12: Experimental set up for determining C_d, using a pressure sensor and a single wave probe in a wooden chamber with the 25 mm orifice plate attached to the opening at the top. The test area with glass observation pane is located approximately 10.6 m from the wave maker.

needs to be widened significantly, from a diameter of 25 mm to 220 mm , with silicon sealant used to create an airtight bond between these three adjoining components. The alterations to the fixed OWC to accommodate the Venturi are shown in Fig. 6.13.
Using the experimental setups shown in Figs. 6.12 and 6.13, a number of regular wave tests were run, obtaining the steady state oscillation required for determining the coefficient of discharge for the orifice plate and to characterise the behaviour of the turbine, discussed in Chapter 7.

6.4 Experimental set up at Lir National Ocean Test Facility

Two separate test campaigns were carried out at Lir NOTF, the first coordinated by collaborators at Dundalk, and the the second specifically designed for this project. Because the tests are carried out on a full size buoy, a deep wave tank is required. Lir NOTF offers a Deep Ocean Basin measuring 35 m $\times$ 12 m $\times$ 3 m deep. Such deep water is essential to prevent any impacts from the buoy on the tank bed, which could not only damage the device, but also the test facilities themselves. This means other nearby test facilities such as those at Queen's University Belfast could not be considered appropriate since they lack sufficient water depth. Experimental facilities further afield, such as in the UK or the EU, could not be used due to the logistics of transporting a full size data buoy on the project's limited budget.
The first of the two test campaigns comprises tests designed to verify results based on at-sea testing of the WASP [111], and therefore mostly focusses on regular and



Figure 6.13: Experimental set up for characterising the behaviour of the Wells turbine. A variable aperture seals where the encoder and generator lines enter the Venturi. The upper and lower pressure sensors are connected to 1/4" BSP fittings to obtain an airtight connection to the air inside the Venturi.

irregular wave tests for the G1250 with a fully sealed moonpool. Initially tested in regular waves, the sealed G1250 was afterwards tested in irregular waves, based on a scaled Bretschneider spectrum of sea states observed at Galway Bay. To represent a turbine PTO, the moonpool of the G1250 was also fitted with a number of orifice plates, with orifice diameters of 5 mm, 15 mm and 25 mm, albeit only using regular waves. Though many of the tests from the first campaign are useful, allowing for the evaluation of both the linear estimator for the sealed moonpool, and the nonlinear estimator for the OWC fitted with the 25 mm orifice plate, there are some notable limitations, further discussed in Chapters 8 and 9. These limitations can be summarised primarily as the proliferation of snatch loads in irregular tests with the sealed buoy, and the lack of any irregular wave tests using the OWC fitted with orifice plates. Thus, a second test campaign, designed specifically for testing the Kalman filter based estimator described in Chapter 8 and evaluated in Chapter 9, was carried out.

Waves in the Deep Ocean Basin at Lir NOTF are measured using three resistive wave probes, placed on an instrument bridge between the wave maker and the buoy, as illustrated in Fig. 6.14. Since the second test campaign was designed specifically for

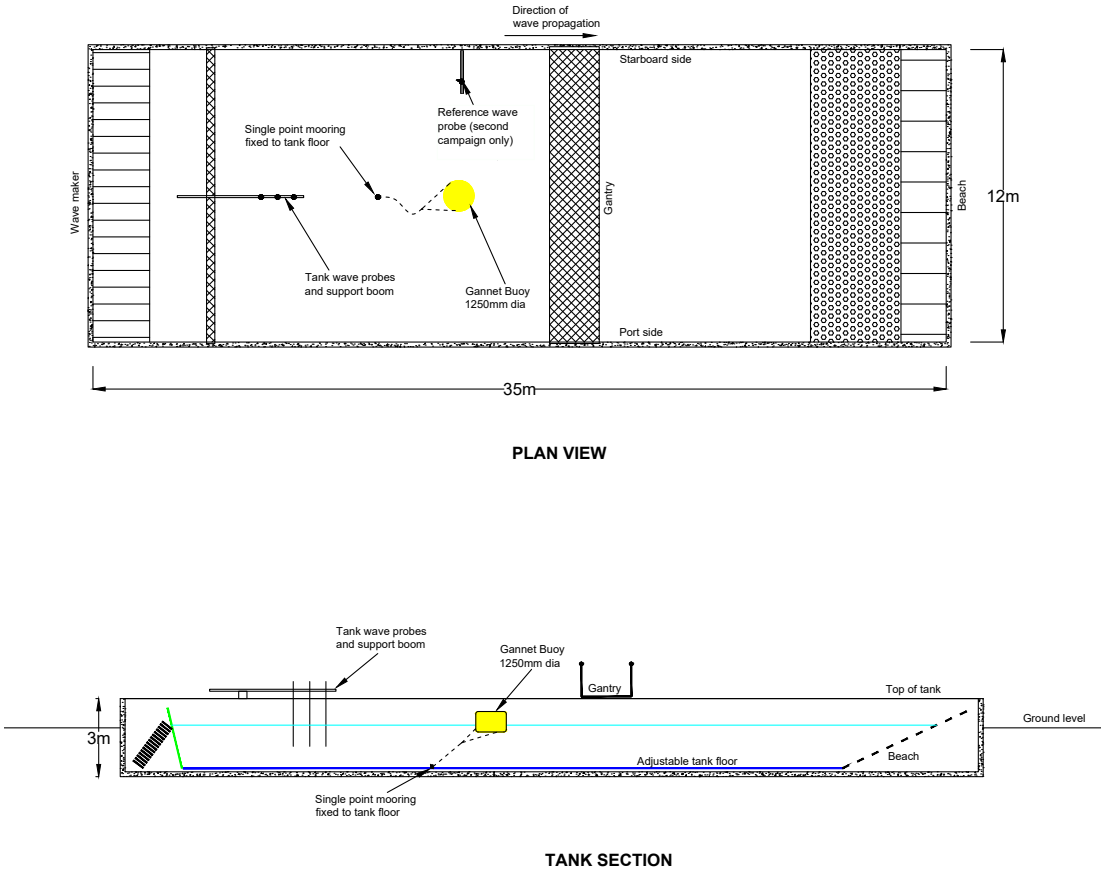


Figure 6.14: Plan view and section view of wave tank testing layout at Lir NOTF, showing the position of wave probes, wavemaker, and the mooring location of the G1250 Gannet buoy.

testing the free surface elevation estimator, an additional reference wave probe was added on the starboard side of the Deep Ocean Basin, in line with the test position of the Gannet. This reference probe should experience mostly identical waves to those of the Gannet, accounting for any wave breaking that could occur between the instrument bridge and the Gannet itself. A pressure sensor is fitted, as described in Section 6.2.2, to record real time pressures within the moonpool chamber. The displacement of the buoy is measured using a Qualisys motion capture system, which records data in 6 DoFs. The Qualisys system is based on a system of cameras pointing toward the test area. The test subject, in this case the buoy, must then be fitted with reflective nodes at points visible to the cameras. These nodes can be observed in Fig. 6.15. The nodes were relatively straightforward to mount on the buoy used in the first test campaign, since the steel mass added to the top of the buoy to represent the onboard batteries presents a clear vantage point to which the Qualisys nodes can be attached. The Venturi presents more of an issue as it is relatively tall, extending more than 0.3 m from the baseplate to which the first Qualisys nodes are attached. Fig. 6.15 shows the initial set up, where the Qualisys

nodes are placed on the side nearest the wavemaker. In initial trial runs at Lir NOTF, however, the pitch and yaw of the buoy, regularly obscure the points at which the nodes are mounted, from the cameras, requiring additional nodes to be added to the lifting eyes and the lip of the Venturi. These are attached directly using silicon adhesive.

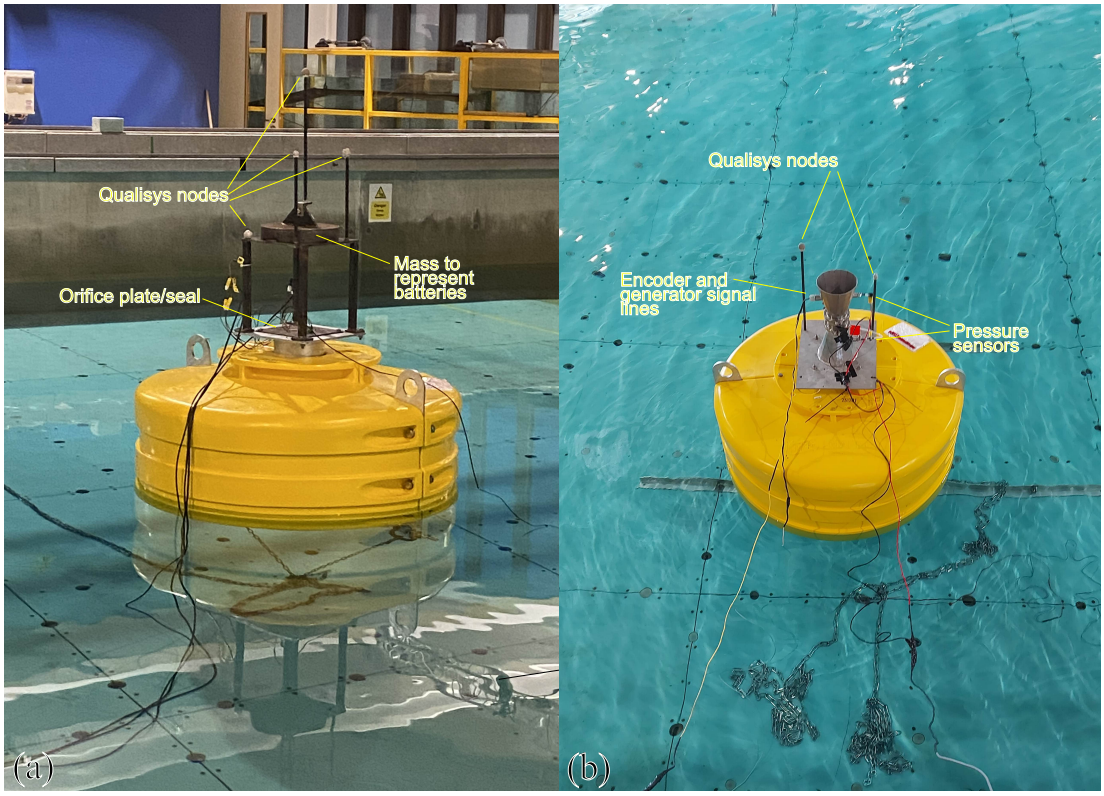


Figure 6.15: a) Shows the experimental set up used for the first campaign with a mass to represent the batteries, and the orifice plate or seal with fitted pressure sensor. b) Shows the set up for the second test campaign with a pressure sensor on both the lower and upper Venturi, as well as cables to transfer power from the generator and encoder readings back to shore.

All tests are carried out using a single anchor point for the mooring. For the first test campaign using a single point mooring was chosen to be reflective of that used for the WASP during deployment at Galway Bay, and for continuity a single point mooring was kept in the second test campaign. The moorings consist of two chains, attached to the two mooring points on the base of the Gannet G1250, which are brought to a point approximately 0.3 m below the base of the buoy using metal carabiner clips. A single anchor point is then used, with the mooring length set to be approximately 3.4 m long in total. A longer mooring of approximately 4 m length was initially tested, but this did not provide adequate station keeping, with significant drift in the direction of wave propagation, as well as yaw, which interferes with the ability of the Qualisys motion capture system to function. Though the tank is 3 m deep, the floor is movable to allow mooring set up to be carried out when the floor is at a fully emersed position.

One of the main issues with results from the first campaign is the prevalence of snatch loads. Particularly noticeable in irregular wave tests, snatch loads, where the buoy reaches the end of its tether and is pulled back suddenly, are present in the measured heave data. These snatch loads present as large spikes in magnitude of the buoy heave measurements, and are an unfortunate artifact of wave tank testing in relatively shallow water with a short mooring line. Snatch loads are problematic for the estimator, since they have an impact on both the magnitude, but more significantly, the phase of the device heave motion, which the model used by the estimator cannot account for. Although snatch loads are also experienced by data buoys at sea, moorings are generally designed to minimise the incidence of snatch loads occurring, as they represent an extreme loading condition on the device [251]. To minimise the incidence of snatch loads in the second test campaign, a force sensor is added between the mooring chain and the anchor point, providing live readings of the force on the mooring line. The force sensor is used as a warning system for determining the threshold for the maximum wave height that may be used before significant snatching becomes a problem. The force sensor used is rated for 500 N, though occasionally exceeding this limit by up to 500 N again is still considered safe for the force sensor operation.

6.4.1 Wave tank limitations

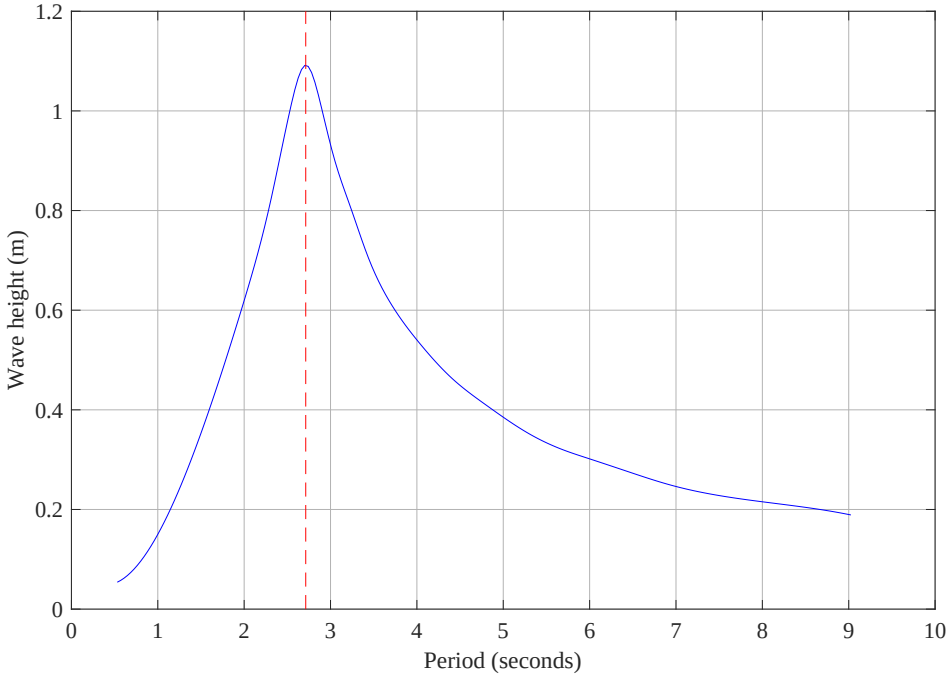


Figure 6.16: Tank envelope for the Deep OCean Basin at Lir NOTF. Note that waves to the left of the dashed red line are limited by the paddle stroke of the wave makers, while those to the right are limited by wave breaking.

In spite of its size, the Deep Ocean Basin at Lir NOTF is still relatively limited in the waves it can produce. Fig. 6.16 shows the tank envelope, which determines the combinations of maximum wave height and wave period that can be used. The limitation of avoiding snatch loads with a relatively short mooring further limits the wave heights that can be tested, with waves of height 0.2 m at the limit of where some occasional snatch loads began to occur. The frequency of the waves is limited in part by the device itself. The turbine on an OWC needs sufficient excitation to spin, with Wells turbines notorious for self starting difficulty [193]. The floater itself, being a navigation buoy, is also not optimised to move with the waves, so some trial and error was required to identify the range of waves that would produce power from the turbine. The upper frequency limit is found to be approximately 1 Hz, with the lower limit at approximately 0.6 Hz. It is possible that waves with a slightly lower frequency could also produce power from the device, but another limitation of the tank is reached in the frequencies around 0.6 Hz, which is the natural frequency of the Deep Ocean Basin.
Similarly to the wave flume at DkIT, the Lir NOTF Deep Ocean basin only has wave makers at one end producing waves which propagate in a single direction, and are opposed by an absorbing beach. This means that it is also only appropriate for two-dimensional waves, with the drawback that it is 12 m wide, meaning that no devices tested at this scale are likely to fully block the tank width. This means reflected waves from the tank starboard and port sides, shown in Fig. 6.14, take a long time to settle fully (more than 60 minutes in some cases), and this settling time increases, the closer the dominant frequency of the test waves is to the wave tank resonant frequency. Tests at 0.6 Hz produce cross waves that are almost as high as the generated waves in the direction of wave propagation, meaning that the free surface is too stochastic and multidirectional for any meaningful measurements to be made using the wave probes. Thus the frequencies used in the second campaign are limited to be between 0.67 Hz to 1 Hz, with wave heights limited to a maximum of 0.2 m.

6.4.2 Selection of test waves and spectra

With the limitations imposed by the tank envelope, shown in Fig. 6.16, and avoiding snatch loads on the device, the range of frequencies and wave heights in which the device could be tested was relatively limited at Lir NOTF. In the first test campaign, though snatch loads were prevalent in irregular waves, there were only a few incidents in regular waves. This is because, once the device is oscillating in steady state, there are few changes that drive it towards reaching the end of its tether. This meant that, for testing the estimator based on results of the first test campaign, regular wave tests were the most useful test cases for determining the ability of the estimator to return

free surface elevation measurements in the time domain, as there were few occurrences of snatch loads that changed the phase response of the device. Real ocean waves are, however, not regular, so assessing the ability of the estimator to return free surface elevation in irregular waves was a key objective in the second test campaign.
The first test campaign used Bretschneider spectra to generate irregular waves, based on scaled down characteristic wave parameters observed at Galway Bay. Due to the limited range of wave frequencies and wave heights that could be tested at Lir NOTF, variation in irregular wave tests was achieved by considering a variety of spectra to generate irregular waves. JONSWAP spectra, which describe fetch limited seas, have a peak enhancement factor γ, which is normally set to 3.3 for North Sea conditions [181]. The effect of this peak enhancement factor is that JONSWAP spectra are more narrow-banded than Bretschneider spectra, resulting in waves that are, in general, close to the peak frequency used to define the spectrum. To test the estimator, irregular waves generated from a JONSWAP spectrum with $\gamma = 3.3$, represent a more forgiving test case that sits between regular waves and the more broad-banded waves generated using a Bretschneider spectrum. This gives three levels of irregularity against which the estimator can be tested, starting with regular waves, then testing against JONSWAP generated waves, and finally waves generated by a Bretschneider spectrum as the most irregular test case.
However, one problem encountered using both JONSWAP and Bretschneider spectra at Lir NOTF are the limitations in frequency and wave height, which mean the irregular waves produced by these spectra are often not sufficiently exciting to cause the Wells turbine to spin for significant amounts of time, resulting in the need for more energy dense methods of producing random waves.
Therefore the pseudo band-limited white noise approach, described in Section 3.2.3, was used in the second test campaign, covering the exciting frequencies of 0.67-1 Hz. Such waves are generally used in system identification though, as shown in [176], the limitations of wavemakers mean that such waves are not true white noise, and are instead relatively broad-banded waves with enough energy to excite the device dynamics across the defined frequency range. The resultant waves are generally energetic enough to produce frequent rotation of the turbine, while producing a series of random waves against which the estimator could be tested.

6.5 Chapter summary

This chapter describes the experimental equipment and facilities used to produce experimental data at two different test locations. The testing at Dundalk is used to characterise the orifice plate and the Wells turbine, described in Chapter 7. The availability of the wave tank at DkIT was also utilised to ensure all subsystems that

would be used in testing at Lir NOTF were functioning correctly on a fixed OWC, to minimise the risk of failure during the test campaign on the full sized floating OWC. The experiments at Lir NOTF are to validate the performance of a free surface elevation soft sensor that accounts for the device dynamics of a floating OWC for three test cases: a buoy with a fully sealed moonpool, an OWC fitted with an orifice plate to represent a turbine PTO, and finally an OWC with a working turbine PTO (including set point tracking control for the turbine speed). The evaluation of the free surface elevation estimator is described in Chapter 9.

The limitations of the Lir NOTF wave tank have been discussed in this chapter, particularly with regards to the tank envelope, shown in Fig. 6.16, and the avoidance of snatch loads. It should further be noted that, while the device tested at Lir NOTF is a full size OWC powered data buoy, the waves against which it is tested, due to the limitations of the wave tank, are not realistic waves for a full scale device. The Gannet G1250 diameter is 1.25 m, which for the waves tested at Lir NOTF represents approximately one wavelength. This results in greater pitch motion and less heave motion than would be expected in real seas, where wavelengths are considerably higher than the diameter of a small data buoy.

7

PTO turbine design

Contents

7.1 Design of a Wells turbine for use in a small-scale OWC 142
7.1.1 Testing the designed turbine 145
7.2 Design and control of the turbine load 153
7.3 Modelling turbines as equivalent orifice 157
7.3.1 Experimental determination of coefficient of discharge for orifice plate 158
7.3.2 Real turbine modelled as equivalent orifice 160
7.4 Chapter summary and conclusions 162

An essential part of an OWC is the turbine used to extract power from the oscillatory airflow generated by the waves in the moonpool chamber. Design of Wells turbines has been well studied since their invention in 1976 [227], with the work of Raghunathan in the 1990's [193] still highly influential and governing much of the decision making for Wells turbine design in the literature [224]. However, one aspect of Wells turbine design that has received little attention, is the design of Wells turbines for small scale applications and very low Reynolds number flows (below 100,000). Indeed most of the literature follows the assumption that Wells turbines operate in flows with a Reynolds Number of at least 1,000,000 [213], and that the turbines have a minimum diameter of 0.6 m [228]. This is largely due to the problems that low Reynolds number flows and small turbine diameters pose to the efficient operation of Wells turbines, with sharp drops in efficiency converting the pneumatic power to turbine power observed even in flows with a Reynolds number of approximately 100,000 [252]. Problems with Wells turbines operating at a

small scale can be summarised by the drag coefficient of the turbine increasing as the Reynolds number drops, which can result in the turbine operating primarily as a drag rather than a lift turbine, and the narrow stall margin at low Reynolds number flows [235]. Exaggerated effects from drag and friction are common in small scale WEC testing, leading to a variety of workaround solutions: for example, frictionless air bearings used on moving parts [253], external power being applied to actuators to counteract friction [254], and most apposite to OWCs , the orifice plates that simulate the effects of a turbine [220]. Solutions requiring external energy to counteract friction are acceptable for scaled down tests of larger devices, where the real WEC will be much larger, and therefore will not experience the effects negated by these external sources. However, when the final scale of the WEC falls into the range where such exaggerated effects from drag and friction will be experienced by the full scale device, dealing with these effects must be considered in the design of the PTO itself.
In this chapter the process for designing a Wells turbine that is suitable for low Reynolds number airflows is described, followed by a description of the obtention of the characteristic curves describing the behaviour of the turbine. The control system used for the turbine PTO is also described, including how the set point, and the PI tuning, is selected for the controller in the tests at DkIT and at Lir NOTF. The chapter also discusses how the coefficient of discharge is experimentally calculated for the orifice plate described in Chapter 6 and the applicability of modelling the designed Wells turbine in a similar way.

7.1 Design of a Wells turbine for use in a small-scale OWC

Designing Wells turbines requires the consideration of a number of aspects describing the turbine geometry. Other than the diameter of the turbine, these design parameters (which are not all independent) are as follows:

- Tip clearance
- Aspect ratio
- Chord length
- Number of blades
- Solidity
- Hub to tip ratio

- Blade profile

In this section the rationale for the choice of each of these parameters is described. In the literature, [193] is a seminal text for designing Wells turbines, which suggests a number of initial values to consider when designing Wells turbines. Though the focus of [193] is not on turbines on a scale as small as those considered for this project, many of the same considerations apply, and there are some suggestions given for some of the changes that should be made when designing turbines for low pressure and low flow applications. Most notably, these suggested changes pertain to the blade profile itself, with thicker aerofoils stated as being better suited to low pressures and low flow applications.
The first design parameter to consider is the turbine diameter. This is primarily determined by the inner diameter of the Venturi which is approximately 82-83 mm. The second determining factor for the turbine diameter is the tip clearance ratio, which has been found to affect the stall of the turbine, with a lower tip clearance advancing the stall limit, but improving the efficiency. Since a higher tip clearance not only increases the range of flow rates over which a turbine can operate without stalling, a tip clearance of approximately 1 mm was used, corresponding with a ratio of 0.0244 (higher than the <0.02 recommendation given in [193] for regular operating conditions). This relatively high tip clearance also accounts for irregularities in the central section of the Venturi, which is not a perfect circle, due to machining tolerance and finish of the central weld beads. A nominal tip clearance of 1 mm is found to give enough margin of error for the turbine to spin freely without touching the sides of the Venturi.
The blade aspect ratio, AR, is one instance where the guidelines set out in [193] are not followed, due to the unique requirements of operating at low Reynolds numbers. The aspect ratio is calculated by:

$$AR = \frac{l_{chord}}{l_{span}}, \tag{7.1}$$

where l_{chord} is the chord length and l_{span} is the span length. It is known that aerofoils for low Reynolds number flows should be thicker [224], to ensure that stall is more gradual. Stall margin is extremely narrow for low Reynolds number flows [235], and a key challenge for turbines at this scale is to broaden the operating range as much as possible, which generally increases the drag on the turbine. The same reasoning, used for turbine thickness, can also be applied to the aspect ratio since, in aerodynamics, a higher aspect ratio also contributes to a more gradual stall [255]. It is not uncommon for Wells turbines used in OWCs to have aspect ratios up to 1.45, such as the Limpet device [256]. However, the higher the aspect ratio used, the higher the drag on the blades, so an aspect ratio of close to 1 was used as a starting point for practical testing.

The solidity of the turbine σ_{turb}, has effects on both the axial force on the blades, and the efficiency of the turbine. High solidity turbines have lower efficiency in converting pneumatic power to turbine power, due to the increase in exit kinetic energy losses, and therefore are best suited to applications where a large pressure drop is expected across the turbine [193]. Solidity is a measure of the ratio of blade area to swept area, and measures the blockage to the airflow by the turbine, as well as the interference between the blades. It is calculated by:

$$\sigma_{turb} = \frac{N_b l_{chord}}{\pi D_{turb}}, \tag{7.2}$$

where N_b is the number of turbine blades, and D_{turb} is the turbine diameter. Seven blades, and a constant chord length of 19 mm, are used to obtain a solidity of approximately 0.5. For the small scale testing in this thesis, the upper limit of the recommended solidity range for a monoplane turbine in [193] is used, since turbines with low solidity cannot reach operational speed from rest.

The hub to tip ratio of 0.57, again follows the recommendation in [193] to keep below 0.6, since higher ratios cause a sharp drop in turbine efficiency. Hub to tip ratio, HTR, is calculated as:

$$HTR = \frac{D_{hub}}{D_{turb}}, \tag{7.3}$$

where D_{hub} is the hub diameter.

General recommendations are for NACA profiles between NACA0012 and NACA0021 to be used for Wells turbines. The latter two digits of these profile names indicate the percentage thickness with respect to the chord length. For low pressures and low flow rates thicker aerofoil profiles are recommended, with [224] recommending NACA0021. An iterative process, testing blade profiles with increasing thickness, found that a profile, which, when measured, is close to a NACA0026 profile, was found to spin for the airflows achieved under experimental conditions, even self starting in most of the experimental tests carried out. FDM 3D-printing has tolerances to the dimensions that can be achieved (approximately ±0.3 mm in the horizontal direction), which limits the resolution at which profile thickness can be increased. The reported profile was measured once 3D-printed and assembled, and found to be close to NACA0026, thicker than what is generally seen in the literature. However, it should be noted that the tests being carried out in this thesis are at flow rates considerably lower than what is seen in the literature, so this thicker profile is deemed to be suitable.

The final dimensions for the turbine described in this section are shown in Fig. 7.1. Through iteratively increasing blade thickness to increase operational range, the design shown in Fig. 7.1 is found to spin in a test wave of 30 mm wave height and a frequency

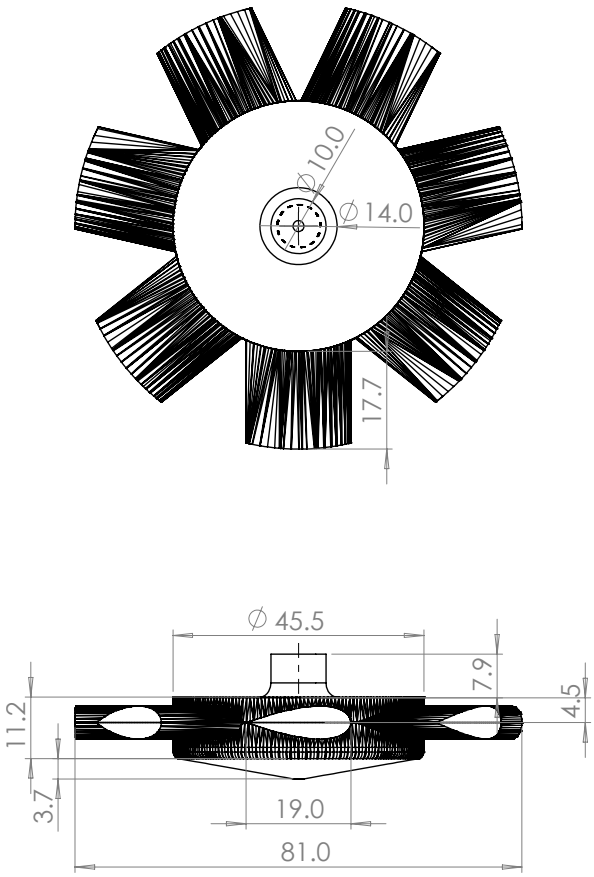


Figure 7.1: Final dimensions (in mm) of Wells turbine used in experimental testing. The aerofoil profile used for the blades is approximately NACA0026, with turbine diameter 81 mm, hub diameter 45.5 mm, chord length 19 mm and span length 17.7 mm. The 7.9 mm extrusion from the flat side of the turbine hub is bored to accommodate the shaft of the DC generator used.

of 0.85 Hz. However, the trade-off for increasing the operational range is that thicker turbine blades increase drag. To test whether a low stall limit and low operational range are challenges that the turbine, designed in this chapter, solves, a series of tests are carried out as described in Section 7.1.1. Another concern with Wells turbines in low Reynolds number flows, is that they operate purely in the stall region. The tests described are carried out to assess the design, not only in terms of its self-starting behaviours, but also assessing whether it reaches operational speed, and that the operational range of the turbine is not only in the stall region.

7.1.1 Testing the designed turbine

Testing the designed Wells turbine was carried out using the experimental set up for a fixed OWC at DkIT, described in Section 6.3. The wave condition initially tested

uses a wave height of 30 mm with a frequency of 0.85 Hz. This wave condition is close to the 0.8 Hz resonant frequency of the fixed OWC, and therefore produces relatively energetic oscillations within the fixed OWC. Importantly though, the free surface within the OWC remains close to horizontal at this frequency, allowing for accurate measurements of volumetric flow rate to be obtained using the wave probe inside the moonpool chamber. Later tests, expand the range of regular wave frequencies tested and also consider wave heights of 25 and 40 mm.

7.1.1.1 Self-starting and crawling behaviour

As mentioned in Section 4.2.3.1, Wells turbines are notorious for not self-starting. However, even when Wells turbines do self-start, another problematic behaviour that can occur is that the turbine 'crawls' rather than spinning. In [193], crawling behaviour in Wells turbines is described as the turbine self-starting but only reaching a speed that is considerably lower than its operational speed and, as with self-starting, it is primarily a characteristic of low solidity turbines. Crawling turbines can only be brought up to operational speed by an external input, such as using the generator as a motor to inject a 'kick' of energy into the system.

To test whether the turbine designed in this chapter for the experiments avoids such crawling behaviour, an experiment is run where the turbine is allowed to self start, and is then assisted by sending a kick through the generator, momentarily using it as a motor. The speed the turbine returns to after the kick is then noted to ensure the speed it reaches naturally is not within the crawl region. This is tested for a variety of turbine loads using fixed resistors and potentiometers to vary the turbine speed as shown in Fig. 6.9. A summary recording the speeds reached both without and with an external kick is given in Table 7.1.

From Table 7.1, it can be determined where the limits of self-starting operation are. Only two test cases have conditions such that a starting kick is needed to reach operational speed, with other cases either returning to rest or to the same operational speed reached using self-starting alone. This implies that the turbine is well designed in terms of its solidity, able to reach full operational speed through self-starting alone, and in no cases demonstrating any crawling behaviour.

Since the turbine never reaches a crawl region, and is generally self-starting, additional control, to govern when an external force to kick start the turbine should be used, can be considered unnecessary for the designed turbine. Though the addition of a self-starting controller could be used to slightly increase the range of frequencies at which the turbine spins, this minor reduction in the range significantly reduces the complexity of the control system needed for the turbine, since no additional logic is required to determine when a kick would be beneficial, and no switching between the generator working as a generator and as a motor is required.

Table 7.1: Comparison of steady state rotational speeds reached before and after applying an external 'kick', momentarily using the generator as a motor to drive the turbine. ω is the speed reached naturally without external help and ω_{kick} is the speed reached once the turbine reaches a steady state spin after receiving the 'kick'.

Resistive Load	Wave Frequency (Hz)	Ω (rad/s)	Ω_{kick} (rad/s)
10	0.85	11.14	11.05
100	0.85	21.32	21.2
1000	0.85	70.54	70.7
10000	0.85	97.64	96.38
10000	0.5	0	0
10000	0.55	0	10.26
10000	0.6	33.41	32.67
10000	0.65	30.05	30.05
10000	0.7	61.05	59.89
10000	0.75	72.78	72.25
10000	0.9	120.85	119.27
10000	1.0	0	83.14
10000	1.1	0	0

7.1.1.2 Nondimensional characteristics of a turbine in low Reynolds number airflows

A significant concern for small scale Wells turbines is that, due to the high levels of drag and narrow stall margin, they can operate entirely in the stalled region, where the conversion efficiency from pneumatic power to turbine power drops significantly. With such small turbines, it is entirely possible to only encounter stall conditions in testing. To assess turbine operational range, nondimensional characteristic curves are used. These characteristic curves express the dimensionless parameters for pressure, volumetric flow rate and power, previously discussed in Chapter 4 (and given in equations (4.26), (4.27) and (4.28)).

Normally, when designing a larger scale OWC, it is typical to select a turbine based on its nondimensional characteristic curves, which indicate the most efficient operating point, as well as the operating region before the turbine reaches stall. An example of these nondimensional characteristic curves can be seen in [257], for the Wells turbines used in the Mutriku power plant, though many examples exist in the literature. Being dimensionless, such characteristic curves describe the operation of a turbine regardless of its diameter (down to a minimum limit, arguably down to 0.4 m, though suggested to be larger than 0.6 m in [224]). These generally applicable nondimensional characteristic curves also have a limitation in terms of the Reynolds number that they can be applied to since, for low Reynolds number flows, drag on the blade is not constant but instead varies with the Reynolds number of the flow [235]. Normally the

relationship between the pressure drop across a turbine and the volumetric flow rate is linear, though this does not hold true in the low volumetric flow rate region of the graph [257]. As demonstrated in [252], where flows with a Reynolds number of approximately 100,000 are considered, similar behaviour is seen, where a linear relationship between dimensionless pressure and volumetric flow rate is evident, again becoming nonlinear for low values of dimensionless volumetric flow rate. There are few studies in the literature studying Wells turbines in Reynolds number flows lower than 100,000, with only [236] considering flows of 78,000. Even when considering airflows over symmetrical aerofoils in general, few papers exist which consider flows as low as 20,000 [258] [259] [260]. Reynolds number, Re, is a dimensionless quantity commonly used in fluid dynamics. It is described by:

$$Re = \frac{uL_c}{\nu_{air}} = \frac{\rho_{air} uL}{\mu_{air}} \tag{7.4}$$

where u is fluid velocity, L_c is the characteristic length, ν_{air} is the kinematic viscosity of the fluid, ρ_{air} is the fluid density and μ_{air} is the dynamic viscosity of the fluid (in this case the fluid is air).

In the experimental set up with the fixed OWC at DkIT, different formulations of Reynolds number can be considered. The form most commonly seen in the literature is the Reynolds number related to the blade performance, Re_{turb}, which uses chord length l_{chord} as the characteristic length. It can be described as:

$$Re_{turb} = \frac{\rho_{air} v_{rel} l_{chord}}{\mu_{air}}, \tag{7.5}$$

where v_{rel} is the relative velocity between the velocity of the air flow across the turbine v_{vent}, and the tip velocity of the turbine v_{tip}:

$$v_{rel} = \sqrt{v_{vent}^2 + v_{tip}^2}, \tag{7.6}$$

with the velocity of the air flow across the turbine calculated as:

$$v_{vent} = \frac{Q}{A_{ori}}, \tag{7.7}$$

and the tip velocity as:

$$v_{tip} = \Omega \times \frac{D_{turb}}{2}, \tag{7.8}$$

The values of Re_{turb} achieved in the experimental set up at DkIT range from a minimum of approximately 2,000 to a maximum of approximately 9,500 for the range of turbine speeds tested.

Another Reynolds number that can be considered in the experimental set up at DkIT is the Reynolds number relating to the airflow through the central section of the venturi, before it reaches the turbine, Re_{vent}, which considers the hydraulic diameter as the characteristic length [261]:

$$Re_{vent} = \frac{\rho V_{vent} D_h}{\mu_{air}}, \tag{7.9}$$

where D_h is the hydraulic diameter, which for the Venturi, being a round duct, is equal to the Venturi diameter.

Re_{vent} is a useful measure since it is independent of the turbine speed, and relates purely to the flow speed at the inlet of the central section of the Venturi.

Since, for low Reynolds numbers, drag is dependent on the Reynolds number, a set of experiments is run, again using the fixed OWC set up at DkIT, this time considering three different wave heights: 25 mm, 30 mm and 40 mm. Again, a variety of resistors are used to vary the load on the generator and thereby the rotational speed of the turbine. The range of wave frequencies that could be used for each wave height varies, since the range of exciting frequencies for the turbine diminishes with wave height. For the 40 mm wave height tests a frequency range of 0.5-1Hz could be used, for 30 mm wave height tests a frequency range of 0.6-0.9 Hz, while 25 mm wave height tests were limited to a frequency range of 0.75-0.85 Hz.

The three wave heights produce 3 different ranges of Re_{vent}, depending on the wave frequency, while varying the turbine speed alters the values of Re_{turb}. For each wave condition, and turbine speed, the values of pressure, volumetric flow rate, torque, and rotational speed are recorded, as per the methods described in Chapter 6.

Usually, in the literature describing the obtention of turbine characteristic curves, unidirectional flow is generated across the test turbine by a high flow wind tunnel [262]. Wind tunnels of the scale and speed used in [262] are only available in specialist facilities, and were not within the budget of this project. Furthermore, since the turbine characterisation in this thesis is to focus on turbines in low Reynolds number flows, achieving high flow rates using a wind tunnel is not required. In lieu of a wind tunnel, the fixed OWC at DkIT is used to generate an oscillating flow of a similar magnitude to that expected in wave tank testing at Lir NOTF.

Usually, when oscillating flows are used for turbine characterisation, it is to investigate the hysteresis phenomena that may occur in Wells turbines [225] [263]. However, in [252], which considers the characterisation of a small Wells turbine in relatively low Reynolds number flows ($Re_{turb} \approx$ 100,000), oscillating flows are used, with RMS approximations over a series of 10s windows used to acquire data points from the time domain test data. Profiling a turbine using oscillating flow does present some issues. While a steady state oscillation is reached when using regular waves, resulting in the turbine reaching

a near constant rotational speed, the exact values for the flow rate and pressure require some element of approximation for inclusion in the data used to generate a turbine dimensionless curve.

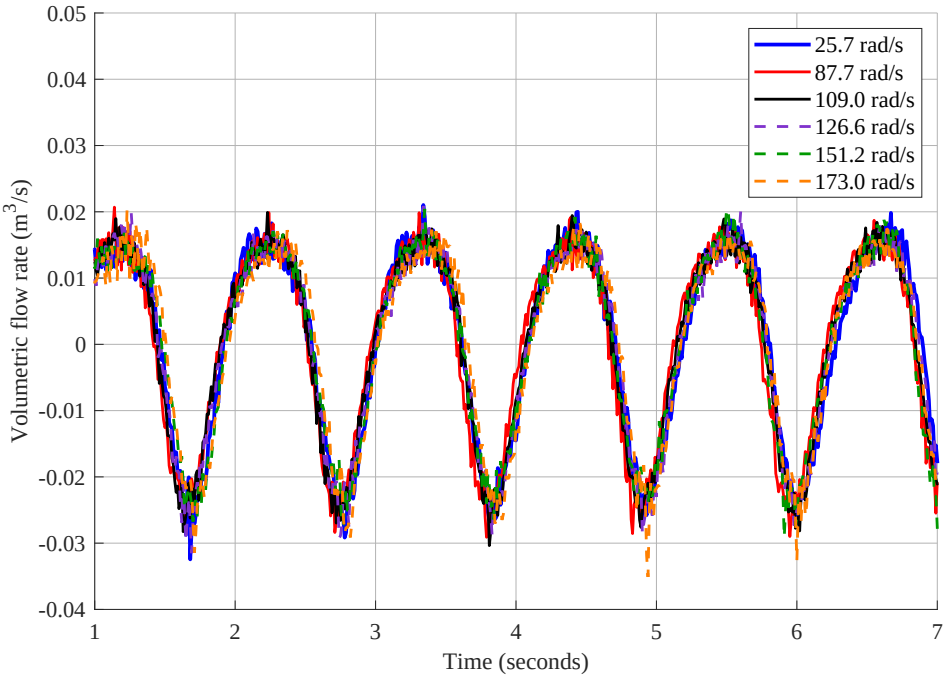


Figure 7.2: Comparison of volumetric flow rates for a 0.85 Hz wave with a 30 mm wave height. As with the pressure, shown in Fig. 7.3 it can be seen that the turbine speed has almost no effect on the behaviour of the volumetric flow rate inside the OWC chamber.

As can be seen in Figs. 7.2 and 7.3, both volumetric flow rate and moonpool pressure, are not zero mean. This is likely due to the wave maker itself, and indeed, at both DkIT and Lir NOTF wave peaks were consistently slightly higher than wave troughs. Another factor affecting the asymmetric oscillations could also be the hysteretic effects of the Wells turbine itself. A number of papers considering oscillating flow across Wells turbines have found that the flow behaves slightly differently for the inhalation and exhalation halves of the cycle [263]. However, as Figs. 7.2 and 7.3 show, the effect that the turbine speed has on the air flow in the chamber is minimal, suggesting that the asymmetry in the oscillations is likely dominated by the effects of the wavemaker and wave flume itself. To approximate an average value of pressure and of volumetric flow rate, to use in equations (4.26) and (4.27), the RMS of the steady state oscillation is found. RMS is commonly used for finding the equivalent magnitude of an oscillating signal, and is also the method used for generating dimensionless curves in [252]. Like in [252], the RMS values for the parameters of current, rotational velocity, pressure, and volumetric flow rate are calculated over a number of windows across the 60 s test period that each wave condition is run for, though in this case the windows are chosen at 5 s,

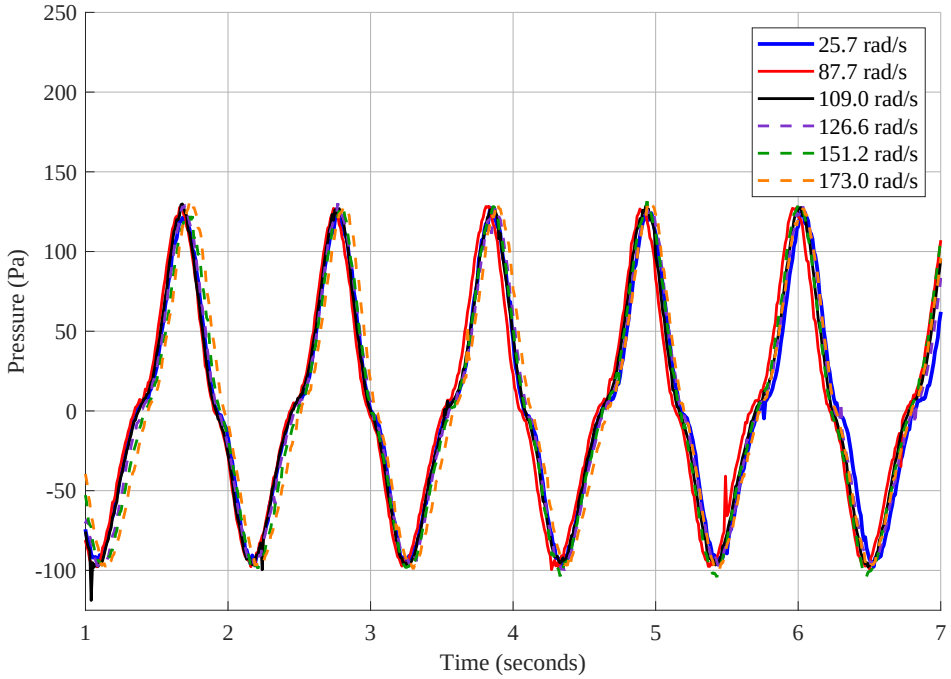


Figure 7.3: Comparison of moonpool pressures for a 0.85 Hz wave with a 30 mm wave height. Again it can be seen that the turbine speed has almost no effect on the behaviour of the pressure inside the OWC chamber.

due to the higher frequency of oscillations used, when compared with [252]. To avoid any transient behaviour, the last 30s of each test have been used, giving six windows for each wave condition.

Using RMS measurements of these parameters, the dimensionless characteristics given in (4.26), (4.27) and (4.28) can be calculated, describing the nondimensional pressure, volumetric flow rate and power respectively. Plotting the dimensionless parameters for the tests considered at DkIT, and grouping the results by wave height (and thereby, by the range of Re_{vent} values), shows three distinct patterns in the results, as shown in Fig. 7.4. The equivalent ranges for Re_{vent} for each wave height are: 5,400-6,000, 6,100-6,520, 7,000-7,800 for wave heights of 25 mm, 30 mm and 40 mm respectively. The mean values for Re_{vent} for each wave height are: 5,850, 6,350, and 7,470 for wave heights of 25 mm, 30 mm and 40 mm respectively, showing a noticeable grouping in values of Re_{vent} between wave heights.

From Fig. 7.4, it can be seen that, for larger wave heights, with greater airflows, a higher peak efficiency point is reached, with the smallest wave height tested only reaching a pneumatic power to turbine power efficiency of 0.3%, while the largest wave height produces a peak efficiency of almost 1.5%. These efficiencies are considerably lower than would be expected for a Wells turbine operating in higher Reynolds number flows, with even the relatively low Reynolds number flow test case in [252] achieving a

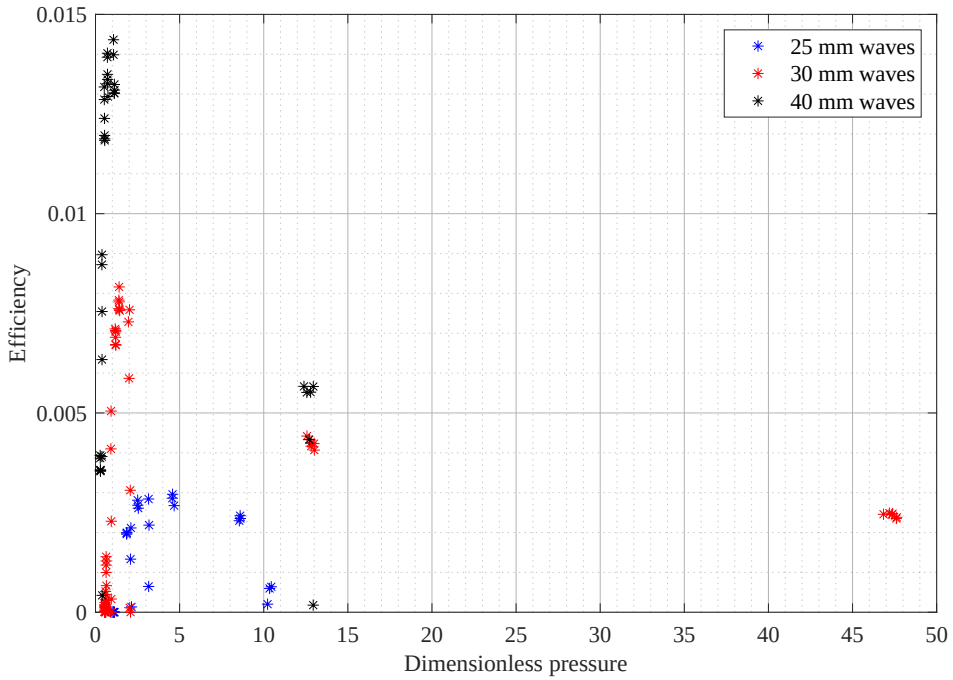


Figure 7.4: The dimensionless characteristic curves resulting, when grouping experimental results by wave height. As the wave height is reduced, lower pneumatic to turbine power efficiency peaks are reached, with 25 mm waves reaching a peak efficiency almost 5 times lower than for 40 mm waves.

conversion efficiency of approximately 25%. However, what the curve in Fig. 7.4 does show, is that there is a point at which the efficiency of the turbine drops significantly, which indicates that the turbine has a stall point within the range of the test conditions investigated at DkIT. In fact, the stall point, for both the 40 mm and 30 mm wave heights, appears to be in a similar position for both, each with an efficiency peak around a dimensionless pressure of 1, with the 40 mm wave height having a slightly earlier stall point than the 30 mm, and the 40 mm efficiency curve also appearing to drop more sharply after stall. The curve for the 25 mm wave height case has a more rounded shape, with a peak at a dimensionless pressure of approximately 4.5.

The relationship between dimensionless pressure and volumetric flow rate is also plotted in Fig. 7.5, showing that the relationship between these two parameters follows the behaviour generally expected of a Wells turbine. Fig. 7.5 shows a close to linear relationship between the dimensionless pressure and volumetric flow rate, except at low volumetric flow rates, where this linear relationship breaks down. What is different in the relationship, when compared to the dimensionless pressure and volumetric flow rate curves in the literature, is that these curves are again dependent on the wave height.

The fact that the turbine demonstrates that there is a peak efficiency point, for all three of the wave heights tested, indicates that the designed turbine does not solely operate in the stall region under the test conditions experienced at DkIT, which are

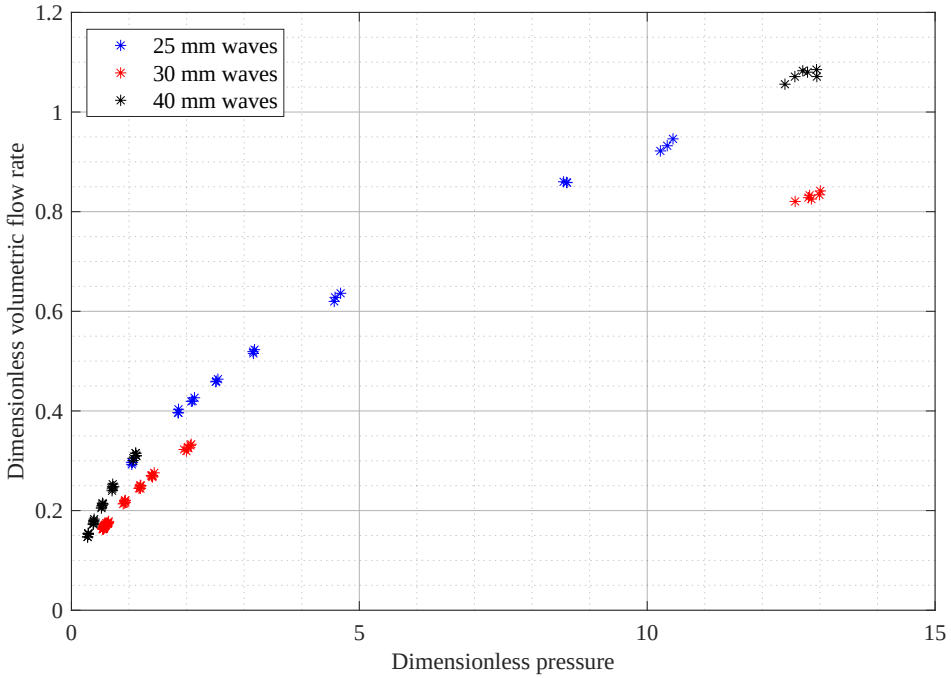


Figure 7.5: Showing the relationship between the dimensionless pressure and volumetric flow rate. As expected for a Wells turbine, the relationship appears to be mostly linear, though as dimensionless volumetric flow rate drops a change in the linear relationship can be noted.

all at low Reynolds number flows, similar in magnitude to those expected when testing the full size floating OWC at Lir NOTF. However, the fact that the point of maximum efficiency changes depending on the Reynolds number of the flow means that the usual approach for determining the set point for the control system cannot be used, as discussed in Section 7.2.

7.2 Design and control of the turbine load

Control of OWCs is normally a set point tracking problem, where the turbine speed is altered to keep the turbine operating at its maximum efficiency point [213]:

$$\Omega_{mep} = \sqrt{\frac{|\Delta p|}{\rho_{air} D_{turb}^2 \Psi_{mep}}}. \tag{7.10}$$

Equation (7.10) is simply (4.26) rearranged, where the dimensionless pressure corresponding to the maximum efficiency point Ψ_{mep}, can normally be included as a constant value, with changes in pressure drop across the turbine changing the maximum efficiency point rotational speed Ω_{mep}. However, since the maximum efficiency point varies with Reynolds number at low flow rates, as demonstrated in Fig. 7.4, full knowledge of the efficiency curves across all of the test conditions at Lir NOTF would be required

to know where the maximum efficiency point of operation is. This would effectively require producing a characteristic efficiency curve in three dimensions, with Reynolds number being the third axis. Furthermore, a measure of the Reynolds number of the flow would then be required to know where the maximum efficiency point is during operation, which would require real-time measurements of the airflow through the orifice. This is to say that attempting to follow the usual approach given in the literature for finding the set point for the controller is insuperable for the tests of the full scale buoy at Lir NOTF. Instead, set point tracking is still used for the tests of the floating OWC at Lir NOTF, but the maximum efficiency setpoint is instead swapped for the point of maximum power production. To find the speed at which maximum power is produced by the generator, each regular wave test condition at Lir NOTF is run twice, the first time for 5 minutes, during which the turbine set point is manually adjusted, sweeping through a range of potential speeds, until the speed corresponding to the highest power is found. This set point is recorded for later runs, where the test is repeated with the set point tracking set to the speed at which maximum power was found for the duration of the test.
To keep the turbine spinning at the set point, a controller is required. For the tests discussed in Section 7.1.1, the circuit shown in Fig. 6.9 is used, where turbine speed is controlled by a simple resistor or potentiometer connected across the generator. A range of resistances is selected to cover a range of turbine speeds from 10 to 180 rad/s in tests at DkIT. However, a primary goal of this project is to use a controller on a real turbine PTO to assess the free surface estimator ability to operate when a working control system is affecting the PTO. In order to control the turbine speed an electronic load is designed, following the method in [264], and adjusted for the needs of this project, namely the use of logic level components for the op-amp and MOSFET to account for the low currents expected from the generator. This results in the circuit shown in Fig. 7.6.

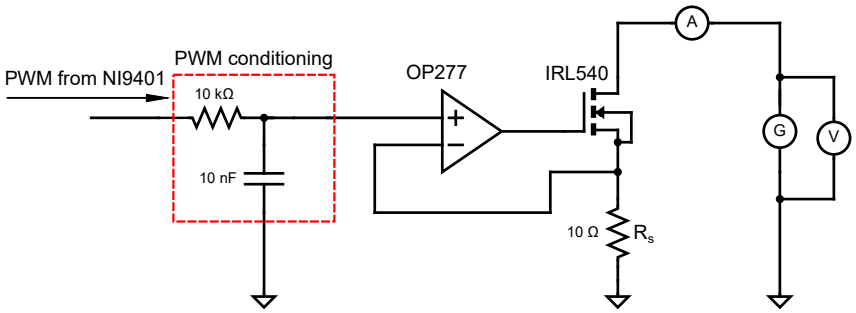


Figure 7.6: Showing design of electronic load which can be varied by the PWM output from the NI9401. Note that the functions of ammeter and voltmeter are performed by the NI9219. The PWM conditioning was found not to be required, and dropped in later experiments.

The op-amp based electronic load in Fig. 7.6 is simple in its operation. By changing the voltage sent to the positive port of the op-amp by the controller, the load changes accordingly. The equivalent resistance R_{eq} resulting from changes in the voltage sent by the controller is given by:

$$R_{eq} = \frac{V_{gen}}{I_D}, \tag{7.11}$$

where V_{gen} is the generator voltage, and I_D is the drain current of the MOSFET, determined by:

$$I_D = \frac{V_c}{R_s}, \tag{7.12}$$

where V_c is the controller output voltage and R_s is the resistance of the resistor connecting the MOSFET source to ground.

Due to the limitations of the voltage output module available to this project, the NI9401, the only voltage output signal that could be sent by the CompactRIO controller is a pulse-width modulation (PWM) pulse with a peak voltage of 5V. The CompactRio can vary the duty cycle of the PWM voltage output, which is then smoothed out by a simple RC filter, as shown in Fig. 7.6. The filter to smooth out the 20kHz PWM input signal from the NI9401 is determined by:

$$RC = \frac{1}{2\pi\omega_c}, \tag{7.13}$$

where ω_c is the cut-off frequency (set to 1.6 kHz). However, after some tests using the PWM conditioning, it was found to be superfluous, since the dynamics of the generator are orders of magnitude slower than the 20kHz PWM signal sent by the CompactRio, and keeping the circuit to the fewest number of components reduces the chance of faults that could hinder testing.

To test that changing the PWM duty cycle of the controller output effectively changes the turbine speed, a test is carried out for a 30 mm 0.85 Hz regular wave, using the fixed OWC at DkIT, where the duty cycle is incrementally increased, and the rotational speed and power recorded. The results of this test are shown in Figs. 7.7 and 7.8, showing that a peak power point exists when the PWM output is approximately 15% of the duty cycle when the turbine is spinning at approximately 100 rad/s.

For set point tracking control in OWCs, two main methods are identified in [213] as PID or sliding mode control. For full wave to wire modelling of OWCs, [213] suggests that sliding mode control is the better choice, as it is a nonlinear controller that can handle the nonlinear system dynamics of an OWC. However, for simpler cases, such as in this thesis where only the generator dynamics are being considered, satisfactory performance can be achieved simply using PID control. Since the CompactRIO is

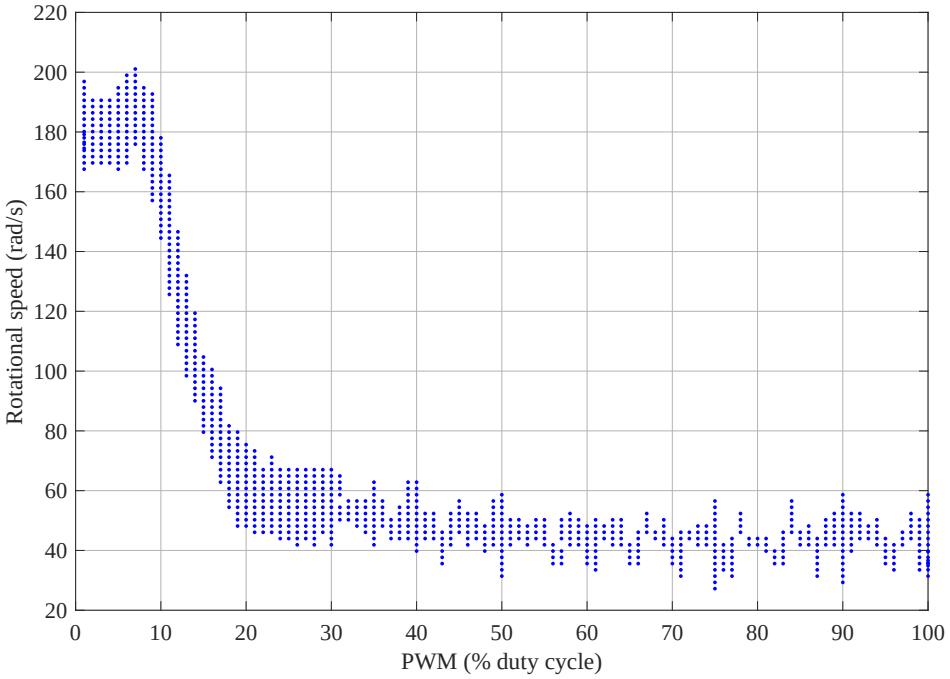


Figure 7.7: Showing the effects of PWM duty cycle on the rotational speed of the generator under steady state waves with a wave height of 0.03 m and frequency of 0.85 Hz. Increasing the duty cycle increases the current drawn, in turn reducing the rotational speed of the turbine.

already being used to acquire real-time measurements of turbine speed, via the encoder on the motor, building a simple set point tracking PI controller in LabVIEW is trivial. To identify a transfer function that describes the generator behaviour, a step test was carried out, using the experimental set up at DkIT. However, instead of sending any waves to excite the turbine, a simple step voltage of 1V is applied to the generator causing it to spin. By recording the generator speed, the time constant of the system can be determined, and a simple transfer function for the generator is identified:

$$G(s) = \frac{\Omega_{step}}{(s/\tau + 1)} \tag{7.14}$$

where Ω_{step} is the rotational speed reached based on a 1V step input, in this case 30 rad/s, and τ is the time constant, also measured from the step response as 1.9 s. The identified transfer function is then also excited using a step input, and the time domain behaviour compared to the experimental results, as shown in Fig. 7.9.

The identified transfer function suggests that the generator is a first-order system with no inherent instability. Through experimental tuning, it was found that a purely proportional controller, with a gain of 4.5, worked well for all of the wave conditions tested at DkIT. However, PI control was found to be more reliable for the range of test conditions at Lir NOTF, with a proportional gain of 0.75 and associated integral gain of 1.5 used in all tests.

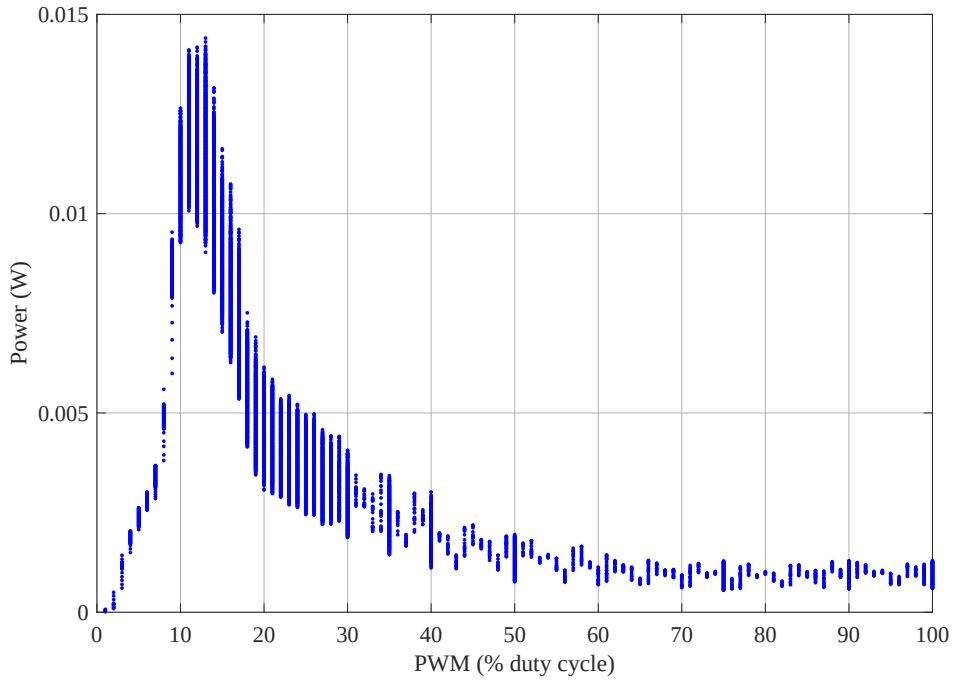


Figure 7.8: Showing the effects of PWM duty cycle on the power captured by the generator for the same waves used in Fig. 7.7. As the generator speed drops, voltage also drops, meaning at slow rotations little power is generated, despite drawing higher current.

During tests on the full floating OWC at Cork, the PI controller is found to be effective at holding the turbine speed at the user determined set point. Fig. 7.10 shows a regular wave test where the set point is set to be 265 rad/s, determined as the speed corresponding to maximum power capture for a 0.725 Hz wave with a wave height of 150 mm. Also included in Fig. 7.10 is the variation in PWM duty cycle, which shows the control action keeping the turbine spinning at the set point of 265 rad/s. For reference, the power generated is also included in Fig. 7.10.
For irregular waves, the turbine spins only when enough pressure has built up in the chamber. The turbine also spins considerably slower due to the generally reduced height of the incident waves. For Bretschneider waves, with a modal frequency of 0.775 Hz, and significant wave height of 100 mm, a set point of 25 rad/s is used, to ensure some control action is required, since the fastest free spin speed observed for this wave condition is around 70 rad/s. Fig. 7.11, shows that the control action is quick to increase the duty cycle, to bring the speed down to the set point, when the turbine begins spinning, and drops again when the turbine slows down again.

7.3 Modelling turbines as equivalent orifice

Using orifice plates to simulate turbines in scale tests, where using a real turbine is impractical, is widespread in the literature, as discussed in Section 4.2.3. In theory,

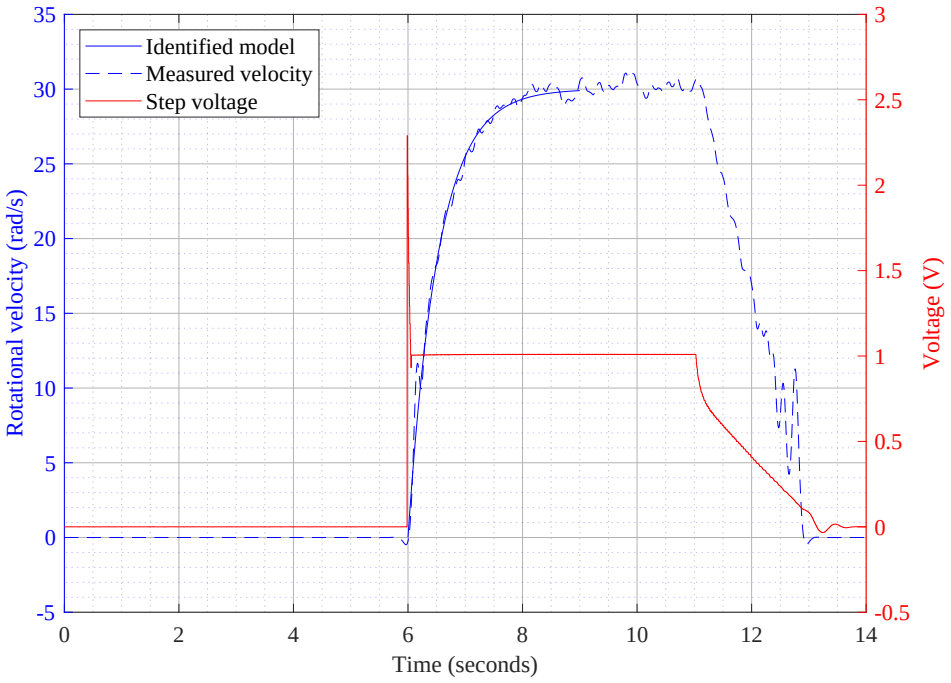


Figure 7.9: Showing comparison of the step responses of the experimental system and the identified transfer function describing the system. The response shown is used to determine the time constant and the rotational speed reached when the system is excited with a 1V step input.

different turbine diameters represent different levels of damping caused by changes in rotational speed. However, as demonstrated in Figs. 7.2 and 7.3, at the turbine speeds and OWC dimensions considered in this thesis, the effects of the turbine speed on the pressure and volumetric flow rate inside the chamber are negligible, as qualified in [160]. This is an interesting phenomenon, which essentially means that the turbine designed and tested in this chapter, functions as an orifice of fixed diameter. This means that the experimental procedure to determine the coefficient of discharge for an orifice plate, described in Section 7.3.1, can also be applied to the turbine, as described in Section 7.3.2.

7.3.1 Experimental determination of coefficient of discharge for orifice plate

Since coefficient of discharge is an essential parameter for modelling the system dynamics of the floating OWC with an orifice plate, a set of experiments is carried out at the DkIT wave flume (18 m $\times$ 0.35 m $\times$ 1 m deep) to determine the value of the coefficient of discharge C_d for the 25 mm orifice, following the approach in [248].
This experimental setup again uses the fixed OWC described in Section 6.3. Low frequency waves, from 0.4 Hz to 0.7 Hz, with an amplitude of 30 mm, are then used to generate a series of measurements, where the free surface inside the chamber

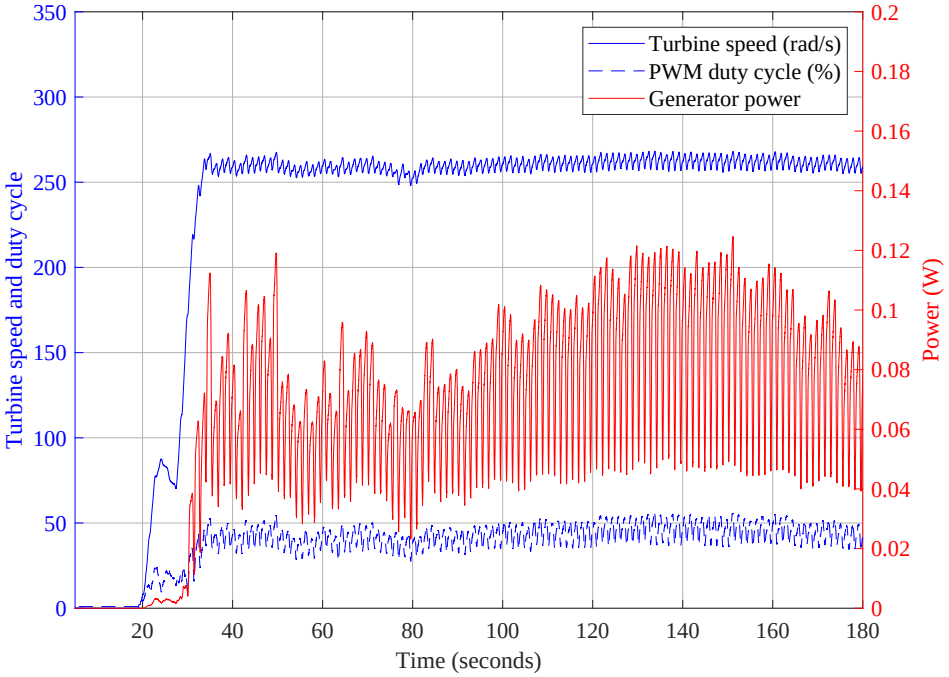


Figure 7.10: Showing the set point tracking controller in a regular wave with a frequency of 0.725 Hz wave and a wave height of 150 mm. A set point speed of 265 rad/s is set to correspond with the maximum power point for this wave condition.

remains close to parallel with the orifice plate, allowing the volumetric flow rate q through the orifice to be calculated using:

$$q = A_{owc}\dot{\eta}_{owc}, \tag{7.15}$$

where A_{owc} is the cross-sectional area of the OWC chamber and $\dot{\eta}_{owc}$ is the differentiated signal of the free surface elevation within the chamber, measured via the wave probe. The orifice equation, given by (4.19), then allows the resultant values to be plotted against the theoretical volumetric flow rate q_t to determine C_d:

$$q_t = \frac{A_{ori}\sqrt{2\rho_{air}\Delta p}}{\rho_{air}}, \tag{7.16}$$

where A_{ori} is the orifice area, ρ_{air} the density of the air within the chamber, and Δp is the difference between the pressure within the chamber and the atmospheric pressure outside the chamber.

The gradient of the resultant plot, shown in Fig. 7.12, gives an experimental value for C_d. The obtained values are slightly higher than the benchmark of approximately 0.6 expected of a sharp-edged orifice. All sensors were calibrated, and the tests repeated to eliminate the possibility of errors in the sensors, confirming the value of $C_d = 0.71$ for the 25 mm orifice.

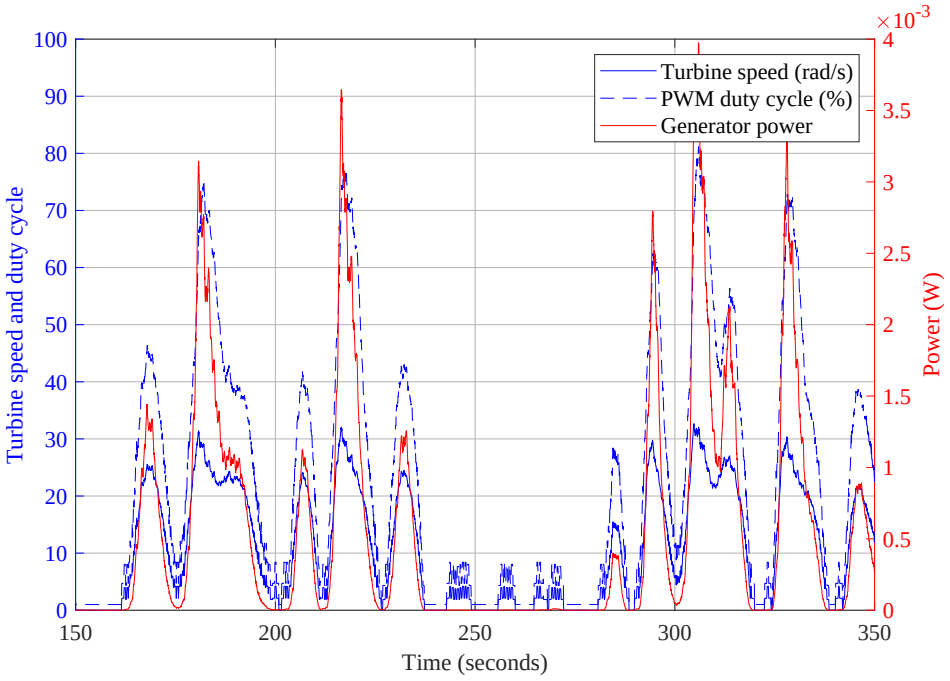


Figure 7.11: Showing the set point tracking controller in irregular Bretschneider waves with a modal frequency of 0.775 Hz, and significant wave height of 100 mm. The set point is determined to be at 25 rad/s, to ensure some control action is generated, since this irregular wave condition produces a maximum free spin velocity of only around 70 rad/s.

7.3.2 Real turbine modelled as equivalent orifice

A similar process can also be applied to characterise the behaviour of the turbine designed in this chapter as an equivalent orifice. Since most of the tests used in earlier sections of this chapter also measured pressure and volumetric flow rate, a wealth of test results is available to determine q, and q_t, for the turbine.

Since volumetric flow rate is calculated from measurements of the water surface within the chamber, results using waves with a frequency close to the chamber resonance frequency of 0.8 Hz have to be omitted from any calculations using volumetric flow rate, because the water surface at resonance does not remain flat. The water surface remaining close to flat within the OWC chamber is a requirement for assuming a correlation between the free surface measurements recorded on the wave probe in the chamber and the volumetric flow rate exists. Despite tests using waves of 0.8 Hz needing to be omitted from calculations for the coefficient of discharge for the turbine, a large set of data could be used, covering a range of waves from 0.55 Hz to 0.95 Hz, with wave heights of 25 mm, 30 mm and 40 mm. From this data, q is plotted against q_t, as shown in Fig. 7.13. Unlike the graph obtained for determining the coefficient of discharge in Fig. 7.12, where the orifice diameter is 25 mm, the graph in Fig. 7.13 has the caveat that the area of the equivalent orifice used to model the turbine must be estimated instead. The

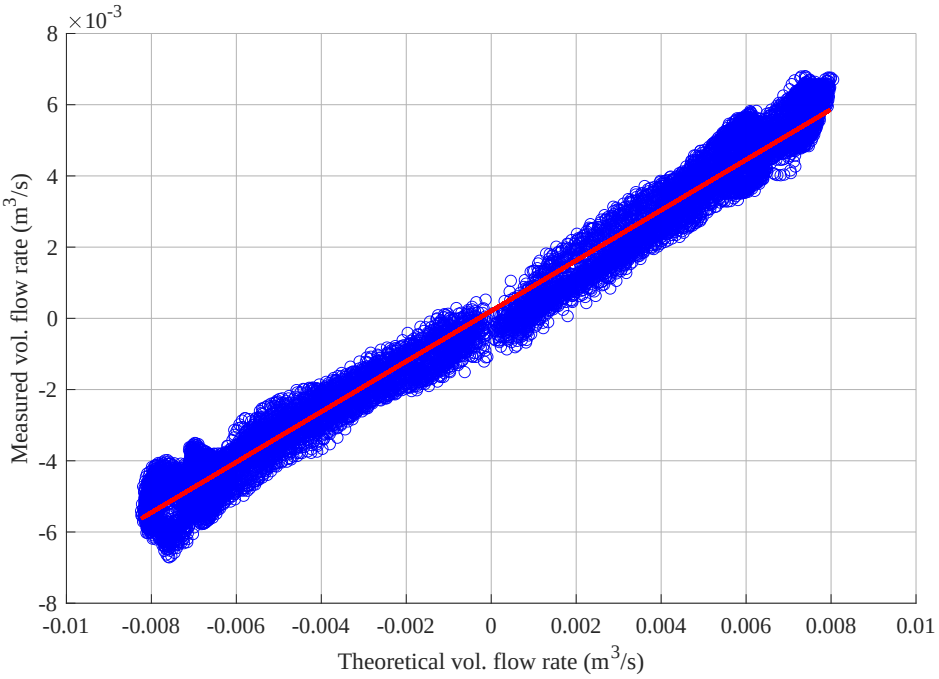


Figure 7.12: Determination of C_d for the 25 mm orifice from experimental results, plotting the measured volumetric flow rate, against the theoretical volumetric flow rate.

choice of effective orifice diameter changes the coefficient of discharge obtained by the straight line in Fig. 7.13, as there is a direct inverse proportionality between the two. Though the orifice equation (4.19) multiplies the terms A_{ori} and C_d, meaning that the product of the two terms remains the same regardless of the choice of orifice area, the orifice area term does appear separately from C_d in (4.24), meaning that the selection of A_{owc} will affect the overall hydrodynamics of the system.

To determine the value of A_{owc}, the graph in Fig. 7.13 is used to obtain the product of A_{owc} and C_d, which is a constant value of 0.0011. From this constant, limits on the potential orifice area can be determined.

The highest that C_d can be is 1, meaning that the smallest possible orifice area is 0.0011 m^2, corresponding to a diameter of 37.4 mm. Conversely, the largest diameter of orifice that makes physical sense for the turbine is the 83 mm diameter of the central section of the Venturi, which gives an orifice area of 0.0054 m^2 and a corresponding value for C_d of 0.203.

To test the sensitivity of the hydrodynamic model to the chosen value of A_{ori}, the model described by (4.24) is run for a regular wave, and the resultant buoy heave displacement compared to the measured heave data obtained for the same wave at Lir NOTF. A series of A_{owc} and C_d values is simulated and the values producing the closest match between the measured heave displacement of the buoy and simulated heave displacement are used for the system model used by the estimator. This process is fully discussed under the hydrodynamic model validation in Section 8.2.3.2.

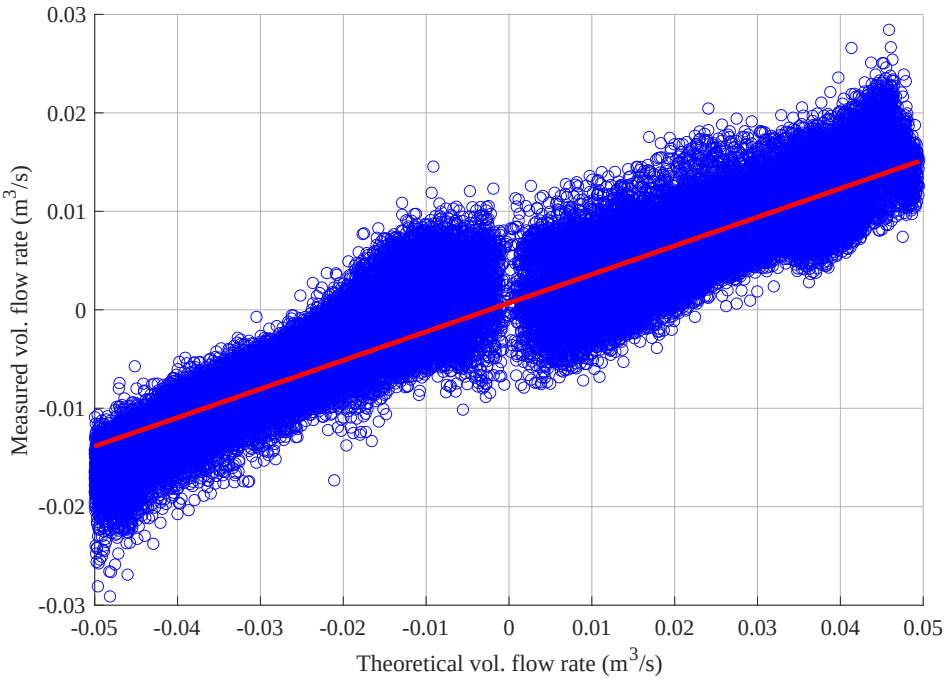


Figure 7.13: Determination of C_d for a turbine modelled as an equivalent orifice from experimental results, plotting measured volumetric flow rate, against the theoretical volumetric flow rate calculated by orifice equation (7.16).

7.4 Chapter summary and conclusions

In this chapter, a Wells turbine is designed which not only self starts, but is shown to consistently reach full operational speed. The focus of the design is on following the guiding principles laid out in [193], with some adjustments made to account for the small size of the turbine and the low flow rates in which it is designed to operate. The main iterative part of the design process is in the choice of aerofoil profile, and future work could look at iterative changes in some of the other design parameters, such as sensitivity to aspect ratio, or tip clearance.

The turbine maximum efficiency point is sensitive to the wave height, which poses a problem when choosing a maximum efficiency set point in the controller. To allow a set point to be determined for the controller, the maximum power point speed is instead experimentally determined for the regular wave test conditions at Lir NOTF, and recorded. Tests are then repeated with the tracking controller set point matching the speed of maximum power. The controller is a simple PI tracking controller and is shown to operate effectively in reaching a chosen set point, using real-time measurements of the turbine speed, and adjusting the load on the generator accordingly; changing the PWM duty cycle output from the NI9401 module, which is attached to an op-amp based electronic load. Through experiments on the fixed OWC at DkIT, it can be shown that the speed of the turbine has a negligible effect on the pressure and volumetric flow rate within the

moonpool chamber. A serendipitous effect of this independence between turbine speed and the pressure and volumetric flow rate, is that the turbine can be modelled as an equivalent orifice, allowing the nonlinear system description given in (4.24) to be used to describe the floating OWC with a working turbine PTO. It also suggests that, since the controller only affects the turbine speed, the effects of the controller can likely also be omitted from the system description in the free surface elevation estimator. The validation of models describing the floating OWC, using a fully sealed moonpool, the 25 mm orifice plate, and the real turbine, are given in Chapter 8, alongside the determination of a suitable equivalent orifice diameter to describe the turbine.

8

Design of a free surface elevation estimator as a sensor for data buoys

Contents

8.1 Choice of unknown input estimation technique 168
8.1.1 Kalman filter with random walk 170
8.1.2 Extended Kalman filter with random walk 171
8.2 Validation of estimator hydrodynamic models 171
8.2.1 Fully sealed moonpool 173
8.2.2 Fitted with orifice plates 175
8.2.3 Fitted with a controlled Wells turbine PTO 175
8.3 Chapter summary 182

The general assumption that data buoys measuring wave parameters should be true wave followers presents a perceived hurdle to the adoption of wave energy PTOs as a power source for sensing buoys. As discussed in Section 2.1.4.1, the majority of wave energy PTOs necessarily interact with passing waves, meaning that most wave powered data buoys cannot be wave followers. The notable exception is with TENGs, where a number of designs exist which have a negligible effect on device dynamics, allowing measurements of free surface elevation to be recovered [131]. TENGs represent only a fraction of wave energy research and, as shown in Chapter 2, there are many other PTO types which are being considered for use in wave powered data buoys.

In this chapter, a free surface elevation estimator is proposed to counter the argument that wave parameters can only be gathered by true wave followers. The free surface

elevation soft sensor, based on Kalman filter-based unknown input estimation techniques, described in this chapter, is designed to be used in conjunction with an existing motion sensor, such as an IMU, which takes into account the dynamics of an OWC based data buoy, as shown in Fig 8.1. .

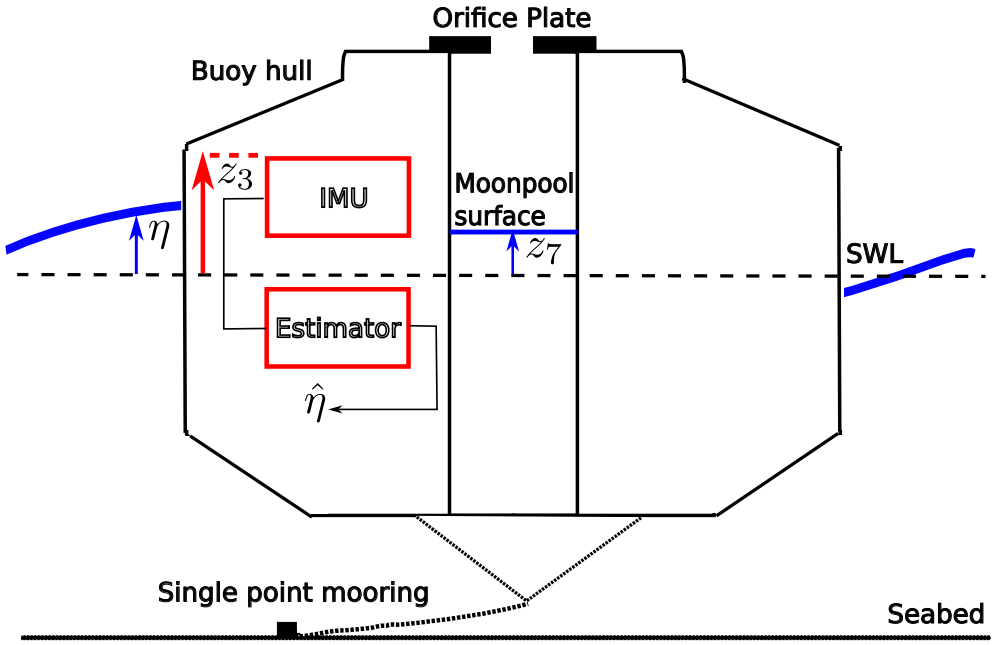


Figure 8.1: Schematic showing how an existing motion sensor feeds buoy heave measurements, z_3, to the estimator which estimates the external free surface elevation, $\hat{\eta}$, accounting for the effects of the piston mode of the OWC, z_7, on the device dynamics. The orifice plate represents the turbine PTO, a functioning version of which is also designed and tested as part of this project.

Additionally the proposed sensor is designed to have the capability to not only return values of wave characteristic parameters such as T_z and H_{mo}, that are most commonly returned by existing data buoys, but also time series estimates of the free surface elevation. The ability to measure free surface elevation data is essential for the development of large-scale (grid power level) WECs, in particular those fitted with energy maximising control. As previously mentioned in Chapter 2, many WEC controllers work on a wave-by-wave basis, tuning the device resonant frequency to match incident waves. Therefore, to validate such controllers, a means of measuring time series free surface elevation is necessary, often limiting such tests to wave tanks, where wave probes can measure the free surface elevation directly.

Although suitable for the majority of current data buoy end-users, using spectral data alone to define wave climates also has broader limitations. As demonstrated in [73],

using time series wave data gathered on the West Coast of Ireland, very different spectral shapes can have the same variance in spectral density and thus be described by the same values of H_{mo} and T_z. Furthermore, [73] shows that, where H_{mo} and T_z are used to describe wave climates which are in fact double peaked spectra, T_z can correlate with a frequency band with a low spectral density. Particularly, for WECs, such shortcomings can have severe implications at the design stage, where the device resonant frequency is often designed around the stated T_z of the location where it is to be deployed.

In [265], the dearth of recorded time-series free surface elevation data is discussed in detail, with [265] specifically addressing the issues that buoy tilt can cause for acceleration measurements in the time domain. Indeed, elsewhere in the literature, when time domain free surface elevation is addressed, it tends to relate to improving the time series accumulation of measurements used to calculate the stated statistical characteristic parameters of H_{mo} and T_z. A recent example is [266], which focusses on a number of gap filling methods, using both nonlinear data driven methods, and linear methods to impute time-domain data. Gaps filled by the approach in [266] are where anomalous or missing data is found, caused either through sensor failure, or where extreme waves cause the device to become submerged and deviate from its wave-following characteristics, resulting in underestimation of H_{mo}. The work in [266] considers a number of wave prediction methods as a foundation for the work, and indeed it is in wave prediction, rather than measurement, where Kalman filters are most often used in wave measurement applications. Examples, such as [267] or [268], use Kalman filters to predict wave elevation, but in both cases assume that free surface elevation is a directly measurable quantity. Kalman filters have also been used for significant wave height estimation on fixed platforms where the free surface elevation is not measured directly, such as in [269], where wind speed measurements are used to estimate the significant wave height of the surrounding sea state. However, the use of Kalman filters in estimating free surface elevation directly remains uncommon in the literature.

In the field of maritime shipping, however, there are a wealth of studies combining Kalman filters with IMU readings. Primarily based around estimating the heave motion of the vessel itself, particularly for offshore service vessels or subsea lifting operations, IMUs have been successfully used in conjunction with Kalman filters as part of the control system for onboard heave compensation systems [270] [271]. A recent study [272] broadens the application of the Kalman filter to estimate the geoid height of the vessel, in this case using the Kalman filter to facilitate sensor fusion between the onboard IMU and global navigation satellite systems data.

The advent of autonomous ships is also driving a demand for time series free surface elevation data. A number of papers have been published, similarly using Kalman filter-based unknown input estimators, to obtain not only free surface elevation, but also

directional wave spectra, from sensors located across a 70 m long vessel [273] [274] [275] [276]. Such an overlap of interests, between the maritime shipping and wave energy sectors, could build momentum in improving sensor technology for returning time-series free surface elevation, which has so far been a mostly niche requirement of the wave energy research community.

This chapter describes the choice of a Kalman filter with random walk (KFRW) as the basis for the free surface elevation estimator, and how this can be extended, to include the nonlinear dynamics of an OWC fitted with an orifice plate or a working turbine PTO, as an extended Kalman filter with random walk (EKFRW). Since the Kalman filter based estimators require an accurate model of the system for which they are designed, validation of the hydrodynamic models of the Gannet G1250, for the three test cases is also included in this chapter. The first of the three cases considers the Gannet G1240 with a fully sealed moonpool, which results in a linear system against which the KFRW can be tested. The second test case considers results from the Gannet G1250 when it is fitted with a 25 mm orifice plate. The introduction of an orifice requires a nonlinear system description, necessitating the use of the EKFRW. Finally, the third test case considers the Gannet G1250, fitted with a Venturi and a controlled turbine PTO. Since Chapter 7 shows that the turbine can be modelled as an orifice, the same EKFRW, used for the orifice plate test case, can again be used, with the model adjusted to account for differences between the two devices.

8.1 Choice of unknown input estimation technique

In wave energy control, unknown input estimators are a relatively well researched topic, since many WEC control strategies, such as model predictive control (MPC), require knowledge of the excitation force [277]. The wave excitation force, f_{ex}, represents the force acting on a body, due only to oncoming waves. For fixed bodies, f_{ex} can be measured by integrating the pressure from the wave over the submerged body surface. In addition, for a fixed body, a force sensor can be used to measure f_{ex} since, with zero velocity and displacement, the total hydrodynamic force on the device is f_{ex}. However, for a floating body, excitation force becomes an unmeasurable quantity, since other hydrodynamic forces, such as the velocity-dependent wave radiation force, also affect the pressure across the submerged body [278]. In [278], an in-depth comparison of eleven different excitation force estimators is presented, considering the normalised root mean square accuracy against a CFD benchmark, as well as the inherent delay and execution time for each estimator.

In this chapter, the same techniques studied for estimating excitation force are turned towards estimating free surface elevation in application as a wave sensor for a data

buoy. As established in Section 3.3.3, free surface elevation is related to excitation force via k_{ex}. A naïve approach to formulating a free surface elevation estimator would be to use an existing excitation force estimator and use the inverse excitation force transfer function to obtain values for free surface elevation. However, such an approach results in an open loop unstable system.
Instead, an approach is taken where the system is redefined with η as the input, with the unknown input estimator directly producing an estimated value for free surface elevation. Redefining a system, with η as the input rather than f_{ex}, requires the excitation force kernel to be rewritten as a state space approximation, with η as the input and f_{ex} as the output, as described in Section 3.3.3.
Though the excitation force estimators in [278], considered a variety of measured outputs, including η and pressure sensors, only those considering displacement are considered for this project. In [278], implementation issues using pressure measurements are found, and η cannot be considered as the measured output on a free surface estimator for obvious reasons. A shortlist of potential unknown input estimation techniques, which use the displacement of the device as the measured output, is drawn from those described in [278] as:

- Kalman filter with harmonic oscillator (KFHO)
- Kalman filter with random walk (KFRW)
- Unknown input observer (UIO)
- Receding horizon estimation (RHE)

Although the UIO and RHE approaches have their merits, particularly around obviating the need for a hydrodynamic model, and the UIO's robustness against model uncertainties, the ease with which Kalman filters can be extended to the nonlinear case ultimately narrows the decision to being between the KFRW and KFHO.
In a KFHO, the unknown input is modelled as a harmonic oscillator, made up of a number of harmonic components, whereas a KFRW models the input as a white noise driven integrator. An in-depth comparison between using a harmonic oscillator and a random walk as the choice of perturbation model for an unknown input estimator is given in [279]. Although the most widely used in the literature, [279] clearly demonstrates the issues with using a harmonic oscillator, finding it to be susceptible to spectral amplification, particularly in noisy real sea conditions. The dependency of the harmonic oscillator on prior knowledge of the frequencies of the harmonic components is also demonstrated. Obtaining information on input frequency components can, in theory, be achieved using measurements from wave buoys, but this same approach for a free

surface elevation sensor would create a circular problem where a wave buoy relies on knowledge of wave measurements to produce wave measurements. Conversely, a random walk, where no prior information about the wave frequencies is required, presents itself as the natural choice of perturbation model for the Kalman filter, especially when coupled with its resilience to noise and complexity, identified in [279]. The KFRW approach used in the linear case is extended to the nonlinear case as an extended Kalman filter with random walk (EKFRW).

8.1.1 Kalman filter with random walk

A random walk can be described, in discrete time, by (8.1):

$$\eta^{\mathrm{KFRW}}(k+1) = \eta^{\mathrm{KFRW}}(k) + \zeta_\eta(k), \tag{8.1}$$

where η^{KFRW} is the estimate for the free surface elevation, and $\zeta_\eta(k)$ is a random number, independently and identically distributed in size, which moves the estimate of η^{KFRW} a random step away from its previous value. An augmented version of the model can be described as:

$$\begin{aligned} \tilde{X}_\mathrm{a}(k+1) &= A_\mathrm{a}^\mathrm{d}\tilde{X}_\mathrm{a}(k) + \epsilon(k), \\ \tilde{Y}(k) &= C_\mathrm{a}\tilde{X}_\mathrm{a}(k) + \mu(k), \end{aligned} \tag{8.2}$$

where ϵ is the process white noise, with covariance matrix Q, and μ is the measurement white noise, with covariance matrix R. The tilde denotes estimated states.
The augmented matrices for the KFRW are described by (8.3), with the superscript d denoting that the matrices, described in (3.53), have been discretised using the zero-order hold method. The matrix C is set so that only the entry corresponding to the heave displacement of the buoy, z_3, is set to 1, setting the measured output $\tilde{Y} = z_3$. X refers to the states in the linear model described in (3.53):

$$X_\mathrm{a} = \begin{bmatrix} X \\ \eta^{\mathrm{KFRW}} \end{bmatrix}, \quad A_\mathrm{a}^\mathrm{d} = \begin{bmatrix} A^\mathrm{d} & B^\mathrm{d} \\ 0 & 1 \end{bmatrix}, \quad C_\mathrm{a} = \begin{bmatrix} C \\ 0 \end{bmatrix}^T, \tag{8.3}$$

The *a priori* time update estimates, $\tilde{x}_\mathrm{a}^-$ and P^-, can be calculated as:

$$\begin{aligned} \tilde{x}_\mathrm{a}^-(k) &= A_\mathrm{a}^\mathrm{d}\tilde{x}_\mathrm{a}(k-1), \\ P^-(k) &= A_\mathrm{a}^\mathrm{d}P(k-1)A_\mathrm{a}^{\mathrm{d}T} + Q, \end{aligned} \tag{8.4}$$

with the *a posteriori* measurement update estimates calculated as:

$$\begin{aligned} K(k) &= P^-(k)C_\mathrm{a}^T\left(C_\mathrm{a}P^-(k)C_\mathrm{a}^T + R\right)^{-1}, \\ P(k) &= \left(\mathbf{I} - K(k)C_\mathrm{a}\right)P^-(k), \\ \tilde{x}_\mathrm{a}(k) &= \tilde{x}_\mathrm{a}^-(k) + K(k)\left(Y(k) - C_\mathrm{a}\tilde{x}_\mathrm{a}^-(k)\right), \end{aligned} \tag{8.5}$$

where I is an identity matrix equal in size to A_a^d.

8.1.2 Extended Kalman filter with random walk

To enable the estimator to handle the nonlinearities introduced by the introduction of an orifice plate or turbine, some changes are required. Similar to equation (8.3), though in continuous rather than discrete time, the augmented matrices are set up as described in (8.6).

$$\tilde{x}_{\mathrm{a}} = \begin{bmatrix} \tilde{X}_{nl} \\ \tilde{\eta}^{\mathrm{KFRW}} \end{bmatrix}, \quad A_{\mathrm{a}} = \begin{bmatrix} A_{nl} & B_{nl1} \\ 0 & 1 \end{bmatrix}, \quad C_{\mathrm{a}} = \begin{bmatrix} C \\ 0 \end{bmatrix}^{T}, \tag{8.6}$$

where matrices A_{nl} and C_{nl} refer to those described in (4.24), and B_{nl1} refers to the first column of the B_{nl} matrix. This is to separate the estimated input (free surface elevation) from the other input in the nonlinear case (the calculated mass flow rate through the orifice). To include the effects of $\dot{m}$, the second column of the B_{nl} matrix, B_{nl2}, is included in the model used by the estimator. X_{nl} refers to the states relating to the nonlinear model in (4.24). The *a priori* time update estimates thus become:

$$\begin{aligned} \dot{\tilde{x}}_{\mathrm{a}}^{-}(t) &= A_{\mathrm{a}}\tilde{x}_{\mathrm{a}}(t) + B_{nl2}\dot{m}(t), \\ \dot{P}^{-}(t) &= A_{\mathrm{a}}P(t)A_{\mathrm{a}} + Q. \end{aligned} \tag{8.7}$$

A continuous-discrete approach is used for the extended Kalman filter, which, as described in [278], only differs from the Kalman filter in its calculation of the time update estimates. The Runge-Kutta method is used to calculate the solution for (8.7) across the discretisation period, for each individual time step. Using only the final solution of the resultant ordinary differential equation for each timestep, a discretised local linearisation of the nonlinear model is achieved. This allows for a discrete measurement update, as given in equation (8.5), to still be used with the EKFRW. The measurement update is a key element of the Kalman filter, since it closes the loop on the estimation. In an open loop estimator, drift in accuracy, due to modelling errors, would be expected over time, since an accumulation of small errors at each timestep would become significant over time. However, in a Kalman Filter the inclusion of a measurement update to continuously correct the estimate based on measured information ensures that the estimator is robust against errors accrued over time.

8.2 Validation of estimator hydrodynamic models

A key part of designing a Kalman filter-based estimator is to have an accurate model of the system. As shown in Section 8.1, the state space matrices of the hydrodynamic models in (3.53) and (4.24), are an integral part of both the KFRW and the EKFRW designed in this chapter. There are three test cases for the free surface elevation estimator considered

in this project: a floating OWC with a fully sealed moonpool, with an orifice plate, and an OWC fitted with a Venturi housing a working turbine PTO (as described in Section 6.1). Validation of the hydrodynamic models for the three test cases is carried out by setting the wave probe measurements for free surface elevation as the input to the hydrodynamic model and comparing the resultant model output with the Qualisys data for the heave displacement of the buoy. Since the wave probe data is measured between the buoy and the wavemaker, cross-correlation between the Qualisys heave data and the model output (which is also affected by the causalisation delay, described in Section 3.3.3) is used to align the two signals.

For all three test cases, a Cummins' equation based approach is used, as set out in Chapter 3. This simplicity does come with a number of caveats which must be noted, pertaining to the linear potential flow theory assumptions required for using Cummins' equation. It must be assumed that the fluid is incompressible; in the case of the OWC this assumption need only apply to the water upon which the body is floating and, as shown in Section 4.2.2, air compressibility effects can still be accounted for. The water particles are assumed to be irrotational, thereby implying the water is also inviscid. Finally, the device motion must be small compared to its dimension, and the wave amplitude small with respect to the wavelength.

For the three test cases, only those DoFs acting in the heave direction are considered: namely the heave motion of the buoy itself, and the first heave mode of the massless disc representing the water column inside the chamber, also known as the piston or pumping mode, which are the main power generating DoFs of a floating OWC.

Considering only the buoy motion acting in the heave direction is a limitation of this study. As Section 4.2.2 shows, the inclusion of DoFs 3 and 7 produces a complex state space model, which imparts significant computational cost to the estimator. Adding further DoFs to the dynamic model used by the estimator is unfortunately not practical with a nonlinear system such as an OWC. An initial assumption is made that heave is the DoF most closely correlated with the free surface in the tests considered. To assess the validity of this assumption, forward selection is used to determine which DoFs are most affected by the free surface elevation. This procedure follows the same process as set out in Section 5.2.2, again using a generalized linear model to relate the free surface elevation to a matrix of 3 input DoFs, with a chi-squared test again used as the fitting criterion for the 10-fold cross-validation. The three input DoFs considered are heave, pitch, and surge. Irregular wave tests show that the correlation between the DoFs considered and the free surface is relatively low, with heave selected at the 60th percentile of the chi-squared fit, and the remaining two DoFs only added when the chi-squared fit drops beneath the 10th percentile. This shows that the correlation between heave and free surface elevation for the tests considered in this paper is significantly higher than either pitch or surge, suggesting that the addition of more DoFs would not significantly improve the performance of the estimator.

8.2.1 Fully sealed moonpool

For the sealed moonpool case, the model output is initially found to be underdamped, when compared to the measured output. This could be due to a number of factors, since the linear model ignores the effects of air compressibility in the chamber, viscous drag, and the dynamics of the mooring lines. To account for the underdamped response, an additional damping term, b_{add}, is introduced to (3.53), giving:

$$A = \begin{bmatrix} A_e & 0 & 0 & 0 \\ 0 & A_{rc} & 0 & B_{rc} \\ 0 & 0 & 0 & 1 \\ \frac{C_e}{M^*_{33}} & \frac{C_{rc}}{M^*_{33}} & -\frac{c_{hs}}{M^*_{33}} & -\frac{b_{add}}{M^*_{33}} \end{bmatrix}, \qquad B = \begin{bmatrix} B_e \\ 0 \\ 0 \\ 0 \end{bmatrix} x = \begin{bmatrix} Y_e \\ Y_{rc} \\ z_3 \\ \dot{z}_3 \end{bmatrix} u = \eta. \tag{8.8}$$

This additional damping term is adjusted until the model output more closely matches the Qualisys measurements, as demonstrated in Fig. 8.2.

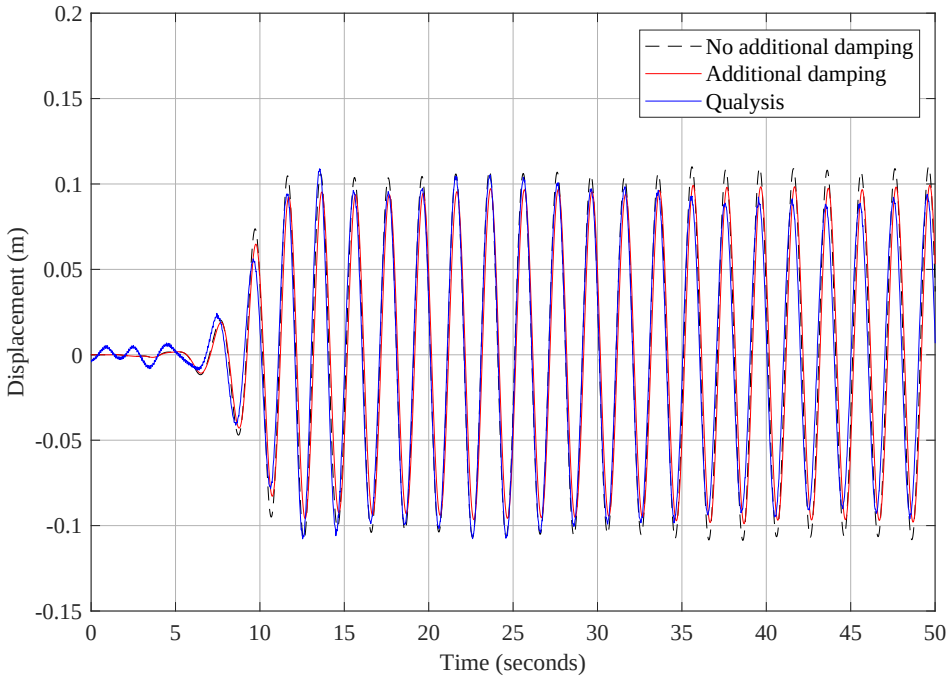


Figure 8.2: Regular wave validation of the linear hydrodynamic model, showing the effects of the additional damping term introduced in (8.8).

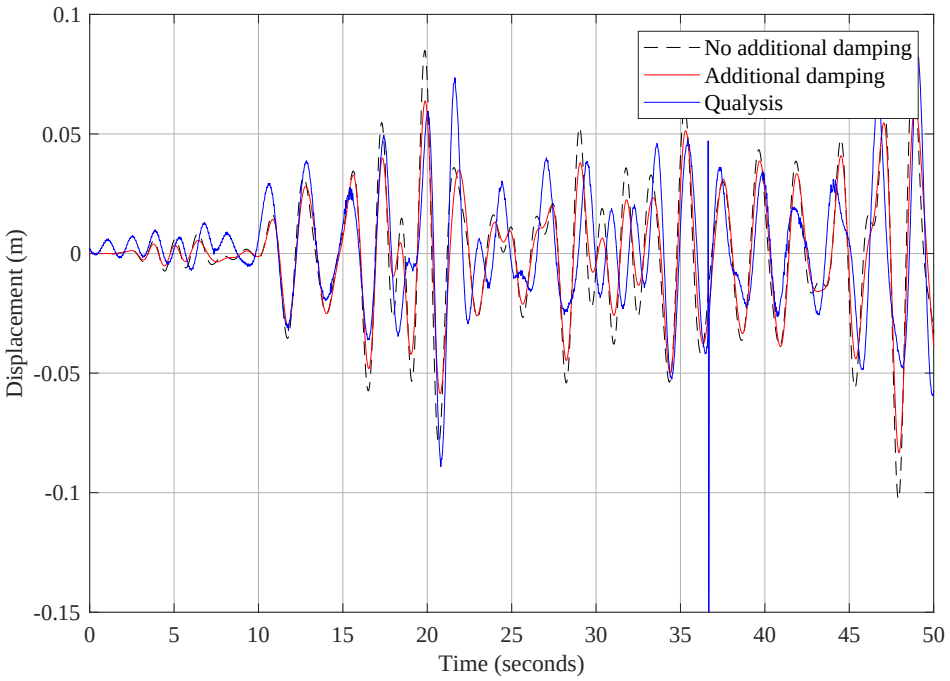


Figure 8.3: Irregular wave validation of the linear hydrodynamic model, showing the effects of the additional damping term introduced in (8.8). Note the anomalous spike in magnitude at approximately 36 s, which is an indicator of a snatch load at this time step.

In irregular waves, the discrepancies between model output and the measured displacement are more noticeable. Although the additional damping term does show some improvement to the fit, there are still strong discrepancies between the model output and the measured displacement as shown in Fig. 8.3. One of the key drivers of such discrepancies is the existence of snatch loads. In irregular wave tests during the first test campaign, snatch loads, where the buoy reaches the end of its tether and is pulled back suddenly, were present in the measured heave data. These snatch loads present as large spikes in magnitude, and are an unfortunate artifact of wave tank testing in relatively shallow water with a short mooring line. The first of such snatch loads unfortunately occurred early in each test, either before, or as, the transient period of the tests starting was beginning to settle. This makes full validation of the model against irregular wave tests problematic, since the snatch loads have an impact on both the magnitude, but more significantly, the phase of the device motion. Finally, it was assumed that the waves measured by the wave probes were the same as those experienced by the device. In regular waves such an assumption holds more strongly, since once the experimental sea state is fully developed there is little change. However, for irregular waves, small variations in the sea state can occur, especially as some splashing and wave breaking was observed, alongside interference from radiated waves from the device itself and reflection from the wave tank walls. These effects from using real tank test data, impose some limitations on the effectiveness of the results obtained by the estimator, as discussed

in Sections 9.2.1 and 9.3.1. For comparison, where ideal simulated irregular wave data is used in Sections 9.1and 9.2.2, the estimator performs particularly strongly.

8.2.2 Fitted with orifice plates

With irregular test results unavailable for validating the nonlinear model representing the buoy with an orifice plate, the measured heave displacement in regular waves is compared to the model output, as shown in Fig. 8.4. It can be seen in Fig. 8.4 that a good match between the model output and the Qualisys data is achieved, without the introduction of any additional linear damping term. This suggests that the nonlinear model more fully captures the dynamics of the device, compared to the linear model. The effects of including air compressibility, by using (4.21) rather than (4.19), in the nonlinear model given in (4.24), can also be compared at this stage, with air compressibility effects found to be negligible, as shown in Fig. 8.4.

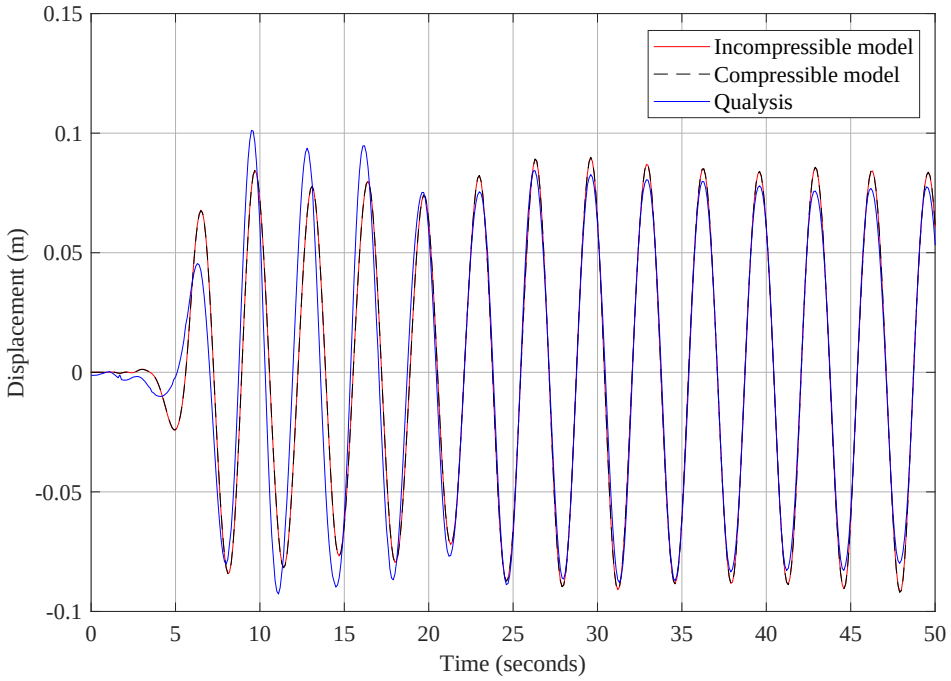


Figure 8.4: Validation results comparing the heave displacement calculated by the 25 mm orifice plate model and the measured heave displacement from Qualisys. Note the imperceptible difference when accounting for air compressibility and the model assuming air incompressibility.

8.2.3 Fitted with a controlled Wells turbine PTO

To validate the test case using a real turbine PTO, the model used for the orifice plate test case was used as the basis for the hydrodynamic model of the floating OWC with a turbine PTO. This requires some changes to be made, since the lack of the steel plates representing the mass of the batteries means that the device fitted with the Venturi and

turbine PTO is somewhat lighter than when fitted with the orifice plate. The difference in draft is approximately 5 cm, so the mass is recalculated, alongside reruns of the WAMIT BEM solver to obtain frequency dependent terms at the new draft. In addition to being lighter, the floating OWC with the working turbine PTO, requires the consideration of some additional steps. Namely, these are the effect of the turbine speed controller on the dynamics of the device, and the determination of which value of A_{ori} is most appropriate for an equivalent orifice representing the effects of the turbine, which are discussed in Section 8.2.3.1 and Section 8.2.3.2 respectively.

8.2.3.1 Effects due to the controller

Since the turbine speed was found not to have a substantial impact on the volumetric flow rate and pressure in the fixed OWC tests, as discussed in Section 7.1.1.2, it was surmised, in Chapter 7, that the effects of the turbine speed on the floating device would also be minimal. To test this hypothesis, tests in both regular and irregular waves are run at Lir NOTF on the floating OWC, using identical waves for two consecutive runs: one with the controller set to a relatively low speed set point, and one with no control acting on the turbine. This hypothesis is tested first in regular waves, with a set point of 200 rad/s for the controlled run. In Fig. 8.5, the heave displacement of the device, when the turbine speed is set to 200 rad/s, is compared to the heave displacement when the turbine is allowed to spin freely.

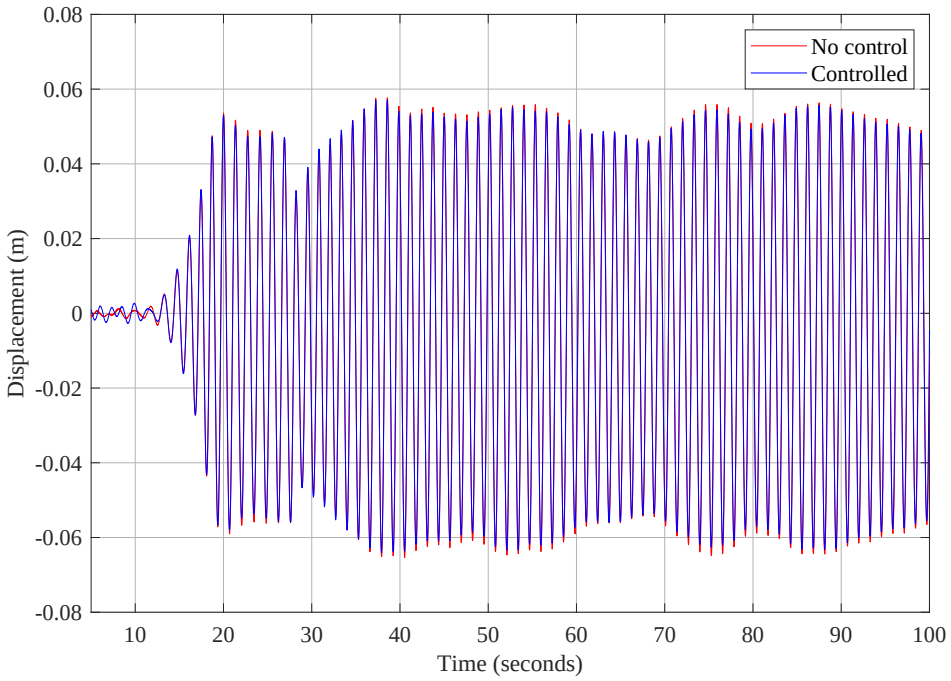


Figure 8.5: Comparison of device heave motion with turbine speed controlled at a set point of 200 rad/s compared to when the turbine is in uncontrolled free spin (approximately 400 rad/s). As shown in Fig. 8.6, any differences in device displacement are due to slight differences in wave height caused by inaccuracies in the wavemaker, rather than turbine speed.

As can be seen in 8.5 the turbine speed initially appears to have a slight impact on the device heave displacement, with some minor differences visible between the two cases. However, the effect is not consistent, with the controlled case at times having a slightly lower amplitude, and at other times, slightly higher. To investigate this further, the wave probe readings of the free surface elevation from the two tests are plotted against one another, in Fig. 8.6.

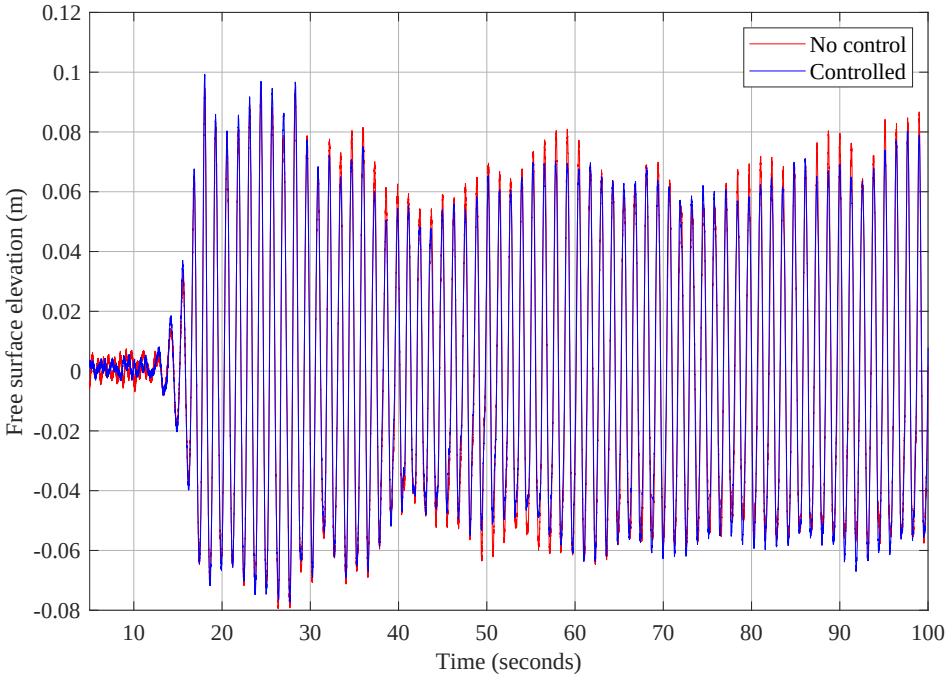


Figure 8.6: Comparison of wave probe measurements for the tests compared in Fig. 8.5. It can be seen that though the wavemaker attempts to recreate identical waves for both runs, the inaccuracies in the wave maker mean that there are variations between the two waves, reflecting the trends seen in Fig. 8.5.

In Fig. 8.6, the cause of the difference between the two runs becomes apparent. Though the two waves are theoretically identical, with the wavemaker attempting to replicate exactly the same wave in each run, inaccuracies in the wavemaker mean that there are some discrepancies between the two waves. To test that this is also the case in irregular waves, two theoretically identical waves are again generated, this time using a Bretschneider spectrum. To exaggerate the difference between the turbine speed in each run, the first run is set to the highest possible generator load, and therefore the slowest possible speed, while, during the second run, the turbine is allowed to free spin. Again, as shown in Fig. 8.7, some slight differences are noticeable in the heave displacements measured across the two runs.

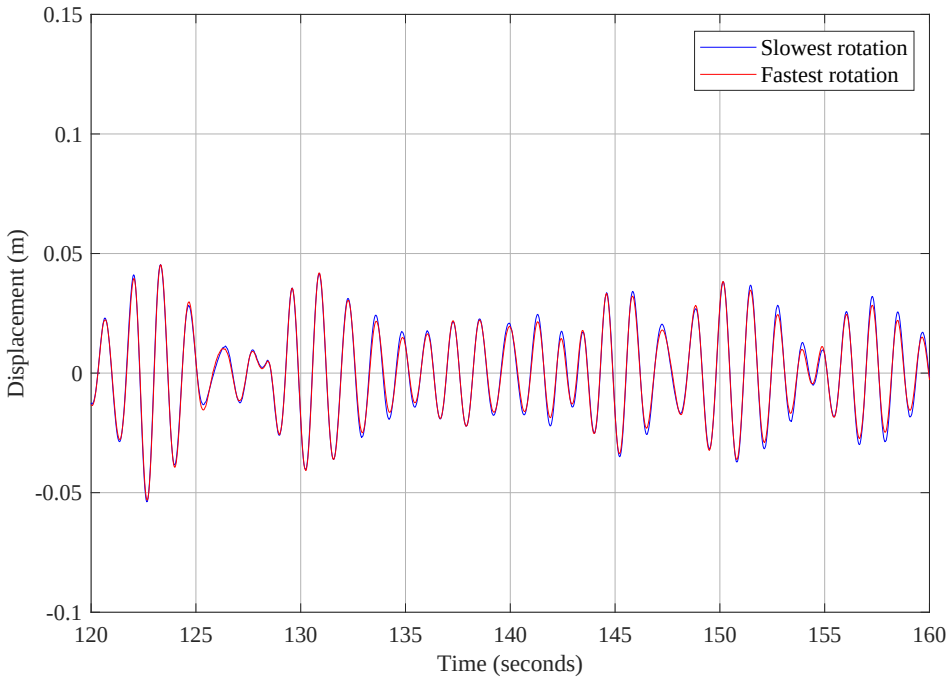


Figure 8.7: A comparison in irregular waves considering the device heave motion with the PWM signal set to 0 (no load/fastest rotation) for one run, and then 100 (maximum load/slowest rotation) for the next. Again there is a very small difference between runs which can again be attributed to slight differences in the waves produced by the wavemaker.

However, once again, when the wave probe readings are compared, there is a slight discrepancy between the two waves, as shown in Fig. 8.8.

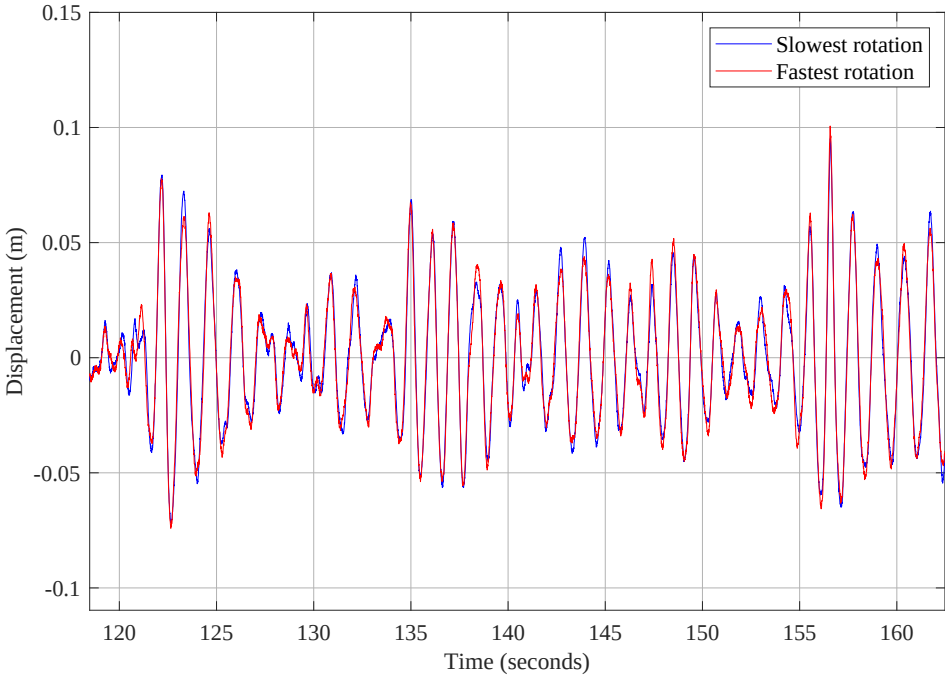


Figure 8.8: Comparison of wave probe measurements of free surface elevation for the tests shown in Fig. 8.7. Like in the regular wave tests, shown in Figs. 8.5 and 8.6, there are slight variations in the free surface elevation between the two irregular wave tests, which again show that turbine speed has a negligible effect on the device dynamics.

Since the difference between runs, with the turbine spinning at full speed and at a slower control speed, are almost negligible, and that similar discrepancies exist between the waves used in the comparisons, it can be concluded that the effects of the turbine speed controller on the overall dynamics of the floating OWC are not significant, as quantified in [160].

8.2.3.2 Determination of equivalent orifice

As discussed in Section 7.3.2, the turbine designed in Chapter 7 can be modelled as an equivalent orifice, since the effects of the turbine speed on the mass flow rate and pressure are negligible. However, the approach in Section 7.3.2 requires an equivalent orifice area in order to calculate the associated value of C_d. As discussed in Section 7.3.2, the terms A_{ori} and C_d frequently appear together in the nonlinear model of the system. Since the product of these two terms is always a constant value of 0.0011, the choice of exact values for A_{ori} and C_d appears relatively arbitrary, except for the fact that there are two terms in the bottom right of the A_{nl} matrix in (4.24), where A_{ori} appears on its own. To assess the sensitivity of the model to the choice of A_{ori}, models using the values at the upper and lower limits for A_{ori} and C_d (identified in Section 7.3.2) are compared with the measured heave displacement of the floating OWC. These values

correspond with a minimum value for C_d of 0.203 with a maximum A_{ori} of 0.0054 m^2, and a maximum value for C_d of 1 with a minimum A_{ori} of 0.0011 m^2.

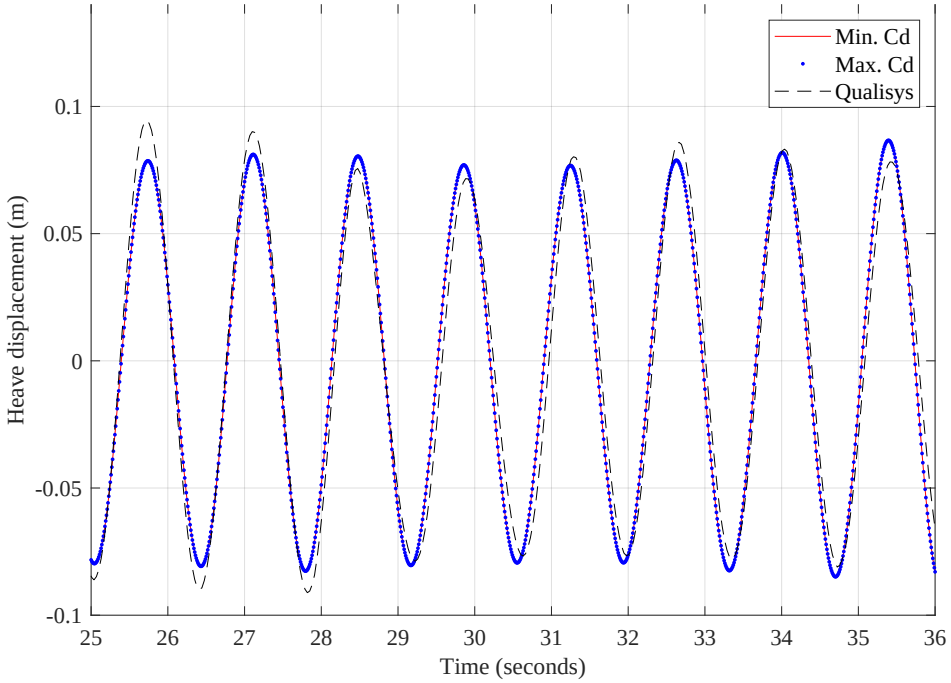


Figure 8.9: Validation results comparing the sensitivity of the OWC model with a turbine to chosen values of C_d. The model output "Min. Cd" uses a C_d of 0.203 and an A_{ori} of 0.0054 m^2, with "Max. Cd" using a C_d of 1 with the minimum A_{ori} of 0.0011 m^2. In both cases the product of A_{ori} and C_d is 0.0011.

Fig. 8.9 shows that the exact choice of A_{ori} and C_d has little bearing on the accuracy of the model, providing that their product is equal to 0.0011. Given that the two extreme cases, compared in Fig. 8.9, produce an almost identical model output, it can be determined that the choice of an exact value for A_{ori} and C_d is indeed arbitrary for this system.
Since Fig. 8.9 shows a good match between the model output and measured heave displacement in regular waves, the model is also tested against irregular waves (arbitrarily sticking with values for C_d of 0.203 and A_{ori} of 0.0054 m^2).
Fig. 8.10 shows that the hydrodynamic model matches the measured heave displacement relatively well, and again does not require the inclusion of an additional damping term. However, there are some notable discrepancies. Unlike the irregular tests carried out in the first test campaign, with a fully sealed moonpool, discussed in Section 8.2.2, the tests for the floating OWC were designed for the avoidance of snatch loads, with no snatch loads observed in irregular waves during the second test campaign at Lir NOTF. However, the limitation of using waves measured by a stationary wave probe as the input to a model which is compared to measurements of a floating device remain, with some drifting from the datum position of the floating device an inevitability. This is

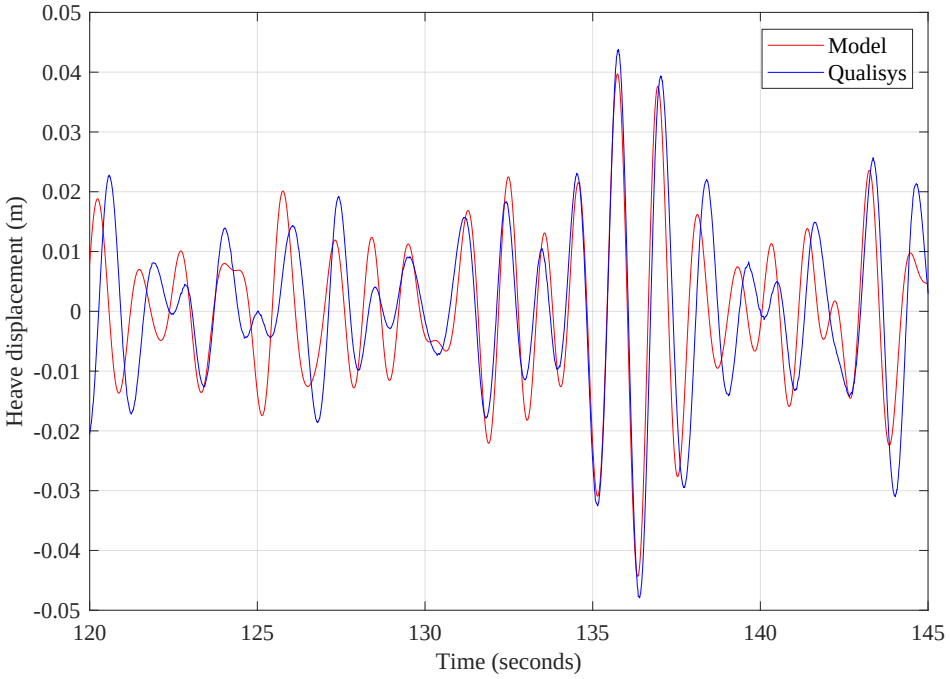


Figure 8.10: Validation results comparing the heave displacement of the model for the floating OWC fitted with a working PTO in irregular waves to the measured heave displacement from Qualisys.

the primary reason for the discrepancies shown in Fig. 8.10, especially with regard to the phase of the two signals, where the device moving from its datum position changes its relative position to the reference wave probe. Furthermore, though the reference wave probe, shown in Fig. 6.14, is positioned in line with the device, to minimise any discrepancies between the waves the device encounters and the recorded data for free surface elevation, the Deep Ocean Basin wave tank used at Lir NOTF, is by no means a perfect tank, and being 12 m wide some differences in wave height across a single wave are unavoidable, particularly in the presence of myriad reflections from device, the sidewalls and absorbing beach (the absorbing beach in the Deep Ocean Basin has a reflection coefficient of approximately 20%). Aside from these caveats, the match between the hydrodynamic model and the measured heave displacement in irregular waves is also relatively good given the limitations of the experimental set up.

8.3 Chapter summary

In this chapter a free surface elevation estimator is designed, considering both a fully linear system and two similar nonlinear systems. The Kalman filter based estimator acts as a soft wave sensor which estimates time series free surface elevation values from measurements of the buoy displacement, in this case measured by a Qualisys

motion capture system but, in real seas, from an onboard IMU. In this chapter, the hydrodynamic models used by the estimator are also validated for all three test cases, against both regular, and, where possible, irregular waves.

Validation of the hydrodynamic models shows that an additional damping term is required in the linear model describing the buoy with a fully sealed moonpool. The fact that such an additional term is not required in either of the nonlinear models, suggests that the nonlinear system description given in (4.24) more fully captures the dynamics of the system, and suggests that, even for the sealed moonpool case, the OWC has some additional damping effect. Air compressibility for an OWC of the dimensions considered in this thesis, is found to be negligible, allowing for the simpler orifice equation given in (4.19) to be used by the estimator. Another simplification confirmed in the validation of the hydrodynamic models is that the effects of the controller on the speed of the turbine do not need to be included in the model of the system, due to the negligible impact on the device dynamics. Finally, it is also determined, that while the term A_{ori} appears on its own in the nonlinear system description, the model is not sensitive to the exact choice of A_{ori} from the range of possible values, provided C_d is scaled accordingly.

The testing of the estimator is discussed in Chapter 9, considering all three test cases and assessing the estimator performance in both regular and irregular waves.

9

Evaluation of a free surface elevation estimator as a sensor for data buoys

Contents

9.1 Simulation results 186
9.2 Test results based on first test campaign at Lir NOTF 189
9.2.1 Fully sealed device 190
9.2.2 Orifice plate representing turbine 193
9.3 Test results based on second test campaign at Lir NOTF 197
9.3.1 Controlled turbine PTO 197
9.4 Conclusions and limitations of case study 203

In this chapter the estimator described in Chapter 8 is tested, first in simulation, and then against experimental wave tank data, in both regular and irregular waves. Three different test cases are considered: first using a fully sealed moonpool, then using an orifice plate to represent the turbine PTO damping, and finally using a real turbine with a set point tracking controller. For all three test cases the estimator is generally shown to not only estimate the wave characteristic parameters of H_s and T_z successfully; but through using measurements of the device heave displacement, and taking into account the effects of the buoy dynamics, the time series free surface elevation can also be recovered. For most of the tests considered within this chapter, the estimated H_s values generally fall within a similar error range to the industry standard of H_{mo}, which is known to overpredict H_s by 5-10% [72].

To compare the estimated free surface elevation against the measured free surface, the causalisation delay (2 s), along with any small delay introduced by the estimator structure itself (approximately 0.1 s), is removed from the estimated signal to properly align the two signals across the tests discussed in this chapter. With the estimated and measured signals aligned, the normalised root mean squared error is calculated and used as a measure of goodness of fit, given in (5.11) as a percentage $\%_{GoF}$.
Since it is assumed the estimator will be used in seas where no prior information is known, all states within the estimator are initialised at 0.

9.1 Simulation results

Wave tanks have a number of restrictions, which affect the waves that can be tested in experiments. Since the tests carried out in the wave tank at Lir NOTF use a full size device, in waves that are not realistically scaled in comparison (the wavelength of waves used during wave tank tests is essentially equal to the device diameter), to assess the ability of the estimator to perform in realistic ocean waves, simulation results must be used instead. The advantage of using a simulated environment is that the estimator can be tested for the three test cases described in Chapter 8 (the fully sealed moonpool, the OWC fitted with an orifice plate, and the OWC with the turbine PTO) against the exact same polychromatic wave time series (as shown in Figs. 8.6 and 8.8, wave maker inaccuracies mean that there are discrepancies between the theoretically identical waves it produces) for a direct comparison of how each test case affects the dynamics of the device and the performance of the estimator.
Using spectral wave characteristics shared with this project by the PLOCAN test site, situated off the east coast of Gran Canaria, an irregular wave is generated to reflect the conditions that the device would encounter if deployed at the test site, since a free surface elevation measuring buoy may be required at such a location. Based on 11 years of data, the wave climate at the PLOCAN test site has been found to be described by a modified JONSWAP spectrum characterised by a very low peak enhancement factor, $\gamma = 0.18$ and $\sigma = 3.3667$ [280]. The peak period, T_p, is 5.85 s with a H_s of 0.712 m. The same irregular wave, generated using these spectral characteristics, is used as the input to the hydrodynamic model describing each of the three test cases (the sealed moonpool, the buoy fitted with a 25 mm orifice plate and the buoy with a turbine PTO), to generate device heave displacement data. This heave displacement data is then used as the measured output for the free surface elevation estimator and the resultant estimated free surface elevation compared in Figs. 9.1, 9.2 and 9.3.
Because there are no modelling uncertainties using purely simulated data with a mathematical system model, and the waves can be measured directly at the device

location, the GoF between the measured and estimated free surface elevation is high for all three test cases, as summarised in Table 9.1.

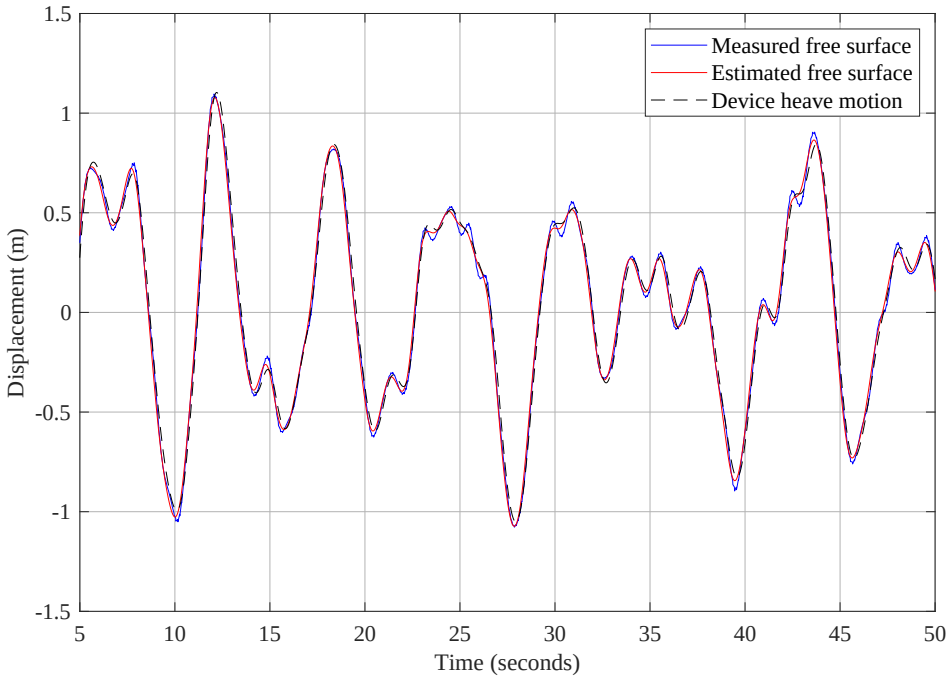


Figure 9.1: Comparison of measured free surface elevation, estimator output and buoy displacement, for the Gannet G1250 with a fully sealed moonpool, in irregular waves, reflective of those at the PLOCAN test site. The device heave motion is close to the measured free surface, since the sealed buoy exhibits behaviour close to a true wave follower.

However, as shown in Figs. 9.1, 9.2 and 9.3, the three test cases behave differently in terms of device motion compared to free surface elevation. In the fully sealed case, shown in Fig. 9.1, the device behaves similarly to a true wave follower, meaning that the device motion could almost be used directly to return free surface elevation. This is borne out in the GoF calculations with the free surface elevation estimator able to achieve only a slightly higher GoF at 93.2%, compared to 91.4% when using the device motion directly.

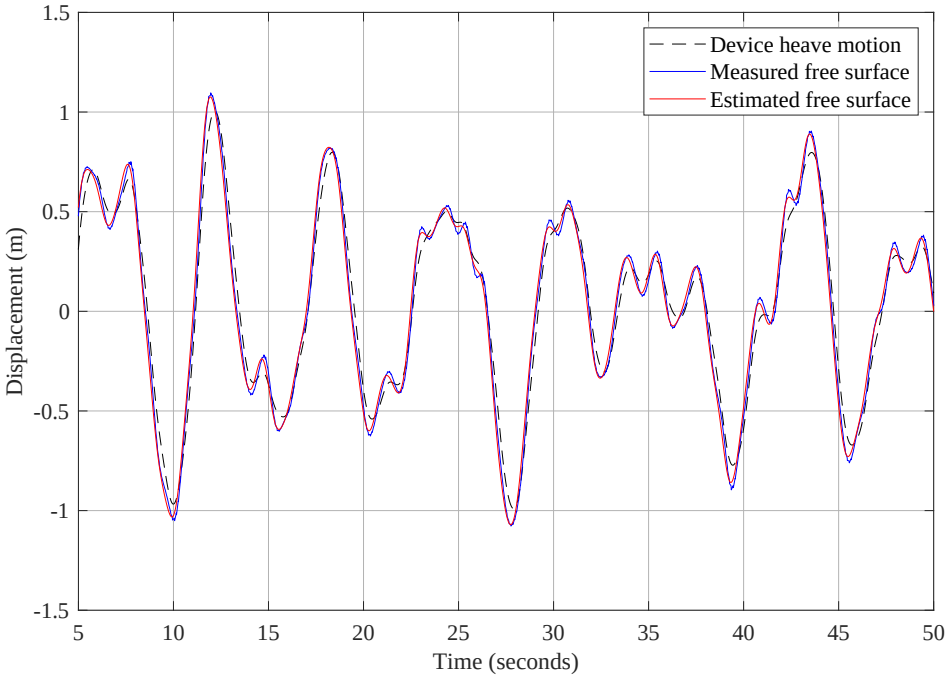


Figure 9.2: Estimator output, compared to measured free surface elevation, and buoy displacement, for the Gannet G1250 fitted with a 25 mm orifice plate, in the same irregular waves used in Fig. 9.1.

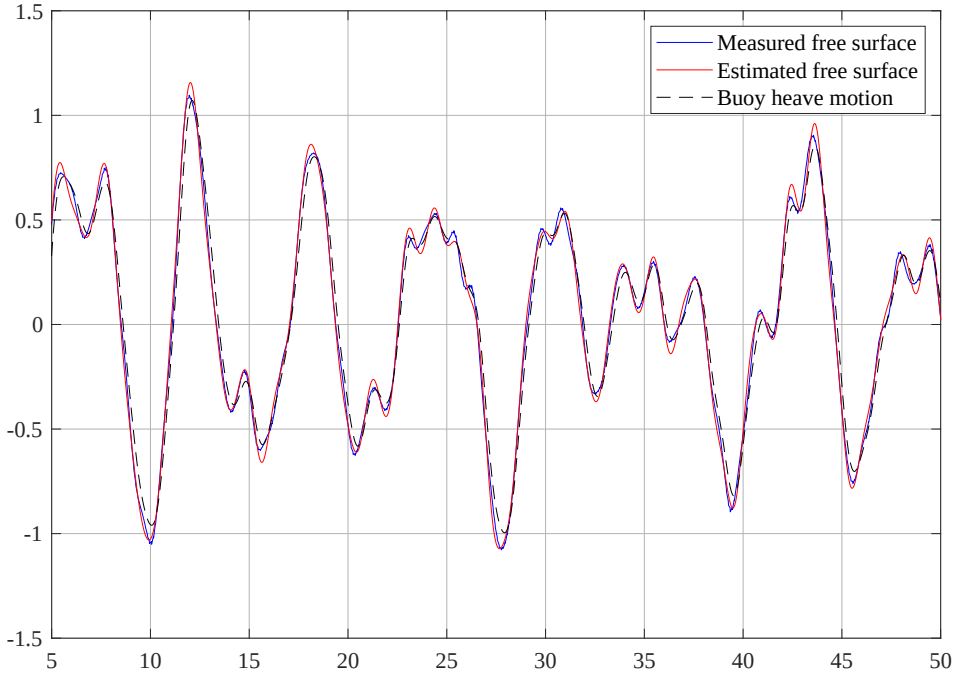


Figure 9.3: Estimator output, compared to measured free surface elevation, and buoy displacement, for the Gannet G1250 fitted with a Venturi and working turbine PTO, in the same irregular waves used in Figs. 9.1 and 9.2.

The device fitted with the 25 mm orifice plate, shown in Fig. 9.2, presents a more

compelling case for the free surface elevation estimator, with a 91.3% GoF between the estimated and measured free surface elevation, and a device motion which is not a true wave follower (only a 85.1% GoF correlation between device motion and free surface elevation). For the test case with the real turbine, shown in Figs. 9.3, the device again does not behave like a true wave follower, with a similar GoF correlation between device motion and free surface elevation to the case with the orifice plate at 85.9%. The estimator itself performs similarly well to the orifice plate test case with a GoF of 92.1% achieved between estimated and measured free surface elevation.

Table 9.1: Goodness of fit comparison in simulated waves, of the estimated free surface elevation, against using the device heave displacement directly.

Test Case	GoF (%)	
	Estimator	Device
Sealed moonpool	93.2	91.4
Orifice plate	91.3	85.1
Turbine PTO	92.1	85.9

9.2 Test results based on first test campaign at Lir NOTF

During the first test campaign at Lir NOTF, two test cases are used in experiments: the fully sealed moonpool and the device fitted with a 25 mm orifice plate. The experimental data discussed in this section was obtained by collaborators at DkIT, where the focus was on using the Gannet buoy as a scale model of the larger WASP which has been tested at Galway Bay with a fully sealed moonpool, as described in Section 6.1.1. Thus the focus of the first campaign is on the device with a fully sealed moonpool, which is tested in both regular and irregular waves, whilst the test case using the orifice plate is only tested in regular waves. However, synthetic irregular data is created for the test case using the orifice plate, by setting the measured free surface elevation, obtained during irregular wave tests at Lir NOTF with the sealed device, as the input to the model, in a similar manner to the simulated tests in Section 9.1.

GoF is again used as a measure of estimator performance. However, an NRMSE-based GoF is a highly sensitive measure of how two signals correlate, particularly with regard to phase. In irregular wave tests for the sealed buoy, a high incidence of snatch loads is observed, which interrupts the natural motion of the buoy, making an NRMSE comparison of the signals obtained difficult, due to a poor match in phase. To gauge whether the estimated values are close to the measured values on a metric which is less sensitive to phase, the significant wave height and zero crossing period of the estimated free surface across relatively short 20 s acquisition windows are also compared.

Calculating H_s from time series data is trivial, as it is simply the average of the highest 1/3 of the waves over the acquisition time. The zero-crossing period is found in the time domain by identifying the up zero-crossing indices of the time series and finding the average of the time between each up zero-crossing across the acquisition time. These results can be found in Tables 9.2, 9.3 and 9.4, for the sealed moonpool, 25 mm orifice plate and turbine PTO test cases respectively.

9.2.1 Fully sealed device

The KFRW used with the sealed moonpool, being a fully linear model, is found to have a very fast execution time, even using Matlab, which is known to be relatively slow interpreted code, at approximately 0.020s for a time series of 150s, using time steps of 0.1 s (on a PC with Intel Core i7-1265U and 32 GB RAM). This indicates the estimator ability to return estimates in real time, albeit, due to the causalisation delay and the small inherent delay of the estimator itself, affected by a small delay.
Some tuning of the process noise covariance matrix, Q, is required for the estimator to work correctly. Q, by virtue of the diagonal entries, determines how much trust is put into each estimated state. In this case, more trust is put in the model states than in the state relating to the random walk, with the highest trust put in the state corresponding to the buoy displacement, as this is the state directly corresponding to the measured output. The measurement noise from the Qualisys data is found to be relatively small, with a corresponding measurement noise covariance value of $1e^{-6}$ used in the R matrix. In real applications, measurements of buoy motion would come from an onboard IMU, with R adjusted appropriately based on the sensor noise level of the IMU.
To analyse the estimator performance, an acquisition window of 20 s is used, across which values for T_z and H_s are obtained, for both the measured and estimated free surface elevation. The GoF between the estimated signal and the measured signal is also calculated. Because all states are initialised at 0, the estimated free surface elevation undergoes a transient period before a steady state is reached. Therefore the acquisition window for any comparisons of estimated free surface elevation to measured free surface elevation is set beyond the point at which transients have settled, better representing the real sea application where the estimator would be expected to be free running for a long time. In irregular wave tests for the fully sealed case, any snatch loads are avoided when selecting the acquisition window.
A single acquisition window is used for the tests in regular waves, since once a steady state is reached there is little change in the motion of the device. The irregular wave tests are run for 1200 s, with a number of acquisition windows chosen to test the estimator against variations in free surface elevation over the test period.

Comparing free surface elevation results obtained by the linear estimator, on a fully sealed buoy, against using the displacement of the buoy directly, shows that the behaviour of the sealed buoy is close to that of a wave follower, particularly in regular waves, as demonstrated in Fig. 9.4.

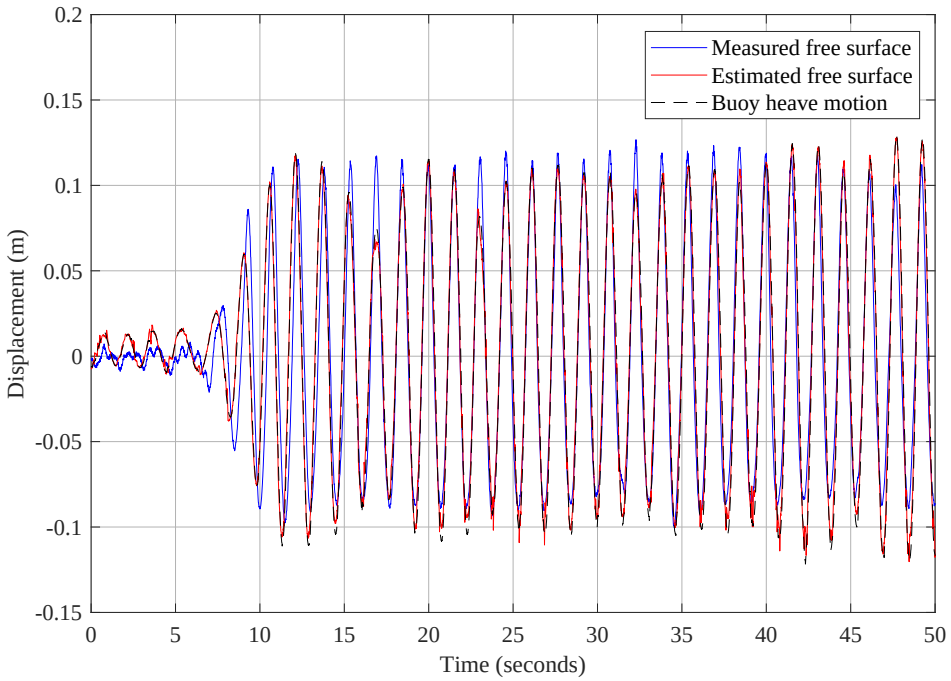


Figure 9.4: Estimated free surface elevation in regular waves for the fully sealed moonpool, compared against the measured free surface, and the heave displacement of the buoy itself.

In irregular waves, the presence of snatch loads reduces the accuracy of the obtained free surface wave elevation, particularly as it changes the relationship between the phase of the buoy and the waves. The result is that accurate GoF values for irregular waves are therefore particularly difficult to obtain, since NRMSE is highly affected by differences in phase. A comparison of the estimated and measured free surface elevation, in irregular waves, is shown in Fig. 9.5, again shown alongside the displacement of the buoy directly.

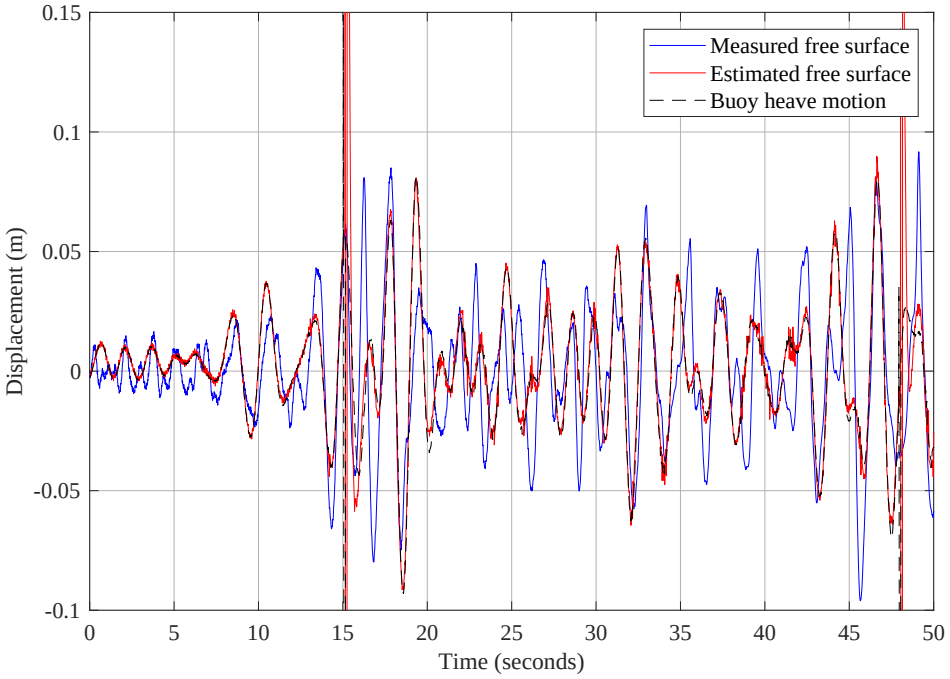


Figure 9.5: Estimated free surface elevation in irregular waves for the fully sealed moonpool, compared against the measured free surface, and the heave displacement of the buoy itself. Again, note the presence of snatch loads at 15 s and 48 s.

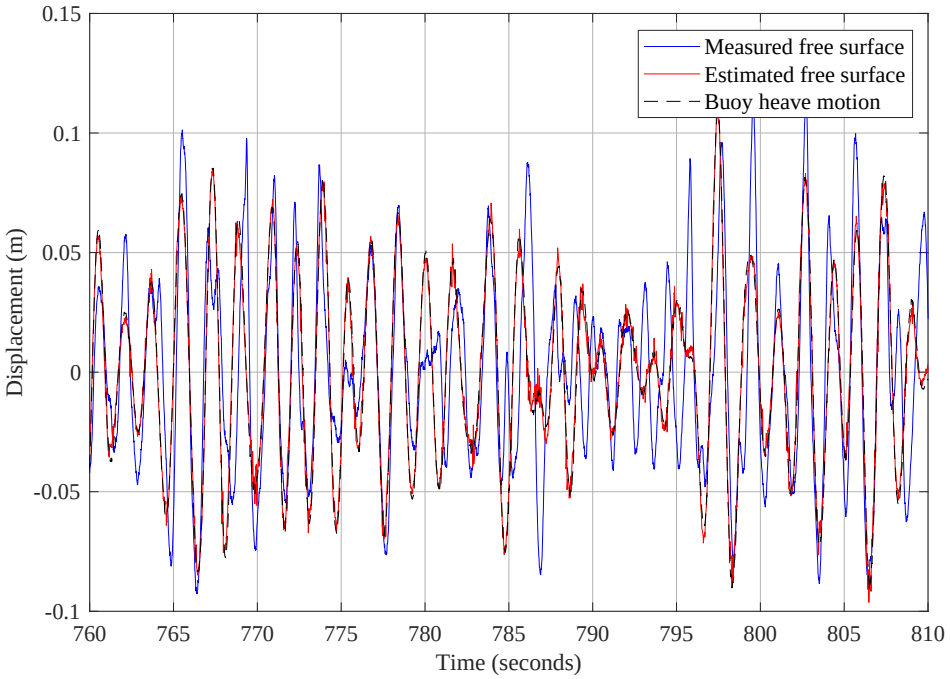


Figure 9.6: Estimated free surface elevation in irregular waves for the fully sealed moonpool, as in Fig. 9.5; here showing performance after running for more than 12 minutes in irregular waves.

For regular waves, a GoF between 72-82% is achieved, when comparing the estimated and the measured free surface elevation. In regular waves, the buoy heave motion is

found to follow the free surface almost identically, as shown in the example in Fig 9.4, with the difference slightly more noticeable in irregular waves, as shown in Fig. 9.5. To demonstrate the ability of the estimator to operate effectively even after a significant number of waves have passed, Fig. 9.6, shows that the accuracy of the estimator does not deteriorate over time. It should also be noted that the results shown in Fig. 9.7 use acquisition windows selected across the full 1200 s test time, which again do not show any correlation between time and estimator accuracy.

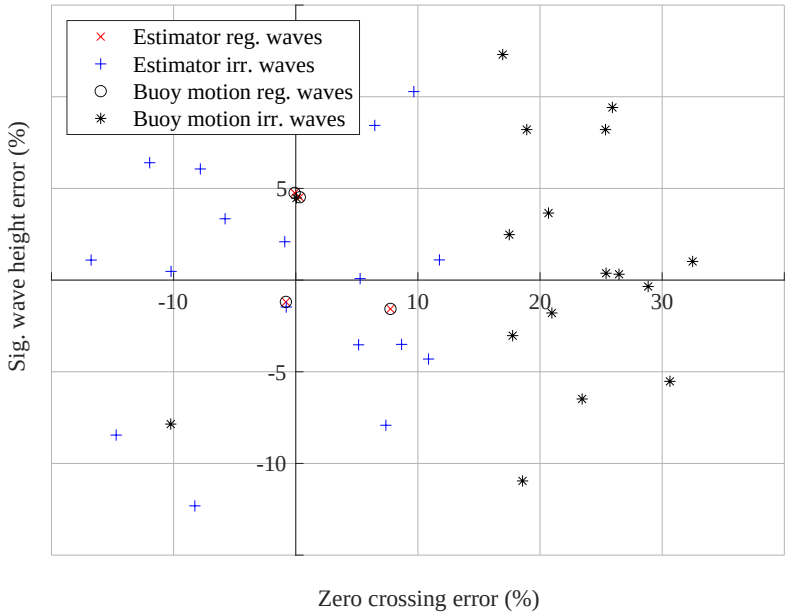


Figure 9.7: Scatter plot for the fully sealed moonpool tests, showing the errors in obtaining T_z and H_s, with positive errors showing overestimation, and negative errors showing underestimation.

A comparison between using the estimator and the buoy displacement directly, summarised in Fig. 9.7, and summarised in Table 9.2, shows that for a buoy whose behaviour is close to a wave follower, there is little advantage to using the estimator in obtaining values for H_s, with both methods obtaining results approximately within a 10% error band of the measured H_s. The biggest difference, in the linear case, can be observed when comparing the obtained values for T_z in irregular waves, with the estimator capable of returning results with only around a 10% error, whereas directly using the heave measurements generally overpredicts T_z, in some cases by more than 20%.

9.2.2 Orifice plate representing turbine

The state space model used to represent the system fitted with 25 mm orifice plate is significantly larger in dimension than that for the sealed chamber, and combined

Table 9.2: Comparison of estimated and measured free surface against using device heave motion directly, for the device using a fully sealed moonpool chamber. Due to the proliferation of snatch loads affecting phase in irregular wave tests, GoF results are only obtained in regular waves.

Wave Type	Tz **(s)**			H_s **(m)**			**GoF**
	Meas.	**Est.**	**Device**	**Meas.**	**Est.**	**Device**	**(%)**
Regular	1.37	1.36	1.36	0.170	0.168	0.168	81.3
	1.54	1.54	1.54	0.173	0.181	0.181	67.0
	1.59	1.59	1.59	0.160	0.168	0.168	73.8
	1.41	1.53	1.53	0.168	0.166	0.166	76.6
Bretschneider	1.23	1.22	1.67	0.077	0.076	0.078	
	1.03	0.90	1.34	0.068	0.063	0.064	
	1.55	1.43	1.90	0.085	0.076	0.076	
	1.57	1.48	1.98	0.091	0.094	0.094	
	1.67	1.51	2.02	0.093	0.094	0.096	
	1.27	1.15	1.53	0.072	0.079	0.082	
	1.29	1.16	1.74	0.065	0.069	0.071	
	1.49	1.24	1.92	0.099	0.095	0.095	
	1.67	1.87	2.40	0.090	0.087	0.086	
	1.38	1.37	2.04	0.076	0.078	0.077	
	1.70	1.83	1.54	0.100	0.093	0.093	
	1.57	1.73	2.11	0.101	0.113	0.111	
	1.29	1.46	1.73	0.080	0.081	0.080	
	1.29	1.38	1.59	0.089	0.097	0.097	
	1.37	1.45	1.93	0.105	0.105	0.104	

with the nonlinearities introduced, it is unsurprising that the execution time using a Matlab interpreter for the estimator in the nonlinear case is considerably slower, at 40-50 s execution time for a simulation time series of 150 s, using time steps of 0.1 s (on a PC with Intel Core i7-1265U and 32 GB RAM).

A fast execution time is only possible with appropriate tuning of the process noise covariance matrix, Q. If Q is poorly tuned, the discretisation time needs to be reduced, in particular cases by up to 100 times, significantly increasing execution times. Poor tuning of Q, can also result in the estimated states tending to positive or negative infinity, as the system can become unstable. To ensure an estimator that is robust against these issues, a relatively high amount of trust must be put into all of the states within the estimator, in this case diagonal entries in Q of 0.1 for all states, except the random walk which is set to 1, and the buoy displacement which is set to 0.01. This tuning of Q is found to work across all test cases considered.

The results for validating the nonlinear estimator against experimental data can be seen in Fig. 9.8, clearly showing that the behaviour of the buoy, when fitted with an orifice plate, is not that of a true wave follower. This makes the buoy fitted with an orifice

plate fitted a significantly more compelling case for using a free surface estimator. Fig. 9.8 clearly demonstrates the estimator ability to handle buoy dynamics which are not representative of a true wave follower, able to return values for T_d and H_s within a 10% error band, as summarised in Fig. 9.9 and Table 9.3. The time series GoF obtained between the estimated and measured free surface elevation for the nonlinear estimator in regular waves is also high, at 67-81%, depending on the particular test.

Table 9.3: Comparison of estimated and measured free surface against using device heave motion directly, for the device fitted with a 25 mm orifice plate. GoF refers to the GoF between the estimated and measured free surface elevation.

Wave Type	Tz **(s)**			H_s **(m)**			**GoF**
	Meas.	**Est.**	**Device**	**Meas.**	**Est.**	**Device**	**(%)**
Regular	3.33	3.33	3.34	0.162	0.153	0.121	80.8
	1.18	1.18	1.19	0.153	0.137	0.107	62.8
	3.32	3.34	3.42	0.505	0.460	0.368	76.3
Bretschneider	2.23	2.56	2.01	0.058	0.054	0.044	69.4
	1.94	1.96	1.98	0.093	0.086	0.064	73.9
	2.18	2.15	2.46	0.100	0.095	0.075	78.0
	1.84	2.29	2.29	0.089	0.084	0.063	71.2
	2.20	2.21	2.24	0.093	0.085	0.066	72.9

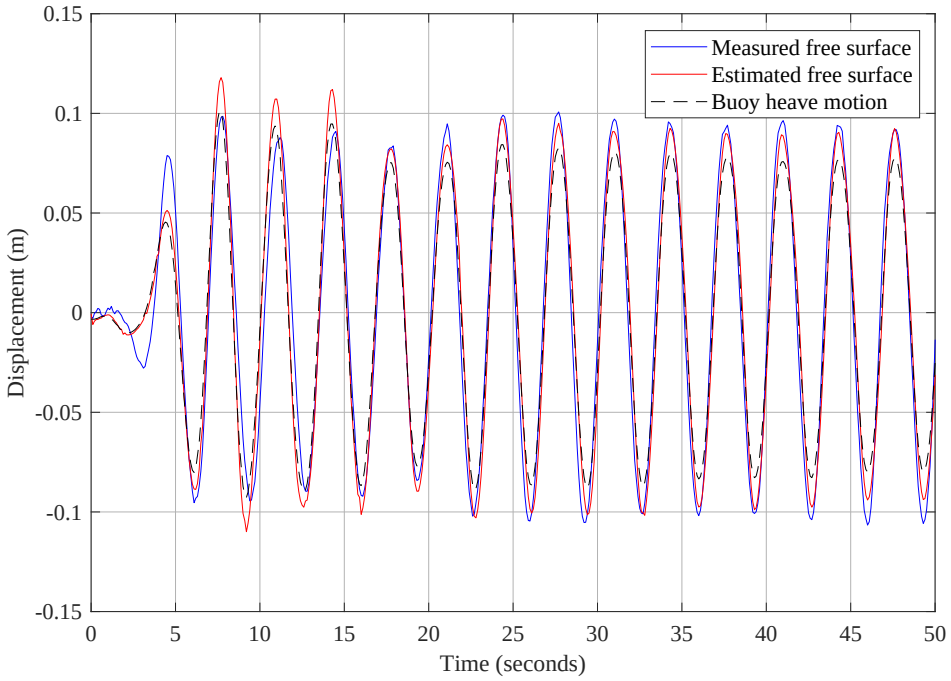


Figure 9.8: Estimated free surface elevation in regular waves for the 25 mm orifice plate, compared against the measured free surface, and buoy heave displacement. Though buoy heave motion follows the free surface elevation closely during the initial transient period, once steady state oscillation is reached the estimator output is a significantly closer match.

Unfortunately, no test data for the orifice plate is available in irregular waves. As discussed in Section 9.2.1, the performance of the linear estimator in irregular waves is poorer than that in regular waves. Therefore, to gauge the nonlinear estimator performance in irregular waves, synthetic measurement data is produced, using experimental irregular wave measurements as the input to the hydrodynamic model fitted with an orifice plate, validated in Section 8.2.2, and using the generated displacements as the measured output for the nonlinear estimator in irregular waves.

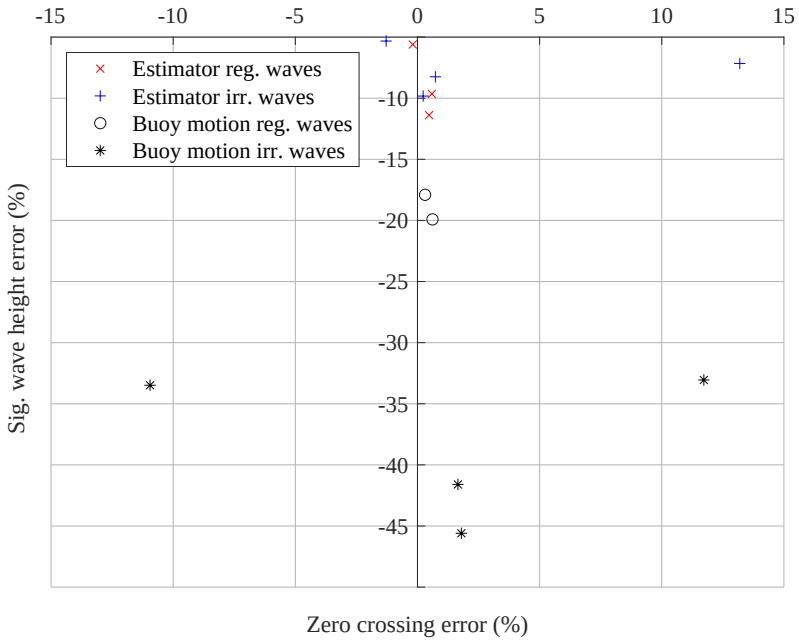


Figure 9.9: Scatter plot for the 25 mm orifice plate tests, showing the errors in obtaining T_z and H_s, with positive errors showing overestimation, and negative errors showing underestimation.

The resultant estimated free surface, for irregular waves, can be seen in Fig. 9.10. In the nonlinear case, a time series GoF of 69-78%, is achieved, with H_s and T_z estimates as accurate as those obtained in regular waves. This high accuracy is perhaps unsurprising, since Kalman filter-based estimators are model dependent, and with no discrepancies between the model used to generate the data and the model used in the estimator, and no unexpected changes in device motion due to snatch loads, it can be expected that the estimator will perform well, as demonstrated in Section 9.1. Nonetheless the ability of the estimator to obtain accurate values for both time averaged parameters T_d and H_s, and time series free surface elevation, is demonstrated.

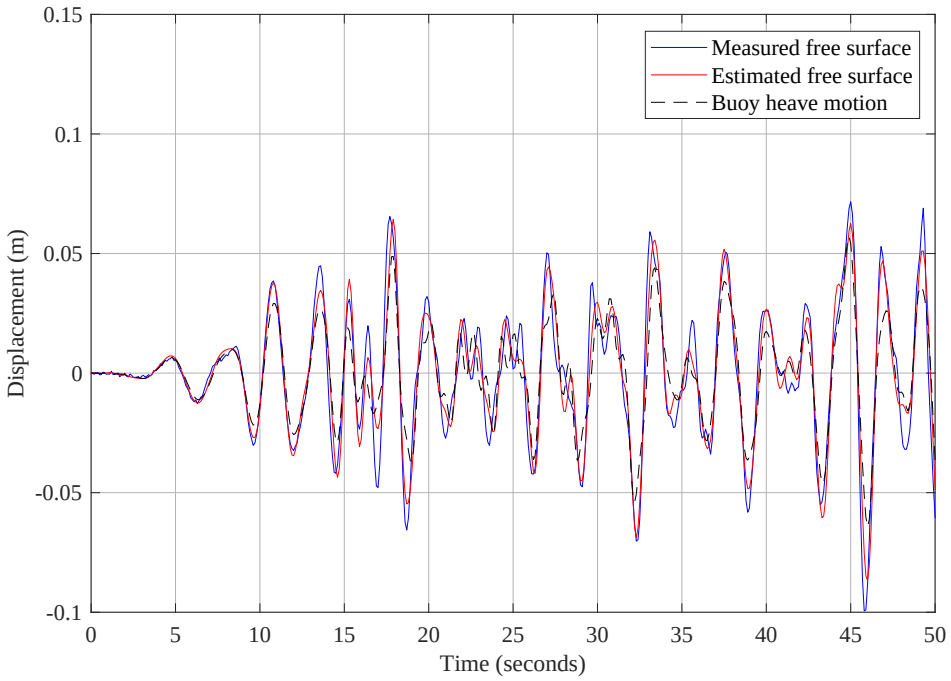


Figure 9.10: Estimated free surface elevation in irregular waves for the 25 mm orifice plate, compared against the measured free surface, and the heave displacement of the buoy itself.

9.3 Test results based on second test campaign at Lir NOTF

The second test campaign was designed purely for this project, and focusses solely on the test case using a real turbine PTO. Lessons learnt from the first test campaign, regarding snatch loads in irregular waves, were taken into consideration when designing the test conditions during the second campaign. The lack of irregular wave test data for the more compelling nonlinear orifice plate case, means that it was also a goal of the second test campaign to ensure the device with the turbine PTO is tested in irregular waves, to assess the nonlinear estimator ability in irregular waves, outside of a simulation environment. It should also be noted that the tests carried out during the second test campaign are all running a set point controller on the turbine speed and that power is being produced. The actual power obtained is relatively modest, with an average of power of 1 mW, 50 mW and 0.3 W achieved in regular waves, with a wave height of 0.1 m, 0.15 m and 0.2 m respectively, and power peaks in the range of 1-16 mW for the irregular wave tests.

9.3.1 Controlled turbine PTO

The estimator structure for the test case, using a controlled turbine PTO, remains largely the same as for the estimator using the orifice plate, since the turbine speed is found

to have little impact on the dynamics of the device, as discussed in Section 8.2.3.1. However, there are some notable changes to the hydrodynamic model parameters, with the mass of the buoy, fitted with the turbine PTO, being approximately 60 kg less, when compared with the buoy fitted with the 25 mm orifice plate. The change in mass also affects the draft of the buoy, requiring the frequency dependent terms to be recalculated in WAMIT. However, the most significant change is in the parameters used to describe the orifice itself, which changes from a 25 mm orifice plate with an A_{ori} of 0.00049 m^2 and C_d of 0.71, to an equivalent orifice with a C_d of 0.203 with an A_{ori} of 0.0054 m^2, as determined in Section 8.2.3.2.

The change in orifice parameters has a significant impact on the computation time of the estimator, since the timestep needs to be reduced to 0.01 s for the nonlinear hydrodynamic model of the system, used by the estimator, to run correctly. This smaller sampling time means that the estimator requires an approximately 2000 s execution time for a simulation time series of 150 s (on a PC with Intel Core i7-1265U and 32 GB RAM). This is significantly slower than for the case using the orifice plate, and even using a stiffer ordinary differential equation solver than the Runge-Kutta method does not improve the execution time. It has been mentioned already that Matlab is known to be relatively slow interpreted code, so given the execution time is only a single order of magnitude longer than the simulation time series, it is possible that the estimator for the controlled case could still execute in close to real time if compiled code were to be used, and this could be an interesting direction for future research.

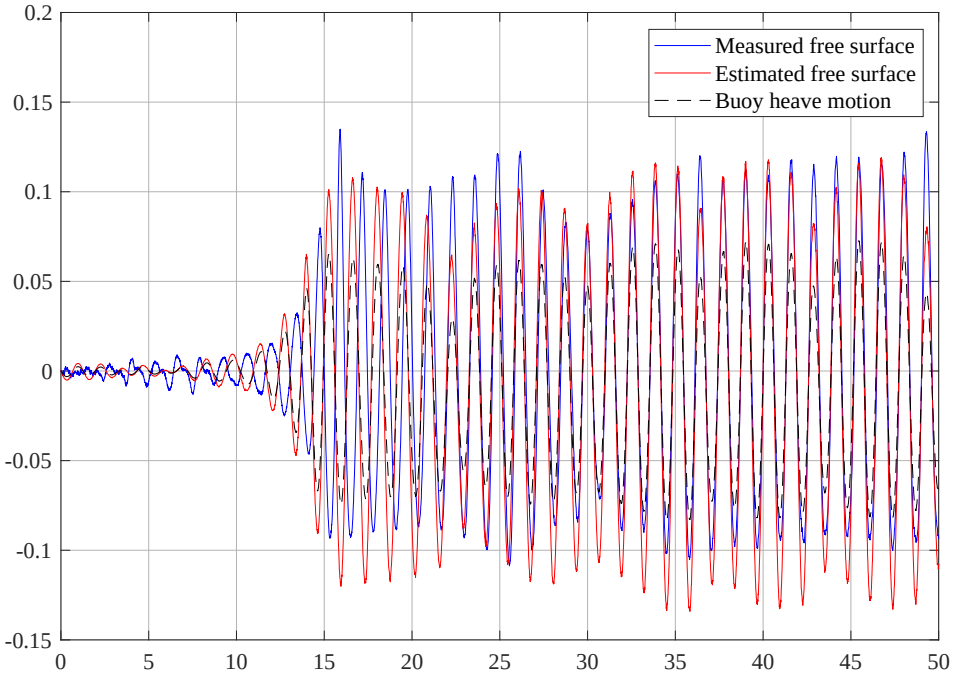


Figure 9.11: Estimated free surface elevation in regular waves, for the test case using a real turbine, compared against the measured free surface, and the heave displacement of the buoy itself.

Aside from the slower execution time, the estimator is still shown to work well in regular waves, as shown in Fig. 9.11. The estimator is tested against a number of regular waves spanning a wave heights of 0.1 m, 0.15 m and 0.2 m, and a range of frequencies from 0.69 Hz to 0.85 Hz, all of which cause the turbine to spin and generate power. As with the previous two test cases it is possible to assess the GoF for the estimated free surface elevation in regular wave tests which is found to be in the range of 56% to 74 %, suggesting a relatively good fit for the regular waves tested. The accuracy for the estimates of T_z and H_s are also relatively good, as shown in Fig. 9.13 and Table 9.4, though the accuracy is lower than for the fully sealed moonpool or orifice plate test cases, with the magnitude of errors on average 13.4% and 4.5% for H_s and T_z respectively. However, when compared to the values for H_s and T_z based on the buoy motion alone, the test case with a working turbine behaves the least like a wave follower, and the improvement in using the estimator values over those from buoy motion alone is considerable.

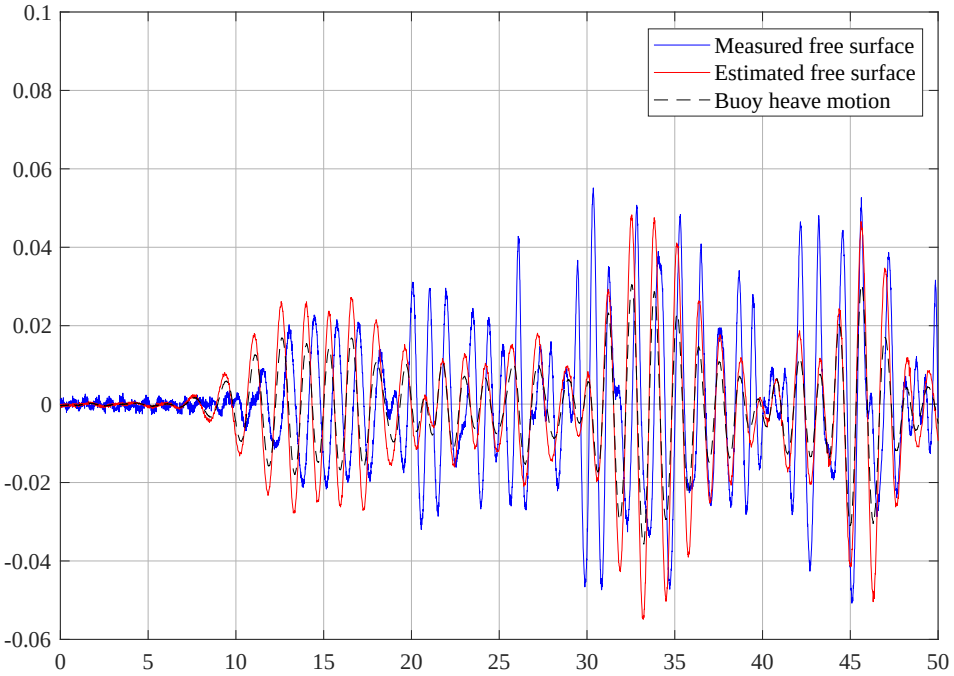


Figure 9.12: Estimated free surface elevation in irregular waves, generated by a JONSWAP spectrum for the test case using a real turbine, compared against the measured free surface, and the heave displacement of the buoy itself.

As well as testing the estimator in regular waves, three different types of wave spectra are also used to generate irregular waves to test the estimator against. The first of these are irregular waves generated using a JONSWAP spectrum, as shown in Fig. 9.12. As can be seen in Fig. 9.12, there is some discrepancy between the measured free surface and the estimated free surface, with a number of large peaks not estimated

between 20 s and 30 s. After these initial missed peaks, the estimator performs better, suggesting that it is likely the peaks measured by the wave probes were on a wave which had breaking in the centre and therefore did not reach the device at the same level of magnitude. Because the aim is for the turbine to spin in the irregular tests, the wave conditions set for the JONSWAP tests are near the limit of where wave breaking occurs, and some waves were observed to break during JONSWAP testing. Though snatch loads were mostly avoided in the second test campaign at Lir NOTF, the comparison between measured and estimated free surface is still affected by changes in phase, driven by the buoy drifting in the surge direction. Despite drifting in surge and some breaking waves making an NRMSE-based GoF fit inaccurate, H_s and T_z are successfully recovered across a range of 20 s acquisition windows across the 20 minute test time for the JONSWAP waves, summarised in Table 9.4.

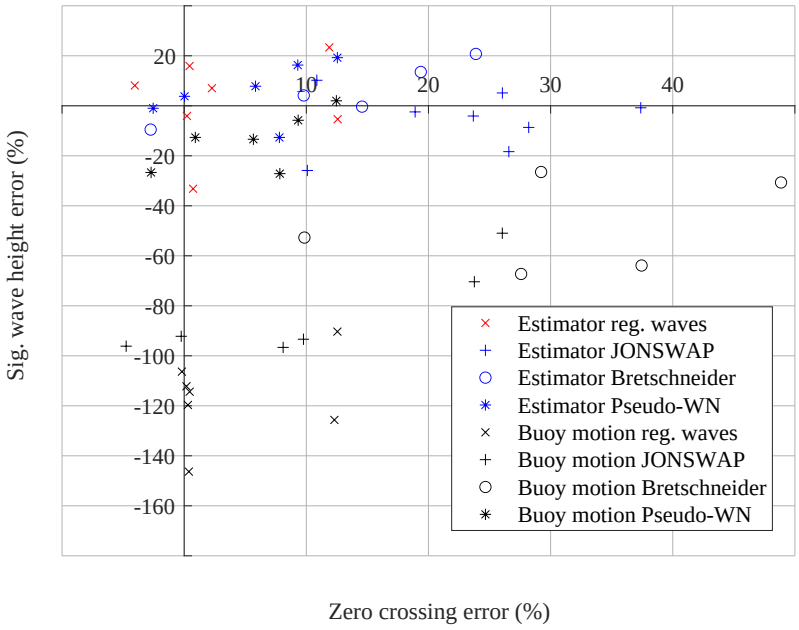


Figure 9.13: Scatter plot for the real turbine tests, showing the errors in obtaining T_z and H_s, with positive errors showing overestimation, and negative errors showing underestimation.

As shown in Fig. 9.13, the free surface estimates in irregular waves using a JONSWAP spectrum, are again less accurate than the orifice plate test case in irregular waves. It must be noted, however, that the irregular waves tested for the orifice plate use synthetic data and, therefore, are not subject to the same drift in the surge direction between buoy and reference wave probe that are evident in the irregular waves tests using the buoy fitted with a turbine. Indeed such drifting, alongside the effects of breaking waves, likely contributes to the relatively poor estimates of T_z obtained in irregular waves generated by a JONSWAP spectrum, where the average magnitude

of error is 22.7%. The estimates of H_s in JONSWAP waves are significantly better, on average falling within a 10% error band.

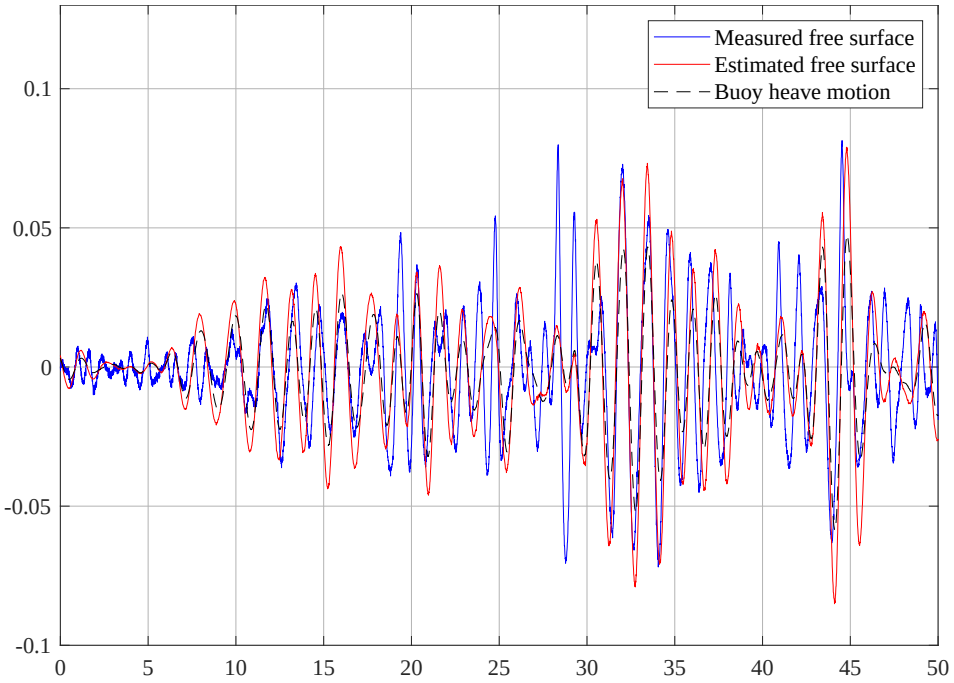


Figure 9.14: Estimated free surface elevation in irregular waves, generated by a Bretschneider spectrum for the test case using a real turbine, compared against the measured free surface, and the heave displacement of the buoy itself.

Using irregular waves generated by a Bretschneider spectrum, shown in Fig. 9.12, a better fit is observed compared to the JONSWAP waves, with little wave breaking evident during testing; though drifting from the device datum position clearly affects the phase when compared to the free surface elevation measured by the reference probe. An improvement in estimated values of T_z is also observed in Fig. 9.13 with an average magnitude of error of 14.1%. Estimates of H_s again mostly fall within a 10% error band, showing a relatively good estimator performance in irregular waves generated by a Bretschneider spectrum, run for 15 minutes.

Finally, the performance in higher energy irregular waves, based on the pseudo band-limited white-noise (PBLWN) spectrum described in Section 3.2.3, is also assessed, again run for 15 minutes. Fig. 9.15 is a clear example of the effect that the buoy drifting from its position with respect to the reference probe has on the estimated free surface elevation. Fig. 9.15 shows a generally strong correlation between the measured and estimated free surface elevation, but when the surge position exceeds the range from approximately -0.25 m to 0.25 m from the datum position there is a clear difference in phase between the measured and estimated free surface, as the buoy changes its position with respect to the reference wave probe. Indeed it can be seen from Fig. 9.15 that

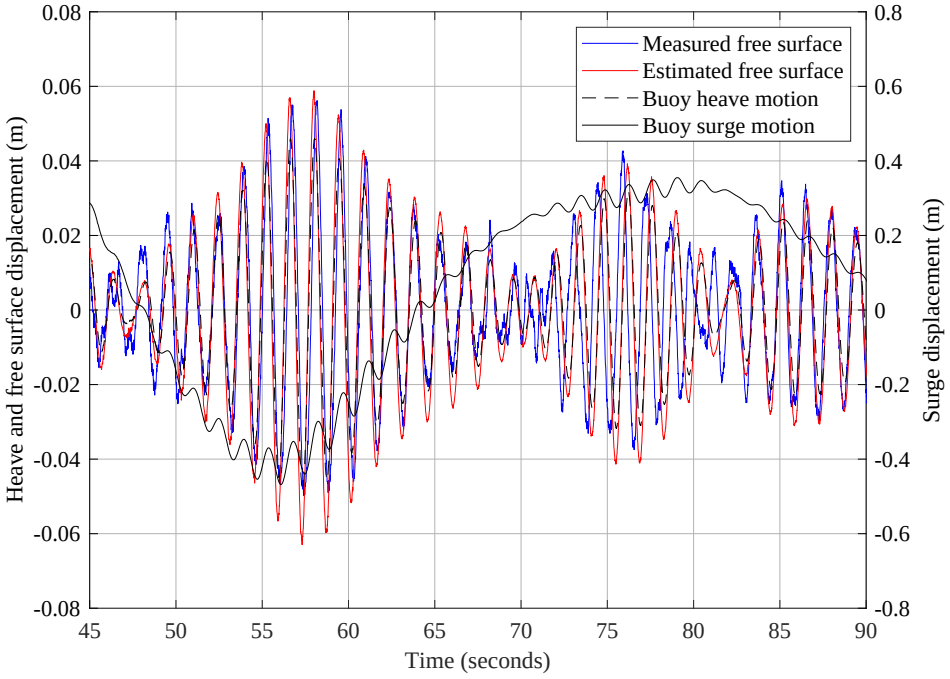


Figure 9.15: Comparison of estimator performance in irregular waves, generated by a pseudo band-limited white-noise spectrum for the test case using a real turbine. Buoy surge motion is also included on the right y-axis, showing the effects that drifting in the surge direction has on the estimator phase (positive surge is in the direction of wave propagation).

when surge is positive (in the direction of wave propagation), the estimates lag behind, while for negative surge values (against the direction of wave propagation) the estimates lead the measured free surface. Overall, for the irregular wave tests, the estimates of free surface elevation, in waves produced by the pseudo band-limited white-noise spectrum, have the highest accuracy in terms of estimates of T_z and H_s, with the errors for both wave characteristic parameters falling close to or within the 10% error band, comparative to the industry standard of H_{mo}. Of the irregular test cases the pseudo band-limited white-noise spectrum also excited the turbine PTO the most, with some power peaks reaching 16 mW during testing, as shown in Fig. 9.16.

Table 9.4: Comparison of estimated and measured free surface, across 20 s acquisition windows, against using device heave motion directly, for the device using an OWC with a controlled turbine PTO. GoF comparing estimated to measured waves is again only obtained in regular tests, where the device surge position does not change with respect to the wave probe once steady state oscillation is reached.

Wave Type	Tz **(s)**			H_s **(m)**			**GoF**
	Meas.	**Est.**	**Device**	**Meas.**	**Est.**	**Device**	**(%)**
Regular	1.29	1.29	1.29	0.169	0.163	0.082	69.6
	1.37	1.38	1.38	0.159	0.189	0.072	59.5
	1.33	1.28	1.33	0.154	0.168	0.063	74.0
	1.17	1.33	1.34	0.104	0.135	0.046	70.8
	1.28	1.31	1.29	0.122	0.131	0.057	56.5
	1.09	1.25	1.25	0.083	0.078	0.043	68.6
JONSWAP	0.92	1.29	1.32	0.050	0.046	0.023	
	1.03	1.40	1.03	0.054	0.046	0.028	
	0.88	1.40	1.17	0.050	0.050	0.024	
	1.15	1.29	1.10	0.051	0.057	0.026	
	1.10	1.35	1.19	0.059	0.057	0.030	
	0.97	1.32	1.32	0.063	0.066	0.042	
	1.03	1.36	1.36	0.061	0.059	0.036	
	1.15	1.27	1.27	0.064	0.051	0.033	
Bretschneider	0.87	1.02	1.39	0.059	0.059	0.036	
	1.05	1.38	1.49	0.073	0.092	0.057	
	0.84	1.04	1.64	0.059	0.068	0.045	
	1.34	1.49	1.49	0.079	0.082	0.052	
	1.08	1.05	1.49	0.074	0.067	0.044	
PBLWN	1.33	1.46	1.46	0.073	0.087	0.069	
	1.35	1.43	1.43	0.054	0.059	0.048	
	1.41	1.41	1.43	0.036	0.037	0.032	
	1.19	1.29	1.29	0.053	0.047	0.042	
	1.41	1.37	1.37	0.103	0.102	0.081	
	1.20	1.38	1.37	0.069	0.085	0.070	

9.4 Conclusions and limitations of case study

In this chapter, it is demonstrated that data buoys measuring wave parameters need not be constrained by the assumption that they must be true wave followers. This is most clearly demonstrated by the more realistic nonlinear cases modelled, both where an orifice plate emulates the effects of a turbine PTO and where a real turbine is fitted to the buoy. In both the nonlinear test cases, the behaviour of the buoy considered cannot be described as a wave follower.

This study demonstrates that, using a Kalman filter-based estimator, wave parameters T_z and H_s, alongside free surface elevation, can generally be successfully recovered from a

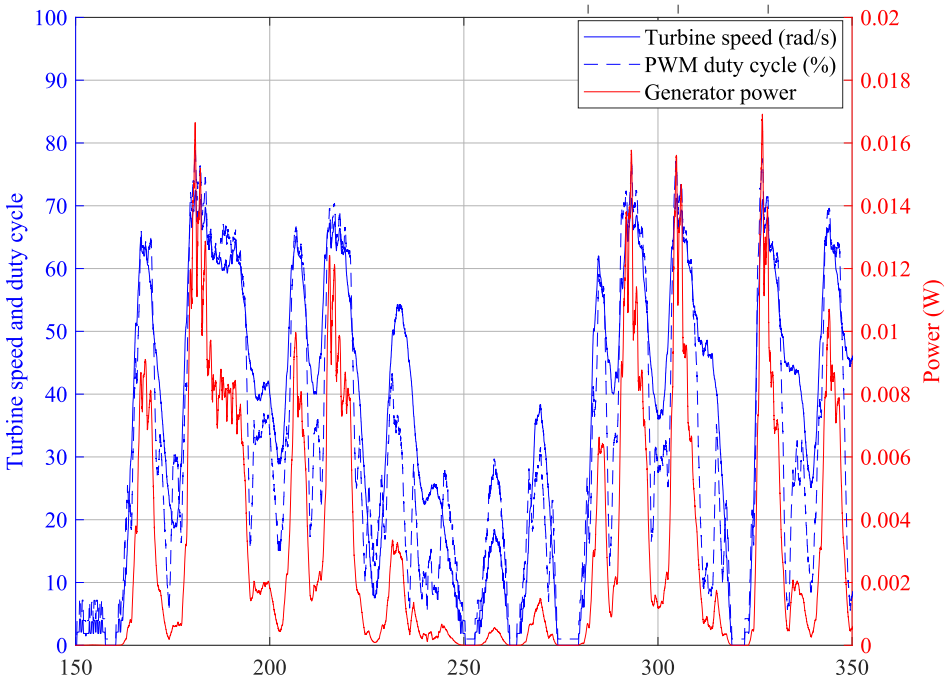


Figure 9.16: Power output during testing at Lir NOTF, in irregular waves generated from a pseudo band-limited white-noise spectrum.

data buoy, accounting for the dynamics of a simulated wave energy PTO. The estimator is also able to recover H_s with an error close to a 10% of the measured values, for almost all of the test cases considered, as shown in Figs. 9.7, 9.9 and 9.13. This accuracy is similar to the current industry standard returned by wave followers of H_{mo}, showing it is entirely possible to use wave powered data buoys to measure wave parameters to the same accuracy as the wave followers currently in use. T_z estimates are generally slightly less accurate than H_s estimates, with the turbine tests in JONSWAP waves being noticeably poorer than any of the other tests considered. During the JONSWAP tests, wave breaking was observed which has an impact on the comparison between measured and estimated waves, since the waves encountered by the reference wave probe do not necessarily match the waves encountered by the device.

The estimated values for T_z, for the turbine test case in irregular waves, are generally larger than the measured values, which is likely due to the device having a low dynamic response to high frequency components in the wave. This is a limitation of using a full size device in waves which are much smaller and higher in frequency than those the device would encounter in real seas. Using a full size device in a relatively small wave tank also means that the wavelength is almost identical to the device dimension. This means that the device pitches significantly, and does not demonstrate the strong heaving behaviour of a point absorber. This has limitations on the amount of power that can be harvested, but also likely has implications for the accuracy of the estimator.

Pitching was most significant for the turbine test case, since the steel Venturi adds a significant mass above the centre of buoyancy.

Though difficult to formally assess for some of the irregular wave tests carried out at Lir NOTF, the ability of the nonlinear estimator to return accurate time series free surface elevation estimates is shown to be strong in regular waves, and in the simulated irregular waves used in Sections 9.1 and 9.2.2. The more realistic waves used in Section 9.1 show a particularly good estimator performance, though a GoF between 69-78% is also achieved in simulated irregular waves for the 25 mm orifice plate in Section 9.2.2. The strong performance in simulated waves, where there is no discrepancy between the measured waves and the waves encountered by the device, suggests that a more accurate method of measuring the incident waves to the device could improve the comparisons between estimated and measured free surface elevation. There are also no unmodelled dynamics in the simulated tests affecting the model used in the estimator, since the model used to generate the simulated device motion is identical to the model used by the estimator.

Although the linear estimator, used in the fully sealed case with no PTO, is able to return accurate values for T_z, outperforming using the buoy displacement directly, there is no difference in accuracy between values obtained for H_s. Since the fully sealed test case is found to be close to a wave follower, and cannot generate power, future work, using a controller with a PTO which can inject energy back into the system, such as a linear generator, could be used with the linear estimator to move the buoy further from being a wave follower, and demonstrate the estimator ability to handle the effects of energy maximising control.

Despite some limitations, the Kalman filter-based soft sensor described in Chapter 8 can be used to account for the effect on device dynamics that a wave energy PTO introduces; both when simulated via an orifice plate and when fitted with a real turbine PTO. The ability to handle changes to the dynamics introduced by a wave energy PTO and still successfully return free surface elevation estimates, shows that wave energy could indeed be used to power data buoys, since the estimator, described in Chapter 8 and tested in this chapter, does not require the device it is mounted on to be a true wave follower.

Tired of running from the question
When the answer is the test

— 49 Winchester, *Leavin' This Holler*.

10 Conclusions and future work

Contents

10.1 Conclusions 208
10.1.1 The state of the art of wave powered data buoys 208
10.1.2 Data based modelling of TENGs 208
10.1.3 Designing and testing a turbine specifically for small scale OWCs 209
10.1.4 Testing a full size wave powered data buoy prototype in a wave tank 210
10.1.5 Designing and testing a free surface elevation estimator for wave powered data buoys 211
10.2 Future work 212
10.3 Final Remarks 212

In this final chapter conclusions are drawn, both on the significance of individual contributions in Section 10.1, but also on the holistic implications drawn from the full body of work presented herein, discussed in Section 10.3. Future work is also suggested which considers the limitations of the research carried out, and suggests how the work described can be built upon to further strengthen the findings of this thesis.

10.1 Conclusions

10.1.1 The state of the art of wave powered data buoys

Within the comprehensive literature review given in Chapter 2, a number of findings stand out, which have implications for the future of wave-powered data buoys. Most notably, the number of new projects given in Table 2.2, considering wave powered data buoys since the publication of the project's first literature review in [14], shows that in spite of the not insignificant challenges posed in using wave energy to power data buoys, momentum is building in this research field. The increase in the rate of wave powered projects being studied shows that solutions are growing which could remove the barriers to more widespread adoption of wave energy as the power source for data buoys.
In [42], the role data buoys have to play in monitoring the oceans, as part of the UN's 17 Goals for Sustainable Development, suggests that research in the area of data buoys will continue to grow, and it is promising that wave energy appears to be rising in visibility as an option for powering the ocean monitoring networks of the future. Indeed, projects such as [55] and [56] show that wave powered data buoy research is seeking to fill a niche in arctic monitoring where solar power is impractical. Furthermore, [58] shows that arctic monitoring is an area where the application of wave energy as a power source for ocean monitoring buoys is particularly suitable, especially as sea ice coverage decreases due to the effects of climate change, increasing fetch length and wave resource in this region, and leaving some Arctic regions free of ice for more than 9 months of the year. This allows it to be concluded that wave energy is not only a promising power source for ocean monitoring buoys, with direct relevance to observation in those areas most affected by changes in the climate, but that through the growing body of research, the hurdles to the widespread adoption of wave powered data buoys are being removed.

10.1.2 Data based modelling of TENGs

TENGs are the PTO chosen in this project as representative of those PTOs directly designed for the small scale. Though the test cases considered in this thesis are relatively limited, being restricted to only wave tank tests in regular waves, it has been shown that data-based modelling methods have promise when it comes to obtaining models of TENGs, which are driven by chaotic movements that cannot be practically modelled from first principles. A wider range of experimental results, covering smaller incremental changes between wave conditions, is needed to further the data-based model discussed in Chapter 5, though the same modelling approach can be used. Since the primary method of testing TENGs, identified in Chapter 2, is through experimental testing, those facilities with access to a greater wealth of test tank data could apply the methods given

in Chapter 5 to build a database of mid-fidelity TENG models. Such an endeavour by a research facility with the capability to manufacture and test their own TENGs, could significantly further the understanding of the relationship between these unusual PTOs and the dynamics of the device upon which they are mounted.
Stronger understanding of the relationship between device movement and TENG output is crucial in truly assessing the advantages that wave energy control could impart on devices using TENGs as PTOs. While there is one study on energy maximising control for TENGs given in [196], the TENG in question has had its motion constrained to the point where it can essentially be modelled as a linear generator. Constraining TENG motion is a trend observed among the few TENGs with existing mid-fidelity models, where constraints on motion are applied in such a way that the actuation is analogous to a conventional linear or rotational generator. However such restrictions on movement undermine the primary appeal of TENGs, which is their ability to harness chaotic movements; be that via the use of tendrils or rolling balls. Furthermore, as shown in [105], rolling-ball-type TENGs can even be stacked on top of one another to increase power output, which cannot be done with these motion constrained TENGs, though stacking further complicates the modelling problem. In such cases, where tendrils, or rolling balls, are used to drive the TENG output, it is difficult to see any alternative to data-based modelling strategies. While reinforcement learning can be used to carry out data-based modelling of TENGs, as shown in [210], the system identification approach described in Chapter 5 is a simpler alternative requiring fewer model inputs (4 compared to 18), with the model trained on the three most similar sea states showing particular promise for simulations where the actual TENG output remains unknown, such as other similar floater geometries.
Obtaining a relatively simple mid-fidelity model of a rolling-ball-type TENG is a contribution of this project, since other mid-fidelity modelling approaches, such as in [196], [198] and [199], impose severe motion constraints on the TENG, to allow a first principles modelling approach to be applied, undermining the unique strength of TENGs as a wave energy PTO.

10.1.3 Designing and testing a turbine specifically for small scale OWCs

The design and characterisation of a self-starting Wells turbine for small scale OWCs is a significant contribution of this project. While some studies do consider aerofoils at low Reynolds numbers [258] [259] [260], none consider flows with as low a Reynolds number as those experienced by either the fixed- or floating OWC in this project. Using a thicker blade profile than is normally considered, is a significant contributing factor to

the performance of the turbine in low Reynolds number flows, though a larger study iterating on other design parameters may also provide indications of what other changes can be made to improve Wells turbine performance in low Reynolds number flows.
The fact that the turbine tests carried out in a fixed OWC in Chapter 7 are enough to show an efficiency peak in the turbine characteristic performance curve in Fig. 7.4, suggests that even at low Reynolds numbers the designed turbine does not operate purely in the stall region. Tests at DkIT also show that the turbine never reaches a crawl speed, always reaching full operational speed in wave conditions where it self-starts. Developing the characteristic curve to incorporate a wider range of test conditions, including the slightly higher Reynolds number flows experienced in wave tank testing at Lir NOTF would enhance the usefulness of the characteristic curves obtained, though unfortunately, with the limitations of the flows achievable in the fixed OWC at DkIT, such an endeavour was unfeasible within this project.

10.1.4 Testing a full size wave powered data buoy prototype in a wave tank

The development and production of a working wave powered data buoy, through retrofitting a commercial off-the-shelf navigation buoy with a custom made Venturi, within the budget of this project, shows that wave-powered data buoys are indeed an affordable platform for proving wave energy converters. Though the wave sensor function of the buoy was handled in post-processing of experimental data, the power achieved, in the range of 10s to 100s of mW, is comparable to other data buoy projects in the literature (see Tables 2.1 and 2.2). It should also be noted that such power levels were achieved in the limited range of waves that the wave tank at Lir NOTF could produce within the other experimental constraints of the project.
The use of a commercial off-the-shelf buoy has parallels with the project in [56], though [56] goes one step further in using a commercially available gyroscopic PTO. Using available off-the-shelf components in a novel way, presents an opportunity for wave powered data buoys to remain affordable, whilst still proving that wave energy is a viable option for ocean monitoring buoys to use. Increasing the use of wave energy in data buoys, particularly where tested and proven components can be adapted for wave energy purposes, stands not only to make wave power more visible as a renewable technology, but reduces the uncertainty that a relatively nascent technology, such as wave energy, presents to investors. The drawback of using off-the-shelf components, particularly floaters, is that they are not optimised for wave energy applications. While this would present a significant issue for a large scale device, where the primary purpose is the production of energy, the modest power requirements of most sensors on data buoys,

mean that it is possible to generate sufficient power even from floaters not designed for this purpose. Furthermore, the use of floaters which are less responsive to incident waves could even have some advantages, providing a more stable platform for onboard sensors.

10.1.5 Designing and testing a free surface elevation estimator for wave powered data buoys

A significant contribution of this thesis is in the development of a Kalman filter-based free surface estimator, which is tested against both simulation and experimental results. The ability of the estimator to take into account the dynamics of a device which is not a true wave follower, and return relatively accurate estimates of the free surface elevation, counters the perceived requirement that all wave measuring buoys must be true wave followers. While improvements to the measurements of free surface elevation in the experimental set up could be made to allow for more thorough comparisons of estimated free surface against the measured free surface to be made, the experiments carried out in this thesis, and published in [16], suggest that it is feasible to use unknown input estimation to recover free surface elevation data, even from a WEC. The fact that time series free surface elevation data can be recovered by the estimator, shows that the estimator has potential for use in measuring waves, even in applications where time series data is required. Though, due to bandwidth restrictions, most data buoys currently only return wave characteristic parameters, gathered over a set acquisition window, advances in communications technology mean data transfer rates are ever increasing, and with higher transfer rates, time series data may soon become a requirement of wave measuring buoys, particularly as technologies like wave energy emerge.

There are significant limitations to the experiments carried out for this project, particularly with regards to the waves that could be tested with the size of the device. Essentially the experiments consider a real device in unrealistic waves, which, due to the short wavelength compared to device size, restrict the amount of heave motion observed in experiments. This means, that although the device does not behave like a true wave follower in the experiments carried out, its behaviour is not far removed from that of a wave following buoy. This relatively wave following behaviour is compounded by the fact that, as shown in [160] and bourne out in Chapters 7 and 8, OWCs do not have a strong effect on the dynamic behaviour of a device. The use case for the estimator could be strengthened further by using a device with the likes of a linear generator, which could use energy maximising control, to produce behaviour far removed from a true wave follower. As shown in this thesis, the estimator can handle complex systems, and with an appropriate model and knowledge of the control system, could be adapted to a device whose behaviour is completely unlike the wave following buoys currently used in measuring wave parameters.

10.2 Future work

Suggestions have already been made in Section 10.1 for strengthening the conclusions drawn in this thesis. However, though the scope of this PhD thesis is relatively broad, considering many aspects of data buoy design, there are a number of aspects of wave powered data buoy design which have been neglected. While some elements such as PTO modelling and wave sensing requirements have been researched in considerable detail, aspects such as floater geometry and advanced control, are areas of wave powered data buoy design that could be explored in future.

Though using an off-the-shelf navigation buoy, in both the TENG testing and the testing of the OWC, has distinct advantages, as discussed in Section 10.1.4, the fact remains that such devices are not designed for wave energy applications. While designing a bespoke hull, optimised around the requirements of a wave powered data buoy, could make for an interesting project, the costs associated with manufacturing bespoke floater geometries are likely unfeasible for most research projects. Instead, a more useful study could be a comparison of the many existing off-the-shelf buoys available on the market, which include geometries more varied than just navigation buoys. Such a study could be tailored to the type of PTO proposed (as well as its control system) and the expected sensors that the data buoy is expected to be outfitted with, to determine the suitability of each geometry as the floater for a wave powered data buoy.

It should also be noted that, though the turbine PTO on the OWC is subject to set point tracking control, the effects of the controller on the device dynamics are found to be negligible. As previously mentioned, a PTO such as a linear generator would have a significantly greater impact on device dynamics, particularly when subject to some form of energy maximising control. As well as being a stronger test case for the free surface elevation estimator, exploring the constraints on the controller could also make an interesting area of study. Since the primary purpose of wave-powered data buoys is to monitor environmental parameters rather than to harness the maximum energy from a passing wave, a study exploring the trade-off for a controller balancing energy requirements with stability could be a valuable field of further research. Though [70] attempts to consider this trade-off, the PTO used is again an OWC, meaning that there are limitations to the effects that the controller can have on the system.

10.3 Final Remarks

This thesis contains a significant contribution to the field of wave-powered data buoy research. Through considering challenges posed in modelling the chaotic PTO behaviour of TENGs, a method is proposed which can be more widely applied towards producing

a mid-fidelity model of this recently invented PTO, while still maintaining its primary strength, namely its ability to harness chaotic motion. Through the development and testing of a Wells turbine specifically for the small scale, the viability of using OWCs on devices smaller than currently considered in the literature is shown, demonstrating a successful example of tackling the challenges in scaling down a conventional PTO to the data buoy scale. A rebuttal of the common presumption that wave measuring buoys to be true wave followers, is also given, via the design and evaluation of a free surface elevation estimator. Given the high number of new data buoy projects that have come into fruition since the publishing of the literature review in [14], as well as the high number of citations that [14] has acquired, it is clear that the interest around wave powered data buoys is growing. Not only do small scale wave powered data buoys present a hopeful vanguard for the adoption of wave energy more generally, with the hope that increased visibility and success at the small scale facilitates the development of more large scale projects in future, but they also represent a relevant and useful alternative to providing power in monitoring our oceans in applications and locations where solar power is unfeasible.

References

[1] A. Meindl, "Guide to moored buoys and other ocean data acquisition systems," *Intergovernmental Oceanographic Commission of UNESCO*, vol. 8, pp. 21–22, 1996.

[2] Y. Masuda, "An experience of wave power generator through tests and improvement," in *Proc. Hydrodynamics of Ocean Wave-Energy Utilization*, (Berlin, Germany), pp. 445–452, 1986.

[3] J. C. C. Henriques, J. C. C. Portillo, L. M. C. Gato, R. P. F. Gomes, D. N. Ferreira, and A. F. O. Falcão, "Design of oscillating-water-column wave energy converters with an application to self-powered sensor buoys," *Energy*, vol. 112, pp. 852–867, 2016.

[4] BBC News Scotland, *Wave power firm Pelamis calls in administrators*, (Accessed on: Aug. 31, 2021), 2014. [Online]. Available: `https://www.bbc.com/news/uk-scotland-scotland-business-30151276`.

[5] Deloitte, *Report to Creditors pursuant to Section 439A of the Corporations Act 2001*, (Accessed on: Aug. 31, 2021), 2014. [Online]. Available: `https://www2.deloitte.com/content/dam/Deloitte/au/Documents/finance/insolvency/oceanlinx/deloitte-au-fas-439a-report-271014.pdf`.

[6] BBC News Scotland, *Aquamarine power calls in administrators*, (Accessed on: Aug. 31, 2021), 2015. [Online]. Available: `https://www.bbc.com/news/uk-scotland-scotland-business-34659324`.

[7] ABC Radio Adelaide, *Wrecked Oceanlinx wave generator 'saga' at Carrickalinga continues with further delays*, (Accessed on: Aug. 31, 2021), 2020. [Online]. Available: `https://www.abc.net.au/news/2020-04-28/oceanlinx-generator-still-stranded-at-carrickalinga/12190502`.

[8] C. A. Barry and J. V. Ringwood, "Wave energy technology development in Ireland: Employing the triple helix model of innovation for pragmatic policy interventions," *Technology in Society*, vol. 81, p. 102 872, 2025.

[9] J. Shepard, *EE Power: Lockheed Martin and Victorian Wave partner on 62MW wave energy project*, (Accessed on: Aug. 31, 2021), 2014. [Online]. Available: `https://eepower.com/news/lockheed-martin-and-victorian-wave-partner-on-62mw-wave-energy-project/`.

[10] OPT, *PB3 PowerBuoy*, (Accessed on: Aug. 30, 2021), 2021. [Online]. Available: https://oceanpowertechnologies.com/pb3-powerbuoy/.

[11] G. Parkinson, *Renew economy: World's "biggest" wave energy project sinks without trace*, (Accessed on: Aug. 31, 2021), 2014. [Online]. Available: https://reneweconomy.com.au/worlds-biggest-wave-energy-project-sinks-without-trace-30448/.

[12] C. Rodrigues, D. Nunes, D. Clemente, N. Mathias, J. M. Correia, P. Rosa-Santos, F. Taveira-Pinto, A. P. T. Morais, and J. Ventura, "Emerging triboelectric nanogenerators for ocean wave energy harvesting: State of the art and future perspectives," *Energy and Environmental Science*, vol. 13, pp. 2657–2683, 2020.

[13] R. Xu, H. Wang, Z. Xi, W. Wang, and M. Xu, "Recent progress on wave energy marine buoys," *Journal of Marine Science and Engineering*, vol. 10, p. 566, 2022.

[14] I. McLeod and J. V. Ringwood, "Powering data buoys using wave energy: A review of possibilities," *Journal of Ocean Engineering and Marine Energy*, vol. 8, pp. 1–16, 2022.

[15] I. McLeod, D. Clemente, P. R. Santos, F. T. Pinto, M. Rosati, and J. V. Ringwood, "Mathematical modelling of a TENG-powered data buoy," in *Proc. OCEANS 2023*, (Limerick, Ireland), pp. 1–10, 2023.

[16] I. McLeod, B. Walsh, T. Kelly, and J. V. Ringwood, "Free surface elevation estimator as a sensor for wave-powered data buoys," *IEEE Journal of Oceanic Engineering*, vol. 50, pp. 2232–2247, 2025.

[17] A. Hamilton, F. Cazenave, D. Forbush, R. G. Coe, and G. Bacelli, "The MBARI-WEC: A power source for ocean sensing," *Ocean Engineering and Marine Energy*, vol. 7, pp. 189–200, 2021.

[18] S. Chen, B. Guo, H. A. Said, K. Yang, and J. V. Ringwood, "Wave-to-wire modelling of a vibro-impact wave energy converter for ocean data buoys," *IFAC-PapersOnline (22nd IFAC World Congress)*, vol. 56, pp. 11 735–11 740, 2023.

[19] E. N. Bernard and C. Meinig, "History and future of deep-ocean tsunami measurements," in *Proc. OCEANS'11 MTS/IEEE KONA*, (Kona, USA), pp. 1–7, 2011.

[20] Datawell, *Product list*, (Accessed on: Aug. 31, 2021), 2021. [Online]. Available: https://www.datawell.nl/products/buoys.aspx.

[21] T. Hlophe, P. H. Taylor, J. E. Hansen, H. Wolgamot, and M. V. Cuttler, "Comparison of vector wave displacements from a moored and a drifting spotter buoy—from an accidental indian ocean voyage," *Ocean Engineering*, vol. 328, p. 120 967, 2025.

[22] P. Ditlevsen and S. Ditlevsen, "Warning of a forthcoming collapse of the Atlantic meridional overturning circulation," *Nature Communications*, vol. 14, p. 4254, 2023.

[23] D. M. Toma, M. Carandell, and J. del Río, "Performance of wavy ocean lagrangian drifters for surface characterization of ocean dynamic structures," in *Proc. IEEE International Workshop on Metrology for the Sea*, (Milazzo, Italy), pp. 133–137, 2022.

[24] Y. Hisaki, "Use of drifting buoys for wave observation: Effect of current on wave data," *Deep Sea Research Part I: Oceanographic Research Papers*, vol. 195, p. 103 986, 2023.

[25] National Oceanic and Atmospheric Administration (NOAA), *Ndbc observation via an interactive map*, (Accessed on: Jul. 21, 2025), 2025. [Online]. Available: `https://www.resenwaves.com/`.

[26] Mobilis, *Data acquisition buoys*, (Accessed on: Aug. 30, 2021), 2021. [Online]. Available: `https://mobilis-sa.com/en/products/data-acquisition-buoys/`.

[27] MET Éireann, *Happy birthday buoys*, (Accessed on: Aug. 31, 2021), 2021. [Online]. Available: `https://www.met.ie/happy-birthday-buoys`.

[28] M. Nic Guidhir, D. Kennedy, A. Berry, B. Christy, C. Clancy, C. Creamer, G. Westbrook, and S. Gallagher, "Irish wave data—rogues, analysis and continuity," *Journal of Marine Science and Engineering*, vol. 10, p. 1073, 2022.

[29] COMPASS, *The COMPASS project*, (Accessed on: Jul. 24, 2025), 2021. [Online]. Available: `https://compass-oceanscience.eu/`.

[30] MELOA, *WAVY drifters*, (Accessed on: Aug. 29, 2021), 2017. [Online]. Available: `https://www.ec-meloa.eu/pages/wavy-drifters`.

[31] M. Carandell, D. M. Toma, M. Carbonell, J. del Rio, and M. Gasulla, "Design and testing of a kinetic energy harvester embedded into an oceanic drifter," *IEEE Sensors Journal*, vol. 20, pp. 13 930–13 939, 2020.

[32] M. Carandell, J. Tichy, J. Smilek, et al., "Electromagnetic rolling mass wave energy harvester for oceanic drifter applications," *European Physical Journal Special Topics*, vol. 231, pp. 1475–1484, 2022.

[33] ESA, *Sea and space meet for business in Ireland*, (Accessed on: Oct. 01, 2021), 2012. [Online]. Available: `https://www.esa.int/Space%5C_in%5C_Member%5C_States/Ireland/Sea%5C_and%5C_space%5C_meet%5C_for%5C_business%5C_in%5C_Ireland`.

[34] A. Pirisi, F. Grimaccia, M. Mussetta, R. E. Zich, R. Johnstone, M. Palaniswami, and S. Rajasegarar, "Optimization of an energy harvesting buoy for coral reef monitoring," in *Proc. IEEE Congress on Evolutionary Computation*, (Cancun, Mexico), pp. 629–634, 2013.

[35] I. Masmitja, N. Palomeras, D. M. Toma, N. Bahamon, M. Carandell, J. A. García del Arco, D. Chatzievangelou, M. Real, A. Sánchez-Márquez, G. Batet, P. Vial, F. Bonin-Font, C. Muntaner, N. Hurtós, J. M. López, A. R. Ripoll, G. de Arcas, J. Grinyó, S. Gomariz, K. Katija, J. Aguzzi, M. Carreras, J. del-Rio, J. Navarro, and J. B. Company, "Interconnected robotic platforms inform deep-sea ecological restoration trends," *Marine Pollution Bulletin*, vol. 219, p. 118 314, 2025.

[36] D. Clemente, P. Rosa-Santos, and F. Taveira-Pinto, "On the potential synergies and applications of wave energy converters: A review," *Renewable and Sustainable Energy Reviews*, vol. 135, p. 110 162, 2021.

[37] M. Carandell, S. Hernández, D. M. Toma, E. Martínez, M. Nogueras, J. Aguzzi, and J. del Río, "Expanding the underwater communication capabilities of seafloor ecosystem monitoring stand-alone platforms using pop-up buoys," in *Proc. OCEANS 2023*, (Limerick, Ireland), pp. 1–7, 2023.

[38] Y. Sun, S. Wu, Y. Chen, Z. Tu, A. Yi, and C. Yang, "Disposable portable buoy for data transmission between seafloor equipment and onshore laboratories," *Ocean Engineering*, vol. 301, p. 117 574, 2024.

[39] M. Gee, J. Aguzzi, G. Picardi, I. Masmitjà Rusiñol, D. Chatzievangelou, N. Bahamón Rivera, J. Grinyó Andreu, N. J. Robinson, M. Clavel-Henry, J. B. Company Claret, J. d. Río Fernández, M. Francescangeli, D. Toma, M. Carandell Widmer, E. Martínez Padró, E. Chatzidouros, M. Karakitsiou, L. Constantinou, A. Chronakis, M. Hlatky, Z. Zhang, F. Hayati, S. Roshanmanesh, G. Fernando, and M. Papaelias, "Technical challenges in achieving widespread implementation of wave energy converter systems and future directions," in *Proc. 77th IIW Annual Assembly and International Conference*, (Rhodes, Greece), pp. 1–4, 2024.

[40] H. Li, J. Wu, X. Shi, L. Kong, W. Kong, Z. Zhang, Y. Pan, D. Luo, and J. Yan, "A self-powered smart wave energy converter for sustainable sea," *Mechanical Systems and Signal Processing*, vol. 220, p. 111 641, 2024.

[41] J. Cortés, F. Lucero, L. Suarez, C. Escauriaza, S. A. Navarrete, G. Tampier, C. Cifuentes, R. Cienfuegos, D. Manriquez, B. Parragué, N. Osiadacz, and R. Finke, "Open sea lab: An integrated coastal ocean observatory powered by wave energy," *Journal of Marine Science and Engineering*, vol. 10, p. 1249, 2022.

[42] T. Dillon, B. Maurer, M. Lawson, D. S. Jenne, D. Manalang, E. Baca, and B. Polagye, "Cost-optimal wave-powered persistent oceanographic observation," *Renewable Energy*, vol. 181, pp. 504–521, 2022.

[43] D. Wang, H. Gu, B. Ren, and P. K. Stansby, "Numerical investigation into wave energy harvesting performance of fish-finding buoy with inner vertical pendulum," *SSRN Preprint*, pp. 1–26, 2025.

[44] B. Fullerton, M. Swift, S. Boduch, O. Eroshkin, and G. Rice, "Design and analysis of an automated feed-buoy for submerged cages," *Aquacultural Engineering*, vol. 32, pp. 95–111, 2004.

[45] Q. Xie, T. Zhang, Y. Pan, Z. Zhang, Y. Yuan, and Y. Liu, "A novel oscillating buoy wave energy harvester based on a spatial double X-shaped mechanism for self-powered sensors in sea-crossing bridges," *Energy Conversion and Management*, vol. 204, p. 112 286, 2020.

[46] P. R. Steenstrup, *Resenwaves*, (Accessed on: Aug. 10, 2021), 2015. [Online]. Available: `https://www.resenwaves.com/`.

[47] K. Kevin, E. F. Simanjuntak, A. R. Utomo, F. Husnayain, F. H. Jufri, and D. Riana Aryani, "Study on micro-scale ocean wave power generator using oscillating water column system with piezoelectric," in *Proc. 8th International Electrical Engineering Congress, Chiang Mai, Thailand*, pp. 1–4, 2020.

[48] J. Curcio, P. McGillivary, K. Fall, A. Maffei, K. Schwehr, B. Twiggs, C. Kitts, and P. Ballou, "Self-positioning smart buoys, the un-buoy solution: Logistic considerations using autonomous surface craft technology and improved communications infrastructure," in *Proc. IEEE OCEANS Conference*, (Boston, USA), pp. 1–5, 2006.

[49] S. F. Nabavi, A. Farshidianfar, and A. Afsharfard, "Novel piezoelectric-based ocean wave energy harvesting from offshore buoys," *Applied Ocean Research*, vol. 76, pp. 174–183, 2018.

[50] TechWorks Marine, *What we do: Data buoys*, (Accessed on: Aug. 10, 2021), 2021. [Online]. Available: `https://techworks.ie/en/what-we-do/data-buoys/`.

[51] Office of Energy Efficiency and Renewable Energy, *Wind Measurement Buoy Advances Offshore Wind Energy*, (Accessed on: Sept. 01, 2021), 2015. [Online]. Available: `https://www.energy.gov/eere/Articles/wind-measurement-buoy-advances-offshore-wind-energy`.

[52] AXYS Technologies, *FLiDAR WindSentinels*, (Accessed on: Sept. 01, 2021), 2021. [Online]. Available: `https://axystechnologies.com/products/flidar-windsentinel/`.

[53] K. Yang, A. Abdelkefi, X. Li, Y. Mao, L. Dai, and J. Wang, "Stochastic analysis of a galloping-random wind energy harvesting performance on a buoy platform," *Energy Conversion and Management*, vol. 238, p. 114 174, 2021.

[54] Commisioners of Irish Lights, *Renewable energy*, (Accessed on: Jul. 23, 2025), 2025. [Online]. Available: `https://www.irishlights.ie/environment/renewable-energy.aspx`.

[55] H. Jung, Z. Lu, W. Hwang, B. Friedman, A. Copping, R. Branch, and Z. D. Deng, "Modeling and sea trial of a self-powered ocean buoy harvesting arctic ocean wave energy using a double-side cylindrical triboelectric nanogenerator," *Nano Energy*, vol. 135, p. 110 641, 2025.

[56] R. Branch, J. R. McVey, F. Ticona Rollano, R. J. Cavagnaro, A. Turpin, E. Geon, B. Roberts, M. Steele, A. Nawaz, M. Wickett, and M. Wickett, "Wave energy converter buoy for arctic observations," *Renewable Energy*, p. 123 497, 2025.

[57] I. G. Rigor, P. Clemente-Colon, and E. Hudson, "The international arctic buoy programme (iabp): A cornerstone of the arctic observing network," in *OCEANS 2008*, (Quebec City, Canada), pp. 1–3, 2008.

[58] R. Branch, F. Ticona Rollano, E. Cotter, J. R. McVey, R. J. Cavagnaro, and I. Rigor, "Marine renewable energy for arctic observations," *Frontiers in Marine Science*, vol. 9, pp. 1–13, 2022.

[59] V. Smil, "Waiting for superbatteries: They still can't match the energy density of liquid fuel," *IEEE Spectrum*, vol. 59, pp. 21–21, 2022.

[60] X. Liu, S. Yue, L. Lu, and J. Li, "Investigation of the dust scaling behaviour on solar photovoltaic panels," *Journal of Cleaner Production*, vol. 295, p. 126 391, 2021.

[61] R. Carolan, B. Walsh, M. Boland, T. Dooley, and T. Kelly, "The design and construction of a prototype WASP - a novel wave measuring buoy," in *Proc. 13th European Wave and Tidal Energy Conference (EWTEC)*, (Napoli, Italy), pp. 1594-1-1594–8, 2019.

[62] M. Boland, T. Kelly, R. Carolan, B. Walsh, and T. Dooley, "Scale model testing of the WASP - a novel wave measuring buoy," in *Proc. 13th European Wave and Tidal Energy Conference (EWTEC)*, (Napoli, Italy), pp. 1531-1-1531–9, 2019.

[63] A. Hegarty, "Broadening out the working footprint of a cabled seabed observatory using an interconnected surface buoy, and examining the potential to achieve similar utility from a stand-alone buoyed platform," Ph.D. dissertation, Centre for Robotics and Intelligent Systems, University of Limerick, 2021.

[64] B. Fenu, V. Attanasio, P. Casalone, R. Novo, G. Cervelli, M. Bonfanti, S. A. Sirigu, G. Bracco, and G. Mattiazzo, "Analysis of a gyroscopic-stabilized floating offshore hybrid wind-wave platform," *Journal of Marine Science and Engineering*, vol. 8, p. 439, 2020.

[65] R. Ahamed, K. McKee, and I. Howard, "Advancements of wave energy converters based on power take off (PTO) systems: A review," *Ocean Engineering*, vol. 204, p. 107 248, 2020.

[66] S. McArthur and T. K. A. Brekken, "Ocean wave power data generation for grid integration studies," in *Proc. IEEE Power and Energy Society General Meeting*, (Minneapolis, USA), pp. 1–6, 2010.

[67] E. R. Silva, A. V. Tulcidas, O. Ferreira, R. Bayón, A. Igartua, G. Mendoza, F. M. Mergulhão, S. I. Faria, L. C. Gomes, S. Carvalho, and J. C. M. Bordado, "Assessment of the environmental compatibility and antifouling performance of an innovative biocidal and foul-release multifunctional marine coating," *Environmental Research*, vol. 198, p. 111 219, 2021.

[68] J. Thomson, J. Talbert, A. de Klerk, A. Brown, M. Schwendeman, J. Goldsmith, J. Thomas, C. Olfe, G. Cameron, and C. Meinig, "Biofouling effects on the response of a wave measurement buoy in deep water," *Journal of Atmospheric and Oceanic Technology*, vol. 32, pp. 1281–1286, 2015.

[69] J. Davidson and V. Nava, "Targeting the high frequency tail of wave spectra for energy harvesting in marine sensor networks," *Renewable Energy*, vol. 237, p. 121 550, 2024.

[70] N. Mathias, R. N. Marini, T. Morais, P. Luís, M. Vaz, and P. Rosa-Santos, "Response of a self-powered offshore floating support structure with an OWC for powering a LIDAR device," *Ocean Engineering*, vol. 220, p. 108 366, 2021.

[71] C. Windt, N. Faedo, M. Penalba, F. Dias, and J. V. Ringwood, "Reactive control of wave energy devices – the modelling paradox," *Applied Ocean Research*, vol. 109, p. 102 574, 2021.

[72] M. D. Earle, "Nondirectional and directional wave data analysis procedures (NDBC technical document 03-01)," *United States of America Department of Commerce*, pp. 1–51, 2003.

[73] G. Nolan, J. Ringwood, and B. Holmes, "Short term wave energy variability off the west coast of Ireland," in *Proc. 7th European Wave and Tidal Energy Conference (EWTEC)*, (Porto, Portugal), pp. 1–10, 2007.

[74] J. V. Ringwood, G. Bacelli, and F. Fusco, "Energy-maximizing control of wave-energy converters: The development of control system technology to optimize their operation," *IEEE Control Systems Magazine*, vol. 34, pp. 30–55, 2014.

[75] R. G. Coe, M. C. Devin, C. A. M. Ströfer, J. Lee, G. Bacelli, A. Keow, D. T. Gaebele, J. Grasberger, S. J. Spencer, J. Spinneken, V. S. Neary, and B. Meuris, "Co-design of a wave energy converter for autonomous power," *IFAC-PapersOnLine (CAMS 2024)*, vol. 58, pp. 446–451, 2024.

[76] S. Lindroth and M. Leijon, "Offshore wave power measurements—a review," *Renewable and Sustainable Energy Reviews*, vol. 15, pp. 4274–4285, 2011.

[77] C. Albaladejo, P. Sánchez, A. Iborra, F. Soto, J. A. López, and R. Torres, "Wireless sensor networks for oceanographic monitoring: A systematic review," *Sensors*, vol. 10, pp. 6948–6968, 2010.

[78] G. Xu, W. Shen, and X. Wang, "Applications of wireless sensor networks in marine environment monitoring: A survey," *Sensors*, vol. 14, pp. 16 932–16 954, 2014.

[79] E. Felemban, F. K. Shaikh, U. M. Qureshi, A. A. Sheikh, and S. B. Qaisar, "Underwater sensor network applications: A comprehensive survey," *International Journal of Distributed Sensor Networks*, vol. 11, 2015.

[80] M. Lehmann, *CalWave xNode*, (Accessed on: Sept. 08, 2021), 2021. [Online]. Available: `https://calwave.energy/solutions/`.

[81] R. Walden, C. Kumar, D. M. Mulvihill, and S. C. Pillai, "Opportunities and challenges in triboelectric nanogenerator (TENG) based sustainable energy generation technologies: A mini-review," *Chemical Engineering Journal Advances*, vol. 9, p. 100 237, 2022.

[82] P. Yadav, K. Sahay, A. Verma, D. Maurya, and B. Yadav, "Applications of multifunctional triboelectric nanogenerator (TENG) devices: Materials and prospects," *Sustainable Energy and Fuels*, vol. 7, pp. 3796–3831, 2023.

[83] A. A. Ahmed, T. F. Qahtan, T. O. Owolabi, A. O. Agunloye, M. Rashid, and M. Sultan, "Waste to sustainable energy based on TENG technology: A comprehensive review," *Journal of Cleaner Production*, vol. 448, p. 141 354, 2024.

[84] S. M. Vahidhosseini, S. Rashidi, and M. H. Ehsani, "Efficient energy harvesting using triboelectric nanogenerators (TENGs): Integration with technologies, wearable applications, and future trends," *Renewable and Sustainable Energy Reviews*, vol. 216, p. 115 662, 2025.

[85] S. M. Vahidhosseini, S. Rashidi, and M. H. Ehsani, "Enhancing sustainable energy harvesting with triboelectric nanogenerators (TENGs): Advanced materials and performance enhancement strategies," *Renewable and Sustainable Energy Reviews*, vol. 216, p. 115 663, 2025.

[86] J. Cui, J. Bao, W. Gao, Z. L. Wang, and B. Chen, "Breakthroughs and challenges in cylindrical TENGs toward high-efficiency harvesting high-entropy energy," *Nano Energy*, vol. 141, p. 111 138, 2025.

[87] Z. L. Wang, T. Jianga, and L. Xu, "Toward the blue energy dream by triboelectric nanogenerator networks," *Nano Energy*, vol. 39, pp. 9–23, 2017.

[88] T. Zhao, M. Xu, X. Xiao, Y. Ma, Z. Li, and Z. L. Wang, "Recent progress in blue energy harvesting for powering distributed sensors in ocean," *Nano Energy*, vol. 88, p. 106 199, 2021.

[89] C. Rodrigues, M. Ramos, R. Esteves, J. Correia, D. Clemente, F. Gonçalves, N. Mathias, M. Gomes, J. Silva, C. Duarte, T. Morais, P. Rosa-Santos, F. Taveira-Pinto, A. Pereira, and J. Ventura, "Integrated study of triboelectric nanogenerator for ocean wave energy harvesting: Performance assessment in realistic sea conditions," *Nano Energy*, vol. 84, p. 105 890, 2021.

[90] H. Joe, H. Roh, H. Cho, and S.-C. Yu, "Development of a flap-type mooring-less wave energy harvesting system for sensor buoy," *Energy*, vol. 133, pp. 851–863, 2017.

[91] O. R. Chowdhury, H. Kim, D. Park, Y. Cho, C. Shin, and J. Park, "Development of a simple and innovative wave energy harvester suitable for ocean sensor network application," *International Journal of Smart Home*, vol. 9, pp. 197–210, 2015.

[92] Y. Li, Q. Guo, M. Huang, X. Ma, Z. Chen, H. Liu, and L. Sun, "Study of an electromagnetic ocean wave energy harvester driven by an efficient swing body toward the self-powered ocean buoy application," *IEEE Access*, vol. 7, pp. 129 758–129 769, 2019.

[93] M. J. Wang, E. Kazyak, N. P. Dasgupta, and J. Sakamoto, "Transitioning solid-state batteries from lab to market: Linking electro-chemo-mechanics with practical considerations," *Joule*, vol. 5, pp. 1371–1390, 2021.

[94] A. Chandrasekhar, V. Vivekananthan, and S.-J. Kim, "A fully packed spheroidal hybrid generator for water wave energy harvesting and self-powered position tracking," *Nano Energy*, vol. 69, p. 104 439, 2020.

[95] X. Chen, L. Gao, J. Chen, S. Lu, H. Zhou, T. Wang, A. Wang, Z. Zhang, S. Guo, X. Mu, Z. L. Wang, and Y. Yang, "A chaotic pendulum triboelectric-electromagnetic hybridized nanogenerator for wave energy scavenging and self-powered wireless sensing system," *Nano Energy*, vol. 69, p. 104 440, 2020.

[96] M. Imran Ullah, T. Badzlin Hashfi, J. S. Döhler, V. M. de Albuquerque, A. Aitkulova, J. Forslund, C. Boström, A. Wahyudie, and I. Temiz, "Isolated grid-forming control of wave energy converter for island electrification," *IEEE Access*, vol. 13, pp. 50 860–50 875, 2025.

[97] A. F. O. Falcão and J. C. C. Henriques, "Oscillating-water-column wave energy converters and air turbines: A review," *Renewable Energy*, vol. 85, pp. 1391–1424, 2016.

[98] F. Fan, Z. Tian, and Z. Wang, "Flexible triboelectric generator," *Nano Energy*, vol. 1, pp. 328–334, 2012.

[99] C. L. Oikonomou, R. P. Gomes, and L. M. Gato, "Unveiling the potential of using a spar-buoy oscillating-water-column wave energy converter for low-power stand-alone applications," *Applied Energy*, vol. 292, p. 116 835, 2021.

[100] A. P. de Almeida Duarte, "Modelling and analysis of a backward bent duct buoy WEC for oceanographic applications," M.S. thesis, Instituto Superior Tecnico, Universidade de Lisboa, Lisbon, Portugal, 2018.

[101] H. Xiao, Z. Liu, R. Zhang, A. Kelham, X. Xu, and X. Wang, "Study of a novel rotational speed amplified dual turbine wheel wave energy converter," *Applied Energy*, vol. 301, p. 117 423, 2021.

[102] H. Wang, W. Wu, L. Zhu, E. Koutroulis, K. Lu, and F. Blaabjerg, "Design and experiment of a new wave power conversion device for self-powered sensor buoy," in *Proc. IECON 2021 – 47th Annual Conference of the IEEE Industrial Electronics Society*, pp. 1–5, 2021.

[103] J. Nolte, R. C. Ertekin, and E. Davis, "In-ocean experiments of a wave energy conversion device moored to an anchor and to a drogue," *Journal of Ocean Technology*, vol. 8, pp. 72–85, 2013.

[104] J. Nolte and R. C. Ertekin, "Wave power calculations for a wave energy conversion device connected to a drogue," *Journal of Renewable and Sustainable Energy*, vol. 6, p. 013 117, 2014.

[105] H. Wang, Z. Fan, T. Zhao, J. Dong, S. Wang, Y. Wang, X. Xiao, C. Liu, X. Pan, Y. Zhao, and M. Xu, "Sandwich-like triboelectric nanogenerators integrated self-powered buoy for navigation safety," *Nano Energy*, vol. 84, p. 105 920, 2021.

[106] M. Carandell, D. M. Toma, M. Carbonell, M. Gasulla, and J. d. Río, "Design and development of a kinetic energy harvester device for oceanic drifter applications," in *Proc. IEEE International Instrumentation and Measurement Technology Conference, Auckland, New Zealand*, pp. 1–6, 2019.

[107] C. Dizon, R. Coe, A. Hamilton, D. Forbush, M. Anderson, T. Brekken, and G. Bacelli, "Analysis on evaluations of Monterey Bay Aquarium Research Institute's wave energy converter's field data using WEC-Sim and gazebo: A simulation tool comparison," *Applied Sciences*, vol. 14, p. 11 169, 2024.

[108] S. Giorgi, R. Coe, M. Reasoner, G. Bacelli, D. Forbush, S. Jensen, F. Cazenave, and A. Hamilton, "Wave energy converter power take-off modeling and validation from experimental bench tests," *IEEE Journal of Oceanic Engineering*, vol. 49, pp. 446–457, 2024.

[109] A. Hamilton, M. Anderson, L. Poubel, D. Dutia, M. Carroll, M. Zhang, R. McEwen, and J. Mayans, *MBARI Wave Energy Conversion Simulation*, version 1.0.0, 2023. [Online]. Available: `https://github.com/osrf/mbari_wec`.

[110] B. Walsh, T. Dooley, R. Carolan, M. Boland, and T. Kelly, "Analysis of data from the full-scale prototype testing of the WASP – a novel wave measuring buoy," in *Proc. 15th European Wave and Tidal Energy Conference(EWTEC)*, (Bilbao, Spain), pp. 1–8, 2023.

[111] B. Walsh, R. Carolan, M. Boland, T. Dooley, and T. Kelly, "The use of air pressure measurements within a sealed moonpool for sea-state estimation," *Journal of Marine Science and Engineering*, vol. 12, p. 2306, 2024.

[112] X. Du, L. Du, X. Cai, Z. Hao, X. Xie, and F. Wu, "Dielectric elastomer wave energy harvester with self-bias voltage of an ancillary wind generator to power for intelligent buoys," *Energy Conversion and Management*, vol. 253, p. 115 178, 2022.

[113] O. Aiello, C. Boragno, D. D. Caviglia, A. L. Schiavo, and F. Nicora, "Analysis of a sea wave energy harvester for environmental monitoring buoys," in *2024 31st IEEE International Conference on Electronics, Circuits and Systems (ICECS)*, (Nancy, France), pp. 1–4, 2024.

[114] H. Wang, W. Wu, X. Hou, L. Cui, and F. Blaabjerg, "A new active motion control strategy for built-in wave energy converter of ocean data buoys," *IEEE Transactions on Industrial Electronics*, vol. 72, pp. 3213–3222, 2025.

[115] T. Dillon, S. Palmer, B. Maurer, M. Gunawan, and B. Polagye, "Techno-economic comparison of resources for powering oceanographic observation," *SSRN Preprint*, pp. 1–58, 2024.

[116] A. Azam, A. Ahmed, H. Li, A. M. Tairab, C. Jia, N. Li, and Z. Zhang, "Design and analysis of the optimal spinning top-shaped buoy for wave energy harvesting in low energy density seas for sustainable marine aquaculture," *Ocean Engineering*, vol. 255, p. 111 434, 2022.

[117] A. Azam, A. Ahmed, M. Yi, Z. Zhang, X. Tan, A. Ali, and N. Li, "A self-stabilizing point absorber wave energy converter with a top-shaped buoy and non-linear power take-off for oceanographic applications," *Ocean Engineering*, vol. 288, p. 116 018, 2023.

[118] A. Ahmed, Y. Wang, A. Azam, N. Li, C. Jia, and Z. Zhang, "Design of an s-shaped point-absorber wave energy converter with a non-linear pto to power the satellite-respondent buoys in the east china sea," *Ocean Engineering*, vol. 275, p. 114 162, 2023.

[119] B. Guo and J. V. Ringwood, "Parametric study of a vibro-impact wave energy converter," *IFAC-PapersOnLine (21st IFAC World Congress)*, vol. 53, pp. 12 283–12 288, 2020.

[120] B. Guo and J. Ringwood, "Non-linear modeling of a vibro-impact wave energy converter," *IEEE Transactions on Sustainable Energy*, vol. 12, pp. 492–500, 2021.

[121] L. Xu, Y. Zuo, B. Guo, and K. Yang, "Parametric study of a vibro-impact point absorber wave energy converter for marine data buoys in irregular wave," in *Proc. 2024 International Conference of Electrical, Electronic and Networked Energy Systems*, (Singapore), pp. 120–127, 2025.

[122] H. Li and L. Wang, "Numerical study on self-power supply of large marine monitoring buoys: Wave-excited vibration energy harvesting and harvester optimization," *Energy*, vol. 285, p. 129 377, 2023.

[123] H. Zhang, Y. Huang, P. Li, and D. Xu, "Bistable built-in ocean wave energy harvester for ocean buoys," *Journal of Cleaner Production*, vol. 496, p. 145 161, 2025.

[124] L. Wang, H. Li, and J. Jiang, "A high-efficiency wave-powered marine observation buoy: Design, analysis, and experimental tests," *Energy Conversion and Management*, vol. 270, p. 116 154, 2022.

[125] L. Wang, J. Lin, H. Li, J. Jiang, S. Wu, and G. Lu, "Achieving efficient power generation for an enclosed drifting buoy by multi-dof wave energy harvesting," *Ocean Engineering*, vol. 305, p. 117 834, 2024.

[126] L. Wang, R. Yang, H. Li, J. Lin, and C. Wen, "Investigating the influence of geometry on the performance of a wave-powered marine observation buoy: The wave-to-wire approach," *Energy*, vol. 309, p. 133 022, 2024.

[127] N. Vella, J. Foley, J. Sloat, A. Sandoval, L. D'Attile, and M. Masoumi, "A modular wave energy converter for observational and navigational buoys," *Fluids*, vol. 7, p. 88, 2022.

[128] C. Zhang, Y. Hao, X. Lu, W. Su, H. Zhang, J. Wang, and X. Li, "Passive wireless marine internet-of-things buoy based on hybrid nanogenerator with omnidirectional water-wave energy harvesting," *Nano Energy*, vol. 138, p. 110 809, 2025.

[129] W. Cui, J. Hu, H. Yang, X. Liu, Y. Wang, Y. Lou, M. Li, Z. Li, A. Yu, Z. L. Wang, and J. Zhai, "Self-powered wireless sensor node enabled by ultra-high-output swinging hybrid generator toward real-time and in-situ marine meteorological observations," *Nano Energy*, vol. 129, p. 110 051, 2024.

[130] T. Guan, W. Wang, X. Wang, C. Wen, R. Xu, C. Zhu, T. Zou, J. Zheng, M. Xu, and H. Wang, "Corrugation-like triboelectric nanogenerators integrated buoys for wave energy harvesting," *Journal of Physics: Conference Series*, vol. 2592, p. 012 052, 2023.

[131] T. Wang, Z. Guo, H. Jin, Y. Li, B. Liu, J. Liu, G. Xu, P. Xu, and M. Xu, "A coral-inspired and fully self-powered wave monitoring system based on hybridized triboelectric-electromagnetic nanogenerator," *Sensors and Actuators A: Physical*, vol. 387, p. 116 451, 2025.

[132] L. He, R. Liu, X. Liu, Z. Zhang, L. Zhang, and G. Cheng, "A novel piezoelectric wave energy harvester based on cylindrical-conical buoy structure and magnetic coupling," *Renewable Energy*, vol. 210, pp. 397–407, 2023.

[133] R. Liu, B. Yang, W. Fan, Z. Liu, C. Wang, and L. He, "Research on a frequency-increasing piezoelectric wave energy harvester based on gear mechanism and magnetic rotor," *Smart Materials and Structures*, vol. 33, p. 105 018, 2024.

[134] W. Feng, X. Luo, S. Yang, and Q. Zou, "Magnetic excitation for coupled pendulum and piezoelectric wave energy harvester," *Micromachines*, vol. 16, p. 252, 2025.

[135] X. Du, P. Li, Z. Li, X. Liu, W. Wang, Q. Feng, L. Du, H. Yu, J. Wang, X. Xie, and L. Tang, "Multi-pillar piezoelectric stack harvests ocean wave energy with oscillating float buoy," *Energy*, vol. 298, p. 131 347, 2024.

[136] M. Carandell, D. M. Toma, A. S. Holmes, J. del Río, and M. Gasulla, "Experimental validation of a fast-tracking focv-mppt circuit for a wave energy converter embedded into an oceanic drifter," *Journal of Marine Science and Engineering*, vol. 11, 2023.

[137] M. Carandell Widmer, "Contributions to the design of energy harvesting systems for autonomous sensors in low power marine applications," Ph.D. dissertation, Universitat Politècnica de Catalunya (UPC), Departament d'Enginyeria Electrònica, Barcelona, Spain, 2022.

[138] J. C. C. Henriques, W. Sheng, A. F. O. Falcão, and L. M. C. Gato, "A comparison of biradial and Wells air turbines on the Mutriku Breakwater OWC wave power plant," in *Proc. ASME 36th International Conference on Ocean, Offshore and Arctic Engineering*, (Trondheim, Norway), pp. 62651-1-62651–12, 2017.

[139] P. R. Steenstrup, *Tank testing and numerical modeling*, (Accessed on: Oct. 22, 2021), 2021. [Online]. Available: `https://www.resenwaves.com/wave-energy-data-communications/tank-testing-and-numerical-modelling/`.

[140] E. Davis, R. C. Ertekin, and R. Riggs, "A Buoy-Based WEC Device to Provide Low Power to Sensors," in *Proc. 28th ASME International Conference on Offshore Mechanics and Arctic Engineering*, (Honolulu, USA), pp. 1109–1118, 2009.

[141] D. Symonds, E. P. Davis, and R. C. Ertekin, "Low-power autonomous wave energy capture device for remote sensing and communications applications," in *Proc. IEEE Energy Conversion Congress and Exposition*, (Atlanta, USA), pp. 2392–2396, 2010.

[142] P. Craig Kohler, L. LeBlanc, and J. Elliott, "SCOOP - NDBC's new ocean observing system," in *OCEANS 2015 - MTS/IEEE Washington*, (Washington, USA), pp. 1–5, 2015.

[143] P. Nicola, B. Giovanni, P. Biagio, S. S. Antonello, V. Giacomo, M. Giuliana, and S. Gianmaria, "Wave tank testing of a pendulum wave energy converter 1:12 scale model," *International Journal of Applied Mechanics*, vol. 09, p. 1 750 024, 2017.

[144] D. Gemme, S. Bastien, R. Sepe, J. Montgomery, S. Grilli, and A. Grilli, "Experimental testing and model validation for ocean wave energy harvesting buoys," in *Proc. 2013 IEEE Energy Conversion Congress and Exposition*, (Denver, USA), pp. 337–343, 2013.

[145] Pelagic Innovation Ltd., *tfi - Gator*, (Accessed on: Nov. 29, 2021), 2021. [Online]. Available: `http://pelagicinnovation.com/tfi-gator/`.

[146] A. Zurkinden, F. Campanile, and L. Martinelli, "Wave energy converter through piezoelectric polymers," in *Proc. COMSOL Users Conference*, (Grenoble, France), pp. 1–7, 2007.

[147] J. Ramello, "Small scale WEC rig for control demonstration," M.S. thesis, Politecnico di Torino, Corso di laurea magistrale in Mechatronic Engineering (Ingegneria Meccatronica), Turin, Italy, 2023.

[148] M. Carandell, D. M. Toma, J. del Río, and M. Gasulla, "Optimum mppt strategy for low-power pendulum-type wave energy converters," in *2020 IEEE SENSORS*, pp. 1–4, 2020.

[149] M. Rosati, J. Henriques, and J. Ringwood, "Oscillating-water-column wave energy converters: A critical review of numerical modelling and control," *Energy Conversion and Management: X*, vol. 16, p. 100 322, 2022.

[150] Clay Mathematics Institute, "The Navier-Stokes equation," 2024, (Accessed on: Sept 21, 2025. [Online]. Available: `https://www.claymath.org/millennium/navier-stokes-equation/`.

[151] C. Windt, J. Davidson, and J. V. Ringwood, "High-fidelity numerical modelling of ocean wave energy systems: A review of computational fluid dynamics-based numerical wave tanks," *Renewable and Sustainable Energy Reviews*, vol. 93, pp. 610–630, 2018.

[152] N. Quartier, T. Vervaet, G. V. Fernandez, J. M. Domínguez, A. J. Crespo, V. Stratigaki, and P. Troch, "High-fidelity numerical modelling of a two-WEC array with accurate implementation of the pto system and control strategy using dualsphysics," *Energy*, vol. 296, p. 130 888, 2024.

[153] H. Qin, H. Su, Z. Wen, and H. Liang, "Latching control of a point absorber wave energy converter in irregular wave environments coupling computational fluid dynamics and deep reinforcement learning," *Applied Energy*, vol. 396, p. 126 282, 2025.

[154] S. Giorgi, J. Davidson, and J. V. Ringwood, "Identification of wave tank models from numerical wave tank data – part 2: Data-based model determination," *IEEE Transactions on Sustainable Energy*, vol. 7, pp. 1020–1027, 2016.

[155] S. Giorgi, J. Davidson, M. Jakobsen, M. Kramer, and J. V. Ringwood, "Identification of dynamic models for a wave energy converter from experimental data," *Ocean Engineering*, vol. 183, pp. 426–436, 2019.

[156] H. Lamb, in *Hydrodynamics (6th Ed.)* Cambridge University Press, Cambridge, UK, 1994.

[157] S. S. Rao, "Chapter 18 - Inviscid and incompressible flows," in *The Finite Element Method in Engineering (6th Ed.)* Butterworth-Heinemann, 2018.

[158] WAMIT, Inc., *WAMIT user manual*, Version 7.5, 2023.

[159] "Analytical representation of nonlinear froude-krylov forces for 3-dof point absorbing wave energy devices," *Ocean Engineering*, vol. 164, pp. 749–759, 2018.

[160] M. Rosati and J. V. Ringwood, "Towards hydrodynamic control of an oscillating water column wave energy converter," in *Proc. of the 5th International Conference on Renewable Energies Offshore (RENEW) 2022*, (Lisbon, Portugal), pp. 411–418, 2022.

[161] S. K. Chakrabarti, "Chapter 3 - Wave theories," in *Hydrodynamics of Offshore Structures*, Computational Mechanics Publications, 1987.

[162] T. Sarpkaya and M. Isaacson, "Chapter 4 - Wave theories," in *Mechanics of Wave Forces on Offshore Structures*, Van Nostrand Reinholt Company, 1981.

[163] M. Folley, T. Whittaker, and A. Henry, "The effect of water depth on the performance of a small surging wave energy converter," *Ocean Engineering*, vol. 34, pp. 1265–1274, 2007.

[164] T. Whittaker and M. Folley, "Nearshore oscillating wave surge converters and the development of Oyster," *Philosophical Transactions of the Royal Society A: Mathematical, Physical and Engineering Sciences*, vol. 370, pp. 345–364, 2012.

[165] N. M. Tom, M. J. Lawson, Y. H. Yu, and A. D. Wright, "Development of a nearshore oscillating surge wave energy converter with variable geometry," *Renewable Energy*, vol. 96, pp. 410–424, 2016.

[166] M. A. Choiniere, N. M. Tom, and K. P. Thiagarajan, "Study of a novel oscillating surge wave energy converter," in *Proc. of Offshore Energy and Storage*, (Cape Cod, USA), pp. 1–13, 2017.

[167] M. E. McCormick, in *Ocean Wave Energy Conversion (Dover Ed.)* Dover Civil and Mechanical Engineering, Mineoala, NY, USA, 2007.

[168] P. Beirão and D. Valério, "Numerical comparison between deep water and intermediate water depth expressions applied to a wave energy converter," *AIMS Energy*, vol. 3, pp. 525–546, 2015.

[169] L. T. Contreras Montoya, S. Lain, M. Issa, and A. Ilinca, "Chapter 4 - Renewable energy systems," in *Hybrid Renewable Energy Systems and Microgrids*, Academic Press, 2021.

[170] "On the principle of impedance-matching for underactuated wave energy harvesting systems," *Applied Ocean Research*, vol. 118, p. 102 958, 2022.

[171] S. P. Neill, "Chapter 5 - Wave energy," in *Fundamentals of Ocean Renewable Energy*, M. R. Hashemi, Ed., Academic Press, 2018.

[172] Y. Goda, in *Random Seas and Design of Maritime Structures*, 3rd ed., World Scientific, Singapore, 2010.

[173] T. R. Mundon and J. Goldsmith, "Chapter 27 - State of the art and future outlook of integrating wave and tidal energy," in *Renewable Energy Integration*, L. E. Jones, Ed., Academic Press, Boston, 2014.

[174] N. D. Katopodes, "Chapter 2 - Air-water interface," in *Free-Surface Flow*, N. D. Katopodes, Ed., Butterworth-Heinemann, 2019.

[175] M. K. Ochi and E. N. Hubble, "On six-parameters wave spectra," in *Proc. 15th International Conference on Coastal Engineering*, (Honolulu, USA), pp. 301–328, 1976.

[176] W. Zhao, M. Efthymiou, S. Wille, and F. McPhail, "Roll performance of an LNGC with partially-filled spherical tanks," in *Offshore Technology Conference*, OTC-27088-MS, 2016.

[177] R. G. Coe, G. Bacelli, and D. Forbush, "A practical approach to wave energy modeling and control," *Renewable and Sustainable Energy Reviews*, vol. 142, p. 110 791, 2021.

[178] F. D. Mosquera, N. Faedo, C. A. Evangelista, J. V. Ringwood, and P. F. Puleston, "Wave energy optimal control structure with second-order sliding mode tracking: Hardware-in-the-loop assessment," *IEEE Transactions on Sustainable Energy*, vol. 15, pp. 1341–1350, 2024.

[179] Y. Chen, J. V. Ringwood, and S. Zhan, "Distributed nonlinear model predictive control of an array of wave energy converters," *Ocean Engineering*, vol. 338, p. 121 915, 2025.

[180] O. M. Phillips, "The equilibrium range in the spectrum of wind-generated waves," *Journal of Fluid Mechanics*, vol. 4, pp. 426–434, 1958.

[181] O. M. Mazzaretto, M. Menéndez, and H. Lobeto, "A global evaluation of the JONSWAP spectra suitability on coastal areas," *Ocean Engineering*, vol. 266, p. 112 756, 2022.

[182] J. Prendergast, M. Li, and W. Sheng, "A study on the effects of wave spectra on wave energy conversions," *IEEE Journal of Oceanic Engineering*, vol. 45, pp. 271–283, 2020.

[183] H. A. Said, "Grid integration aspects of wave energy," Ph.D. dissertation, Faculty of Science and Engineering, National University of Ireland Maynooth, 2024.

[184] H. A. Said and J. V. Ringwood, "Intelligent control of a DC microgrid consisting of wave energy converter (WEC) and hybrid energy storage system (HESS)," in *Proc. 14th European Wave and Tidal Energy Conference EWTEC 2021*, (Plymouth, UK), pp. 1884-1-1884–9, 2021.

[185] I. Tsukrov, O. Eroshkin, W. Paul, and B. Celikkol, "Numerical modeling of nonlinear elastic components of mooring systems," *IEEE Journal of Oceanic Engineering*, vol. 30, pp. 37–46, 2005.

[186] W. E. Cummins, "The impulse response function and ship motions," *Schiffstechnik*, vol. 9, pp. 101–109, 1962.

[187] T. Ogilvie, "Recent progress towards the understanding and prediction of ship motions," in *Proc. of the 6th Symposium on Naval Hydrodynamics*, (Bergen, Norway), pp. 3–80, 1964.

[188] B. Guo, R. J. Patton, S. Jin, and J. Lan, "Numerical and experimental studies of excitation force approximation for wave energy conversion," *Renewable Energy*, vol. 125, pp. 877–889, 2018.

[189] R. Luck and Y. Liu, "Continuous-time and discrete-time singular value decomposition of an impulse response function," *Applied Mathematics*, vol. 12, pp. 336–347, 2021.

[190] Y. Peña-Sanchez, N. Faedo, M. Penalba, G. Giuseppe, A. Mérigaud, C. Windt, D. García-Violini, L. Wang, and J. V. Ringwood, "Finite-order hydrodynamic approximation by moment-matching (FOAMM) toolbox for wave energy applications," in *Proc. 13th European Wave and Tidal Energy Conference (EWTEC)*, (Napoli, Italy), pp. 1448-1-1448–9, 2019.

[191] J. S. Bay, in *Fundamentals of Linear State Space Systems*, McGraw-Hill, Boston, MA, 1999.

[192] D. V. Evans, "The oscillating water column wave-energy device," *IMA Journal of Applied Mathematics*, vol. 22, pp. 423–433, 1978.

[193] S. Raghunathan, "A methodology for the wells turbine design," *Journal of Power and Energy*, vol. 209, pp. 221–232, 1995.

[194] L. M. C. Gato and J. C. C. Henriques, "Optimization of symmetrical profiles for the Wells turbine rotor blades," in *Proc. the ASME Fluids Engineering Division Summer Meeting*, (San Diego, USA), 1996.

[195] H. Askari, E. Hashemi, A. Khajepour, M. Khamesee, and Z. Wang, "Towards self-powered sensing using nanogenerators for automotive systems," *Nano Energy*, vol. 53, pp. 1003–1019, 2018.

[196] P. Qian, B. Feng, H. Wen, X. Jiang, Y. Ying, Y. Si, and D. Zhang, "Maximum power point tracking for triboelectric nanogenerator based wave energy converters," *Nano Energy*, vol. 98, p. 107 249, 2022.

[197] L. Liu, X. Guo, and C. Lee, "Promoting smart cities into the 5G era with multi-field internet of things (IoT) applications powered with advanced mechanical energy harvesters," *Nano Energy*, vol. 88, p. 106 304, 2021.

[198] Y. Fu, H. Ruan, and D. Ning, "Hydro-electromechanical modeling of TENG-based wave energy converter," *International Journal of Mechanical Sciences*, p. 110 828, 2025.

[199] "Advanced modular rotary triboelectric nanogenerator: Pushing boundaries in peak power density and impedance reduction," *Nano Energy*, vol. 134, p. 110 557, 2025.

[200] S. Pan and Z. Zhang, "Fundamental theories and basic principles of triboelectric effect: A review," *Friction*, vol. 7, pp. 2–17, 2019.

[201] Z. Xu, L. N. Cao, and Z. L. Wang, "Triboelectric nanogenerators for scientific instruments and devices," *Advanced Devices & Instrumentation*, vol. 5, p. 0026, 2024.

[202] A. Kaur, S. Jadaun, M. Sharma, A. Gupta, and G. Sapra, "Single electrode triboelectric nanogenerator integrated pacemaker lead for cardiac energy harvesting," *Sensors and Actuators A: Physical*, vol. 390, p. 116 606, 2025.

[203] S. Meleshko, N. Moshkin, V. Pukhnachev, and V. Samatova, "On steady two-dimensional analytical solutions of the viscoelastic maxwell equations," *Journal of Non-Newtonian Fluid Mechanics*, vol. 270, pp. 1–7, 2019.

[204] Z. L. Wang, "On the expanded Maxwell's equations for moving charged media system – general theory, mathematical solutions and applications in TENG," *Materials Today*, vol. 52, pp. 348–363, 2022.

[205] H. Hertz, "On the relations between Maxwell's fundamental equations of the opposing electromagnetics," *Wiedemann's Annalen*, vol. 23, pp. 84–103, 1884.

[206] H. Minkowski, "Die grundgleichungen für die elektromagnetischen vorgänge in bewegten körpern," *Nachrichten von der Gesellschaft der Wissenschaften zu Göttingen, Mathematisch-Physikalische Klasse*, vol. 1908, pp. 53–111, 1908.

[207] C. Wang, "Minkowski tensor in electrodynamics of moving media and three rules for construction of the physical tensors in Einstein's special relativity," *Optik*, vol. 223, p. 165 469, 2020.

[208] A. Cammarata, J. Y. Damte, and T. Polcar, "First-principles guidelines to select promising van der Waals materials for hybrid photovoltaic-triboelectric nanogenerators," *Nanoscale*, vol. 16, pp. 16 582–16 592, 2024.

[209] M. V. Berry, "Regular and irregular motion," AIP Conference Proceedings, vol. 46, pp. 16–120, 1978.

[210] H. Cestaro, N. Mathias, N. D. Gonçalves, and T. Morais, "TENG estimation model of voltage production for buoys using particle swarm optimization," *Applied Ocean Research*, vol. 125, p. 103 231, 2022.

[211] I. Torre-Enciso, I. Ortubia, L. López De Aguileta, and J. Marqués, "Mutriku wave power plant: From the thinking out to the reality," in *Proc. 8th European Wave and Tidal Energy Conference (EWTEC)*, (Uppsala, Sweden), pp. 319–329, 2009.

[212] A. Vega-Valladares, M. Garcia-Diaz, and B. Pereiras, "Multi-objective response surface optimization of a centrifugal turbine for application in oscillating water column devices equipped with a twin turbine configuration," *Ocean Engineering*, vol. 324, p. 120 629, 2025.

[213] M. Rosati, "Real-time control of oscillating water column wave energy converters," Ph.D. dissertation, Departament of Electronic Engineering, National University of Ireland Maynooth, 2024.

[214] H. B. Bingham, Y.-H. Yu, K. Nielsen, T. T. Tran, K.-H. Kim, S. Park, K. Hong, H. A. Said, T. Kelly, J. V. Ringwood, R. W. Read, E. Ransley, S. Brown, and D. Greaves, "Ocean energy systems wave energy modeling task 10.4: Numerical modeling of a fixed oscillating water column," *Energies*, vol. 14, p. 1718, 2021.

[215] W. Sheng, R. Alcorn, and A. Lewis, "On thermodynamics in the primary power conversion of oscillating water column wave energy converters," *Journal of Renewable and Sustainable Energy*, p. 023 105, 2013.

[216] C. Josset and A. Clément, "A time-domain numerical simulator for oscillating water column wave power plants," *Renewable Energy*, vol. 32, pp. 1379–1402, 2007.

[217] K. S. Schmitz, "Chapter 4 - Thermodynamics of the gas state," in *Physical Chemistry*, K. S. Schmitz, Ed., Elsevier, Boston, 2017.

[218] M. Rosati, T. Kelly, and J. V. Ringwood, "Nonlinear data-based hydrodynamic modeling of a fixed oscillating water column wave energy device," *IEEE Access*, vol. 9, pp. 149 756–149 765, 2021.

[219] T. Kelly, I. Zabala, Y. Peña-Sanchez, J. V. Ringwood, J. Henriques, and J. M. Blanco, "A post-processing technique for removing irregular frequencies and other issues in the results from BEM solvers," *International Journal of Marine Energy*, pp. 123–131, 2022.

[220] M. B. Mandev, A. Çelik, and A. Altunkaynak, "Optimization of OWC efficiency: Experimental insights into geometrically modified chambers," *Energy*, vol. 337, p. 138 689, 2025.

[221] F. He, J. Pan, Y. Lin, M. Song, and S. Zheng, "Laboratory modelling of nonlinear power take-off damping and its effects on an offshore stationary cylindrical owc device," *Energy*, vol. 296, p. 131 217, 2024.

[222] X. Zhang, R. Mayon, F. Zhou, and D. Ning, "Experimental and numerical investigation on a novel dual-chamber OWC-WEC integrated with an energy-focusing breakwater," *Coastal Engineering*, vol. 201, p. 104 814, 2025.

[223] W. Sheng, "An experimental study for improving performance of a cylindrical OWC WEC with a heave plate," *Renewable and Sustainable Energy Reviews*, vol. 214, p. 115 517, 2025.

[224] A. Falcão, L. Gato, and E. Nunes, "A novel radial self-rectifying air turbine for use in wave energy converters," *Renewable Energy*, vol. 50, pp. 289–298, 2012.

[225] A. F. Falcão, J. C. Henriques, and L. M. Gato, "Self-rectifying air turbines for wave energy conversion: A comparative analysis," *Renewable and Sustainable Energy Reviews*, vol. 91, pp. 1231–1241, 2018.

[226] C. Moisel and T. H. Carolus, "A facility for testing the aerodynamic and acoustic performance of bidirectional air turbines for ocean wave energy conversion," *Renewable Energy*, vol. 86, pp. 1340–1352, 2016.

[227] A. Wells, "Fluid driven rotary transducer," British Patent 1 595 700, 1976.

[228] A. F. O. Falcão, "Chapter 8 - Air turbines," in *Wave Energy Utilization: A Review of the Technologies*, Elsevier, 2010.

[229] A. A. Babintsev, "Apparatus for converting sea wave energy into electrical energy," U.S. Patent 3 922 739, 1978.

[230] L. A. Pelton, "Water wheel," U.S. Patent 233 692, 1880.

[231] R. Starzmann, in *Aerodynamic and Aeroacoustic Performance of Wells Turbines for Wave Energy Conversion*, ser. Fortschritt-Berichte VDI, Reihe 7: Stroemungstechnik, vol. 500, 163 pages, VDI Verlag, 2012.

[232] L. Gato, D. Ferreira, and D. Sá, "Biradial turbine rotor aerodynamic design and parametric analysis," *Energy Conversion and Management*, vol. 278, p. 116 651, 2023.

[233] T. K. Das, P. Halder, and A. Samad, "Optimal design of air turbines for oscillating water column wave energy systems: A review," *The International Journal of Ocean and Climate Systems*, vol. 8, pp. 37–49, 2017.

[234] S. Raghunathan, C. P. Tan, and N. A. J. Wells, "Test on 0.2m diameter Wells turbine," The Queen's University of Belfast, Report WE/80/14R, 1980.

[235] E. N. Jacobs and A. Sherman, "Airfoil section characteristics as affected by variations of the Reynolds Number," National Advisory Committee for Aeronautics, Report 586, 1939, Reprint of Report No. 66, originally published September 1939.

[236] K. Tongsawang, "Stall control of a NACA0015 aerofoil at low Reynolds numbers," M.S. thesis, University of Sheffield, Sheffield, United Kingdom, 2015.

[237] J. Julian, W. Iskandar, F. Wahyuni, and Ferdyanto, "Computational fluid dynamics analysis based on the fluid flow separation point on the upper side of the NACA 0015 airfoil with the coefficient of friction," *Journal Media Mesin*, vol. 23, pp. 70–82, 2022.

[238] L. Ljung, in *System Identification: Theory for the User (2nd Ed.)* Prentice-Hall, Upper Saddle River, NJ, USA, 1999.

[239] L. Ljung, "Perspectives on system identification," *Annual Reviews in Control*, vol. 34, pp. 1–12, 2010.

[240] Sealite, *Sealite Atlantic-2600 navigation buoy*, (Accessed on: Jan. 08, 2023), 2021. [Online]. Available: `https://www.sealite.com/large-ocean-buoy-2600mm-diameter/`.

[241] M. Rosati, T. Kelly, D. G. Violini, and J. V. Ringwood, "Data-based hydrodynamic modelling of a fixed OWC wave energy converter," in *Proc. 14th European Wave and Tidal Energy Conference EWTEC 2021*, (Plymouth, UK), pp. 281-1-281–10, 2021.

[242] M. Rosati, H. Bingham, B. Joensen, K. Nielsen, and J. V. Ringwood, "A data-based modelling approach for a vented oscillating water column wave energy converter," in *Proc. RENEW 2022*, (Lisbon, Portugal), pp. 339–347, 2022.

[243] S. Chen, "Orthogonal-least-squares forward selection for parsimonious modelling from data," *Engineering*, vol. 01, pp. 55–74, 2009.

[244] N. N. Narisetty, "Chapter 4 - Bayesian model selection for high-dimensional data," in *Principles and Methods for Data Science*, ser. Handbook of Statistics, A. S. Srinivasa Rao and C. Rao, Eds., vol. 43, Elsevier, 2020.

[245] T. Söderström and P. Stoica, in *System Identification*, Prentice Hall, Upper Saddle River, NJ, USA, 1989.

[246] Almarin, *B1600S Balizamar buoy*, (Accessed on: Dec. 14, 2022), 2021. [Online]. Available: `https://www.almarin.es/en/marine-aids-to-navigation/navigation-buoys/b1600s-buoys`.

[247] JFC Marine, "Aids to navigation: Gannet buoys," *(Accessed on: Sept. 21, 2024)*, 2023. [Online]. Available: `https://jfcmarine.com/product/o1200-gannet-navigation-buoy/`.

[248] T. Kelly, "Experimental and numerical modelling of a multiple oscillating water column structure," Ph.D. dissertation, Faculty of Science and Engineering, National University of Ireland Maynooth, 2018.

[249] M. Paderi and P. Puddu, "Experimental investigation in a wells turbine under bi-directional flow," *Renewable Energy*, vol. 57, pp. 570–576, 2013.

[250] T. K. Das, K. Kumar, and A. Samad, "Experimental analysis of a biplane wells turbine under different load conditions," *Energy*, vol. 206, p. 118 205, 2020.

[251] A. Governo, J. Henriques, and L. Gato, "Modelling mooring line snap loads using a high-order finite-volume approach," *Ocean Engineering*, vol. 275, p. 113 803, 2023.

[252] S. Camporeale and P. Filianoti, "Behaviour of a small wells turbine under randomly varying oscillating flow," in *Proc. 8th European Wave and Tidal Energy Conference EWTEC*, (Uppsala, Sweden), pp. 690–696, 2009.

[253] M. Van Wieren, T. D. Gonzalez, H. Yassin, N. Jeanetta-Wark, T. Kumpula, J. Naglak, and G. Parker, "Development of a low-friction testbed for model scale wave energy converter control system studies," in *Proc. OCEANS 2023*, (Biloxi, USA), pp. 1–7, 2023.

[254] F. Ferri, "Numerical model development and validation for the WEC COMP control competition: Preprint," in *Proc. 37th International Conference on Ocean, Offshore and Arctic Engineering*, (Madrid, Spain), pp. 1–10, 2018.

[255] J. D. A. Jr., "Chapter 5 - Incompressible flow over finite wings," in *Fundamentals of Aerodynamics*, McGraw-Hill Education, 2016.

[256] T. Heath, T. J. T. Whittaker, and C. B. Boake, "The design, construction and operation of the LIMPET wave energy converter (islay, scotland)," in *Proc. 4th European Wave Energy Conference (EWTEC)*, (Aalborg, Denmark), pp. 49–55, 2000.

[257] "Sea trial results of the biradial and wells turbines at mutriku wave power plant," *Energy Conversion and Management*, vol. 268, p. 115 936, 2022.

[258] T. K. Sengupta, V. Vikas, and A. Johri, "An improved method for calculating flow past flapping and hovering airfoils," *Theoretical and Computational Fluid Dynamics*, vol. 19, pp. 417–440, 2005.

[259] L.-H. Feng, T. N. Jukes, K.-S. Choi, and J.-J. Wang, "Flow control over a NACA 0012 airfoil using dielectric-barrier-discharge plasma actuator with a Gurney flap," *Experiments in Fluids*, vol. 52, pp. 1533–1546, 2012.

[260] A. Javed, K. Djidjeli, A. Naveed, and J. T. Xing, "Low Reynolds number effect on energy extraction performance of semi-passive flapping foil," *Journal of Applied Fluid Mechanics*, vol. 11, pp. 1613–1627, 2018.

[261] F. M. White, "Chapter 6 - Viscous flow in ducts," in *Fluid Mechanics*, 8th, McGraw-Hill Education, 2016.

[262] A. Carrelhas, L. Gato, J. Henriques, A. Falcão, and J. Varandas, "Test results of a 30kW self-rectifying biradial air turbine-generator prototype," *Renewable and Sustainable Energy Reviews*, vol. 109, pp. 187–198, 2019.

[263] P. Puddu, M. Paderi, and C. Manca, "Aerodynamic characterization of a wells turbine under bi-directional airflow," *Energy Procedia*, vol. 45, pp. 278–287, 2014.

[264] M. Costa, K. Damasceno, E. Nepomuceno, and F. Tofoli, "Modeling and design of a low-cost constant current electronic load," in *Proc. 15th Seminar on Power Electronics and Control (SEPOC)*, (Santa Maria, Brazil), pp. 1–6, Oct. 2023.

[265] C. Collins III, B. Lund, T. Waseda, and H. Graber, "On recording sea surface elevation with accelerometer buoys: Lessons from itop (2010)," *Ocean Dynamics*, vol. 64, pp. 1–10, 2014.

[266] S. Chakraborty, K. Ide, and B. Balachandran, "Missing values imputation in ocean buoy time series data," *Ocean Engineering*, vol. 318, p. 120 145, 2025.

[267] K. Budal, J. Falnes, L. C. Iversen, P. M. Lillebekken, G. Oltedal, T. H. amd T. Onshus, and A. S. Høy, "The Norwegian wave-power buoy project," in *Proc. Second International Symposium on Wave Energy Utilization,*, (Trondheim, Norway), pp. 323–344, 1982.

[268] A. Altunkaynak, "Adaptive estimation of wave parameters by Geno-Kalman filtering," *Ocean Engineering*, vol. 35, pp. 1245–1251, 2008.

[269] A. Altunkaynak and M. Özger, "Temporal significant wave height estimation from wind speed by perceptron Kalman filtering," *Ocean Engineering*, vol. 31, pp. 1245–1255, 2004.

[270] S. Küchler, J. Eberharter, K. Langer, K. Schneider, and O. Sawodny, "Heave motion estimation of a vessel using acceleration measurements," in *Proc. 18th IFAC World Congress*, (Milan, Italy), pp. 14742–14747, 2011.

[271] Ø. F. Auestad, J. T. Gravdahl, and T. I. Fossen, "Heave motion estimation on a craft using a strapdown inertial measurement unit," in *Proc. 9th IFAC Conference on Control Applications in Marine Systems*, (Osaka, Japan), pp. 298–303, 2013.

[272] H. Øveraas, T. H. Bryne, and T. A. Johansen, "A linear time-invariant Kalman filter for estimating height in the presence of ocean waves," *Ocean Engineering*, vol. 320, p. 120 214, 2025.

[273] R. Pascoal and C. Guedes Soares, "Kalman filtering of vessel motions for ocean wave directional spectrum estimation," *Ocean Engineering*, vol. 36, pp. 477–488, 2009.

[274] R. Pascoal, L. Perera, and C. Guedes Soares, "Estimation of directional sea spectra from ship motions in sea trials," *Ocean Engineering*, vol. 132, pp. 126–137, 2017.

[275] H. Kim, H. Kang, and M.-H. Kim, "Real-time inverse estimation of ocean wave spectra from vessel-motion sensors using adaptive Kalman filter," *Applied Sciences*, vol. 9, p. 2729, 2019.

[276] H. Kim, J. Park, C. Jin, M. Kim, and D. Lee, "Real-time inverse estimation of multi-directional random waves from vessel-motion sensors using Kalman filter," *Ocean Engineering*, vol. 280, p. 114 501, 2023.

[277] J. V. Ringwood, S. Zhan, and N. Faedo, "Empowering wave energy with control technology: Possibilities and pitfalls," *Annual Reviews in Control*, vol. 55, pp. 18–44, 2023.

[278] Y. Peña-Sanchez, C. Windt, J. Davidson, and J. V. Ringwood, "A critical comparison of excitation force estimators for wave-energy devices," *IEEE Transactions on Control Systems Technology*, vol. 28, pp. 2263–2275, 2020.

[279] D. García-Violini, N. Faedo, Y. Peña-Sanchez, V. Nava, and J. V. Ringwood, "Revisiting excitation force estimation in WECs: On the (mis)use of structure-based estimation approaches," *Ocean Engineering*, vol. 311, p. 118 864, 2024.

[280] J. González, *Oceanie platform of the Canary Islands (PLOCAN): Marine test site for emerging ocean technologies*, Scientific & Technical Department, Área Científico-Técnica, PLOCAN, 2023.